UNIVERSITAT POLITÈCNICA DE CATALUNYA BARCELONATECH

Desarrollo de un sistema de monitorización de la integridad estructural para aplicaciones en ingeniería mediante técnicas de reducción de la dimensionalidad

David Agis

TESIS DOCTORAL
POR COMPENDIO DE PUBLICACIONES

Desarrollo de un sistema de monitorización de la integridad estructural para aplicaciones en ingeniería mediante técnicas de reducción de la dimensionalidad

Autor:
David AGIS

Director:
Dr. Francesc POZO

Programa de Doctorado en Matemática Aplicada

Departament de Matemàtiques
Facultat de Matemàtiques i Estadística

Barcelona, Septiembre 2020

Universitat Politècnica de Catalunya

Abstract

Facultat de Matemàtiques i Estadística

Departament de Matemàtiques

Desarrollo de un sistema de monitorización de la integridad estructural para aplicaciones en ingeniería mediante técnicas de reducción de la dimensionalidad

by David AGIS

This thesis describes a structural health monitoring (SHM) strategy to detect and classify changes in structures that can be equipped with sensors. SHM is an area of great interest, because its main objective is to verify the health of the structure to ensure its correct operation and, in turn, save maintenance costs. This objective is achieved by using algorithms and equipping the structure with a network of sensors that continuously monitor it.

Researchers from around the world focus their efforts on the development of new forms of continuous monitoring to know the current state of the structure and to avoid possible failures or catastrophes. In this sense, in this work, a network of piezoelectric sensors (PZTs) is used for the development of the strategy of detection and classification of structural changes. This network of PZTs, attached to the surface of the structure to be diagnosed, applies vibrational excitation signals and, at the same time, collects the responses propagated through the structure. With this collected information, certain mathematical algorithms are developed.

To carry out the main task of the proposed methodology, detection and classification of structural changes, the technique called t-distributed stochastic neighbor embedding (t-SNE) is essentially used. This technique is capable of representing the local structure of the high-dimensional data collected by the sensor network in two-dimensional or three-dimensional space. Furthermore, for the classification of structural changes, the detection methodology is expanded by adding the use of three strategies: (a) the smallest point-centroid distance; (b) the majority vote; and (c) the sum of the inverses of the distances.

The methodology proposed in this study is tested and validated using an aluminum plate equipped with four PZT sensors and for certain predefined structural changes. The promising results obtained show the great classification capacity and the strong performance of this methodology, successfully classifying about 100% of the cases in various experimental scenarios.

The main contribution of this project is the combination of the t-SNE technique with a carefully selected pre-processing of the data and with the three proposed classification strategies. This combination significantly improves the quality of the groups or clusters obtained with the damage detection and classification method, which represent the different structural states. Likewise, said combination diagnoses a structure with a low computational cost and high reliability.

Regarding the applicability of the suggested strategy, there is no prescribed field of application: if a network of sensors can be installed in the structure to be diagnosed and several phases of action can be considered, the approach presented here can be, *a priori*, implemented.

KEYWORDS: Classification, detection, parametric *t*-distributed stochastic neighbor embedding (P-*t*-SNE), piezoelectric transducer (PZT), principal component analysis (PCA), structural changes, structural health monitoring (SHM), *t*-distributed stochastic neighbor embedding (*t*-SNE).

Universitat Politècnica de Catalunya

Resumen

Facultat de Matemàtiques i Estadística

Departament de Matemàtiques

Desarrollo de un sistema de monitorización de la integridad estructural para aplicaciones en ingeniería mediante técnicas de reducción de la dimensionalidad

por David AGIS

Esta tesis describe una estrategia de monitorización de la salud estructural (SHM, por sus siglas en inglés) para detectar y clasificar fallos en estructuras que pueden ser equipadas con sensores. La SHM es un área de gran interés, ya que su objetivo principal es la verificación de la salud de la estructura para asegurar su correcto funcionamiento y, a su vez, ahorrar costes de mantenimiento. Este objetivo se consigue haciendo uso de algoritmos y equipando a la estructura con una red de sensores que la monitorizan de forma continuada.

Investigadores de todo el mundo centran sus esfuerzos en el desarrollo de nuevas formas de monitorización continua para conocer el estado actual de la estructura y evitar posibles fallos o catástrofes. En este sentido, en este trabajo, se utiliza una red de sensores piezoeléctricos (PZT, por sus siglas en inglés) para el desarrollo de la estrategia de detección y clasificación de los cambios estructurales. Esta red de PZT, adherida a la superficie de la estructura a diagnosticar, aplica señales vibracionales de excitación y al mismo tiempo recoge las respuestas propagadas a través de la estructura. Con esta información recopilada se desarrollan ciertos algoritmos matemáticos.

Para llevar a cabo la tarea principal de la metodología propuesta, detección y clasificación de fallos, se utiliza esencialmente la técnica denominada *t-distributed stochastic neighbor embedding* (*t*-SNE). Dicha técnica es capaz de representar la estructura local de los datos de alta dimensionalidad recopilados por la red de sensores en un espacio bidimensional o tridimensional. Además, para la clasificación de los cambios estructurales, se amplía la metodología de detección añadiendo el uso de tres estrategias: (a) la distancia punto-centroide más pequeña; (b) el voto mayoritario; y (c) la suma de las inversas de las distancias.

La metodología propuesta en este estudio se prueba y valida utilizando una placa de aluminio equipada con cuatro sensores PZT y para ciertos daños predefinidos. Los prometedores resultados obtenidos ponen de manifiesto la gran capacidad de clasificación y el fuerte rendimiento de esta metodología, clasificando con éxito cerca del 100 % de los casos en varios escenarios experimentales.

La principal contribución de este proyecto es la combinación de la técnica *t*-SNE con un preprocesamiento de los datos cuidosamente seleccionado y con las tres estrategias de clasificación propuestas. Esta combinación mejora significativamente la calidad de los grupos o clústeres obtenidos con el método de detección y clasificación de daños,

que representan los diferentes estados estructurales. Asimismo, dicha combinación diagnostica una estructura con un bajo coste computacional y una alta fiabilidad.

En cuanto a la aplicabilidad de la estrategia sugerida, no hay un campo de aplicación prescrito: si se puede instalar una red de sensores en la estructura a diagnosticar y se pueden considerar varias fases de actuación, el enfoque aquí presentado puede implementarse *a priori*.

PALABRAS CLAVE: Análisis de componentes principales (PCA, por sus siglas en inglés), cambios estructurales, clasificación, detección, monitorización de la salud estructural (SHM, por sus siglas en inglés), parametric *t*-distributed stochastic neighbor embedding (P-*t*-SNE), *t*-distributed stochastic neighbor embedding (*t*-SNE), transductor piezoeléctrico (PZT, por sus siglas en inglés).

Agradecimientos

En primer lugar, quiero dar las gracias a mi director de tesis, el Dr. Francesc Pozo Montero, por abrirme las puertas del mundo de la investigación y por haberme acompañado durante todo este viaje. Gracias por guiar mis pasos en esta etapa de mi vida, especialmente por orientarme en los momentos de oscuridad. Gracias a tu dedicación, esfuerzo y apoyo incondicional hoy estoy escribiendo estas líneas. Y sobre todo, gracias por tu calidad humana, que ha hecho de estos años una experiencia maravillosa.

Agradezco al Dr. Diego Alexander Tibaduiza Burgos y a Jaime Vitola Oyaga su importante colaboración en la obtención de los datos experimentales (nos proporcionaron todos los datos necesarios) y su ayuda sobre cuestiones técnicas específicas relacionadas con los experimentos.

También quisiera agradecer a la Dra. Yolanda Vidal Seguí su amistad y sus valiosas aportaciones que han mejorado la calidad de mi investigación.

Quiero dar las gracias en especial a mi familia, Silvia y Carla. Ellas son los pilares de mi vida. Gracias Silvia por no fallarme nunca y por estar siempre a mi lado en los buenos y malos momentos. Gracias Carla por transmitirme, a través de tu sonrisa, la fuerza necesaria para continuar avanzando. Espero devolveros algún día todo el tiempo que os he robado para realizar este trabajo.

Agradecer a los Proyectos DPI2014-58427-C2-1-R, DPI2017-82930-C2-1-R (Agencia Estatal de Investigación - Ministerio de Economía, Industria y Competitividad y Fondo Europeo de Desarrollo Regional) y 2017 SGR 388 (Generalitat de Catalunya) por servirme de soporte económico.

Finalmente, quiero agradecer a la Universitat Politècnica de Catalunya el haber financiado esta tesis doctoral a través de la beca predoctoral FPI-UPC 2017.

Índice general

Abstract I

Resumen III

Agradecimientos V

1. Tesis por compendio de publicaciones 1

2. Introducción 3

3. Hipótesis del estudio y objetivos de investigación 9

4. Aportaciones de la tesis 11

5. Metodología utilizada 13
5.1. Preprocesamiento de los datos y *clustering*: datos de referencia 13
5.1.1. Integración de los datos 13
5.1.1.1. Despliegue tipo *E* 14
5.1.1.2. *Mean-centered group scaling* (MCGS) 14
5.1.2. Transformación de los datos 16
5.1.3. Reducción de los datos 16
5.1.3.1. Análisis de componentes principales (PCA) 16
5.1.3.2. *t-Distributed stochastic neighbor embedding* (*t*-SNE) . . . 18
5.1.3.3. *Parametric t*-SNE (P-*t*-SNE) 22
5.1.4. Efecto del *clustering* 24
5.2. Detección y clasificación de los daños: estructura a diagnosticar 25
5.2.1. Estandarización (MCGS) 25
5.2.2. Proyección (PCA) 26
5.2.3. *t*-SNE/P-*t*-SNE y clasificación final 26
5.3. Aplicación del método propuesto a una placa de aluminio con 4 PZT . 29
5.3.1. Configuración experimental 29
5.3.2. Escenarios y fases de actuación 30
5.3.3. Integración de los datos experimentales 32
5.3.4. *κ-fold non-exhaustive leave-*p*-out cross-validation* 33
5.3.5. Detección y clasificación de los daños 34

6. Discusión global de los resultados 39
6.1. Artículo 1 40
6.1.1. Escenario 1 40
6.1.2. Escenario 2 40
6.1.3. Escenario 3 41
6.2. Artículo 2 44
6.2.1. Escenario 1 44

6.2.2. Escenario 2 44
6.2.3. Escenario 3 45
6.2.4. Ejemplo ilustrativo de clasificación 47
6.3. Artículo 3 48
6.3.1. Escenario 1 48
6.3.2. Escenario 3 49
6.3.3. Repetibilidad 51
6.4. Comentarios generales 53

7. Conclusiones **55**

8. Futuras líneas de investigación y limitaciones **59**

9. Compendio de artículos publicados **61**

A. Factor de impacto y categoría de las revistas **127**

B. Contribución del doctorando **129**

C. Otros trabajos **131**

Bibliografía **185**

Índice de figuras

5.1. El preprocesamiento en tres etapas 13
5.2. Estructura de la RBM 23
5.3. Distancia punto-centroide más pequeña 27
5.4. Diagrama de flujo, *t*-SNE, dominio tiempo 28
5.5. Diagrama de flujo, *t*-SNE, dominio frecuencia 28
5.6. Diagrama de flujo, P-*t*-SNE, dominio frecuencia 29
5.7. Placa de aluminio con cuatro PZT 30
5.8. Señal *BURST* 31
5.9. Voto mayoritario 37
5.10. Suma de las inversas de las distancias 38

6.1. Ejemplo ilustrativo del *t*-SNE 48
6.2. Gráficos con barras de error 53

Índice de tablas

6.1. Matriz de confusión, *t*-SNE, Escenario 1, uso individual de las fases de actuación, dominio tiempo . . . 40
6.2. Matriz de confusión, *t*-SNE, Escenario 1, se tienen en cuenta las 4 fases de actuación, dominio tiempo . . . 41
6.3. Matriz de confusión, PCA, Escenario 1, uso individual de las fases de actuación, dominio tiempo . . . 41
6.4. Matriz de confusión, *t*-SNE, Escenario 2, uso individual de las fases de actuación, dominio tiempo . . . 42
6.5. Matriz de confusión, *t*-SNE, Escenario 2, se tienen en cuenta las 4 fases de actuación, dominio tiempo . . . 42
6.6. Matriz de confusión, PCA, Escenario 2, uso individual de las fases de actuación, dominio tiempo . . . 42
6.7. Matriz de confusión, *t*-SNE, Escenario 3, uso individual de las fases de actuación, dominio tiempo, artículo 1 . . . 43
6.8. Matriz de confusión, *t*-SNE, Escenario 3, se tienen en cuenta las 4 fases de actuación, dominio tiempo, artículo 1 . . . 43
6.9. Precisión global, FPR y FNR, *t*-SNE, Escenario 3, dominio tiempo, artículo 1 . . . 43
6.10. Matriz de confusión, *t*-SNE, Escenario 1, uso individual de las fases de actuación, dominio frecuencia . . . 44
6.11. Matriz de confusión, *t*-SNE, Escenario 1, se tienen en cuenta las 4 fases de actuación, dominio frecuencia . . . 44
6.12. Matriz de confusión, *t*-SNE, Escenario 2, uso individual de las fases de actuación, dominio frecuencia . . . 45
6.13. Matriz de confusión, *t*-SNE, Escenario 2, se tienen en cuenta las 4 fases de actuación, dominio frecuencia . . . 45
6.14. Matriz de confusión, *t*-SNE, Escenario 3, uso individual de las fases de actuación, dominio frecuencia . . . 46
6.15. Matriz de confusión, *t*-SNE, Escenario 3, se tienen en cuenta las 4 fases de actuación, dominio frecuencia . . . 46
6.16. Matriz de confusión, *t*-SNE, Escenario 3, uso individual de las fases de actuación, dominio tiempo, artículo 2 . . . 47
6.17. Matriz de confusión, *t*-SNE, Escenario 3, se tienen en cuenta las 4 fases de actuación, dominio tiempo, artículo 2 . . . 47
6.18. Precisión global, FPR y FNR, *t*-SNE, Escenario 3, artículo 2 . . . 47
6.19. Matriz de confusión, P-*t*-SNE y *t*-SNE, Escenario 1, voto mayoritario, dominio frecuencia . . . 49
6.20. Matriz de confusión, P-*t*-SNE y *t*-SNE, Escenario 1, suma de las inversas de las distancias, dominio frecuencia . . . 49
6.21. Precisión, PPV, TPR, F_1 score y TNR, P-*t*-SNE y *t*-SNE, Escenario 1, voto mayoritario, dominio frecuencia . . . 50

6.22. Precisión, PPV, TPR, F_1 score y TNR, P-t-SNE y t-SNE, Escenario 1, suma de las inversas de las distancias, dominio frecuencia 50
6.23. Matriz de confusión, P-t-SNE y t-SNE, Escenario 3, voto mayoritario, dominio frecuencia 51
6.24. Matriz de confusión, P-t-SNE y t-SNE, Escenario 3, suma de las inversas de las distancias, dominio frecuencia 51
6.25. Precisión, PPV, TPR, F_1 score y TNR, P-t-SNE y t-SNE, Escenario 3, voto mayoritario, dominio frecuencia 51
6.26. Precisión, PPV, TPR, F_1 score y TNR, P-t-SNE y t-SNE, Escenario 3, suma de las inversas de las distancias, dominio frecuencia 52
6.27. Repetibilidad, Escenario 1, voto mayoritario 52
6.28. Repetibilidad, Escenario 1, suma de las inversas de las distancias . . . 52
6.29. Repetibilidad, Escenario 3, voto mayoritario 52
6.30. Repetibilidad, Escenario 3, suma de las inversas de las distancias . . . 53

Lista de Abreviaciones

CD	*Contrastive Divergence*
CM	*Condition Monitoring*
EOC	*Environmental and Operational Conditions*
FFT	*Fast Fourier Transform*
FNR	*False-Negative Rate*
FPR	*False-Positive Rate*
ISOMAP	*ISOmetric MAPping*
JCR	*Journal CitationReport*
KL	*Kullback-Leibler*
LDA	*Linear Discriminant Analysis*
MCGS	*Mean-Centered Group Scaling*
NN	*Neural Network*
PCA	*Principal Component Analysis*
PPV	*Positive Predictive Value*
P-*t*-SNE	*Parametric t-distributed Stochastic Neighbor Embedding*
PZT	*PieZoelectric Transducer*
RBM	*Restricted Boltzmann Machine*
ReLU	*Rectified Linear Unit*
SHM	*Structural Health Monitoring*
SJR	*Scimago Journal Ranking*
SNE	*Stochastic Neighbor Embedding*
TNR	*True Negative Rate*
TPR	*True Positive Rate*
***t*-SNE**	*t-distributed Stochastic Neighbor Embedding*

Lista de Símbolos

$\mathbf{X}$	Matriz que contiene todas las realizaciones bajo los diferentes estados estructurales
N	Número de sensores
L	Número de componentes en cada señal
E	Número de los diferentes estados estructurales
n	Número de realizaciones
$\check{\mathbf{X}}$	Matriz de datos originales estandarizados
μ	Media aritmética
σ	Desviación estándar
$\mathbf{P}$	Modelo de PCA (caso completo)
$\mathbf{P}_\ell$	Modelo de PCA (reducido)
ℓ	Números de componentes principales del modelo de PCA reducido
$\mathbf{T}$	Proyección del conjunto de datos estandarizado, $\check{\mathbf{X}}$, en el subespacio asociado al modelo de PCA completo
$\mathbf{T}_\ell$	Proyección del conjunto de datos estandarizado, $\check{\mathbf{X}}$, en el subespacio asociado al modelo de PCA reducido
ρ_k	Vector propio k-ésimo
λ_k	Valor propio k-ésimo
Λ	Valores propios en una matriz diagonal
$\mathbf{C}_{\check{\mathbf{X}}}$	Matriz de covarianza de $\check{\mathbf{X}}$
$\mathcal{X}$	Conjunto de datos de alta dimensión
$\mathcal{X}'$	Conjunto de datos de alta dimensión que incluye el dato a diagnosticar
$\mathcal{Y}$	Conjunto de puntos de baja dimensión
$\mathcal{Y}'$	Conjunto de puntos de baja dimensión que incluye el punto a diag - nosticar
$\mathcal{Y}_l$	Centroide asociado con el estado estructural l-ésimo
$d(\mathbf{x}^i, \mathbf{x}^j)$	Distancia euclídea entre los datos $\mathbf{x}^i$ y $\mathbf{x}^j$
$p_{j\|i}$	Probabilidad condicional
p_{ij}	Probabilidad conjunta
$\mathcal{P}$	Matriz de similitud para los datos de alta dimensión
$\mathcal{Q}$	Matriz de similitud para los puntos de baja dimensión
$\mathcal{C}$	Divergencia Kullback-Leibler
η	*Learning rate*
$\alpha(t)$	Término *momentum* en la iteración t
p	*Perplexity*
α	Grados de libertad de la distribución t de Student
$\mathbf{v}$	Nodos visibles de la red neuronal
$\mathbf{h}$	Nodos ocultos de la red neuronal
$E(\mathbf{v}, \mathbf{h})$	Función de energía
$P(\mathbf{v}, \mathbf{h})$	Distribución conjunta sobre todos los nodos
W	Pesos de conexión de la red neuronal prealimentada

b	Sesgos de los nodos visibles de la red neuronal
a	Sesgos de los nodos ocultos de la red neuronal
P_{model}	Distribución basada en el modelo
P_{data}	Distribución basada en los datos
$\mathbf{e}_i$	i-ésimo vector de la base canónica
$\mathbf{z}$	Vector de datos originales a diagnosticar
$\check{\mathbf{z}}$	Vector de datos originales estandarizados a diagnosticar
φ	Fase de actuación
$\mathbf{S}$	Matriz selectora
$\mathbf{\mathfrak{X}}$	Matriz con los datos de referencia para construir el modelo
$\check{\mathbf{\mathfrak{X}}}$	Matriz con los datos de referencia estandarizados para construir el modelo

A mi madre

Capítulo 1

Tesis por compendio de publicaciones

La presente tesis doctoral, autorizada por el director de la tesis y por la Comisión Académica del programa de doctorado en Matemática Aplicada, se presenta como un compendio de tres artículos previamente publicados en revistas del *Journal Citation Report* (JCR). A continuación, se detallan las referencias completas de dichos artículos que conforman el cuerpo de la tesis y que pueden consultarse en el Capítulo 9:

 Agis, D.; Tibaduiza, D.A.; Pozo, F. Vibration-based detection and classification of structural changes using principal component analysis and *t*-distributed stochastic neighbor embedding. *Structural Control and Health Monitoring* 2020; 27:e2533. https://doi.org/10.1002/stc.2533

 Agis, D.; Pozo, F. A frequency-based approach for the detection and classification of structural changes using *t*-SNE. *Sensors* 2019, 19(23), 5097. https://doi.org/10.3390/s19235097

 Agis, D.; Pozo, F. Vibration-based structural health monitoring using piezoelectric transducers and parametric *t*-SNE. *Sensors* 2020, 20(6), 1716. https://doi.org/10.3390/s20061716

A lo largo del texto, se hará referencia a ellos como Artículo 1, 2 y 3.

Asimismo, se considera oportuno incluir en el apéndice C de esta tesis los siguientes artículos, en los cuales el doctorando participa como coautor y que constituyen parte de su base formativa:

 Agis, D.; Vidal, Y.; Pozo, F. Damage diagnosis for offshore fixed wind turbines. *Renewable energy and power quality journal* 2019, 17(10), 366-370. https://doi.org/10.24084/repqj17.313

 Tibaduiza, D.A.; Gómez, R.C.; Pedraza, C.; Agis, D.; Pozo, F. Damage identification in structural health monitoring: A brief review from its implementation to the use of data-driven applications. *Sensors* 2020, 20(3), 733. https://doi.org/10.3390/s20030733

Capítulo 2

Introducción

La monitorización de la salud estructural (SHM, por sus siglas en inglés) es un método esencial para la ingeniería estructural, ya que controla la seguridad, la integridad y el rendimiento de una estructura (Ou y Li, 2010; Li y Hao, 2016; Li *et al.*, 2016; Mesquita *et al.*, 2016). El estado saludable de la estructura tiene que permanecer dentro de unos límites especificados, sin embargo, estos límites se suelen traspasar debido al uso de la estructura, a su envejecimiento o a las condiciones ambientales y operativas (EOC, por sus siglas en inglés). Por ello, en los sistemas de SHM, es importante detectar y clasificar los cambios estructurales para mantenerse dentro de dichos límites, mejorando la seguridad y reduciendo los costes de mantenimiento. Si se detecta y clasifica el daño justo en el momento que ocurre, se pueden tomar medidas antes de que suceda un desastre económico y/o humano.

En la SHM, se aplican muchos métodos para la detección de daños, he aquí algunos ejemplos: en Sohn *et al.*, 2001, se proyecta la SHM en el contexto del reconocimiento de patrones estadísticos, detectándose daños o cambios estructurales utilizando dos técnicas basadas en el análisis de series temporales. En Liu *et al.*, 2011, se propone una metodología de SHM, basada en las técnicas de identificación del sistema, para cuantificar la degradación estructural en los sistemas de estabilidad de actitud pasiva por gradientes de gravedad utilizados en los satélites. En Gui *et al.*, 2017, se presentan tres máquinas de soporte vectorial basadas en algoritmos de optimización para la detección de daños en la SHM, que se espera que ayuden a los ingenieros a procesar datos de alta dimensionalidad. En Worden y Cross, 2018, se usa el modelo *Treed Gaussian Process* en el contexto de la SHM de los puentes. En Tibaduiza *et al.*, 2018, se presenta una metodología de detección y clasificación de daños, que incluye el uso de datos recopilados de una estructura bajo diferentes estados estructurales por medio de una red de sensores piezoeléctricos, aprovechando el uso del aprendizaje automático. Como se puede observar, existe una creciente necesidad de investigar acerca de métodos para la detección de daños y es por ello que en la presente tesis doctoral se propone una nueva metodología capaz de detectar y clasificar cambios estructurales, empleando técnicas de reducción de la dimensionalidad.

Una revisión del estado del arte revela que la SHM es un área de investigación muy activa, ya que se aplica en innumerables estructuras como edificios (Raju *et al.*, 2015; Blanco *et al.*, 2018), turbinas eólicas (Ciang *et al.*, 2008; Loh *et al.*, 2017; Vidal *et al.*, 2020) y aviones (Nisha, 2014; Ochôa *et al.*, 2019), entre otras muchas.

Durante los últimos años, las redes de sensores han ido adquiriendo cada vez más importancia hasta llegar a estar presentes en prácticamente todos los sectores de nuestra sociedad, sin ser una excepción la SHM (Giurgiutiu, 2005; López-Higuera *et al.*, 2011; Kinet *et al.*, 2014; Tibaduiza *et al.*, 2016; Qing *et al.*, 2019). Para monitorizar

el estado de la estructura, se recogen datos a través de múltiples sensores colocados en su superficie. Las señales obtenidas de la red de sensores se almacenan formando un conjunto de datos de alta dimensionalidad, debido a las continuas mediciones del sistema de monitorización. Para la gestión de datos de alta dimensionalidad, se proponen varios métodos y entre éstos destacan las técnicas de representación bidimensional o tridimensional, ya que permiten detectar fácilmente grupos o clústeres naturales, identificar patrones ocultos, etc. (Ward *et al.*, 2015). Las técnicas de representación bidimensional o tridimensional están relacionadas de alguna manera con la reducción de la dimensionalidad. La reducción de la dimensionalidad es el proceso mediante el cual se reduce la dimensión de los datos originales manteniendo la información intrínseca más importante (Tenenbaum *et al.*, 2000). La reducción de la dimensionalidad es muy importante, porque facilita el procesamiento de los datos y alivia las propiedades no deseadas de los espacios de alta dimensión, como "la maldición de la dimensionalidad" (Jiménez y Landgrebe, 1998). En la literatura, se proponen varios métodos de reducción de la dimensionalidad: (i) métodos lineales, tales como el análisis de componentes principales —PCA, por sus siglas en inglés— (Tibaduiza *et al.*, 2013; Caggiano, 2018) y el análisis discriminante lineal —LDA, por sus siglas en inglés— (Sharma *et al.*, 2006; Elvira *et al.*, 2019), y (ii) métodos no lineales, como el *isometric mapping* —ISOMAP— (Jeong *et al.*, 2014; Ullah *et al.*, 2018) y el *t-distributed stochastic neighbor embedding* —*t*-SNE— (Van Der Maaten e Hinton, 2008).

En general, es muy probable que los datos del mundo real sean altamente no lineales. Por lo tanto, las técnicas de reducción de la dimensionalidad no lineales y no supervisadas se utilizan ampliamente en muchas aplicaciones. Entre este tipo de técnicas, el *t*-SNE es ampliamente adoptado. Esta técnica representa la estructura local de los datos originales de alta dimensión en un espacio de baja dimensión como, por ejemplo, un gráfico de dispersión. Dicha técnica detecta patrones mediante la identificación de grupos o clústeres basados en la similitud de datos. El *t*-SNE es ampliamente utilizado en la literatura para reducir la dimensionalidad (Lu *et al.*, 2016; Seok, 2019; Gu *et al.*, 2019), para clasificar o reconocer patrones (Taskesen y Reinders, 2016; Gierahn *et al.*, 2017; He *et al.*, 2018) y para visualizar y comprimir grandes conjuntos de datos (Kirk *et al.*, 2016; Macaulay *et al.*, 2016; Balamurali y Melkumyan, 2016). Sin embargo, este método no está diseñado para admitir la incorporación de datos de fuera de la muestra, es decir, la incorporación de nuevos datos. Para evitar este problema, se propone el llamado método *parametric t*-SNE —P-*t*-SNE— (Van Der Maaten, 2009). Esta otra metodología utiliza una red neuronal (NN, por sus siglas en inglés) para aprender una función de mapeo paramétrico explícito desde un espacio de datos de alta dimensión a un espacio de baja dimensión. Por lo tanto, el P-*t*-SNE puede incorporar datos de fuera de la muestra. Otras ventajas del P-*t*-SNE son: (i) reduce de forma drástica el coste computacional, y (ii) se puede aplicar a grandes conjuntos de datos (el *t*-SNE sólo se puede aplicar a unos cuantos miles de datos). Aunque se han aplicado el *t*-SNE y el P-*t*-SNE en varios campos de investigación, este es uno de los primeros enfoques que utiliza estos métodos en el campo de la SHM.

La revisión del estado del arte, en la cual se ha prestado especial atención a la SHM y a la técnica *t*-SNE/P-*t*-SNE, ha revelado la necesidad de obtener una nueva estrategia para detectar y clasificar los cambios producidos en las estructuras a diagnosticar. Tras revisar el estado del arte, las conclusiones obtenidas son las siguientes:

- No existe en la actualidad ninguna aplicación de la técnica *t*-SNE/P-*t*-SNE en el área de investigación de la SHM.

- Existe la necesidad de obtener una estrategia que permita utilizar datos de diferentes fases de actuación de forma eficiente.
- La combinación del PCA y el *t*-SNE/P-*t*-SNE resulta novedosa, permitiendo obtener una mejor detección y clasificación de los cambios estructurales.
- Existe una serie de herramientas matemáticas que hacen posible proponer una estrategia para la clasificación del estado actual de la estructura a diagnosticar.

Con esta problemática en mente, en este estudio se investiga acerca de (i) el diseño de una nueva metodología para la detección y clasificación de daños estructurales, y (ii) los mecanismos para facilitar una manipulación eficiente de los datos masivos proporcionados por la red de sensores. Una metodología que permita la detección y clasificación de fallos es de vital importancia para evitar desastres y/o reducir costes de mantenimiento, e investigar acerca de cómo procesar la gran cantidad de datos recopilados por los múltiples sensores instalados en la estructura es de sumo interés en la era del Big Data en la que vivimos hoy en día. La metodología que se propone en este trabajo garantiza un porcentaje muy elevado de correctas detecciones y clasificaciones, así como una manipulación inteligente de los datos. Pese a que se han llevado a cabo distintas iniciativas para abordar esta problemática en el campo de la SHM (Carden y Brownjohn, 2008; Rizzo *et al.*, 2009; Langone *et al.*, 2017; Gulgec *et al.*, 2017; Cremona y Santos, 2018), no se ha aplicado en ninguna de ellas el *t*-SNE/P-*t*-SNE, una técnica que reporta muy buenos resultados y una fácil interpretación de los mismos.

En esta tesis doctoral, se propone una estrategia de SHM, para abordar las necesidades y carencias detectadas en la detección y clasificación de cambios estructurales, mediante tres etapas:

1. la integración de los datos en dos pasos: el despliegue tipo *E* (Westerhuis *et al.*, 1999) y el llamado *mean-centered group scaling* —MCGS— (Pozo *et al.*, 2018);
2. la transformación de los datos mediante el PCA; y
3. la reducción de los datos en dos pasos, combinando el PCA y el *t*-SNE/P-*t*-SNE.

El PCA es una técnica que se utiliza principalmente para la reducción de la dimensionalidad o la extracción de características en el campo del reconocimiento de patrones (Mujica *et al.*, 2011). Además, también se puede utilizar para detectar y clasificar cambios estructurales o fallos (Vidal *et al.*, 2018). En el presente trabajo, el modelo de PCA ayudará a detectar diferentes tipos de daños y no solamente las estructuras sanas. Sin embargo, en algunos casos, se observa que usar sólo los primeros componentes principales, es decir, sólo el PCA, no ayuda con el *clustering* o la separación (Mujica *et al.*, 2013; Pozo *et al.*, 2016). Por esta razón, aquí se propone detectar daños o fallos utilizando la combinación del PCA y el *t*-SNE/P-*t*-SNE. Por lo tanto, se utilizan los siguientes pasos para la detección y clasificación de cambios estructurales:

1. primero se estandarizan los datos recopilados usando el MCGS, debido a las diferentes escalas y magnitudes de las mediciones;
2. a continuación, se aplica el PCA para transformar los datos estandarizados y reducir su dimensionalidad; y
3. finalmente, se aplica el *t*-SNE/P-*t*-SNE a los datos resultantes del apartado anterior para representarlos en un plano.

En este estudio, se muestra que la calidad de los grupos o clústeres, relacionados con diferentes estados estructurales, mejora significativamente con la combinación del PCA y el *t*-SNE/P-*t*-SNE, en comparación con el uso del PCA únicamente.

La estructura a diagnosticar se clasifica, es decir, se asocia con un estado estructural concreto, utilizando tres estrategias diferentes:

1. la distancia más pequeña entre el punto y el centroide, cuando se considera una sola fase de actuación;
2. el voto mayoritario, cuando se combinan varias fases de actuación; y
3. la suma de las inversas de las distancias, también cuando se combinan varias fases de actuación.

El método propuesto para la detección y clasificación de cambios estructurales se evalúa utilizando datos experimentales de una placa de aluminio equipada con transductores piezoeléctricos (PZT, por sus siglas en inglés). Debido a que las estrategias de SHM basadas en la propagación de ondas guiadas han demostrado su capacidad para identificar adecuadamente los defectos en las estructuras (Sikdar *et al.*, 2019; Yan *et al.*, 2019; Cho *et al.*, 2019; Jiménez *et al.*, 2019), en la presente tesis, también se considera el paradigma de las ondas guiadas. En este paradigma, la estructura se excita con una señal y la respuesta se mide para crear un patrón de referencia. Cuando se debe diagnosticar una nueva estructura, ésta se excita con la misma señal y la respuesta se mide y se compara con el patrón de referencia. Los resultados obtenidos muestran una alta precisión de clasificación y un alto rendimiento de este método, con un porcentaje de decisiones correctas cercano al 100 % en varios escenarios.

La idea de encontrar una nueva metodología capaz de detectar y clasificar cambios estructurales nos llevó a experimentar con la técnica *t*-SNE. De esta forma, esta idea inicial se convirtió en la base de los tres artículos que conforman la presente tesis doctoral:

El primer artículo (*VIBRATION-BASED DETECTION AND CLASSIFICATION OF STRUCTURAL CHANGES USING PRINCIPAL COMPONENT ANALYSIS AND t-DISTRIBUTED STOCHASTIC NEIGHBOR EMBEDDING*) se centró principalmente en destacar, en el campo de la SHM, los buenos resultados obtenidos por la técnica *t*-SNE en la detección y clasificación de cambios estructurales con los datos originales, es decir, en el dominio del tiempo. Posteriormente, se observó que en el campo de la SHM y de la monitorización de la condición (CM, por sus siglas en inglés) era muy común el análisis del dominio de la frecuencia (Rutherford *et al.*, 2007; Alonso y Salgado, 2008; Gryllias y Antoniadis, 2012; Hou *et al.*, 2015; Hoshyarmanesh *et al.*, 2017; Tsogka *et al.*, 2017). Además, en la fase de revisión del estado del arte, se encontraron trabajos como por ejemplo el de Xu *et al.*, 2019, que mostraba como un método de *clustering* en el dominio de la frecuencia superaba a otros métodos de *clustering* en el dominio del tiempo. Esta nueva idea fue determinante para iniciar el estudio que se expone en el segundo artículo (*A FREQUENCY-BASED APPROACH FOR THE DETECTION AND CLASSIFICATION OF STRUCTURAL CHANGES USING t-SNE*). En este trabajo, se transformaron los datos originales, en el dominio del tiempo, para obtenerlos en el dominio de la frecuencia. De este modo, se pudieron comparar los resultados de ambos dominios. El segundo artículo reveló que la calidad de los grupos o clústeres, relacionados con los diferentes estados estructurales, mejoraba significativamente en el dominio de la frecuencia. En estos dos primeros artículos, se empleó la versión no paramétrica del *t*-SNE, por lo que cada vez que llegaba una nueva estructura a

diagnosticar, se tenía que ejecutar toda la estrategia propuesta desde el inicio, lo que conllevaba un enorme coste computacional y un tiempo de ejecución muy elevado. Para resolver este problema, el tercer artículo (*VIBRATION-BASED STRUCTURAL HEALTH MONITORING USING PIEZOELECTRIC TRANSDUCERS AND PARAMETRIC t-SNE*) se basó en el método P-*t*-SNE. En este último artículo, se mostró como la versión paramétrica del *t*-SNE lograba un rendimiento similar al de la versión no paramétrica, pero con un coste computacional y un consumo de tiempo muchísimo más bajos.

Esta tesis doctoral, presentada en formato de compendio de publicaciones, está organizada en nueve capítulos. En primer lugar, en el Capítulo 1, se enumeran los artículos que constituyen el cuerpo de la tesis, así como otros artículos que forman parte de la base formativa del doctorando. El Capítulo 2 introduce el tema de estudio. La hipótesis y los objetivos del trabajo se encuentran en el Capítulo 3. En el Capítulo 4, se comentan las aportaciones de la tesis. A continuación, el Capítulo 5 presenta la metodología utilizada. La discusión de los resultados obtenidos, las conclusiones, y las futuras líneas de investigación y limitaciones se encuentran en los Capítulos 6, 7 y 8, respectivamente. El Capítulo 9 incluye los tres artículos publicados en revistas indexadas. Finalmente, en los Apéndices A, B y C se muestran el factor de impacto y la categoría de las revistas, la justificación de la contribución del doctorando, y otros trabajos, respectivamente.

Capítulo 3

Hipótesis del estudio y objetivos de investigación

La hipótesis de esta tesis doctoral es que es posible diseñar y desarrollar una nueva metodología para monitorizar la integridad estructural en base a los datos recogidos por una red de sensores instalada en la estructura a diagnosticar.

El objetivo general del presente trabajo es encontrar una estrategia que permita detectar y clasificar cambios estructurales mediante técnicas de reducción de la dimensionalidad. Por lo tanto, los objetivos específicos son los siguientes:

1. Estudiar las posibles alternativas de prepocesar los datos masivos recopilados por la red de sensores.
2. Estudiar en profundidad la técnica denominada *t*-SNE.
3. Estudiar la combinación de las técnicas PCA y *t*-SNE.
4. Utilizar la técnica *t*-SNE en el dominio del tiempo.
5. Estudiar las posibles mejoras de la técnica *t*-SNE trabajando en el dominio de la frecuencia.
6. Estudiar en profundidad la técnica P-*t*-SNE para facilitar un método mucho más rápido.
7. Establecer una clasificación de los daños estructurales mediante el estudio de diferentes estrategias.

Capítulo 4

Aportaciones de la tesis

La principal contribución de la presente tesis es la aplicación, por primera vez, de las técnicas t-SNE y P-t-SNE en el campo de la SHM, seguida de las siguientes contribuciones para encontrar un nuevo método que permita detectar y clasificar cambios estructurales:

- **Preprocesamiento de los datos: Integración de los datos (I)**. Según el artículo de Westerhuis *et al.*, 1999, una matriz de datos crudos tridimensional se puede desplegar de seis formas diferentes (despliegue tipo A, ..., despliegue tipo F), obteniéndose seis matrices bidimensionales diferentes. La forma en que se despliegan estos datos crudos afecta al análisis posterior. En nuestros artículos, hemos considerado el despliegue tipo E.
- **Preprocesamiento de los datos: Integración de los datos (II)**. Un segundo paso, previo a la transformación de los datos, es su normalización. Aplicamos el MCGS a los datos tal y como se detalla en Pozo *et al.*, 2018.
- **Preprocesamiento de los datos: Transformación de los datos**. Construimos el modelo de PCA ($\mathbf{P}$) para que los datos normalizados $\mathbf{X}$ se transformen en los datos proyectados $\mathbf{T} = \mathbf{XP}$. Vale la pena señalar que las matrices $\mathbf{X}$ y $\mathbf{T}$ tienen exactamente la misma dimensión, por lo que no se realiza ninguna reducción de la dimensionalidad en esta etapa.
- **Preprocesamiento de los datos: Reducción de los datos (I)**. Utilizamos el PCA para reducir la dimensionalidad de los datos, eligiendo el número de componentes principales $\ell \in \mathbb{N}$ de tal forma que la proporción de la varianza explicada sea mayor o igual al 95 %.
- **Preprocesamiento de los datos: Reducción de los datos (II)**. Ahora utilizamos la técnica t-SNE/P-t-SNE como segunda fase para reducir la dimensionalidad de ℓ a 2. Demostramos en nuestro artículo *VIBRATION-BASED DETECTION AND CLASSIFICATION OF STRUCTURAL CHANGES USING PRINCIPAL COMPONENT ANALYSIS AND t-DISTRIBUTED STOCHASTIC NEIGHBOR EMBEDDING* que esta combinación, PCA y t-SNE, mejora la calidad de los grupos o clústeres.
- **Postprocesamiento de los datos: Clasificación**. Para la clasificación, hemos propuesto varias configuraciones. Cuando la decisión se toma con una sola fase de actuación, usamos la distancia punto-centroide más pequeña. Sin embargo, también combinamos la contribución de todas las fases de actuación en dos enfoques diferentes: el voto mayoritario y la suma de las inversas de las distancias. En el primer caso, el voto mayoritario, cada fase de actuación emite un

voto. En el segundo caso, la suma de las inversas de las distancias, cada fase de actuación contribuye a una clasificación final.

Sabemos que hay una gran cantidad de artículos científicos que tratan sobre aplicaciones de aprendizaje automático o ciencia de datos, pero creemos que nuestra contribución puede asemejarse a un producto químico que es una combinación apropiada de elementos químicos básicos. Hemos tratado de combinar varios métodos o algoritmos existentes, de una manera inteligente utilizando nuestros conocimientos previos en el campo, con una integración, transformación y reducción particulares de los datos.

Capítulo 5

Metodología utilizada

5.1. Preprocesamiento de los datos y *clustering*: datos de referencia

Entre las contribuciones de nuestro estudio, se incluyen los métodos de preprocesamiento de los datos: cómo se recopilan, organizan, estandarizan, transforman y reducen. En las siguientes secciones, el preprocesamiento de los datos se presenta con suficiente detalle, de modo que el enfoque propuesto pueda reproducirse fácilmente. El preprocesamiento se divide en tres etapas: integración de los datos (Sección 5.1.1), transformación de los datos (Sección 5.1.2) y reducción de los datos (Sección 5.1.3). La Figura 5.1 ilustra estas tres etapas. Finalmente, los datos se organizan en grupos o clústeres en la Sección 5.1.4.

5.1.1. Integración de los datos

En este estudio, la integración de los datos se define como la combinación de las diferentes señales medidas en una vista única y unificada. En nuestro caso, esta vista unificada se representa por una matriz. La sección 5.1.1.1 presenta el despliegue de los datos sin procesar, que se almacenan en una matriz tridimensional, y la sección 5.1.1.2 describe la estandarización de estos datos.

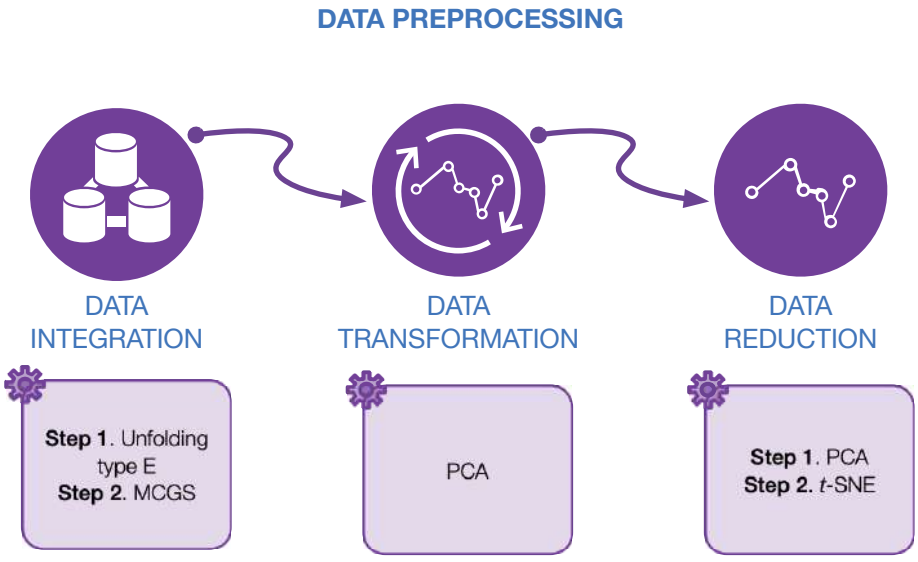

FIGURA 5.1: El preprocesamiento se divide en tres etapas: integración de los datos, transformación de los datos y reducción de los datos.

5.1.1.1. Despliegue tipo E

Los datos recopilados incluyen diferentes señales de respuesta medidas por sensores en una estructura que vibra. Múltiples observaciones de estas señales se miden bajo diferentes estados estructurales. La matriz que recoge todas las observaciones, bajo los diferentes estados estructurales, se define de la siguiente manera:

$$\mathbf{X} = \left(x_{i,l}^{k,j}\right) = \left[\begin{array}{ccc:ccc:c:ccc} x_{1,1}^{1,1} & \cdots & x_{1,1}^{1,L} & x_{1,1}^{2,1} & \cdots & x_{1,1}^{2,L} & \cdots & x_{1,1}^{N,1} & \cdots & x_{1,1}^{N,L} \\ \vdots & \ddots & \vdots & \vdots & \ddots & \vdots & \ddots & \vdots & \ddots & \vdots \\ x_{n_1,1}^{1,1} & \cdots & x_{n_1,1}^{1,L} & x_{n_1,1}^{2,1} & \cdots & x_{n_1,1}^{2,L} & \cdots & x_{n_1,1}^{N,1} & \cdots & x_{n_1,1}^{N,L} \\ \hdashline x_{1,2}^{1,1} & \cdots & x_{1,2}^{1,L} & x_{1,2}^{2,1} & \cdots & x_{1,2}^{2,L} & \cdots & x_{1,2}^{N,1} & \cdots & x_{1,2}^{N,L} \\ \vdots & \ddots & \vdots & \vdots & \ddots & \vdots & \ddots & \vdots & \ddots & \vdots \\ x_{n_2,2}^{1,1} & \cdots & x_{n_2,2}^{1,L} & x_{n_2,2}^{2,1} & \cdots & x_{n_2,2}^{2,L} & \cdots & x_{n_1,2}^{N,1} & \cdots & x_{n_2,2}^{N,L} \\ \hdashline \vdots & \ddots & \vdots & \vdots & \ddots & \vdots & \ddots & \vdots & \ddots & \vdots \\ \hdashline x_{1,E}^{1,1} & \cdots & x_{1,E}^{1,L} & x_{1,E}^{2,1} & \cdots & x_{1,E}^{2,L} & \cdots & x_{1,E}^{N,1} & \cdots & x_{1,E}^{N,L} \\ \vdots & \ddots & \vdots & \vdots & \ddots & \vdots & \ddots & \vdots & \ddots & \vdots \\ x_{n_E,E}^{1,1} & \cdots & x_{n_E,E}^{1,L} & x_{n_E,E}^{2,1} & \cdots & x_{n_E,E}^{2,L} & \cdots & x_{n_E,E}^{N,1} & \cdots & x_{n_E,E}^{N,L} \end{array}\right] = \left[\begin{array}{c} \mathbf{X}_1 \\ \hdashline \mathbf{X}_2 \\ \hdashline \vdots \\ \hdashline \mathbf{X}_E \end{array}\right] \tag{5.1}$$

$$= \left[\begin{array}{c|c|c|c} \mathbf{X}^1 & \mathbf{X}^2 & \cdots & \mathbf{X}^N \end{array}\right] \in \mathcal{M}_{(n_1+\cdots+n_E)\times(N\cdot L)}(\mathbb{R}), \tag{5.2}$$

donde $N \in \mathbb{N}$ es el número de sensores y $k = 1, \ldots, N$ identifica el sensor que está midiendo; $L \in \mathbb{N}$ es el número de componentes en cada señal y $j = 1, \ldots, L$ indica la medición j-ésima; $E \in \mathbb{N}$ es el número de estados estructurales diferentes que se consideran y $l = 1, \ldots, E$ representa el estado estructural que se está midiendo. Finalmente, n_l, $l = 1, \ldots, E$, es el número de observaciones por estado estructural e $i = 1, \ldots, n_l$ es la observación i-ésima relacionada con el l-ésimo estado estructural. Téngase en cuenta que la matriz $\mathbf{X}$ está formada por E bloques horizontales (véase Ecuación (5.1)), $\mathbf{X}_l$, $l = 1, \ldots, E$, donde cada bloque está relacionado con un estado estructural diferente. Asimismo, la matriz $\mathbf{X}$ también se puede ver como N bloques verticales (véase Ecuación (5.2)), $\mathbf{X}^k$, $k = 1, \ldots, N$, donde cada bloque está relacionado con un sensor diferente.

En particular, la matriz $\mathbf{X}$ es una versión singular de una matriz de datos tridimensional $(n_1 + \cdots + n_E) \times N \times L$ desplegada, donde la primera dimensión está relacionada con las múltiples observaciones, la segunda está relacionada con los sensores y la tercera es el tiempo. Para manejar matrices tridimensionales, se han propuesto varios enfoques, siendo los más utilizados los basados en el despliegue de dichas matrices. Según Westerhuis *et al.*, 1999, hay seis formas de desplegar una matriz de datos tridimensional, que afectan al rendimiento de la estrategia general. En nuestro estudio, de estas seis posibles matrices desplegadas, hemos considerado el tipo E. Esta elección, despliegue tipo E, simplifica el estudio de la variabilidad entre muestras, ya que se recopila información relacionada con las mediciones del sensor y sus variaciones a lo largo del tiempo.

5.1.1.2. *Mean-centered group scaling* (MCGS)

Principalmente, existen dos razones para estandarizar los datos crudos de la matriz $\mathbf{X}$ (Ecuación (5.1)): primero, para poder procesar datos que pueden tener diferentes

magnitudes por proceder de distintos sensores; segundo, para simplificar los cálculos en la transformación de los datos (Sección 5.1.2).

La forma en que se estandarizan los datos sin procesar puede afectar gravemente al rendimiento general de los métodos posteriores que deben aplicarse (Pozo *et al.*, 2018). Algunas estrategias consideran cada vector columna de la matriz $\mathbf{X}$ como una entidad independiente y cada elemento del vector columna es estandarizado restando la media de todos los elementos de la columna y dividiendo por la desviación estándar del mismo conjunto de datos. Por lo tanto, en este caso, que se puede definir como *column scaling*, la media de cada columna es cero y su desviación estándar es uno. Una segunda estrategia (Pozo *et al.*, 2018), la llamada *group scaling*, considera los bloques verticales, donde todas las medidas provienen del mismo sensor. En este caso, cada elemento del bloque se estandariza restando la media de todos los elementos del bloque y dividiendo por la desviación estándar del mismo conjunto de datos. El principal inconveniente de este enfoque es que la media de cada columna ya no es cero y su desviación estándar ya no es uno. Como solución práctica a este inconveniente, Pozo *et al.*, 2018 sugieren la versión centrada en la media del *group scaling*, es decir, el MCGS, donde la media de cada columna es cero nuevamente. Sin embargo, no se puede garantizar que la desviación estándar de cada columna sea uno. Por lo tanto, en nuestro estudio, se aplica el MCGS a la matriz $\mathbf{X}$ (Ecuación (5.1)), es decir, los elementos $x_{i,l}^{k,j}$ se estandarizan definiéndose una nueva matriz $\check{\mathbf{X}}$ como:

$$\check{x}_{i,l}^{k,j} = \frac{x_{i,l}^{k,j} - \mu^{k,j}}{\sigma^k},\ k = 1,\dots,N,\ j = 1,\dots,L,\ i = 1,\dots,n_l,\ l = 1,\dots,E, \tag{5.3}$$

donde

$$\mu^{k,j} = \frac{1}{n}\sum_{l=1}^{E}\sum_{i=1}^{n_l} x_{i,l}^{k,j},\ k = 1,\dots,N,\ j = 1,\dots,L, \tag{5.4}$$

$$\sigma^k = \sqrt{\frac{1}{nL}\sum_{l=1}^{E}\sum_{i=1}^{n_l}\sum_{j=1}^{L}\left(x_{i,l}^{k,j} - \mu^k\right)^2},\ k = 1,\dots,N, \tag{5.5}$$

donde

$$n = \sum_{i=1}^{E} n_i, \tag{5.6}$$

$$\mu^k = \frac{1}{nL}\sum_{l=1}^{E}\sum_{i=1}^{n_l}\sum_{j=1}^{L} x_{i,l}^{k,j},\ k = 1,\dots,N, \tag{5.7}$$

donde $\mu^{k,j}$ (Ecuación (5.4)) es la media aritmética de todos los elementos de la columna $[(k-1)L + j]$-ésima de la matriz $\mathbf{X}$, es decir, de la columna j-ésima del bloque vertical $\mathbf{X}^k$; σ^k (Ecuación (5.5)) es la desviación estándar de todos los elementos del bloque vertical $\mathbf{X}^k$ con respecto al valor medio μ^k; n (Ecuación (5.6)) es el número total de realizaciones; y μ^k (Ecuación (5.7)) es la media aritmética de todos los elementos del bloque vertical $\mathbf{X}^k$. Con la estandarización de los datos crudos definida en la Ecuación (5.3), no se puede garantizar que la desviación estándar de cada columna sea uno. Sin

embargo, la media de cada vector columna se puede calcular fácilmente como:

$$\begin{aligned}\check{\mu}^{k,j} &= \frac{1}{n}\sum_{l=1}^{E}\sum_{i=1}^{n_l}\check{x}_{i,l}^{k,j} = \frac{1}{n}\sum_{l=1}^{E}\sum_{i=1}^{n_l}\frac{x_{i,l}^{k,j}-\mu^{k,j}}{\sigma^k} = \frac{1}{n\sigma^k}\sum_{l=1}^{E}\sum_{i=1}^{n_l}\left(x_{i,l}^{k,j}-\mu^{k,j}\right)\\ &= \frac{1}{n\sigma^k}\left[\left(\sum_{l=1}^{E}\sum_{i=1}^{n_l}x_{i,l}^{k,j}\right)-n\mu^{k,j}\right] = \frac{1}{n\sigma^k}\left[n\mu^{k,j}-n\mu^{k,j}\right] = 0.\end{aligned}$$

5.1.2. Transformación de los datos

En el marco actual, la transformación de datos se entiende como una aplicación de una función matemática particular a cada fila de la matriz estandarizada $\check{\mathbf{X}}$ (Ecuación (5.3)). Debido a que el objetivo final es la reducción de la dimensionalidad, la transformación que se utiliza en este estudio es el PCA. Por lo tanto, la transformación se calcula como una multiplicación de matrices:

$$\mathbf{T} = \check{\mathbf{X}}\mathbf{P} \in \mathcal{M}_{(n_1+\cdots+n_E)\times(N\cdot L)}(\mathbb{R})$$

donde

$$\mathbf{P} = \begin{bmatrix} \rho_1 & \rho_2 & \cdots & \rho_{N\cdot L} \end{bmatrix} \in \mathcal{M}_{(N\cdot L)\times(N\cdot L)}(\mathbb{R})$$

es el llamado modelo de PCA, que contiene sus vectores propios ρ_k, $k = 1, \ldots, N \cdot L$, en columnas. Estos vectores se conocen como los componentes principales. El PCA se explica con más detalle en la Sección 5.1.3.1.

5.1.3. Reducción de los datos

En este trabajo, se utilizan dos enfoques para la reducción de los datos. En primer lugar, se aplica el PCA (Sección 5.1.3.1) para representar la matriz estandarizada $\check{\mathbf{X}}$ en un nuevo espacio vectorial con una dimensión reducida y sin pérdida significativa de información. En segundo lugar, se aplica el *t*-SNE (Sección 5.1.3.2) o el P-*t*-SNE (Sección 5.1.3.3) como una técnica de representación bidimensional. Estos dos métodos, PCA y *t*-SNE/P-*t*-SNE, se combinan para reducir la complejidad de los datos, así como para reducir el tiempo y el coste computacional.

5.1.3.1. Análisis de componentes principales (PCA)

Una de las razones principales para usar el MCGS, resumido en la Ecuación (5.3), es que la matriz de covarianza de la matriz $\check{\mathbf{X}}$ se puede calcular de una manera muy simple como:

$$\mathbf{C}_{\check{\mathbf{X}}} = \frac{1}{n-1}\check{\mathbf{X}}^{\top}\check{\mathbf{X}} \in \mathcal{M}_{(N\cdot L)\times(N\cdot L)}(\mathbb{R}).$$

Dicha matriz de covarianza $\mathbf{C}_{\check{\mathbf{X}}}$ es una matriz cuadrada que satisface la propiedad de simetría:

$$\mathbf{C}_{\check{\mathbf{X}}}^{\top}\mathbf{C}_{\check{\mathbf{X}}} = \mathbf{C}_{\check{\mathbf{X}}}\mathbf{C}_{\check{\mathbf{X}}}^{\top}.$$

Además, esta matriz mide el alcance de la relación lineal dentro del conjunto de datos con respecto a todos los posibles pares de columnas.

Los valores propios y los vectores propios de la matriz de covarianza $\mathbf{C}_{\check{\mathbf{X}}}$ definen los subespacios en el modelo de PCA. Los valores propios λ_k, $k = 1, \ldots, N \cdot L$, y los vectores propios ρ_k, $k = 1, \ldots, N \cdot L$, de $\mathbf{C}_{\check{\mathbf{X}}}$ se calculan de acuerdo con la siguiente expresión:

$$\mathbf{C}_{\check{\mathbf{X}}}\rho_k = \lambda_k \rho_k,\ k = 1, \ldots, N \cdot L.$$

A continuación, los valores propios λ_k (todos ellos no son negativos, ya que $\mathbf{C}_{\check{\mathbf{X}}}$ es una matriz simétrica cuadrada) se ordenan en orden decreciente

$$\lambda_1 \geq \lambda_2 \geq \cdots \geq \lambda_{N \cdot L}$$

en la matriz diagonal $\Lambda \in \mathcal{M}_{(N \cdot L) \times (N \cdot L)}(\mathbb{R})$ y la matriz $\mathbf{P} \in \mathcal{M}_{(N \cdot L) \times (N \cdot L)}(\mathbb{R})$ contiene, en columnas, sus vectores propios ρ_k correspondientes:

$$\mathbf{P}^\top \mathbf{C}_{\check{\mathbf{X}}} \mathbf{P} = \Lambda.$$

Estos vectores propios se conocen como los componentes principales y los valores propios definen la varianza parcial de cada vector propio.

Cuando el *column scaling* se aplica a la matriz $\mathbf{X}$ (Ecuación (5.1)), éste no es el caso de este trabajo, se tiene que la traza de la matriz de covarianza $\mathbf{C}_{\check{\mathbf{X}}}$, que es la suma de los valores propios, es igual al número de columnas de $\mathbf{X}$, es decir, $N \cdot L$:

$$\mathrm{Tr}\left(\mathbf{C}_{\check{\mathbf{X}}}\right) = \sum_{k=1}^{N \cdot L} \lambda_k = N \cdot L.$$

Esto significa que la proporción de la varianza acumulada por los primeros $\ell \in \mathbb{N}$ componentes principales viene dada por:

$$\frac{\lambda_1 + \cdots + \lambda_\ell}{N \cdot L}.$$

Sin embargo, cuando se aplica el MCGS para estandarizar los datos crudos de la matriz $\mathbf{X}$, la traza de la matriz de covarianza $\mathbf{C}_{\check{\mathbf{X}}}$ ya no es necesariamente igual a $N \cdot L$, es decir,

$$\mathrm{Tr}\left(\mathbf{C}_{\check{\mathbf{X}}}\right) = \sum_{k=1}^{N \cdot L} \lambda_k \neq N \cdot L.$$

Como consecuencia, la proporción de la varianza explicada por los primeros ℓ componentes principales viene dada por:

$$\frac{\lambda_1 + \cdots + \lambda_\ell}{\lambda_1 + \cdots + \lambda_{N \cdot L}}.$$

En este trabajo, se utiliza el PCA para reducir la dimensionalidad del conjunto de datos estandarizados $\check{\mathbf{X}}$ seleccionando un reducido, pero aún significativo, número $\ell = D < N \cdot L$ de componentes principales. Esta reducción de la dimensionalidad se realiza a través de la matriz reducida

$$\mathbf{P}_\ell = \mathbf{P}_D = \begin{bmatrix} \rho_1 & \rho_2 & \cdots & \rho_\ell \end{bmatrix} \in \mathcal{M}_{(N \cdot L) \times \ell}(\mathbb{R}), \tag{5.8}$$

que está compuesta por la concatenación de los vectores propios ρ_k asociados a los valores propios más altos. La matriz $\mathbf{P}_\ell = \mathbf{P}_D$ (Ecuación (5.8)) es el modelo de PCA. A continuación, el conjunto de datos estandarizados $\check{\mathbf{X}}$ se proyecta en el espacio vectorial generado por los primeros $\ell = D$ componentes principales a través de la premultiplicación de $\mathbf{P}_\ell$ por $\check{\mathbf{X}}$:

$$\mathbf{T}_\ell = \mathbf{T}_D = \check{\mathbf{X}}\mathbf{P}_\ell \in \mathcal{M}_{n\times\ell}(\mathbb{R}). \tag{5.9}$$

P_ℓ (Ecuación (5.8)) se ha definido como el modelo de PCA que incluye múltiples realizaciones bajo diferentes estados estructurales. Al mismo tiempo, $\mathbf{T}_\ell$ (Ecuación (5.9)) es la proyección del conjunto de datos estandarizados $\check{\mathbf{X}}$ en el subespacio asociado al modelo de PCA. El número de componentes principales $\ell = D \in \mathbb{N}$ se elige de modo que la proporción de la varianza explicada sea mayor o igual al 95 %. Más precisamente, $\ell = D$ es el número natural que satisface las siguientes dos desigualdades:

$$\frac{\lambda_1 + \cdots + \lambda_{\ell-1}}{\lambda_1 + \cdots + \lambda_{N\cdot L}} < 0{,}95, \quad \text{y}$$
$$\frac{\lambda_1 + \cdots + \lambda_{\ell-1} + \lambda_\ell}{\lambda_1 + \cdots + \lambda_{N\cdot L}} \geq 0{,}95.$$

Se espera que las proyecciones de las $n = n_1 + \cdots + n_E$ realizaciones bajo los E diferentes estados estructurales formen grupos o clústeres en el espacio euclídeo ℓ-dimensional $\mathbb{R}^\ell$. Por desgracia, este no es siempre el caso. Por ejemplo, en trabajos anteriores de Mujica *et al.*, 2013 y de Pozo y Vidal, 2015, se puede observar que la proyección en los primeros componentes principales no permite una agrupación visual, *clustering* o separación. En estos trabajos, la detección de daños o fallos se basa en una prueba de hipótesis unidimensional para la igualdad de medias, el llamado método *Welch-Satterthwaite* (Ugarte *et al.*, 2015).

5.1.3.2. *t-Distributed stochastic neighbor embedding* (*t*-SNE)

El objetivo del *t*-SNE

El *t*-SNE es una variación mejorada de la técnica llamada *stochastic neighbor embedding* (SNE, Hinton y Roweis, 2003). Con respecto al SNE, el *t*-SNE es mucho más fácil de optimizar y produce mejores representaciones de los datos originales en el plano y en el espacio, ya que reduce la tendencia a acumular puntos en el centro de la distribución (el llamado *crowding problem*). El SNE sufre del *crowding problem*, que es el resultado de la diferencia exponencial de volumen entre espacios de alta y baja dimensión (Van Der Maaten e Hinton, 2008). Parte de las mejoras del *t*-SNE con respecto al SNE se deben al hecho de que la función de coste utilizada por el *t*-SNE difiere de la utilizada por el SNE en dos aspectos:

(i) El *t*-SNE utiliza una versión simétrica de la función de coste del SNE con gradientes más simples; y

(ii) El *t*-SNE utiliza una distribución *t* de Student, en lugar de una distribución normal, para calcular la similitud entre dos puntos en el espacio de baja dimensión.

Dada una colección de datos de alta dimensión

$$\mathcal{X} = \{\mathbf{x}^1, \ldots, \mathbf{x}^\nu\} \subset \mathbb{R}^D, \quad \nu, D \in \mathbb{N}, \tag{5.10}$$

el objetivo es encontrar una colección de puntos de baja dimensión

$$\mathcal{Y} = \{\mathbf{y}^1, \ldots, \mathbf{y}^\nu\} \subset \mathbb{R}^d, \quad d \in \mathbb{N}$$

que formen una representación fiel de los datos originales $\mathcal{X}$ en un espacio de dimensión inferior. Los valores típicos para d son 2, representación en un plano, o 3, representación en el espacio, donde $d \ll D$. Con representación fiel nos referimos a que los puntos $\mathcal{Y}$ del espacio de dimensión inferior conserven, tanto como sea posible, la estructura local de los datos originales $\mathcal{X}$. Es decir, si dos datos $\mathbf{x}^i$ y $\mathbf{x}^j$, $i, j = 1, \ldots, \nu$, $i \neq j$, son vecinos, con el t-SNE se quiere que los dos puntos correspondientes $\mathbf{y}^i$ e $\mathbf{y}^j$, $i, j = 1, \ldots, \nu$, $i \neq j$, también sean vecinos.

Similitudes por pares

Para conservar las similitudes locales de los datos originales $\mathcal{X}$, el t-SNE primero convierte las distancias euclídeas entre los datos $\mathbf{x}^i$ y $\mathbf{x}^j$

$$d(\mathbf{x}^i, \mathbf{x}^j) = \|\mathbf{x}^i - \mathbf{x}^j\|_2 = \sqrt{(x_1^i - x_1^j)^2 + \cdots + (x_D^i - x_D^j)^2} = \sqrt{\sum_{k=1}^{D} (x_k^i - x_k^j)^2}$$

(donde x_k^i y x_k^j son el componente k-ésimo de los vectores $\mathbf{x}^i$ y $\mathbf{x}^j$, $k = 1, \ldots, D$, respectivamente) en probabilidades condicionales centrando una distribución normal en $\mathbf{x}^i$, calculando la densidad de $\mathbf{x}^j$ bajo esta distribución normal y renormalizando:

$$p_{j|i} = \frac{\exp\left(\dfrac{-\|\mathbf{x}^i - \mathbf{x}^j\|_2^2}{2\sigma_i^2}\right)}{\displaystyle\sum_{\substack{l=1 \\ l \neq i}}^{\nu} \exp\left(\dfrac{-\|\mathbf{x}^i - \mathbf{x}^l\|_2^2}{2\sigma_i^2}\right)}, \quad i, j = 1, \ldots, \nu, \; i \neq j, \tag{5.11}$$

donde $\dfrac{\|\mathbf{x}^i - \mathbf{x}^j\|_2^2}{2\sigma_i^2}$ (distancia euclídea al cuadrado normalizada o afinidad) es la disimilitud entre los datos $\mathbf{x}^i$ y $\mathbf{x}^j$. La varianza de la distribución normal, σ_i^2, se calcula automáticamente (Van Der Maaten e Hinton, 2008). Dado que sólo las similitudes por pares entre los datos son de interés, el t-SNE establece que $p_{i|i} = 0$. Esta probabilidad condicional (Ecuación (5.11)) mide la similitud de $\mathbf{x}^j$ con $\mathbf{x}^i$, es decir, la probabilidad de que $\mathbf{x}^i$ elija a $\mathbf{x}^j$ como vecino. Si dos datos están cerca, $p_{j|i}$ será grande. Sin embargo, si están separados, $p_{j|i}$ será pequeño.

A continuación, al convertir en simétrica la probabilidad condicional (Ecuación (5.11)), el t-SNE define la probabilidad conjunta de la siguiente manera:

$$p_{ij} = \frac{p_{j|i} + p_{i|j}}{2\nu}, \quad i, j = 1, \ldots, \nu, \; i \neq j,$$
$$p_{ii} = 0.$$

Esta probabilidad conjunta es una versión simétrica de la similitud condicional porque tiene la propiedad

$$p_{ij} = p_{ji}, \quad i, j = 1, \dots, \nu.$$

La probabilidad conjunta también mide la similitud por pares entre los datos $\mathbf{x}^i$ y $\mathbf{x}^j$. Como resultado, permite definir la matriz de similitud $\mathcal{P} \in \mathcal{M}_{\nu\times\nu}(\mathbb{R})$ para los datos de alta dimensión como:

$$\mathcal{P} = \begin{bmatrix} 0 & p_{12} & \cdots & p_{1\nu} \\ p_{12} & 0 & \cdots & p_{2\nu} \\ \vdots & \vdots & \ddots & \vdots \\ p_{1\nu} & p_{2\nu} & \cdots & 0 \end{bmatrix}.$$

En la práctica, el uso de probabilidades condicionales o conjuntas produce resultados similares, pero es menos costoso computacionalmente la optimización del modelo conjunto (Van Der Maaten e Hinton, 2008).

Una vez obtenida la matriz de similitud $\mathcal{P}$ para los datos originales $\mathcal{X}$, se define también la matriz de similitud $\mathcal{Q} \in \mathcal{M}_{\nu\times\nu}(\mathbb{R})$ para los puntos $\mathcal{Y}$. Básicamente, se construye la matriz $\mathcal{Q}$ siguiendo la misma idea que para la matriz de similitud $\mathcal{P}$. La única diferencia es que para la matriz $\mathcal{Q}$ se utiliza una distribución t de Student renormalizada con un grado de libertad y $\sigma_i^2 = \frac{1}{2}$ para toda i, en lugar de una distribución normal:

$$q_{ij} = \frac{\dfrac{1}{1 + \|\mathbf{y}^i - \mathbf{y}^j\|_2^2}}{\displaystyle\sum_{k=1}^{\nu}\sum_{\substack{l=1 \\ l\neq k}}^{\nu} \frac{1}{1 + \|\mathbf{y}^k - \mathbf{y}^l\|_2^2}}, \quad i, j = 1, \dots, \nu,\ i \neq j, \tag{5.12}$$

$$q_{ii} = 0. \tag{5.13}$$

Está claro que, por su definición en las Ecuaciones (5.12)–(5.13), $q_{ij} = q_{ji}$. La probabilidad conjunta q_{ij} es la homóloga, de baja dimensión, de p_{ij} y representa la estructura local de los puntos en el espacio de baja dimensión.

Las colas pesadas de la distribución t de Student permiten que los datos $\mathbf{x}^i$ y $\mathbf{x}^j$ que no son vecinos sean modelados por los puntos $\mathbf{y}^i$ e $\mathbf{y}^j$ que están separados: la probabilidad de ser vecino disminuye más lentamente y, por lo tanto, hay menos necesidad de alejar algunos puntos y agrupar los puntos restantes en el centro de la distribución (*crowding problem*). En otras palabras, el t-SNE permite que los datos que son sólo un poco similares se representen más separados en el espacio de baja dimensión. Pero la elección de la distribución t de Student para los puntos de baja dimensión va más allá, ya que alivia tanto el *crowding problem* como los problemas de optimización del SNE (Van Der Maaten e Hinton, 2008).

Mientras que la matriz de similitud $\mathcal{P}$ es fija y está unívocamente determinada por los datos de alta dimensión $\mathcal{X}$, la matriz de similitud $\mathcal{Q}$ depende de los puntos de baja dimensión $\mathcal{Y}$.

Comparación de matrices de similitud: la función de coste

El objetivo es seleccionar los puntos de baja dimensión para que las dos matrices de similitud, $\mathcal{P}$ y $\mathcal{Q}$, sean lo más similares posible. La similitud entre estas dos matrices se define en términos de la divergencia Kullback-Leibler (KL). La divergencia KL es una medida de cómo una distribución de probabilidad difiere de una segunda distribución de probabilidad y se puede definir como (Hinton y Roweis, 2003; Min, 2005; Van Der Maaten e Hinton, 2008):

$$\mathcal{C} = \mathcal{D}_{KL}\left(\mathcal{P} \| \mathcal{Q}\right) = \sum_{i=1}^{\nu} \sum_{\substack{j=1 \\ j \neq i}}^{\nu} p_{ij} \log\left(\frac{p_{ij}}{q_{ij}}\right). \tag{5.14}$$

La divergencia KL entre las distribuciones de probabilidad conjunta $\mathcal{P}$ y $\mathcal{Q}$ mide la distancia entre las dos matrices de similitud. Por lo tanto, minimizar la divergencia KL reduce el error entre estas dos matrices. En otras palabras, los puntos de baja dimensión de datos de alta dimensión similares deben estar muy juntos y los puntos de baja dimensión de datos de alta dimensión diferentes deben estar separados para minimizar la función de coste $\mathcal{C}$ (Ecuación (5.14)). Téngase en cuenta que:

(i) la divergencia KL no es negativa y es 0 si, y solo si, ambas distribuciones son iguales, es decir, la similitud entre los datos $\mathbf{x}^i$ y $\mathbf{x}^j$ está perfectamente modelada por los puntos $\mathbf{y}^i$ e $\mathbf{y}^j$—; y

(ii) la función de coste $\mathcal{C}$ generalmente no es convexa y diferentes simulaciones pueden producir resultados diferentes.

Para minimizar la función de coste $\mathcal{C}$, se utiliza el método de descenso del gradiente:

$$\frac{\partial \mathcal{C}}{\partial \mathbf{y}^i} = 4 \sum_{\substack{j=1 \\ j \neq i}}^{\nu} \frac{p_{ij} - q_{ij}}{1 + \|\mathbf{y}^i - \mathbf{y}^j\|_2^2} \left(\mathbf{y}^i - \mathbf{y}^j\right).$$

Este gradiente expresa la suma de todas las fuerzas aplicadas al punto $\mathbf{y}^i$, es decir, la suma de las fuerzas con las que se atraen o repelen el punto $\mathbf{y}^i$ y todos los demás puntos $\mathbf{y}^j$. Las ubicaciones de los puntos $\mathcal{Y}$ se determinan minimizando $\mathcal{C}$.

Actualización del punto de baja dimensión

Dado que el descenso del gradiente es un algoritmo de optimización iterativo, el punto $\mathbf{y}^i$ se actualiza en cada iteración utilizando la siguiente expresión:

$$\mathbf{y}^i_{(t)} = \mathbf{y}^i_{(t-1)} + \eta \frac{\partial \mathcal{C}}{\partial \mathbf{y}^i} + \alpha(t)\left(\mathbf{y}^i_{(t-1)} - \mathbf{y}^i_{(t-2)}\right), \tag{5.15}$$

donde $\mathbf{y}^i_{(t)}$ es la solución en la iteración t, η es la tasa de aprendizaje (*learning rate*) y $\alpha(t)$ es el término de impulso (*momentum*) en la iteración t. La tasa de aprendizaje determina el tamaño del salto entre cada iteración durante la optimización de la función de coste $\mathcal{C}$. Asimismo, en la Ecuación (5.15), se añade un término de impulso relativamente grande para acelerar la optimización.

Esquema algorítmico

Data: datos de alta dimensión $\mathcal{X} = \{\mathbf{x}^1, \ldots, \mathbf{x}^\nu\}$;
parámetros de la función de coste: *perplexity* p;
parámetros de optimización: número de iteraciones τ, *learning rate* η, *momentum* $\alpha(t)$.
Result: puntos de baja dimensión $\mathcal{Y}_{(\tau)} = \{\mathbf{y}^1_{(\tau)}, \ldots, \mathbf{y}^\nu_{(\tau)}\}$.

```
begin
    calcular la matriz de similitud P = (p_ij) para los datos de alta dimensión X;
    solución inicial de la muestra Y_(−1) = {0, ..., 0}, Y_(0) = {y^1_(0), ..., y^ν_(0)};
    for t = 1 to t = τ do
        calcular la matriz de similitud Q = (q_ij) para los puntos de baja
          dimensión Y_(t);
        for i = 1 to i = ν do
            calcular el gradiente ∂C/∂y^i de la función de coste C = D_KL(P‖Q);
            actualizar y^i_(t) con la fórmula:
              y^i_(t) = y^i_(t−1) + η ∂C/∂y^i + α(t) (y^i_(t−1) − y^i_(t−2));
        end
    end
end
```

Algorithm 1: Esquema algorítmico del t-SNE.

5.1.3.3. *Parametric t*-SNE (P-*t*-SNE)

El t-SNE tiene un enorme coste computacional de optimización al tratarse de una técnica no paramétrica: para proyectar nuevos datos, la optimización debe ejecutarse con todo el conjunto de datos completo nuevamente. Para evitar la pesada optimización del t-SNE, se propone su versión paramétrica, el P-t-SNE. El P-t-SNE es una técnica de reducción de la dimensionalidad no supervisada que aprende una proyección paramétrica entre el espacio de datos de alta dimensión y el espacio latente de baja dimensión, conservando la estructura local de los datos de alta dimensión en el espacio latente tan bien como sea posible.

En el método P-t-SNE, la función $f : X \to Y$, desde el espacio de alta dimensión X hasta el espacio de baja dimensión Y, se parametriza a través de una NN prealimentada (*feed-forward* en inglés) con pesos W. La NN está entrenada de tal manera que retiene la estructura local de los datos de alta dimensión en el espacio de baja dimensión. Se distinguen dos etapas principales en el entrenamiento de la NN:

1. Preentrenamiento con una *restricted Boltzmann machine* (RBM). La RBM se utiliza para construir una red preentrenada del P-t-SNE. El objetivo principal de la etapa de preentrenamiento es definir una inicialización de los parámetros del modelo para la siguiente etapa.

2. Sintonización fina utilizando la función de coste del P-t-SNE. En esta etapa, los pesos de la NN preentrenada se sintonizan de tal manera que la NN conserva la estructura local de los datos de alta dimensión en el espacio de baja dimensión. En la NN prealimentada, el término q_{ij} del t-SNE (Ecuación (5.12)) se adapta de

la siguiente manera:

$$q_{ij} = \frac{\left[1 + \|f(x_i|W) - f(x_j|W)\|^2/\alpha\right]^{-(\alpha+1)/2}}{\sum_{k \neq l}\left[1 + \|f(x_k|W) - f(x_l|W)\|^2/\alpha\right]^{-(\alpha+1)/2}},$$

donde α denota los grados de libertad de la distribución t de Student.

Restricted Boltzmann machine

En esta sección, se introduce de forma breve la RBM (Smolensky, 1986; Hinton, 2012).

Una RBM es una NN estocástica de dos capas. Esta red consta de una capa visible o de entrada (nodos visibles $\mathbf{v}$) y una capa oculta (nodos ocultos $\mathbf{h}$). Los valores de los nodos siguen, normalmente, una distribución de Bernoulli. Cada nodo visible está conectado a todos los nodos ocultos mediante conexiones ponderadas, pero no hay conexiones intracapa, es decir, no se dan conexiones entre nodos de una misma capa. La estructura de la RBM se ilustra en la Figura 5.2.

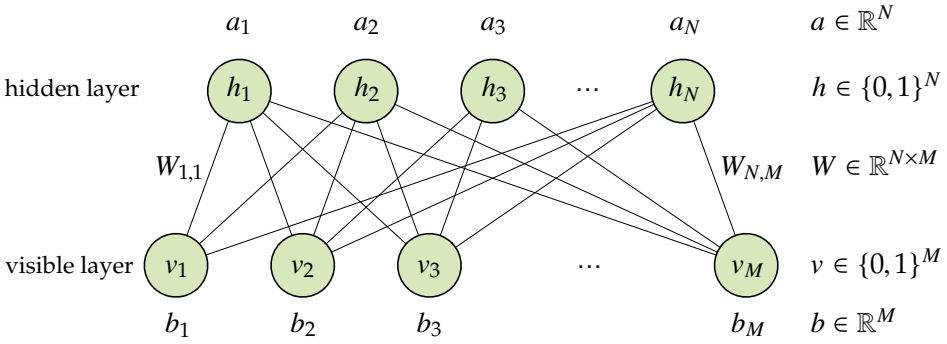

FIGURA 5.2: Estructura de la RBM.

La distribución de Boltzmann se especifica mediante la función de energía $E(\mathbf{v}, \mathbf{h})$ y esta distribución proporciona la distribución conjunta sobre todos los nodos, $P(\mathbf{v}, \mathbf{h})$:

$$E(\mathbf{v}, \mathbf{h}) = -\sum_{i,j} W_{ij} v_i h_j - \sum_i b_i v_i - \sum_j a_j h_j,$$
$$P(\mathbf{v}, \mathbf{h}) = \frac{\exp(-E(\mathbf{v}, \mathbf{h}))}{\sum_{\mathbf{v},\mathbf{h}} \exp(-E(\mathbf{v}, \mathbf{h}))},$$

donde W_{ij} es el peso de la conexión entre un nodo visible v_i y un nodo oculto h_j; y b_i y a_j son los sesgos de los nodos visibles y ocultos, respectivamente. Además, las probabilidades condicionales $P(v_i = 1|\mathbf{h})$ y $P(h_j = 1|\mathbf{v})$ están dadas por la función sigmoidea:

$$P(v_i = 1|\mathbf{h}) = \frac{1}{1 + \exp(-\sum_j W_{ij} h_j - b_i)}, \tag{5.16}$$
$$P(h_j = 1|\mathbf{v}) = \frac{1}{1 + \exp(-\sum_i W_{ij} v_i - a_j)}. \tag{5.17}$$

La RBM puede calcular los valores de los nodos visibles a partir de los valores de los nodos ocultos a través de la Ecuación (5.16); de manera similar, la RBM puede

calcular los valores de los nodos ocultos a partir de los nodos visibles mediante la Ecuación (5.17).

Los parámetros del modelo (W, b y a) se actualizan de modo que la distribución marginal sobre los nodos visibles bajo el modelo, $P_{\text{model}}(\mathbf{v})$, esté próxima a la verdadera distribución de los datos, $P_{\text{data}}(\mathbf{v})$. En particular, la RBM usa la divergencia KL para medir la distancia entre la distribución verdadera, $P_{\text{data}}(\mathbf{v})$, y la distribución basada en el modelo, $P_{\text{model}}(\mathbf{v})$. El gradiente de la divergencia KL con respecto a W_{ij} viene dado por

$$\frac{\partial \text{KL}(P_{\text{data}}||P_{\text{model}})}{\partial W_{ij}} = \mathbb{E}[v_i h_j]_{P_{\text{data}}} - \mathbb{E}[v_i h_j]_{P_{\text{model}}},$$

donde $\mathbb{E}[v_i h_j]_{P_{\text{data}}}$ es el valor esperado bajo la distribución verdadera y $\mathbb{E}[v_i h_j]_{P_{\text{model}}}$ es el valor esperado bajo la distribución del modelo. Sin embargo, $\mathbb{E}[v_i h_j]_{P_{\text{model}}}$ no se puede calcular analíticamente. Para evitar calcular el modelo, se sigue una aproximación: el gradiente de una función objetivo ligeramente diferente que se llama *contrastive divergence* (CD, Hinton, 2002). La CD mide cómo la distribución del modelo se aleja de la verdadera distribución de los datos a través de

$$\text{KL}(P_{\text{data}}||P_{\text{model}}) - \text{KL}(P_1||P_{\text{model}}),$$

donde $P_1(\mathbf{v})$ es la distribución sobre los nodos visibles, ya que la RBM puede ejecutarse para una iteración (es decir, un barrido de Gibbs) cuando se inicializa de acuerdo con la verdadera distribución. Usando técnicas de descenso del gradiente estándar, la CD se puede minimizar de manera eficiente:

$$\mathbb{E}[v_i h_j]_{P_{\text{data}}} - \mathbb{E}[v_i h_j]_{P_1}.$$

El segundo término, $\mathbb{E}[v_i h_j]_{P_1}$, se estima a partir de las muestras obtenidas mediante el muestreo de Gibbs.

5.1.4. Efecto del *clustering*

En la Sección 5.1.3.1, la reducción de la dimensionalidad se realiza utilizando el PCA. Específicamente, $n = n_1 + \cdots + n_E$ observaciones bajo E diferentes estados estructurales, las filas de la matriz estandarizada $\check{\mathbf{X}}$ (Ecuación (5.3)), que pueden verse como vectores $N \cdot L$-dimensionales, se proyectan y transforman en vectores ℓ-dimensionales. Esta reducción de la dimensión de los datos originales estandarizados se realiza con una pequeña pérdida de información (menos del 5 %) y se espera que ℓ sea mucho más pequeña que $N \cdot L$.

Seguidamente se aplica una segunda reducción de la dimensionalidad a los datos proyectados en la matriz $\mathbf{T}_\ell$ (Ecuación (5.9)) usando el t-SNE/P-t-SNE (Secciones 5.1.3.2 y 5.1.3.3): se define

$$\mathbf{x}^i = \mathbf{e}_i^\top \mathbf{T}_\ell = \mathbf{e}_i^\top \check{\mathbf{X}} \mathbf{P}_\ell \in \mathbb{R}^\ell,\ i = 1, \ldots, n$$

como la fila i-ésima de la matriz $\mathbf{T}_\ell$. El vector $\mathbf{e}_i \in \mathbb{R}^n$ es el i-ésimo vector de la base canónica. Se define también

$$\mathcal{X} = \{\mathbf{x}^1, \ldots, \mathbf{x}^n\} \subset \mathbb{R}^\ell \tag{5.18}$$

como una colección de datos de "alta" dimensión (ha sufrido ya una primera reducción de la dimensión con el PCA). El objetivo es encontrar una colección de puntos bidimensionales

$$\mathcal{Y} = \{\mathbf{y}^1, \ldots, \mathbf{y}^n\} \subset \mathbb{R}^2$$

que represente al conjunto original $\mathcal{X}$ (Ecuación 5.18) sin pérdida explícita de información y conservando la estructura local de este conjunto. Después de la aplicación del t-SNE/P-t-SNE, se espera observar E grupos o clústeres relacionados con los E diferentes estados estructurales. Estos grupos o clústeres estarán formados por los puntos:

$$\begin{aligned}
\{\mathbf{y}^1, \ldots, \mathbf{y}^{n_1}\} &\subset \mathcal{Y}, && \text{relacionado con el primer estado estructural;}\\
\{\mathbf{y}^{n_1+1}, \ldots, \mathbf{y}^{n_1+n_2}\} &\subset \mathcal{Y}, && \text{relacionado con el segundo estado estructural;}\\
\{\mathbf{y}^{n_1+n_2+1}, \ldots, \mathbf{y}^{n_1+n_2+n_3}\} &\subset \mathcal{Y}, && \text{relacionado con el tercer estado estructural;}\\
&\vdots &&\\
\{\mathbf{y}^{n-n_{E-1}-n_E+1}, \ldots, \mathbf{y}^{n-n_E}\} &\subset \mathcal{Y}, && \text{relacionado con el penúltimo estado estructural; y}\\
\{\mathbf{y}^{n-n_E+1}, \ldots, \mathbf{y}^{n}\} &\subset \mathcal{Y}, && \text{relacionado con el último estado estructural.}
\end{aligned}$$

5.2. Detección y clasificación de los daños: estructura a diagnosticar

En la Sección 5.1.4, se describe cómo las observaciones originales estandarizadas bajo diferentes estados estructurales definen un conjunto de grupos o clústeres en un plano. En esta sección, se presenta el procedimiento de detección y clasificación de daños para una estructura que tiene que ser diagnosticada.

Para la detección y clasificación de daños, se necesita una sola observación de la estructura actual para diagnosticarla. Los datos recopilados incluyen diferentes señales medidas por el mismo número de sensores, N, y con el mismo número de componentes en cada señal, L, como en la Ecuación (5.1). Cuando se obtienen estas medidas, se construye un nuevo vector de datos $\mathbf{z}$:

$$\mathbf{z}^\top = \left[\begin{array}{ccc|ccc|c|ccc} z^{1,1} & \ldots & z^{1,L} & z^{2,1} & \ldots & z^{2,L} & \ldots & z^{N,1} & \ldots & z^{N,L} \end{array}\right] \in \mathbb{R}^{N\cdot L}.$$

5.2.1. Estandarización (MCGS)

Antes de que los datos $\mathbf{z}^\top$, que provienen de la estructura a diagnosticar, se proyecten en el espacio generado por los ℓ primeros componentes principales, se deben estandarizar para definir el vector fila $\check{\mathbf{z}}^\top$:

$$\check{z}^{k,j} = \frac{z^{k,j} - \mu^{k,j}}{\sigma^k}, \quad k = 1, \ldots, N,\ j = 1, \ldots, L, \tag{5.19}$$

donde $\mu^{k,j}$ es la media aritmética calculada en la Ecuación (5.4) y σ^k es la desviación estándar de todos los elementos en el bloque vertical $\mathbf{X}^k$ calculado en la Ecuación (5.5).

5.2.2. Proyección (PCA)

La proyección del vector fila estandarizado $\check{\mathbf{z}}^\top \in \mathbb{R}^{N\cdot L}$ en el espacio generado por los ℓ primeros componentes principales se realiza a través de la siguiente multiplicación:

$$\mathbf{x}^{n+1} = \check{\mathbf{z}}^\top \cdot \mathbf{P}_\ell \in \mathbb{R}^\ell.$$

Hay que remarcar que el vector $N \cdot L$-dimensional que contiene los datos de la estructura a diagnosticar se transforma en un vector ℓ-dimensional. Este nuevo vector se añade al conjunto de datos $\mathcal{X}$ (Ecuación (5.18)) para definir un nuevo conjunto:

$$\mathcal{X}' = \mathcal{X} \cup \{\mathbf{x}^{n+1}\} = \{\mathbf{x}^1, \ldots, \mathbf{x}^n, \mathbf{x}^{n+1}\} \subset \mathbb{R}^\ell. \tag{5.20}$$

5.2.3. *t*-SNE/P-*t*-SNE y clasificación final

El *t*-SNE/P-*t*-SNE se aplica al conjunto de datos ℓ-dimensional $\mathcal{X}'$ (Ecuación (5.20)) para encontrar una colección de puntos bidimensional

$$\mathcal{Y}' = \{\mathbf{y}^1, \ldots, \mathbf{y}^n, \mathbf{y}^{n+1}\} \subset \mathbb{R}^2$$

que represente al conjunto original $\mathcal{X}$ (Ecuación 5.18) sin pérdida explícita de información y conservando la estructura local de este conjunto, además de incluir el punto $\mathbf{y}^{n+1}$ asociado al dato $\mathbf{x}^{n+1}$.

Tras aplicar el *t*-SNE/P-*t*-SNE, se espera observar E grupos o clústeres, los relacionados con los E diferentes estados estructurales. Como en la Sección 5.1.4, estos grupos o clústeres estarán formados por los puntos:

$$\begin{aligned}
\{\mathbf{y}^1, \ldots, \mathbf{y}^{n_1}\} &\subset \mathcal{Y}, && \text{relacionado con el primer estado estructural;}\\
\{\mathbf{y}^{n_1+1}, \ldots, \mathbf{y}^{n_1+n_2}\} &\subset \mathcal{Y}, && \text{relacionado con el segundo estado estructural;}\\
\{\mathbf{y}^{n_1+n_2+1}, \ldots, \mathbf{y}^{n_1+n_2+n_3}\} &\subset \mathcal{Y}, && \text{relacionado con el tercer estado estructural;}\\
&\vdots &&\\
\{\mathbf{y}^{n-n_{E-1}-n_E+1}, \ldots, \mathbf{y}^{n-n_E}\} &\subset \mathcal{Y}, && \text{relacionado con el penúltimo estado estructural; y}\\
\{\mathbf{y}^{n-n_E+1}, \ldots, \mathbf{y}^{n}\} &\subset \mathcal{Y}, && \text{relacionado con el último estado estructural.}
\end{aligned}$$

A continuación, para cada grupo o clúster, se calcula su centroide, es decir, la media de los valores de los puntos en el grupo o clúster. Por ejemplo, el centroide asociado con el primer estado estructural será:

$$\mathcal{Y}_1 := \frac{1}{n_1}\sum_{i=1}^{n_1} \mathbf{y}^i = \frac{\mathbf{y}^1 + \cdots + \mathbf{y}^{n_1}}{n_1} \in \mathbb{R}^2,$$

mientras que el centroide asociado con el segundo estado estructural será:

$$\mathcal{Y}_2 := \frac{1}{n_2}\sum_{i=1}^{n_2} \mathbf{y}^{n_1+i} = \frac{\mathbf{y}^{n_1+1} + \cdots + \mathbf{y}^{n_1+n_2}}{n_2} \in \mathbb{R}^2.$$

En general, el centroide asociado con el l-ésimo estado estructural, $l = 1, \ldots, E$, será el punto del plano definido como

$$\mathcal{Y}_l := \frac{1}{n_l} \sum_{i=1}^{n_l} \mathbf{y}^{\left(\sum_{j=0}^{l-1} n_j\right)+i} \in \mathbb{R}^2, \; l = 1, \ldots, E, \tag{5.21}$$

donde $n_0 = 0$. Por lo tanto, la estructura actual a diagnosticar estará asociada al l-ésimo estado estructural si

$$l = \arg \min_{l=1,\ldots,E} \|\mathcal{Y}_l - \mathbf{y}^{n+1}\|_2,$$

es decir, si la distancia mínima entre $\mathbf{y}^{n+1}$ y cada uno de los centroides corresponde a la distancia euclídea entre $\mathbf{y}^{n+1}$ y $\mathcal{Y}_l$. Llamamos a este enfoque la distancia punto-centroide más pequeña (ver Figura 5.3).

En las Figuras 5.4, 5.5 y 5.6, se muestran los diagramas de flujo de los diferentes enfoques propuestos.

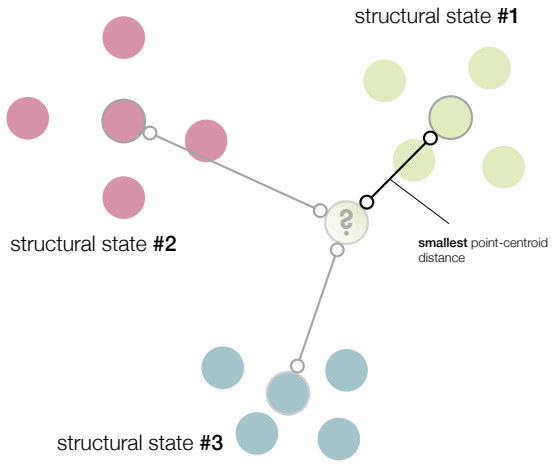

FIGURA 5.3: La estructura actual a diagnosticar se asocia al estado estructural con la distancia punto-centroide más pequeña.

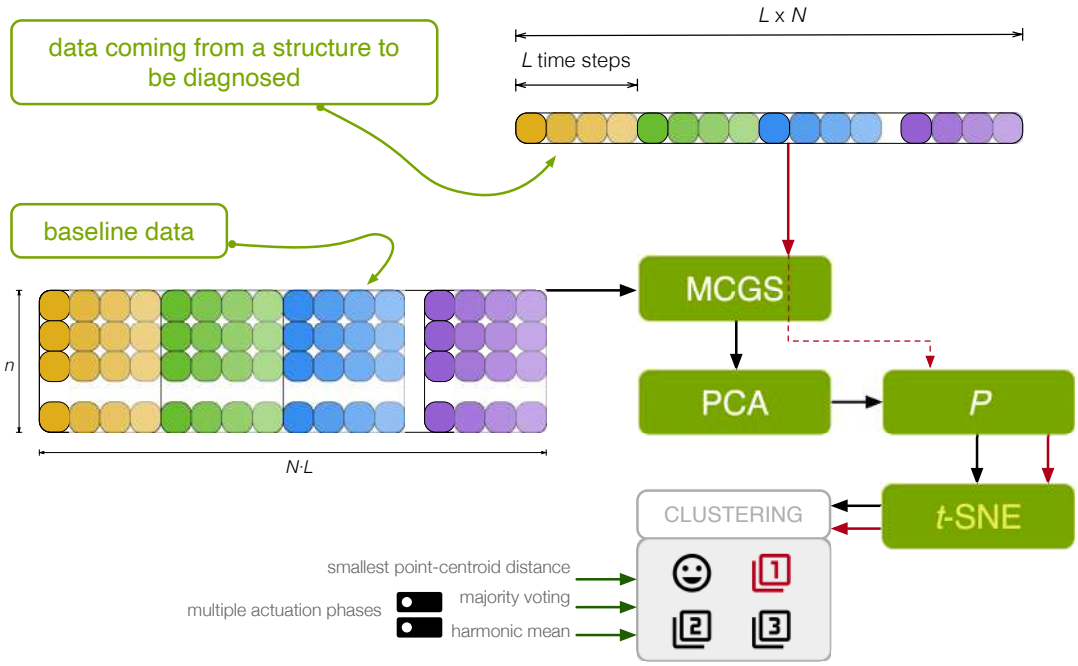

FIGURA 5.4: Diagrama de flujo del primer enfoque propuesto. Los datos que provienen de una estructura se estandarizan primero y luego se proyectan en el modelo de PCA. Finalmente, el *t*-SNE se aplica para crear los grupos o clústeres que se utilizarán en la detección y clasificación de los cambios estructurales.

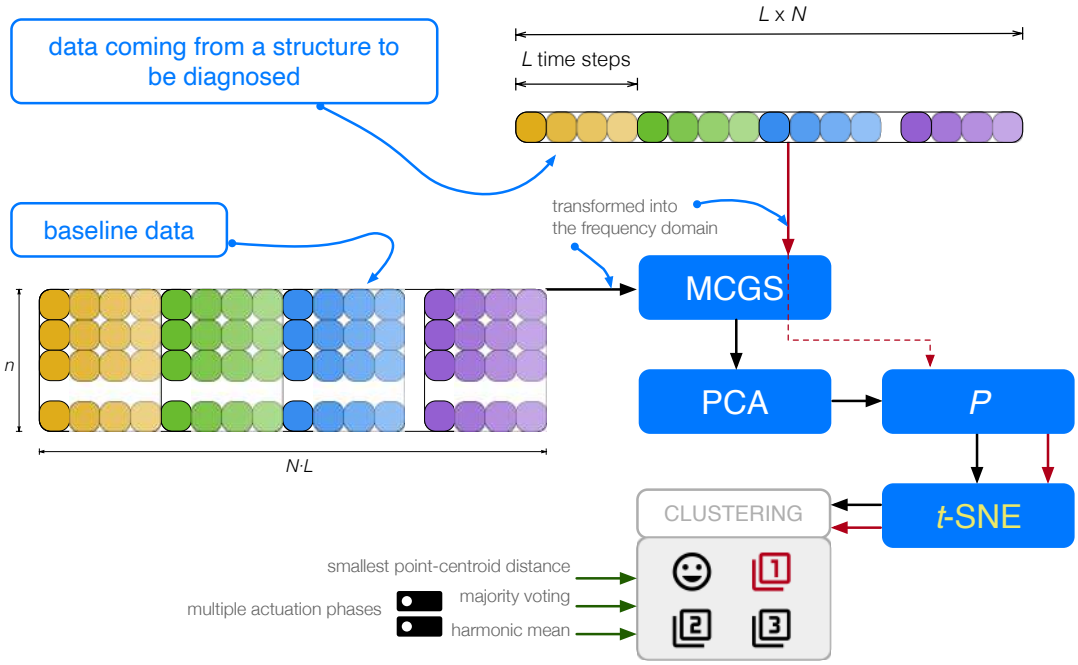

FIGURA 5.5: Diagrama de flujo del segundo enfoque propuesto. Los datos procedentes de una estructura se transforman primero en el dominio de la frecuencia y se estandarizan, y luego se proyectan en el modelo de PCA. Finalmente, el *t*-SNE se utiliza para crear los grupos o clústeres que se utilizarán en la detección y clasificación de los cambios estructurales.

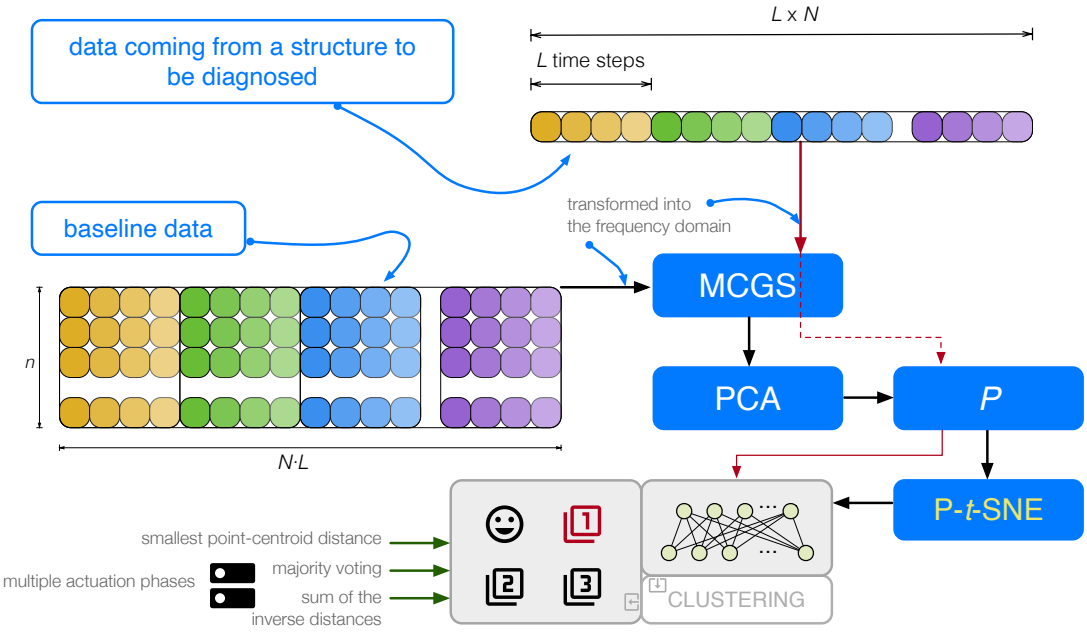

FIGURA 5.6: Diagrama de flujo del tercer enfoque propuesto. Los datos procedentes de una estructura se transforman primero en el dominio de la frecuencia y se estandarizan mediante el MCGS, y luego se proyectan en el modelo de PCA. Finalmente, el P-*t*-SNE se aplica para generar los grupos o clústeres que se utilizarán en la detección y clasificación de los cambios estructurales.

5.3. Aplicación del método propuesto a una placa de aluminio con 4 PZT

5.3.1. Configuración experimental

Se considera una placa cuadrada de aluminio con un área de 1600 cm^2 (40 cm $\times$ 40 cm y un grosor de 0,2 cm) equipada con cuatro PZT para demostrar la fiabilidad del método propuesto de detección y clasificación de daños. Los discos PZT están unidos a la superficie y su ubicación exacta se muestra en la Figura 5.7(a): suponiendo que el origen de las coordenadas se coloca en la esquina inferior izquierda de la placa, los sensores piezoeléctricos se instalan en las coordenadas (unidades en centímetros)

- $(20, 35)$, primer PZT (S1);
- $(35, 20)$, segundo PZT (S2);
- $(20, 5)$, tercer PZT (S3) y
- $(5, 20)$, cuarto PZT (S4).

Por lo tanto, la distancia entre los cuatro sensores no es la misma. Por ejemplo, la distancia entre los centros de los sensores 1 y 4 y la distancia entre los centros de los sensores 1 y 2 son iguales ($15\sqrt{2} \approx 21{,}21$ cm). Sin embargo, la distancia entre los centros de los sensore 1 y 3 es mayor (30 cm).

Estos PZT pueden funcionar tanto en modo actuador (excitando la placa con la señal *BURST* de la Figura 5.8, produciendo así una vibración mecánica) como en modo sensor (detectando una respuesta mecánica que varía en el tiempo).

Para simular el daño, de manera no destructiva, se añade una masa de 17,2916 gramos en la placa de aluminio. Esta masa es un imán unido a ambos lados de la placa, ya que el aluminio es un metal no magnético. Se utiliza este tipo de daño para cambiar las propiedades de la estructura y para producir cambios en la onda propagada. La ubicación de la masa define cada daño y, por lo tanto, se obtienen diferentes escenarios para validar el método propuesto. Estas ubicaciones son las siguientes (unidades en centímetros):

- el daño 1 se sitúa en las coordenadas $(12{,}5, 27{,}5)$;
- el daño 2 se sitúa en las coordenadas $(27{,}5, 27{,}5)$ y
- el daño 3 se sitúa en las coordenadas $(12{,}5, 12{,}5)$.

En consecuencia, se consideran $E = 4$ estados estructurales (Figura 5.7(b)):

- el primer estado estructural corresponde al estado saludable de la estructura, es decir, corresponde a la placa de aluminio sin daños (sin la masa);
- los estados estructurales segundo (daño 1), tercero (daño 2) y cuarto (daño 3) corresponden a la placa con una masa añadida en las posiciones indicadas en la Figura 5.7(a).

La placa de aluminio está aislada de la vibración y del ruido del laboratorio, como se muestra en la Figura 5.7(b).

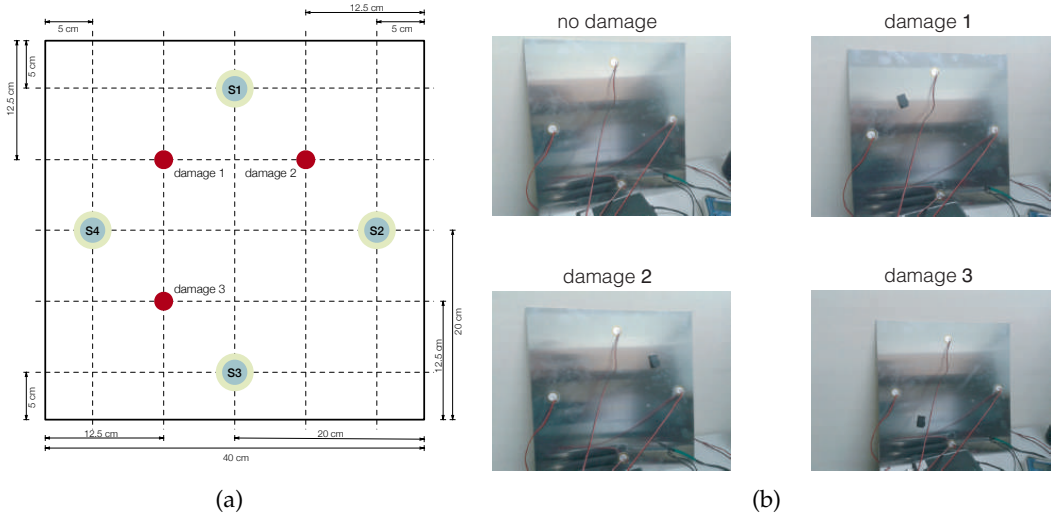

(a) (b)

FIGURA 5.7: (a) Placa de aluminio equipada con cuatro PZT (S1, S2, S3 y S4). (b) Los cuatro estados estructurales de la placa de aluminio.

5.3.2. Escenarios y fases de actuación

La configuración experimental incluye tres escenarios diferentes:

- **Escenario 1**. Las señales se adquieren utilizando un cable corto (0,5 m) desde el digitalizador hasta los sensores y estas señales se filtran con el algoritmo Savitzky–Golay (Orfanidis, 1995) después de añadir ruido blanco gaussiano. El filtro se aplica para suavizar los datos.
- **Escenario 2**. Las señales no filtradas se adquieren utilizando un cable corto (0,5 m) desde el digitalizador hasta los sensores.

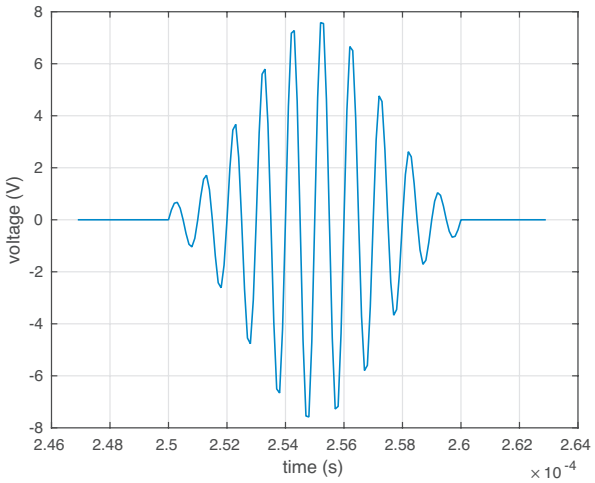

FIGURA 5.8: En el modo actuador, los PZT aplican esta señal *BURST* para producir una vibración mecánica.

- **Escenario 3**. Las señales se adquieren utilizando un cable largo (2,5 m) desde el digitalizador hasta los sensores. Las señales también se filtran con el algoritmo Savitzky–Golay.

De este modo, se podrá observar el efecto de los siguientes parámetros en el rendimiento del método propuesto: usar un cable corto o largo desde el digitalizador hasta los sensores, añadir ruido blanco gaussiano a las señales medidas y filtrar las señales con un filtro Savitzky–Golay.

Como se menciona en la Sección 5.3.1, se utilizan cuatro PZT (S1, S2, S3 y S4) para excitar la placa de aluminio y recoger la respuesta medida. Esta red de sensores funciona en lo que llamamos fases de actuación. En cada fase de actuación, se usa un único PZT como actuador (sensor activo: el PZT excita la estructura con la señal *BURST* de la Figura 5.8) y el resto de los PZT se usan como sensores (sensores pasivos: los PZT miden las señales). Por lo tanto, tenemos tantas fases de actuación como sensores:

- **Fase de actuación 1**. S1 se utiliza como actuador. S2, S3 y S4 se utilizan como sensores.
- **Fase de actuación 2**. S2 se utiliza como actuador. S1, S3 y S4 se utilizan como sensores.
- **Fase de actuación 3**. S3 se utiliza como actuador. S1, S2 y S4 se utilizan como sensores.
- **Fase de actuación 4**. S4 se utiliza como actuador. S1, S2 y S3 se utilizan como sensores.

Es muy común en la literatura fusionar los datos que provienen de diferentes fases de actuación en una única matriz de datos (Vitola *et al.*, 2017a; Vitola *et al.*, 2017b). En este estudio, se utiliza el enfoque con una única matriz de datos, pero también se examina el caso en el que cada fase de actuación funciona como un clasificador (Sección 5.3.5).

5.3.3. Integración de los datos experimentales

Dado un escenario particular (Sección 5.3.2), se obtienen cuatro matrices $\mathbf{X}[\varphi],\ \varphi = 1,\dots,4$, una por cada fase de actuación. Cada matriz $\mathbf{X}[\varphi],\ \varphi = 1,\dots,4$, se organiza de la siguiente manera:

- hay $n_1 = n_2 = n_3 = n_4 = 25$ observaciones por cada uno de los 4 estados estructurales. En consecuencia, cada matriz $\mathbf{X}[\varphi],\ \varphi = 1,\dots,4$, consta de 100 filas, es decir, $n_1 + n_2 + n_3 + n_4 = 25 \cdot 4$. En concreto, las primeras 25 filas son la estructura sin daño, las siguientes 25 filas son la estructura con el daño 1, y así sucesivamente hasta el daño 3.
- Para cada fase de actuación $\varphi,\ \varphi = 1,\dots,4$, $N = 3$ PZT, que funcionan como sensores, toman mediciones durante $L = 60000$ instantes de tiempo. Por lo tanto, el número de columnas de la matriz $\mathbf{X}[\varphi],\ \varphi = 1,\dots,4$, es igual a $N \cdot L = 3 \cdot 60000 = 180000$.

Así pues, la matriz que recopila todas las realizaciones bajo los 4 estados estructurales, en el dominio del tiempo, es:

$$\mathbf{X}[\varphi] = \left(x[\varphi]_{i,l}^{k,j}\right) = \left[\begin{array}{ccc:ccc:ccc} x[\varphi]_{1,1}^{1,1} & \cdots & x[\varphi]_{1,1}^{1,60000} & x[\varphi]_{1,1}^{2,1} & \cdots & x[\varphi]_{1,1}^{2,60000} & x[\varphi]_{1,1}^{3,1} & \cdots & x[\varphi]_{1,1}^{3,60000} \\ \vdots & \ddots & \vdots & \vdots & \ddots & \vdots & \vdots & \ddots & \vdots \\ x[\varphi]_{25,1}^{1,1} & \cdots & x[\varphi]_{25,1}^{1,60000} & x[\varphi]_{25,1}^{2,1} & \cdots & x[\varphi]_{25,1}^{2,60000} & x[\varphi]_{25,1}^{3,1} & \cdots & x[\varphi]_{25,1}^{3,60000} \\ \hdashline x[\varphi]_{1,2}^{1,1} & \cdots & x[\varphi]_{1,2}^{1,60000} & x[\varphi]_{1,2}^{2,1} & \cdots & x[\varphi]_{1,2}^{2,60000} & x[\varphi]_{1,2}^{3,1} & \cdots & x[\varphi]_{1,2}^{3,60000} \\ \vdots & \ddots & \vdots & \vdots & \ddots & \vdots & \vdots & \ddots & \vdots \\ x[\varphi]_{25,2}^{1,1} & \cdots & x[\varphi]_{25,2}^{1,60000} & x[\varphi]_{25,2}^{2,1} & \cdots & x[\varphi]_{25,2}^{2,60000} & x[\varphi]_{25,2}^{3,1} & \cdots & x[\varphi]_{25,2}^{3,60000} \\ \hdashline \vdots & \ddots & \vdots & \vdots & \ddots & \vdots & \vdots & \ddots & \vdots \\ \hdashline x[\varphi]_{1,4}^{1,1} & \cdots & x[\varphi]_{1,4}^{1,60000} & x[\varphi]_{1,4}^{2,1} & \cdots & x[\varphi]_{1,4}^{2,60000} & x[\varphi]_{1,4}^{3,1} & \cdots & x[\varphi]_{1,4}^{3,60000} \\ \vdots & \ddots & \vdots & \vdots & \ddots & \vdots & \vdots & \ddots & \vdots \\ x[\varphi]_{25,4}^{1,1} & \cdots & x[\varphi]_{25,4}^{1,60000} & x[\varphi]_{25,4}^{2,1} & \cdots & x[\varphi]_{25,4}^{2,60000} & x[\varphi]_{25,4}^{3,1} & \cdots & x[\varphi]_{25,4}^{3,60000} \end{array}\right] \in \mathcal{M}_{100\times 180000}(\mathbb{R}), \tag{5.22}$$

donde $\varphi = 1,\dots,4$ es la fase de actuación; $k = 1,\dots,N$ ($N = 3$) identifica el sensor que está midiendo; $j = 1,\dots,L$ ($L = 60000$) indica la medición j-ésima; $l = 1,\dots,E$ ($E = 4$) representa el estado estructural que se mide; finalmente, $i = 1,\dots,n_l$ ($n_l = 25$) es la realización i-ésima relacionada con el estado estructural correspondiente.

Cuando se trabaja en el dominio de la frecuencia, las señales de respuesta medidas en el dominio del tiempo se transforman utilizando el algoritmo de la transformada rápida de Fourier (FFT, por sus siglas en inglés), y las características se extraen del espectro para reducir la dimensión de los datos, dividiendo por dos y añadiendo uno al número de componentes en cada señal. Por lo tanto, el número de columnas de la matriz $\mathbf{X}[\varphi],\ \varphi = 1,\dots,4$, en el dominio de la frecuencia es igual a $N \cdot L = 3 \cdot ((60000/2) + 1) = 90003$ (aquí $L = 30001$). Por consiguiente, la matriz que recoge todas las realizaciones bajo los diferentes estados estructurales en el dominio de la

frecuencia se define como:

$$\mathbf{X}[\varphi] = \left(x[\varphi]_{i,l}^{k,j}\right) = \left[\begin{array}{ccc|ccc|ccc} x[\varphi]_{1,1}^{1,1} & \cdots & x[\varphi]_{1,1}^{1,30001} & x[\varphi]_{1,1}^{2,1} & \cdots & x[\varphi]_{1,1}^{2,30001} & x[\varphi]_{1,1}^{3,1} & \cdots & x[\varphi]_{1,1}^{3,30001} \\ \vdots & \ddots & \vdots & \vdots & \ddots & \vdots & \vdots & \ddots & \vdots \\ x[\varphi]_{25,1}^{1,1} & \cdots & x[\varphi]_{25,1}^{1,30001} & x[\varphi]_{25,1}^{2,1} & \cdots & x[\varphi]_{25,1}^{2,30001} & x[\varphi]_{25,1}^{3,1} & \cdots & x[\varphi]_{25,1}^{3,30001} \\ \hline x[\varphi]_{1,2}^{1,1} & \cdots & x[\varphi]_{1,2}^{1,30001} & x[\varphi]_{1,2}^{2,1} & \cdots & x[\varphi]_{1,2}^{2,30001} & x[\varphi]_{1,2}^{3,1} & \cdots & x[\varphi]_{1,2}^{3,30001} \\ \vdots & \ddots & \vdots & \vdots & \ddots & \vdots & \vdots & \ddots & \vdots \\ x[\varphi]_{25,2}^{1,1} & \cdots & x[\varphi]_{25,2}^{1,30001} & x[\varphi]_{25,2}^{2,1} & \cdots & x[\varphi]_{25,2}^{2,30001} & x[\varphi]_{25,2}^{3,1} & \cdots & x[\varphi]_{25,2}^{3,30001} \\ \hline \vdots & \ddots & \vdots & \vdots & \ddots & \vdots & \vdots & \ddots & \vdots \\ \hline x[\varphi]_{1,4}^{1,1} & \cdots & x[\varphi]_{1,4}^{1,30001} & x[\varphi]_{1,4}^{2,1} & \cdots & x[\varphi]_{1,4}^{2,30001} & x[\varphi]_{1,4}^{3,1} & \cdots & x[\varphi]_{1,4}^{3,30001} \\ \vdots & \ddots & \vdots & \vdots & \ddots & \vdots & \vdots & \ddots & \vdots \\ x[\varphi]_{25,4}^{1,1} & \cdots & x[\varphi]_{25,4}^{1,30001} & x[\varphi]_{25,4}^{2,1} & \cdots & x[\varphi]_{25,4}^{2,30001} & x[\varphi]_{25,4}^{3,1} & \cdots & x[\varphi]_{25,4}^{3,30001} \end{array}\right] \in \mathcal{M}_{100\times 90003}(\mathbb{R}). \tag{5.23}$$

El procedimiento de detección y clasificación de los daños propuesto (Secciones 5.1 y 5.2) se puede aplicar a cada matriz $\mathbf{X}[\varphi]$, $\varphi = 1, \ldots, 4$, (Ecuaciones (5.22) y (5.23)), lo que lleva a una clasificación por cada fase de actuación. Sin embargo, también se puede usar la concatenación horizontal de las cuatro matrices $\mathbf{X}[\varphi]$, $\varphi = 1, \ldots, 4$, para obtener la matriz

$$\mathbf{X}[1,2,3,4] = \left[\mathbf{X}[1]\,\mathbf{X}[2]\,\mathbf{X}[3]\,\mathbf{X}[4]\right] \in \mathcal{M}_{100\times(4\cdot 180000)}(\mathbb{R}) = \mathcal{M}_{100\times 720000}(\mathbb{R}) \tag{5.24}$$

en el dominio del tiempo, y la matriz

$$\mathbf{X}[1,2,3,4] = \left[\mathbf{X}[1]\,\mathbf{X}[2]\,\mathbf{X}[3]\,\mathbf{X}[4]\right] \in \mathcal{M}_{100\times(4\cdot 90003)}(\mathbb{R}) = \mathcal{M}_{100\times 360012}(\mathbb{R}) \tag{5.25}$$

en el dominio de la frecuencia.

Si a la matriz $\mathbf{X}[1,2,3,4]$ (Ecuaciones (5.24) y (5.25)) se le aplica el método de detección y clasificación de daños propuesto, se obtiene un único clasificador que combina las cuatro fases se actuación, es decir, esto permite analizar los datos de todas las fases de forma simultánea. También se puede usar cada fase de actuación como un clasificador individual: cada fase emite un voto y la decisión final se basa en los cuatro votos emitidos. Estas dos estrategias se explicarán en la Sección 5.3.5.

5.3.4. *κ-fold non-exhaustive leave-*p*-out cross-validation*

Se evalúa el enfoque propuesto comparando los datos de test, los nuevos experimentos en estado desconocido bajo las mismas condiciones, con los datos de referencia, los datos de la estructura bajo los cuatro estados estructurales.

Para mayor claridad, escribiremos $\mathbf{X}[\Phi]$ para referirnos tanto a la matriz $\mathbf{X}[\varphi]$ (Ecuaciones (5.22) y (5.23)) como a la matriz $\mathbf{X}[1,2,3,4]$ (Ecuaciones (5.24) y (5.25)). Algunas filas de $\mathbf{X}[\Phi]$ se usan como datos de referencia para construir el modelo y los grupos o clústeres ($v = 5$ filas por estado estructural), y las filas restantes se usan para la validación. En concreto, se realizan cinco iteraciones ($\kappa = 5$) de una *κ-fold non-exhaustive leave-*p*-out cross-validation*, donde $p = \sum_{i=1}^{E}(n_i - v) = n_1 + n_2 + n_3 + n_4 - v \cdot E = 80$, para estimar la precisión global y evitar el sobreajuste. Para cada estado estructural

$l = 1, \ldots, E$, se define la permutación σ_l:

$$\begin{aligned} \sigma_l : \{1, 2, \ldots, n_l\} &\to \{1, 2, \ldots, n_l\}, \\ i &\to \sigma_l(i). \end{aligned}$$

En este caso particular, $n_1 = n_2 = n_3 = n_4 = 25$. Por lo tanto, en la primera iteración, los datos de referencia para construir el modelo son la matriz:

$$\mathfrak{X} = \mathbf{S}^\top \cdot \mathbf{X}[\Phi], \tag{5.26}$$

$$\mathbf{S} = \left[\begin{array}{ccc|ccc|c|ccc} \mathbf{e}_{\sigma_1(1)} & \cdots & \mathbf{e}_{\sigma_1(5)} & \mathbf{e}_{n_1+\sigma_2(1)} & \cdots & \mathbf{e}_{n_1+\sigma_2(5)} & \cdots & \mathbf{e}_{n_1+n_2+n_3+\sigma_4(1)} & \cdots & \mathbf{e}_{n_1+n_2+n_3+\sigma_4(5)} \end{array} \right],$$

donde $\mathbf{e}_j \in \mathbb{R}^{n_1+n_2+n_3+n_4} = \mathbb{R}^{100}$ es el vector j-ésimo de la base canónica del espacio vectorial $\mathbb{R}^{n_1+n_2+n_3+n_4} = \mathbb{R}^{100}$ y $\mathbf{S} \in \mathcal{M}_{(n_1+n_2+n_3+n_4)\times(v\cdot E)}(\mathbb{R})$ es la matriz selectora. La matriz $\mathfrak{X}$ (Ecuación (5.26)) se crea seleccionando aleatoriamente $v = 5$ filas por cada estado estructural. Las $\sum_{i=1}^{E}(n_i - v) = 80$ filas de la matriz $\mathbf{X}[\Phi]$ que no se seleccionan para construir el modelo se usan para la validación.

En la iteración i-ésima, $i = 1, \ldots, \kappa$, los datos de referencia para construir el modelo son la matriz:

$$\begin{aligned} \mathfrak{X} &= \mathbf{S}^\top \cdot \mathbf{X}[\Phi], \\ \mathbf{S} &= \left[\begin{array}{ccc|ccc|c} \mathbf{e}_{\sigma_1(5(i-1)+1)} & \cdots & \mathbf{e}_{\sigma_1(5(i-1)+5)} & \mathbf{e}_{n_1+\sigma_2(5(i-1)+1)} & \cdots & \mathbf{e}_{n_1+\sigma_2(5(i-1)+5)} & \cdots \\ \cdots & & & & & & \\ \hline \mathbf{e}_{n_1+n_2+n_3+\sigma_4(5(i-1)+1)} & \cdots & \mathbf{e}_{n_1+n_2+n_3+\sigma_4(5(i-1)+5)} & & & & \end{array} \right] \end{aligned}$$

Debido a que $\sum_{i=1}^{E}(n_i - v) = 80$ filas de la matriz $\mathbf{X}[\Phi]$ se usan para la validación y a que se realizan $\kappa = 5$ iteraciones, la suma de todos los elementos de las matrices de confusión que se presentan en el Capítulo 6 es igual a $\left(\sum_{i=1}^{E}(n_i - v)\right) \cdot \kappa = 400$.

5.3.5. Detección y clasificación de los daños

En esta sección, se presentan dos estrategias para la detección y clasificación de los daños:

(1) la clasificación se basa en una matriz única: $\mathbf{X}[1], \mathbf{X}[2], \mathbf{X}[3], \mathbf{X}[4]$ (Ecuaciones (5.22) y (5.23)) o $\mathbf{X}[1, 2, 3, 4]$ (Ecuaciones (5.24) y (5.25)), con una *κ-fold non-exhaustive leave*-p-*out cross-validation*;

(2) la clasificación se basa teniendo en cuenta las cuatro matrices $\mathbf{X}[1], \mathbf{X}[2], \mathbf{X}[3]$ y $\mathbf{X}[4]$ (Ecuaciones (5.22) y (5.23)), con una *κ-fold non-exhaustive leave*-p-*out cross-validation*. Cada fase de actuación emite un voto para determinar la decisión final.

En la primera estrategia, se siguen los siguientes siete pasos:

- **Paso 1**. Los datos de la matriz $\mathfrak{X}$ se estandarizan usando el MCGS para definir una nueva matriz $\breve{\mathfrak{X}}$.
- **Paso 2**. El PCA se aplica a $\breve{\mathfrak{X}}$ para obtener el modelo de PCA $\mathbf{P}$.
- **Paso 3**. El número $\ell \in \mathbb{N}$ de componentes principales se elige de modo que la proporción de varianza explicada sea al menos del 95 %. Por lo tanto, el modelo de PCA reducido es $\mathbf{P}_\ell$.

- **Paso 4**. Se necesita la observación $\mathbf{z}^\top$ de la estructura actual a diagnosticar:

$$\mathbf{z}^\top \in \mathbb{R}^{3\cdot 60000} = \mathbb{R}^{180000} \text{ (dominio del tiempo)}$$
$$\mathbf{z}^\top \in \mathbb{R}^{3\cdot 30001} = \mathbb{R}^{90003} \text{ (dominio de la frecuencia)}$$

para $\mathbf{X}[1], \mathbf{X}[2], \mathbf{X}[3]$ y $\mathbf{X}[4]$, o

$$\mathbf{z}^\top \in \mathbb{R}^{4\cdot 180000} = \mathbb{R}^{720000} \text{ (dominio del tiempo)}$$
$$\mathbf{z}^\top \in \mathbb{R}^{4\cdot 90003} = \mathbb{R}^{360012} \text{ (dominio de la frecuencia)}$$

para $\mathbf{X}[1,2,3,4]$. A continuación, el vector $\mathbf{z}^\top$ se estandariza como en la Ecuación (5.19) para definir $\check{\mathbf{z}}^\top$.

- **Paso 5 (t-SNE)**. El conjunto de datos $\mathcal{X}'$ se define como:

$$\mathcal{X}' = \{\mathbf{x}^i \in \mathbb{R}^\ell \mid i = 1, \ldots, 21\}, \tag{5.27}$$

donde

$$\mathbf{x}^i = \mathbf{e}_i^\top \check{\mathbf{X}} \mathbf{P}_\ell, \; i = 1, \ldots, 20,$$
$$\mathbf{x}^{21} = \check{\mathbf{z}}^\top \mathbf{P}_\ell.$$

Posteriormente, el t-SNE se aplica a este conjunto de datos ℓ-dimensional $\mathcal{X}'$ para encontrar una colección de puntos bidimensionales:

$$\mathcal{Y}' = \{\mathbf{y}^i \in \mathbb{R}^2 \mid i = 1, \ldots, 21\}.$$

- **Paso 5 (p-t-SNE)**. Del conjunto de datos $\mathcal{X}'$ (Ecuación (5.27)) se utilizan $\{\mathbf{x}^1, \ldots, \mathbf{x}^{20}\}$ para entrenar la red y $\{\mathbf{x}^{21}\}$ se pasa a través de la red entrenada.

  A continuación, el P-t-SNE se aplica a $\mathcal{X}'$ para encontrar un conjunto de puntos bidimensionales $\mathcal{Y}' = \{\mathbf{y}^1, \ldots, \mathbf{y}^{20}, \mathbf{y}^{21}\} \subset \mathbb{R}^2$. Por lo tanto, los datos incrustados se construyen utilizando la red entrenada: entrada $\mathcal{X}'$ y salida $\mathcal{Y}'$.

- **Paso 6**. $E = 4$ grupos o clústeres se obtienen, que están relacionados con los cuatro estados estructurales. Estos grupos o clústeres están formados por los puntos

$$\{\mathbf{y}^1, \ldots, \mathbf{y}^5\} \subset \mathcal{Y}, \quad \text{relacionado con el estado saludable;}$$
$$\{\mathbf{y}^6, \ldots, \mathbf{y}^{10}\} \subset \mathcal{Y}, \quad \text{relacionado con el daño 1;}$$
$$\{\mathbf{y}^{11}, \ldots, \mathbf{y}^{15}\} \subset \mathcal{Y}, \quad \text{relacionado con el daño 2; y}$$
$$\{\mathbf{y}^{16}, \ldots, \mathbf{y}^{20}\} \subset \mathcal{Y}, \quad \text{relacionado con el daño 3.}$$

El centroide $\mathcal{Y}_l$, $l = 1, \ldots, E$, asociado con el estado estructural l-ésimo se calcula como en la Ecuación (5.21).

- **Paso 7**. Finalmente, la estructura actual a diagnosticar se asocia con el estado estructural l-ésimo si

$$l = \arg \min_{l=1,\ldots,E} \|\mathcal{Y}_l - \mathbf{y}^{21}\|_2.$$

En la segunda estrategia, se siguen los 6 primeros pasos anteriores en cada una de las cuatro matrices $\mathbf{X}[\varphi],\ \varphi = 1,\ldots,4$, relacionadas con las cuatro fases de actuación. Con la información proporcionada por las cuatro fases de actuación, se consideran varios enfoques para finalmente clasificar la estructura que debe diagnosticarse. Uno de estos enfoques, el voto mayoritario, se usa ampliamente en los esquemas de fusión estándar (Tardy *et al.*, 2019), así como en el voto mayoritario ponderado o *soft voting*. Para los casos de estudio de este trabajo, se utiliza el voto mayoritario, así como un enfoque basado en la suma de las inversas de las distancias entre los centroides y el punto bidimensional, que de alguna manera está relacionado con el voto mayoritario ponderado. Aquí están los detalles de ambos enfoques:

- **Voto mayoritario**. En este caso, la estrategia de la distancia punto-centroide más pequeña se aplica cuatro veces, una por cada fase de actuación. Por lo tanto, se obtienen cuatro clasificaciones para diagnosticar una sola estructura, es decir, cada fase de actuación actúa como un clasificador. La Figura 5.9 ilustra esta idea para tres fases de actuación.

  La estructura actual a diagnosticar en la fase de actuación φ-ésima, $\varphi = 1,\ldots,4$, se asocia con el estado estructural l_φ-ésimo si

  $$l_\varphi = \arg \min_{l=1,\ldots,E} \|\mathcal{Y}_l^\varphi - \mathbf{y}_\varphi^{21}\|_2.$$

  Vale la pena recordar que $\mathbf{y}_\varphi^{21} \in \mathbb{R}^2$ es el punto asociado con la observación de la estructura actual a diagnosticar. La estructura finalmente se clasifica según la clasificación más repetida. Es decir, la estructura actual a diagnosticar está asociada con el estado estructural l-ésimo si

  $$l = \text{moda}\{l_1, l_2, l_3, l_4\},$$

  en el caso de un conjunto unimodal. En el caso de un conjunto bimodal, si los dos valores modales son l_α y l_β, la estructura actual a diagnosticar está asociada con el estado estructural l-ésimo si

  $$l = \arg \min_{l \in \{l_\alpha, l_\beta\}} \sum_{\varphi=1}^{4} \|\mathcal{Y}_l^\varphi - \mathbf{y}_\varphi^{21}\|_2.$$

  Finalmente, si el conjunto $\{l_1, l_2, l_3, l_4\}$ es un conjunto sin moda, la estructura se asocia con el estado estructural l-ésimo si

  $$l = \arg \min_{l=1,\ldots,E} \sum_{\varphi=1}^{4} \|\mathcal{Y}_l^\varphi - \mathbf{y}_\varphi^{21}\|_2.$$

- **Suma de las inversas de las distancias**. En este caso, para un estado estructural dado, sumamos el inverso de las distancias entre los centroides $\mathcal{Y}_l^\varphi$ y el punto $\mathbf{y}_\varphi^{21}$ para todas las fases de actuación $\varphi = 1,\ldots,4$. El estado estructural asignado es el que obtiene la suma más alta. De manera específica, la estructura actual a diagnosticar está asociada con el estado estructural l-ésimo si

  $$l = \arg \max_{l=1,\ldots,E} \sum_{\varphi=1}^{4} \frac{1}{\|\mathcal{Y}_l^\varphi - \mathbf{y}_\varphi^{21}\|_2}.$$

Cabe destacar que los argumentos del máximo de la suma de las inversas de las distancias son equivalentes a los argumentos del mínimo de la media armónica de estas distancias. Concretamente, para un estado estructural dado, la media armónica de las distancias entre los centroides $\mathcal{Y}_l^{\varphi}$ y el punto $\mathbf{y}_{\varphi}^{21}$ para todas las fases de actuación $\varphi = 1, \ldots, 4$ es

$$\frac{1}{\frac{1}{4}\sum_{\varphi=1}^{4}\frac{1}{\|\mathcal{Y}_l^{\varphi} - \mathbf{y}_{\varphi}^{21}\|_2}}.$$

Por lo tanto,

$$l = \arg\max_{l=1,\ldots,E}\sum_{\varphi=1}^{4}\frac{1}{\|\mathcal{Y}_l^{\varphi} - \mathbf{y}_{\varphi}^{21}\|_2} = \arg\min_{l=1,\ldots,E}\frac{1}{\frac{1}{4}\sum_{\varphi=1}^{4}\frac{1}{\|\mathcal{Y}_l^{\varphi} - \mathbf{y}_{\varphi}^{21}\|_2}}.$$

Mehta *et al.*, 2018 también usan la distancia armónica para definir una técnica de clasificación de patrones similar al *k-nearest neighbor classifier*. La Figura 5.10 ilustra la idea de la suma de las inversas de las distancias para tres fases de actuación.

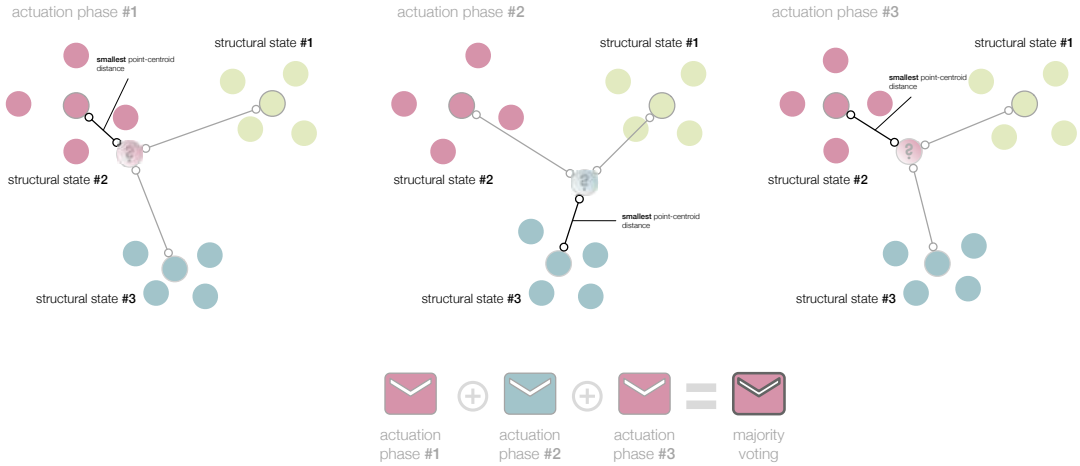

FIGURA 5.9: En el voto mayoritario, la estrategia de la distancia punto-centroide más pequeña se realiza por cada fase de actuación. La estructura actual a diagnosticar se asocia con el estado estructural más votado.

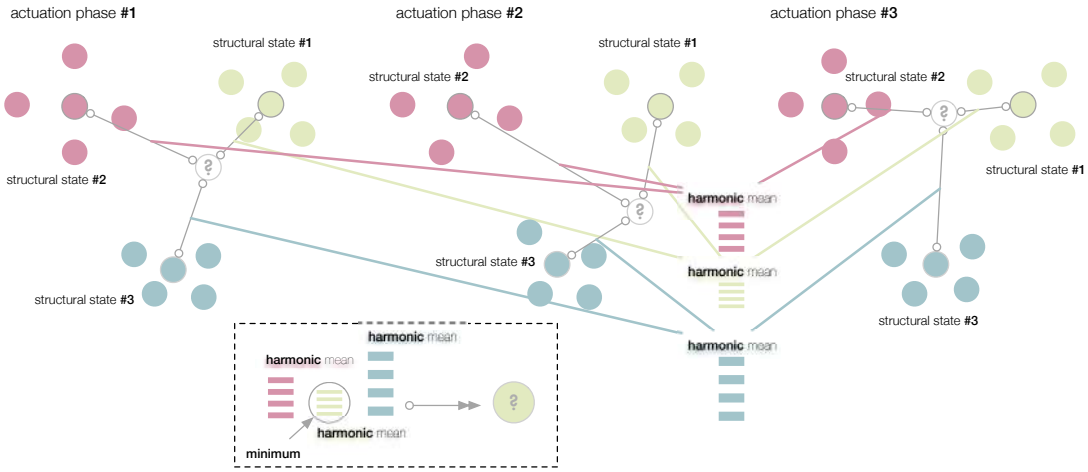

FIGURA 5.10: En el enfoque de la suma de las inversas de las distancias, la estructura actual a diagnosticar se asocia con el estado estructural con la media armónica mínima de las distancias entre los centroides (los puntos con un trazo gris) y el punto (los puntos con un signo de interrogación).

Capítulo 6

Discusión global de los resultados

A continuación, se presentan los resultados más relevantes que aparecen en el contenido de los artículos que constituyen esta tesis doctoral.

Los resultados del método de detección y clasificación de cambios estructurales (introducido en las Secciones 5.1 y 5.2 y detallado en las Secciones 5.3.3–5.3.5) son presentados en términos de matrices de confusión para cada uno de los tres escenarios definidos en la Sección 5.3.2. Las celdas de la matriz de confusión de fondo verde corresponden a las observaciones que están clasificadas correctamente, mientras que las celdas de fondo rojo representan las clasificaciones erróneas. La intensidad del color (verde o rojo) está relacionada con la proporción de decisiones correctas o incorrectas (a mayor intensidad, mayor proporción).

En cada escenario, se consideran cuatro estados estructurales diferentes. El primer estado estructural es el estado saludable, es decir, la placa de aluminio sin daño (denotado como $D0$, de *Damage* 0). El segundo, tercer y cuarto estado estructural corresponden a la placa con un daño simulado de manera no destructiva por una masa añadida en las posiciones indicadas en las Figuras 5.7(a) y 5.7(b) (denotados como $D1$, $D2$ y $D3$, respectivamente).

Para validar este método de detección y clasificación de cambios estructurales, se realizan cinco iteraciones ($\kappa = 5$) de un $\kappa-$*fold non-exhaustive leave-p-out cross-validation* ($p = 80$) como se describe en la Sección 5.3.4. En cada iteración, se consideran 80 observaciones, más concretamente 20 observaciones de cada estado estructural ($D0$, $D1$, $D2$ y $D3$). Por este motivo, la suma de todos los elementos de cada matriz de confusión es igual a $\kappa \cdot p = 5 \cdot 80 = 400$.

Las diferentes matrices de confusión que se presentan son:

- **Fase de actuación** $1, 2, 3$ **ó** 4. El método de detección y clasificación se aplica a una única matriz individual, $\mathbf{X}[1], \mathbf{X}[2], \mathbf{X}[3]$ ó $\mathbf{X}[4]$ (Ecuaciones (5.22) y (5.23)), utilizando la distancia punto-centroide más pequeña.
- **Fases de actuación 1–4**. El método de detección y clasificación se aplica a una matriz individual formada por la concatenación horizontal de las cuatro matrices $\mathbf{X}[\varphi],\ \varphi = 1, \ldots, 4$, es decir, $\mathbf{X}[1, 2, 3, 4]$ (Ecuaciones (5.24) y (5.25)), utilizando la distancia punto-centroide más pequeña.
- **Voto mayoritario**. El método de detección y clasificación se aplica a cada una de las cuatro matrices $\mathbf{X}[\varphi],\ \varphi = 1, \ldots, 4$. Cada fase de actuación emite un voto, utilizando la distancia punto-centroide más pequeña, y la decisión final se toma según el voto mayoritario (Sección 5.3.5).

- **Suma de las inversas de las distancias**. El método de detección y clasificación se aplica a cada una de las cuatro matrices $\mathbf{X}[\varphi]$, $\varphi = 1, \ldots, 4$. Cada fase de actuación emite un voto y la decisión final se toma en base a la suma máxima de las inversas de las distancias (Sección 5.3.5).

Todos los análisis se realizan con el programa matemático MATLAB versiones R2018b y R2019b.

6.1. Artículo 1

6.1.1. Escenario 1

En este escenario, se utiliza un cable corto (0,5 m) y las señales medidas se filtran con un algoritmo Savitzky–Golay. Las tablas 6.1 y 6.2 muestran las matrices de confusión obtenidas. Cuando la decisión se basa en una única fase de actuación (Tabla 6.1), la precisión global es bastante buena: 396 y 397 observaciones de 400 se clasifican correctamente en las fases de actuación 1 y 3, respectivamente, que corresponde a una precisión global del 99 % (fase de actuación 1) y del 99,25 % (fase de actuación 3). Cuando las cuatro fases de actuación se tienen en cuenta (fases de actuación 1–4 (Ecuación (5.24)), voto mayoritario y suma de las inversas de las distancias), se alcanza una precisión global del 100 %, como se muestra en la Tabla 6.2.

En este escenario, que es el más favorable desde el punto de vista de los resultados obtenidos, la detección y clasificación de daños basadas sólo en el PCA también funcionan bien. Sin embargo, la precisión global se reduce hasta el 94,5 % (Tabla 6.3). Esta es la primera indicación de que los grupos o clústeres creados a partir de la combinación PCA más *t*-SNE tienen una mejor calidad que los grupos o clústeres creados sólo con el PCA.

TABLA 6.1: Matriz de confusión de la aplicación del procedimiento de detección y clasificación de daños basado en el *t*-SNE (**Escenario 1**), cuando las fases de actuación se usan individualmente.

		Fase de actuación 1				**Fase de actuación** 3			
Real \ **Predicho**		*D*0	*D*1	*D*2	*D*3	*D*0	*D*1	*D*2	*D*3
*D*0		96	0	2	2	99	0	0	1
*D*1		0	100	0	0	0	100	0	0
*D*2		0	0	100	0	1	0	98	1
*D*3		0	0	0	100	0	0	0	100

*D*0: estado saludable; *D*1, *D*2 y *D*3: masas añadidas en las posiciones indicadas en la Fig. 5.7.

6.1.2. Escenario 2

En este caso, se utiliza un cable corto (0,5 m) y las señales medidas no se filtran. Las tablas 6.4 y 6.5 muestran los resultados obtenidos. Cuando la decisión se basa en una única fase de actuación (Tabla 6.4), la precisión global es bastante remarcable: 382 observaciones de 400 se han clasificado correctamente en la fase de actuación 1, lo que corresponde a una precisión global del 95,5 %; en la fase de actuación 3 y cuando las cuatro fases de actuación se tienen en cuenta (fases de actuación 1–4 (Ecuación (5.24)), voto mayoritario y suma de las inversas de las distancias), se logra una precisión global del 100 % (Tablas 6.4 y 6.5).

TABLA 6.2: Matriz de confusión de la aplicación del procedimiento de detección y clasificación de daños basado en el *t*-SNE (**Escenario 1**), cuando las cuatro fases de actuación se tienen en cuenta.

Real \ Predicho	**Fases 1–4**				**Voto mayoritario**				**Distancias inversas**			
	*D*0	*D*1	*D*2	*D*3	*D*0	*D*1	*D*2	*D*3	*D*0	*D*1	*D*2	*D*3
*D*0	100	0	0	0	100	0	0	0	100	0	0	0
*D*1	0	100	0	0	0	100	0	0	0	100	0	0
*D*2	0	0	100	0	0	0	100	0	0	0	100	0
*D*3	0	0	0	100	0	0	0	100	0	0	0	100

*D*0: estado saludable; *D*1, *D*2 y *D*3: masas añadidas en las posiciones indicadas en la Fig. 5.7.

TABLA 6.3: Matriz de confusión de la aplicación del procedimiento de detección y clasificación de daños basado en el PCA (**Escenario 1**), cuando las fases de actuación se usan individualmente.

Real \ Predicho	**Fase de actuación** 1				**Fase de actuación** 3			
	*D*0	*D*1	*D*2	*D*3	*D*0	*D*1	*D*2	*D*3
*D*0	78	0	0	22	100	0	0	0
*D*1	0	100	0	0	0	100	0	0
*D*2	0	0	100	0	2	0	78	20
*D*3	0	0	0	100	0	0	0	100

*D*0: estado saludable; *D*1, *D*2 y *D*3: masas añadidas en las posiciones indicadas en la Fig. 5.7.

Por otro lado, los resultados de la detección y clasificación de daños basados en el *t*-SNE (PCA más *t*-SNE) se comparan con los del método basado simplemente en el PCA. En este último caso, 289 observaciones de 400 se han clasificado correctamente en la fase de actuación 1 (Tabla 6.6). Esto corresponde a una precisión global del 72,25 %. Como se puede observar, la detección y clasificación de daños basadas en el *t*-SNE, con una precisión global del 95,5 % (Tabla 6.4), supera claramente al enfoque basado sólo en el PCA. Además, en el método basado sólo en el PCA y en la fase de actuación 1 (Tabla 6.6), la tasa de falsos positivos (FPR, por sus siglas en inglés) —definida como la relación de falsos positivos del número total de negativos— es del $49/100 = 49\,\%$, lo cual es insatisfactorio. Del mismo modo, la tasa de falsos negativos (FNR, por sus siglas en inglés) —la relación de falsos negativos del número total de positivos— es del $34/300 = 11{,}3\,\%$. Para calcular la FNR, los tres tipos de daño (*D*1, *D*2 y *D*3) se consideran como una sola categoría, se consideran como lo opuesto al estado saludable de la estructura.

6.1.3. Escenario 3

En los dos escenarios anteriores, se utiliza un cable corto de 0,5 m. Sin embargo, en este caso, las señales se adquieren utilizando un cable largo de 2,5 m. Las Tablas 6.7 y 6.8 muestran las matrices de confusión. Cuando la decisión se basa en una única fase de actuación (Tabla 6.7), la precisión global disminuye significativamente en comparación con el **Escenario** 1 y el **Escenario** 2. Específicamente, 244 y 280 observaciones de 400 se han clasificado correctamente en las fases de actuación 1 (precisión global del 61 %) y 3 (precisión global del 70 %), respectivamente. En la

TABLA 6.4: Matriz de confusión de la aplicación del procedimiento de detección y clasificación de daños basado en el *t*-SNE (**Escenario 2**), cuando las fases de actuación se usan individualmente.

Real \ Predicho	**Fase de actuación 1**				**Fase de actuación 3**			
	*D*0	*D*1	*D*2	*D*3	*D*0	*D*1	*D*2	*D*3
*D*0	82	6	12	0	100	0	0	0
*D*1	0	100	0	0	0	100	0	0
*D*2	0	0	100	0	0	0	100	0
*D*3	0	0	0	100	0	0	0	100

*D*0: estado saludable; *D*1, *D*2 y *D*3: masas añadidas en las posiciones indicadas en la Fig. 5.7.

TABLA 6.5: Matriz de confusión de la aplicación del procedimiento de detección y clasificación de daños basado en el *t*-SNE (**Escenario 2**), cuando las cuatro fases de actuación se tienen en cuenta.

Real \ Predicho	**Fases 1–4**				**Voto mayoritario**				**Distancias inversas**			
	*D*0	*D*1	*D*2	*D*3	*D*0	*D*1	*D*2	*D*3	*D*0	*D*1	*D*2	*D*3
*D*0	100	0	0	0	100	0	0	0	100	0	0	0
*D*1	0	100	0	0	0	100	0	0	0	100	0	0
*D*2	0	0	100	0	0	0	100	0	0	0	100	0
*D*3	0	0	0	100	0	0	0	100	0	0	0	100

*D*0: estado saludable; *D*1, *D*2 y *D*3: masas añadidas en las posiciones indicadas en la Fig. 5.7.

TABLA 6.6: Matriz de confusión de la aplicación del procedimiento de detección y clasificación de daños basado en el PCA (**Escenario 2**), cuando las fases de actuación se usan individualmente.

Real \ Predicho	**Fase de actuación 1**				**Fase de actuación 3**			
	*D*0	*D*1	*D*2	*D*3	*D*0	*D*1	*D*2	*D*3
*D*0	51	8	40	1	100	0	0	0
*D*1	4	76	20	0	0	100	0	0
*D*2	26	2	70	2	0	0	100	0
*D*3	4	0	4	92	0	0	0	100

*D*0: estado saludable; *D*1, *D*2 y *D*3: masas añadidas en las posiciones indicadas en la Fig. 5.7.

fase de actuación 1, la FPR es del 50 % y la FNR es del 16 %, siendo ambos valores inaceptables.

El potencial de los enfoques donde se tienen en cuenta las cuatro fases de actuación se puede observar en este último escenario (ver Tabla 6.8):

- Cuando las cuatro fases de actuación se fusionan en una única matriz (Ecuación (5.24)), 354 observaciones de 400 se clasifican correctamente, lo que representa una precisión global del 88,5 %, una FPR del 14 % y una FNR del 4 %.
- Cuando cada fase de actuación emite un voto y se toma una decisión final utilizando la estrategia del voto mayoritario, la precisión global aumenta hasta el 91,25 %, la FPR se reduce hasta el 2 % y la FNR se incrementa ligeramente hasta el 6 %.

- Finalmente, cuando cada fase de actuación emite un voto y se toma una decisión final utilizando la estrategia de la suma de las inversas de las distancias, la precisión global aumenta hasta el 97 % y la FPR y la FNR se reducen ambas significativamente hasta el 1 %.

La Tabla 6.9 resume los valores para la precisión global, la FPR y la FNR en este escenario.

TABLA 6.7: Matriz de confusión de la aplicación del procedimiento de detección y clasificación de daños basado en el *t*-SNE (**Escenario 3**), cuando las fases de actuación se usan individualmente.

Real \ Predicho	**Fase de actuación 1**				**Fase de actuación 3**			
	*D*0	*D*1	*D*2	*D*3	*D*0	*D*1	*D*2	*D*3
*D*0	50	6	19	25	93	1	3	3
*D*1	19	66	11	4	16	50	23	11
*D*2	14	3	73	10	5	19	70	6
*D*3	15	9	21	55	0	23	10	67

*D*0: estado saludable; *D*1, *D*2 y *D*3: masas añadidas en las posiciones indicadas en la Fig. 5.7.

TABLA 6.8: Matriz de confusión de la aplicación del procedimiento de detección y clasificación de daños basado en el *t*-SNE (**Escenario 3**), cuando las cuatro fases de actuación se tienen en cuenta.

Real \ Predicho	**Fases 1–4**				**Voto mayoritario**				**Distancias inversas**			
	*D*0	*D*1	*D*2	*D*3	*D*0	*D*1	*D*2	*D*3	*D*0	*D*1	*D*2	*D*3
*D*0	86	1	7	6	98	0	0	2	99	0	1	0
*D*1	8	88	4	0	12	85	2	1	1	99	0	0
*D*2	1	8	89	2	6	2	90	2	1	1	95	3
*D*3	3	4	2	91	0	3	5	92	1	2	2	95

*D*0: estado saludable; *D*1, *D*2 y *D*3: masas añadidas en las posiciones indicadas en la Fig. 5.7.

TABLA 6.9: Precisión global, FPR y FNR de la aplicación del procedimiento de detección y clasificación de daños basado en el *t*-SNE (**Escenario 3**), cuando las fases de actuación se usan de forma individual y cuando se tienen en cuenta las cuatro.

	Precisión global	FPR	FNR
Fase de actuación 1	61,0 %	50,0 %	16,0 %
Fase de actuación 3	70,0 %	7,0 %	7,0 %
Fases 1-4	88,5 %	14,0 %	4,0 %
Voto mayoritario	91,3 %	2,0 %	6,0 %
Distancias inversas	97,0 %	1,0 %	1,0 %

6.2. Artículo 2

6.2.1. Escenario 1

Se recuerda que en este escenario se utiliza un cable corto de 0,5 m y que las señales medidas se filtran con un algoritmo Savitzky–Golay. Las matrices de confusión obtenidas se pueden encontrar en las Tablas 6.10 y 6.11. Cuando la decisión se basa en una única fase de actuación (Tabla 6.10), la precisión global es bastante buena: 397 (fase de actuación 1), 399 (fase de actuación 2), 395 (fase de actuación 3) y 397 (fase de actuación 4) observaciones de 400 se han clasificado correctamente, lo que representa una precisión globlal del 99,25 %, 99,75 %, 98,75 % y 99,25 %, respectivamente. Cuando las cuatro fases de actuación se tienen en cuenta (fases de actuación 1–4 (Ecuación (5.25)), voto mayoritario y suma de las inversas de las distancias), se logra una precisión global del 99 % − 100 % (Tabla 6.11).

TABLA 6.10: Matriz de confusión de la aplicación del procedimiento de detección y clasificación de daños basado en *t*-SNE (**Escenario 1**), en el **dominio de la frecuencia**. Las filas representan los valores reales, mientras que las columnas representan los valores predichos.

	Fase de actuación 1				**Fase de actuación 2**				**Fase de actuación 3**				**Fase de actuación 4**			
	*D*0	*D*1	*D*2	*D*3	*D*0	*D*1	*D*2	*D*3	*D*0	*D*1	*D*2	*D*3	*D*0	*D*1	*D*2	*D*3
*D*0	97	0	2	1	100	0	0	0	100	0	0	0	100	0	0	0
*D*1	0	100	0	0	0	100	0	0	0	100	0	0	0	100	0	0
*D*2	0	0	100	0	0	0	100	0	3	0	96	1	0	0	98	2
*D*3	0	0	0	100	0	0	1	99	1	0	0	99	0	0	1	99

*D*0: estado saludable; *D*1, *D*2 y *D*3: masas añadidas en las posiciones indicadas en la Fig. 5.7.

TABLA 6.11: Matriz de confusión de la aplicación del procedimiento de detección y clasificación de daños basado en *t*-SNE (**Escenario 1**), cuando las cuatro fases de actuación se tienen en cuenta, en el **dominio de la frecuencia**.

		Fases 1–4				**Voto mayoritario**				**Distancias inversas**			
Real \ **Predicho**		*D*0	*D*1	*D*2	*D*3	*D*0	*D*1	*D*2	*D*3	*D*0	*D*1	*D*2	*D*3
*D*0		100	0	0	0	100	0	0	0	100	0	0	0
*D*1		0	99	1	0	0	100	0	0	0	100	0	0
*D*2		1	0	99	0	0	0	100	0	0	0	100	0
*D*3		0	0	0	100	0	0	0	100	0	0	0	100

*D*0: estado saludable; *D*1, *D*2 y *D*3: masas añadidas en las posiciones indicadas en la Fig. 5.7.

6.2.2. Escenario 2

Se recuerda que en este escenario se utiliza un cable corto de 0,5 m y que no se filtran las señales medidas. Las diferentes matrices de confusión se presentan en las Tablas 6.12 y 6.13. Cuando la decisión se basa en una única fase de actuación (Tabla 6.12), la precisión global es sobresaliente: en las fases de actuación 1, 2 y 3, todas las observaciones se clasifican correctamente (precisión global del 100 %); en la fase de actuación 4, 399 observaciones de 400 se clasifican correctamente, es decir, se obtiene una precisión global del 99,75 %. Cuando las cuatro fases de actuación se

tienen en cuenta (fases de actuación 1–4 (Ecuación (5.25)), voto mayoritario y suma de las inversas de las distancias), se alcanza una precisión global del 100 % (Tabla 6.13).

TABLA 6.12: Matriz de confusión de la aplicación del procedimiento de detección y clasificación de daños basado en *t*-SNE (**Escenario 2**), en el **dominio de la frecuencia**. Las filas representan los valores reales, mientras que las columnas representan los valores predichos.

	Fase de actuación 1				**Fase de actuación 2**				**Fase de actuación 3**				**Fase de actuación 4**			
	*D*0	*D*1	*D*2	*D*3	*D*0	*D*1	*D*2	*D*3	*D*0	*D*1	*D*2	*D*3	*D*0	*D*1	*D*2	*D*3
*D*0	100	0	0	0	100	0	0	0	100	0	0	0	100	0	0	0
*D*1	0	100	0	0	0	100	0	0	0	100	0	0	0	100	0	0
*D*2	0	0	100	0	0	0	100	0	0	0	100	0	0	0	100	0
*D*3	0	0	0	100	0	0	0	100	0	0	0	100	0	0	1	99

*D*0: estado saludable; *D*1, *D*2 y *D*3: masas añadidas en las posiciones indicadas en la Fig. 5.7.

TABLA 6.13: Matriz de confusión de la aplicación del procedimiento de detección y clasificación de daños basado en *t*-SNE (**Escenario 2**), cuando las cuatro fases de actuación se tienen en cuenta, en el **dominio de la frecuencia**.

		Fases 1–4				**Voto mayoritario**				**Distancias inversas**			
Real \ **Predicho**		*D*0	*D*1	*D*2	*D*3	*D*0	*D*1	*D*2	*D*3	*D*0	*D*1	*D*2	*D*3
*D*0		100	0	0	0	100	0	0	0	100	0	0	0
*D*1		0	100	0	0	0	100	0	0	0	100	0	0
*D*2		0	0	100	0	0	0	100	0	0	0	100	0
*D*3		0	0	0	100	0	0	0	100	0	0	0	100

*D*0: estado saludable; *D*1, *D*2 y *D*3: masas añadidas en las posiciones indicadas en la Fig. 5.7.

6.2.3. Escenario 3

En este escenario, las señales se adquieren utilizando un cable largo de 2,5 m. Las Tablas 6.14 y 6.15 incluyen las matrices de confusión obtenidas. Cuando la decisión se basa en una única fase de actuación (Tabla 6.14), la precisión global también es bastante buena: 384 (fase de actuación 1), 395 (fase de actuación 2), 395 (fase de actuación 3) y 398 (fase de actuación 4) observaciones de 400 se han clasificado correctamente, lo que representa una precisión global del 96 %, 98,75 %, 98,75 % y 99,5 %, respectivamente. Cuando las cuatro fases de actuación se tienen en cuenta (fases de actuación 1–4 (Ecuación (5.25)), voto mayoritario y suma de las inversas de las distancias), se logra una precisión global del 99,5 % − 100 % (Tabla 6.15).

En este último escenario, al igual que en el artículo anterior, se puede observar el potencial de los enfoques donde se utilizan las cuatro fases de actuación (Tabla 6.15):

- Cuando las cuatro fases de actuación se juntan en una única matriz como en la Ecuación (5.25), 398 observaciones de 400 se clasifican correctamente, lo que representa una precisión global del 99,5 %.
- Cuando cada fase de actuación emite un voto y se toma una decisión final basada en el voto mayoritario, la precisión global aumenta hasta el 100 %.

- Finalmente, cuando cada fase de actuación emite un voto y se toma una decisión final basada en la suma de las inversas de las distancias, la precisión global también aumenta hasta 100 %.

También, en este tercer escenario, los resultados en el dominio de la frecuencia se comparan con los resultados obtenidos en el dominio del tiempo. En el dominio del tiempo, cuando la decisión se basa en una única fase de actuación (Tabla 6.16), 244 (fase de actuación 1), 398 (fase de actuación 2), 280 (fase de actuación 3) y 277 (fase de actuación 4) observaciones de 400 se clasifican correctamente. Esto representa una precisión global del 61 %, 99,5 %, 70 % y 69,25 %, respectivamente. Claramente, la estrategia en el dominio de la frecuencia, cuya precisión global fluctúa entre el 96 % y el 99,5 % (Tabla 6.14), supera al enfoque en el dominio del tiempo. Además, la FPR y FNR son claramente insatisfactorias en el dominio del tiempo. Sin embargo, en el dominio de la frecuencia, la FPR y la FNR se reducen significativamente hasta valores cercanos al 0 %. En el dominio del tiempo, cuando las cuatro fases de actuación se tienen en cuenta (Tabla 6.17), la precisión global es del 88,5 % (fases de actuación 1–4), del 91,25 % (voto mayoritario) y del 97 % (suma de las inversas de las distancias), mientras que la precisión global se incrementa hasta el 99,5 %, 100 % y 100 %, respectivamente, en el dominio de la frecuencia. Al mismo tiempo, la FPR y la FNR se reducen hasta el 0 % en el dominio de la frecuencia, mientras que aumentan ligeramente en el dominio del tiempo. Todo esto indica que la calidad de los grupos o clústeres creados en el dominio de la frecuencia es mejor que la obtenida en el dominio del tiempo. La Tabla 6.18 resume los valores de la precisión global, de la FPR y de la FNR en este escenario, en ambos dominios, tiempo y frecuencia.

TABLA 6.14: Matriz de confusión de la aplicación del procedimiento de detección y clasificación de daños basado en *t*-SNE (**Escenario 3**), en el **dominio de la frecuencia**. Las filas representan los valores reales, mientras que las columnas representan los valores predichos.

	Fase de actuación 1				**Fase de actuación** 2				**Fase de actuación** 3				**Fase de actuación** 4			
	*D*0	*D*1	*D*2	*D*3	*D*0	*D*1	*D*2	*D*3	*D*0	*D*1	*D*2	*D*3	*D*0	*D*1	*D*2	*D*3
*D*0	98	2	0	0	99	0	1	0	100	0	0	0	100	0	0	0
*D*1	6	90	2	2	0	99	1	0	0	95	5	0	1	99	0	0
*D*2	1	1	97	1	0	1	97	2	0	0	100	0	0	0	100	0
*D*3	0	1	0	99	0	0	0	100	0	0	0	100	0	0	1	99

*D*0: estado saludable; *D*1, *D*2 y *D*3: masas añadidas en las posiciones indicadas en la Fig. 5.7.

TABLA 6.15: Matriz de confusión de la aplicación del procedimiento de detección y clasificación de daños basado en *t*-SNE (**Escenario 3**), cuando las cuatro fases de actuación se tienen en cuenta, en el **dominio de la frecuencia**.

		Fases 1–4				**Voto mayoritario**				**Distancias inversas**			
Real \ **Predicho**		*D*0	*D*1	*D*2	*D*3	*D*0	*D*1	*D*2	*D*3	*D*0	*D*1	*D*2	*D*3
*D*0		100	0	0	0	100	0	0	0	100	0	0	0
*D*1		0	99	0	1	0	100	0	0	0	100	0	0
*D*2		0	1	99	0	0	0	100	0	0	0	100	0
*D*3		0	0	0	100	0	0	0	100	0	0	0	100

*D*0: estado saludable; *D*1, *D*2 y *D*3: masas añadidas en las posiciones indicadas en la Fig. 5.7.

TABLA 6.16: Matriz de confusión de la aplicación del procedimiento de detección y clasificación de daños basado en *t*-SNE (**Escenario 3**), en el **dominio del tiempo**. Las filas representan los valores reales, mientras que las columnas representan los valores predichos.

	Fase de actuación 1				**Fase de actuación 2**				**Fase de actuación 3**				**Fase de actuación 4**			
	*D*0	*D*1	*D*2	*D*3	*D*0	*D*1	*D*2	*D*3	*D*0	*D*1	*D*2	*D*3	*D*0	*D*1	*D*2	*D*3
*D*0	50	6	19	25	100	0	0	0	93	1	3	3	53	21	1	25
*D*1	19	66	11	4	0	100	0	0	16	50	23	11	17	61	2	20
*D*2	14	3	73	10	0	1	98	1	5	19	70	6	5	3	76	16
*D*3	15	9	21	55	0	0	0	100	0	23	10	67	10	3	0	87

*D*0: estado saludable; *D*1, *D*2 y *D*3: masas añadidas en las posiciones indicadas en la Fig. 5.7.

TABLA 6.17: Matriz de confusión de la aplicación del procedimiento de detección y clasificación de daños basado en *t*-SNE (**Escenario 3**), cuando las cuatro fases de actuación se tienen en cuenta, en el **dominio del tiempo**.

Real \ **Predicho**	**Fases 1–4**				**Voto mayoritario**				**Distancias inversas**			
	*D*0	*D*1	*D*2	*D*3	*D*0	*D*1	*D*2	*D*3	*D*0	*D*1	*D*2	*D*3
*D*0	86	1	7	6	98	0	0	2	99	0	1	0
*D*1	8	88	4	0	12	85	2	1	1	99	0	0
*D*2	1	8	89	2	6	2	90	2	1	1	95	3
*D*3	3	4	2	91	0	3	5	92	1	2	2	95

*D*0: estado saludable; *D*1, *D*2 y *D*3: masas añadidas en las posiciones indicadas en la Fig. 5.7.

TABLA 6.18: Precisión global, FPR y FNR de la aplicación del procedimiento de detección y clasificación de daños basado en el *t*-SNE (**Escenario 3**), cuando las cuatro fases de actuación se usan de forma individual y cuando se tienen en cuenta las cuatro, en ambos dominios, tiempo y frecuencia.

	Precisión global		**FPR**		**FNR**	
	Tiempo	Frecuencia	Tiempo	Frecuencia	Tiempo	Frecuencia
Fase de actuación 1	61,0 %	96,0 %	50,0 %	2,0 %	16,0 %	2,3 %
Fase de actuación 2	99,5 %	98,8 %	0,0 %	1,0 %	0,0 %	0,0 %
Fase de actuación 3	70,0 %	98,8 %	7,0 %	0,0 %	7,0 %	0,0 %
Fase de actuación 4	69,3 %	99,5 %	47,0 %	0,0 %	10,7 %	0,3 %
Fases 1-4	88,5 %	99,5 %	14,0 %	0,0 %	4,0 %	0,0 %
Voto mayoritario	91,3 %	100,0 %	2,0 %	0,0 %	6,0 %	0,0 %
Distancias inversas	97,0 %	100,0 %	1,0 %	0,0 %	1,0 %	0,0 %

6.2.4. Ejemplo ilustrativo de clasificación

Como ejemplo ilustrativo, se incluye en la Figura 6.1 los grupos o clústeres formados por los diferentes estados estructurales en el Escenario 3 después de aplicar el método basado en el *t*-SNE. En esta figura, el diamante representa la estructura a diagnosticar.

Se puede observar como el método separa claramente los cuatro estados estructurales y como el diamante, que es un daño 3, está cerca del grupo con el daño 3.

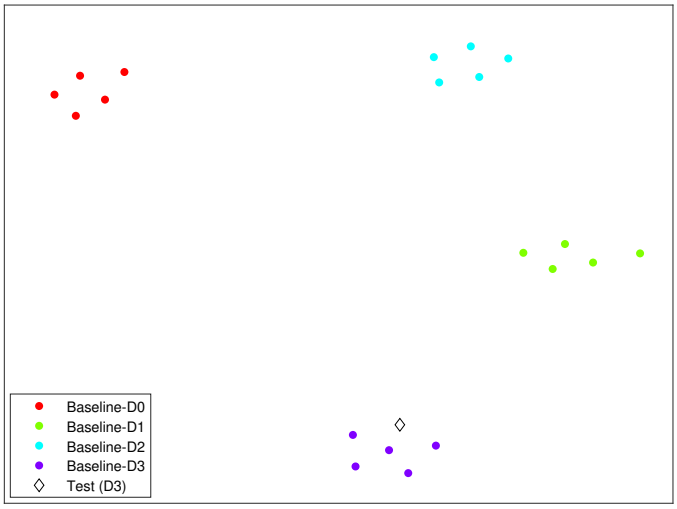

FIGURA 6.1: Los grupos o clústeres formados por los diferentes estados estructurales después de la aplicación del procedimiento de detección y clasificación de daños basado en el *t*-SNE (**Escenario 3**). El diamante representa la estructura a diagnosticar.

6.3. Artículo 3

6.3.1. Escenario 1

Las Tablas 6.19 y 6.20 muestran las matrices de confusión obtenidas. Por un lado, con el P-*t*-SNE y la estrategia del voto mayoritario (Tabla 6.19), la precisión global obtenida es muy buena: 398 de 400 observaciones se han clasificado correctamente, lo que corresponde a una precisión global del 99,5 %. Y por otro lado, con el *t*-SNE y la estrategia del voto mayoritario (Tabla 6.19), la precisión global alcanzada es del 100 %. Utilizando la estrategia de la suma de las inversas de las distancias (Tabla 6.20) para la clasificación de daños basada en el P-*t*-SNE, 399 de 400 observaciones se clasifican correctamente (99,75 % de precisión); mientras que haciendo uso del *t*-SNE, todas las observaciones son clasificadas correctamente (100 % de precisión).

Además, en este estudio, se calculan otras métricas, las más comunes para elegir la mejor solución en un problema de clasificación binaria:

- *Precisión*, definida como la proporción de resultados verdaderos entre el número total de casos examinados.
- *Valor predictivo positivo* (PPV, por sus siglas en inglés), definida como la proporción de verdaderos positivos contra todos los resultados positivos (tanto verdaderos positivos, como falsos positivos).
- *Tasa positiva verdadera* (TPR, por sus siglas en inglés), mide la proporción de positivos verdaderos que se identifican correctamente como tales.
- F_1 *score*, definido como la media armónica del PPV y la TPR.
- *Tasa negativa verdadera* (TNR, por sus siglas en inglés), mide la proporción de negativos verdaderos que se identifican correctamente como tales.

Estas métricas son fáciles de calcular para problemas de clasificación binaria y multiclase (Hossin, 2015). Cuando el problema de clasificación es multiclase, como lo es el presente estudio, de acuerdo con Krüger, 2016 y Hameed *et al.*, 2019, el resultado es el promedio obtenido al sumar el resultado de cada clase y dividirlo por el número total de clases. En todos los casos (P-*t*-SNE, *t*-SNE, voto mayoritario y suma de las inversas de las distancias), estas cinco métricas varían entre el 99,5 % y el 100 % (Tablas 6.21 y 6.22).

Como se puede observar, los enfoques paramétrico y no paramétrico obtienen prácticamente los mismos resultados. Sin embargo, el P-*t*-SNE reduce drásticamente el tiempo de procesamiento: se pasa de 40 minutos y 15 segundos (*t*-SNE) a 2 minutos y 34 segundos (P-*t*-SNE) en un ordenador Intel Core i7 4.20 GHz con 32 GB de RAM. Usando el P-*t*-SNE, se toma una decisión en tan sólo unos pocos milisegundos. El tiempo reducido (2 minutos y 34 segundos) incluye tanto el preentrenamiento como la sintonización fina de la NN, así como la clasificación del estado actual de la estructura. El coste computacional total del P-*t*-SNE se reduce aproximadamente en un 94 %, en comparación con el *t*-SNE.

TABLA 6.19: Matriz de confusión de la aplicación del método de detección y clasificación de daños basado en el P-*t*-SNE y el *t*-SNE (**Escenario 1**), estrategia del voto mayoritario.

		P-*t*-SNE				***t*-SNE**			
Real \ **Predicho**		*D*0	*D*1	*D*2	*D*3	*D*0	*D*1	*D*2	*D*3
*D*0		100	0	0	0	100	0	0	0
*D*1		0	100	0	0	0	100	0	0
*D*2		0	0	100	0	0	0	100	0
*D*3		0	0	2	98	0	0	0	100

*D*0: estado saludable; *D*1, *D*2 y *D*3: masas añadidas en las posiciones indicadas en la Fig. 5.7.

TABLA 6.20: Matriz de confusión de la aplicación del método de detección y clasificación de daños basado en el P-*t*-SNE y el *t*-SNE (**Escenario 1**), estrategia de la suma de las inversas de las distancias.

		P-*t*-SNE				***t*-SNE**			
Real \ **Predicho**		*D*0	*D*1	*D*2	*D*3	*D*0	*D*1	*D*2	*D*3
*D*0		100	0	0	0	100	0	0	0
*D*1		0	100	0	0	0	100	0	0
*D*2		0	0	99	1	0	0	100	0
*D*3		0	0	0	100	0	0	0	100

*D*0: estado saludable; *D*1, *D*2 y *D*3: masas añadidas en las posiciones indicadas en la Fig. 5.7.

6.3.2. Escenario 3

Las tablas 6.23 y 6.24 muestran las diferentes matrices de confusión obtenidas. Con el P-*t*-SNE y la estrategia del voto mayoritario (Tabla 6.23), la precisión global también es muy buena: 398 de 400 observaciones son clasificadas correctamente, es decir, la

TABLA 6.21: Precisión, PPV, TPR, F_1 score y TNR de la aplicación del método de detección y clasificación de daños basado en el P-*t*-SNE y el *t*-SNE (**Escenario 1**), estrategia del voto mayoritario.

	P-*t*-SNE	***t*-SNE**
Precisión	99,8 %	100,0 %
PPV	99,5 %	100,0 %
TPR	99,5 %	100,0 %
F_1 score	99,5 %	100,0 %
TNR	99,8 %	100,0 %

TABLA 6.22: Precisión, PPV, TPR, F_1 score y TNR de la aplicación del método de detección y clasificación de daños basado en el P-*t*-SNE y el *t*-SNE (**Escenario 1**), estrategia de la suma de las inversas de las distancias.

	P-*t*-SNE	***t*-SNE**
Precisión	99,9 %	100,0 %
PPV	99,8 %	100,0 %
TPR	99,8 %	100,0 %
F_1 score	99,7 %	100,0 %
TNR	99,9 %	100,0 %

precisión global es del 99,5 %. En cambio, con el *t*-SNE y el voto mayoritario (Tabla 6.23), la precisión global es del 100 %. Usando la suma de las inversas de las distancias para tomar una decisión final (Tabla 6.24), 399 de 400 observaciones se clasifican correctamente con el P-*t*-SNE (precisión global del 99,75 %); con el *t*-SNE, la totalidad de las observaciones se clasifican correctamente (precisión global del 100 %).

En el enfoque no paramétrico (*t*-SNE), utilizando ambas estrategias (el voto mayoritario y la suma de las inversas de las distancias), las cinco métricas presentadas en la Sección 6.3.1 (precisión, PPV, TPR, F_1 score y TNR) alcanzan el 100 %. En cambio, en el enfoque paramétrico (P-*t*-SNE), estas métricas disminuyen ligeramente, entre un 0,1 % y un 0,5 % (Tablas 6.25 y 6.26).

Nuevamente, como en el escenario 1, los métodos paramétrico y no paramétrico obtienen resultados similares. Sin embargo, como antes, el enfoque del P-*t*-SNE reduce drásticamente el tiempo de procesamiento: de 42 minutos y 1 segundo (*t*-SNE) se pasa a 2 minutos y 32 segundos (P-*t*-SNE). Como en el escenario anterior, el coste computacional total del P-*t*-SNE se reduce aproximadamente en un 94 %, en comparación con el *t*-SNE.

TABLA 6.23: Matriz de confusión de la aplicación del método de detección y clasificación de daños basado en el P-*t*-SNE y el *t*-SNE (**Escenario 3**), estrategia del voto mayoritario.

	P-*t*-SNE				*t*-SNE			
Real \ **Predicho**	*D*0	*D*1	*D*2	*D*3	*D*0	*D*1	*D*2	*D*3
*D*0	100	0	0	0	100	0	0	0
*D*1	1	99	0	0	0	100	0	0
*D*2	1	0	99	0	0	0	100	0
*D*3	0	0	0	100	0	0	0	100

*D*0: estado saludable; *D*1, *D*2 y *D*3: masas añadidas en las posiciones indicadas en la Fig. 5.7.

TABLA 6.24: Matriz de confusión de la aplicación del método de detección y clasificación de daños basado en el P-*t*-SNE y el *t*-SNE (**Escenario 3**), estrategia de la suma de las inversas de las distancias.

	P-*t*-SNE				*t*-SNE			
Real \ **Predicho**	*D*0	*D*1	*D*2	*D*3	*D*0	*D*1	*D*2	*D*3
*D*0	100	0	0	0	100	0	0	0
*D*1	1	99	0	0	0	100	0	0
*D*2	0	0	100	0	0	0	100	0
*D*3	0	0	0	100	0	0	0	100

*D*0: estado saludable; *D*1, *D*2 y *D*3: masas añadidas en las posiciones indicadas en la Fig. 5.7.

TABLA 6.25: Precisión, PPV, TPR, F_1 score y TNR de la aplicación del método de detección y clasificación de daños basado en el P-*t*-SNE y el *t*-SNE (**Escenario 3**), estrategia del voto mayoritario.

	P-*t*-SNE	*t*-SNE
Precisión	99,8 %	100,0 %
PPV	99,5 %	100,0 %
TPR	99,5 %	100,0 %
F_1 score	99,5 %	100,0 %
TNR	99,8 %	100,0 %

6.3.3. Repetibilidad

En este artículo, se realiza un estudio de repetibilidad: se utilizan las barras de error para dar una idea general de la incertidumbre en los resultados. La Figura 6.2 muestra la media de cada estado estructural con barras de error que representan el error estándar. Como se puede ver, tanto en la Figura 6.2 como en las Tablas 6.27–6.30, el error estándar es muy pequeño cuando se repite el procedimiento 10 veces.

TABLA 6.26: Precisión, PPV, TPR, F_1 score y TNR de la aplicación del método de detección y clasificación de daños basado en el P-*t*-SNE y el *t*-SNE (**Escenario 3**), estrategia de la suma de las inversas de las distancias.

	P-*t*-SNE	***t*-SNE**
Precisión	99,9 %	100,0 %
PPV	99,8 %	100,0 %
TPR	99,8 %	100,0 %
F_1 score	99,7 %	100,0 %
TNR	99,9 %	100,0 %

TABLA 6.27: Repetibilidad de la estrategia SHM (10 veces): **Escenario 1**, estrategia del voto mayoritario. *D*0: estado saludable; *D*1, *D*2 y *D*3: masas añadidas en las posiciones indicadas en la Fig. 5.7.

	***D*0**	***D*1**	***D*2**	***D*3**
Media	100,00	100,00	99,80	99,40
Desviación estándar	0,00	0,00	0,42	0,84
Error estándar	0,00	0,00	0,13	0,27

TABLA 6.28: Repetibilidad de la estrategia SHM (10 veces): **Escenario 1**, estrategia de la suma de las inversas de las distancias. *D*0: estado saludable; *D*1, *D*2 y *D*3: masas añadidas en las posiciones indicadas en la Fig. 5.7.

	***D*0**	***D*1**	***D*2**	***D*3**
Media	100,00	100,00	99,80	100,00
Desviación estándar	0,00	0,00	0,42	0,00
Error estándar	0,00	0,00	0,13	0,00

TABLA 6.29: Repetibilidad de la estrategia SHM (10 veces): **Escenario 3**, estrategia del voto mayoritario. *D*0: estado saludable; *D*1, *D*2 y *D*3: masas añadidas en las posiciones indicadas en la Fig. 5.7.

	***D*0**	***D*1**	***D*2**	***D*3**
Media	100,00	98,10	99,70	100,00
Desviación estándar	0,00	2,33	0,67	0,00
Error estándar	0,00	0,74	0,21	0,00

TABLA 6.30: Repetibilidad de la estrategia SHM (10 veces): **Escenario 3**, estrategia de la suma de las inversas de las distancias. *D*0: estado saludable; *D*1, *D*2 y *D*3: masas añadidas en las posiciones indicadas en la Fig. 5.7.

	***D*0**	***D*1**	***D*2**	***D*3**
Media	100,00	99,90	100,00	99,90
Desviación estándar	0,00	0,32	0,00	0,32
Error estándar	0,00	0,10	0,00	0,10

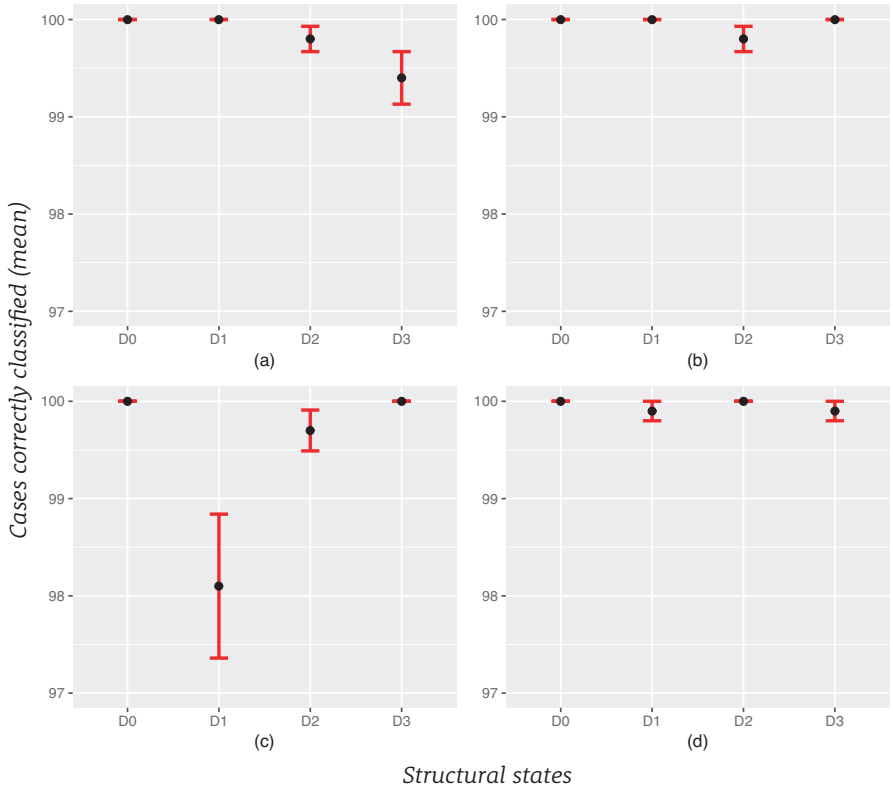

FIGURA 6.2: Repetibilidad de la estrategia SHM (10 veces), gráficos con barras de error: (a) **Escenario 1**, estrategia del voto mayoritario; (b) **Escenario 1**, estrategia de la suma de las inversas de las distancias; (c) **Escenario 3**, estrategia del voto mayoritario; (d) **Escenario 3**, estrategia de la suma de las inversas de las distancias. *D*0: estado saludable; *D*1, *D*2 y *D*3: masas añadidas en las posiciones indicadas en la Fig. 5.7.

6.4. Comentarios generales

De acuerdo con los resultados presentados, es mejor tomar una decisión considerando todas las fases de actuación, ya sea juntando todas las fases en una sola matriz de datos o utilizando cada fase para emitir un voto, y no trabajar con cada una de las fases por separado. Además, los resultados revelan el sólido rendimiento de la estrategia de la suma de las inversas de las distancias en comparación con el voto

mayoritario o la concatenación horizontal de las cuatro fases de actuación. A su vez, el voto mayoritario supera a la concatenación horizontal de todas las fases.

En general, una estructura sana se confunde con una estructura dañada sólo en unos pocos casos. Del mismo modo, una estructura dañada se identifica como una estructura sin daños en un número muy limitado de veces.

Cabe destacar los siguientes aspectos:

- El enfoque basado en la combinación PCA y *t*-SNE supera significativamente al enfoque basado sólo en el PCA.
- Es mejor trabajar en el dominio de la frecuencia que en el dominio del tiempo porque los resultados mejoran significativamente.
- Es mejor trabajar con la versión paramétrica del *t*-SNE que con la versión no paramétrica, ya que el enfoque paramétrico puede hacer inferencia sobre nuevas muestras a diagnosticar y reduce drásticamente el tiempo de procesamiento.

Finalmente, el rendimiento del método propuesto, en general, es muy satisfactorio cuando las señales se adquieren utilizando un cable corto (0,5 m), añadiendo o no ruido blanco gaussiano. Si se añade ruido blanco gaussiano, éste se cancela al utilizarse el PCA como un paso de preproceso. Siguiendo con la longitud del cable, el tercer escenario presenta el peor de los casos, porque utiliza un cable largo (2,5 m) desde los digitalizadores hasta los sensores. En este escenario, las señales están mal digitalizadas debido a la impedancia del cable, al bajo voltaje del estímulo y a otras características experimentales. Por lo tanto, se observa que el uso de un cable largo desde el digitalizador hasta los sensores afecta a la calidad del método de detección y clasificación. Sin embargo, combinando las cuatro fases de actuación con la estrategia de la suma de las inversas de las distancias o del voto mayoritario, se pueden obtener resultados muy precisos.

Capítulo 7

Conclusiones

En este estudio, proponemos una estrategia de SHM para la detección y clasificación de cambios estructurales mediante la integración de datos en dos pasos (despliegue tipo *E* y MCGS), la transformación de datos a través del PCA y la reducción de datos en dos pasos combinando el PCA y el *t*-SNE/P-*t*-SNE.

La metodología propuesta a lo largo de los tres artículos que componen esta tesis doctoral la evaluamos utilizando datos experimentales. En general, los resultados obtenidos muestran que el rendimiento del método es muy satisfactorio, dada su alta precisión de clasificación, demostrando ser una prometedora herramienta para la detección y clasificación de daños estructurales. El rendimiento es muy bueno y similar en todos los conjuntos de datos. En los diferentes casos de estudio, obtenemos resultados muy precisos, independientemente de si se añade ruido blanco gaussiano o no, ya que el PCA cancela dicho ruido. Sin embargo, el uso de un cable largo (2,5 m) desde los digitalizadores hasta los sensores reduce la calidad de detección y clasificación.

A continuación, destacamos las principales conclusiones extraídas de cada uno de los tres artículos que conforman esta tesis doctoral.

- Artículo 1: *Vibration-based detection and classification of structural changes using principal component analysis and t-distributed stochastic neighbor embedding*.

  De este artículo cabe destacar que la calidad de los grupos o clústeres bidimensionales creados con el *t*-SNE, después de aplicar el PCA, es mejor que la calidad de los grupos o clústeres bidimensionales equivalentes creados sólo con el PCA: se compara la metodología propuesta basada en la técnica *t*-SNE con una estrategia similar, que comparte la integración y la transformación de los datos (Secciones 5.1.1 y 5.1.2), pero cuya diferencia radica en el hecho que los grupos o clústeres se crean utilizando solamente el PCA. Por lo tanto, el mejor rendimiento del enfoque basado en la combinación PCA más *t*-SNE lleva a cabo una mejor clasificación y esto le permite obtener unos mejores resultados en comparación con el enfoque basado sólo en el PCA.

- Artículo 2: *A frequency-based approach for the detection and classification of structural changes using t-SNE*.

  De este artículo destacamos que la estrategia propuesta en el dominio de la frecuencia supera significativamente al enfoque en el dominio del tiempo, ya que la calidad de los grupos o clústeres bidimensionales creados con el *t*-SNE en el dominio de la frecuencia es mejor que la calidad de los grupos o clústeres bidimensionales creados con el *t*-SNE en el dominio del tiempo, lo que conduce

a una mejor clasificación. Por lo tanto, es mejor trabajar en el dominio de la frecuencia que en el dominio del tiempo.

- Artículo 3: *Vibration-based structural health monitoring using piezoelectric transducers and parametric t-SNE*.

  A pesar de obtener resultados muy satisfactorios y similares en ambos enfoques, *t*-SNE y P-*t*-SNE, en términos de tiempo de procesamiento, es mejor tomar una decisión considerando la detección y clasificación de daños basada en el P-*t*-SNE en lugar de trabajar con el método basado en el *t*-SNE: aunque el enfoque no paramétrico supera ligeramente al enfoque paramétrico, el enfoque paramétrico reduce el coste computacional total aproximadamente en un 94 %. Esta es la primera indicación de que el P-*t*-SNE es mejor en comparación con el *t*-SNE. Otras ventajas de usar el P-*t*-SNE son las siguientes:

  1. El P-*t*-SNE puede manipular conjuntos de datos a gran escala, mientras que el *t*-SNE sólo puede manipular unos pocos miles de datos.
  2. El método del *t*-SNE requiere un coste computacional extremadamente grande para la optimización: para proyectar una nueva muestra de datos, la optimización debe ejecutarse nuevamente para todo el conjunto de datos. Sin embargo, el P-*t*-SNE puede aprender de los datos de entrenamiento y aplicarse cuando surge una nueva observación, es decir, puede trabajar con observaciones en tiempo real. Por lo tanto, el enfoque paramétrico puede hacer inferencias sobre nuevas muestras a diagnosticar sin tener que calcularlo todo de nuevo, ya que el modelo predice sobre datos fuera de la muestra, clasificando una nueva estructura en sólo unos pocos milisegundos.

  En base a todo lo anterior, de este artículo concluimos que es mejor trabajar con la versión paramétrica del *t*-SNE que con la versión no paramétrica.

Algunos aspectos generales a destacar del método propuesto son los siguientes:

- La técnica *t*-SNE/P-*t*-SNE se ha extendido y adaptado al campo de la SHM para detectar y clasificar cambios estructurales.
- El método clasifica el estado actual de una estructura a diagnosticar utilizando un análisis basado en datos, es decir, utilizando los datos recopilados de la estructura en diferentes estados estructurales y sin el uso de modelos matemáticos complejos.
- Los resultados muestran que es mejor tomar una decisión teniendo en cuenta todas las fases de actuación (juntando estas fases o emitiendo cada una de ellas un voto), en lugar de trabajar con las fases de forma individual.
- Nuestros hallazgos muestran que ambas estrategias, el voto mayoritario y la suma de las inversas de las distancias, superan ligeramente a la concatenación horizontal de las cuatro fases de actuación en el dominio de la frecuencia; en el dominio del tiempo, la estrategia de la suma de las inversas de las distancias supera al voto mayoritario, y esta última estrategia supera a la concatenación horizontal de todas las fases.
- En general, el estado saludable de la estructura se confunde con una estructura dañada sólo en unos pocos casos; de manera similar, una estructura dañada

se identifica como una estructura sin daño en un número muy limitado de observaciones.

Con respecto a los posibles campos de aplicación, en el presente estudio, se ha utilizado una placa de aluminio como las que se utilizan para simular partes de un avión (alas o fuselaje). Creemos que también podemos aplicar este enfoque para detectar daños y fallos en turbinas eólicas. En general, no existe un campo de aplicación prescrito: si se puede instalar una red de sensores en una estructura y se pueden considerar varias fases de actuación, el enfoque aquí propuesto se puede implementar *a priori*.

Capítulo 8

Futuras líneas de investigación y limitaciones

En base a los resultados tan satisfactorios obtenidos, se plantea seguir profundizando en las bases teóricas de la técnica *t*-SNE, por ejemplo explorando otras variantes más actuales de dicha técnica, tales como *kernel t-SNE* (Gisbrecht *et al.*, 2015), *perplexity-free t-SNE* (De Bodt *et al.*, 2018) y *parametric t-distributed stochastic exemplar-centered embedding* (Min *et al.*, 2018).

En cuanto a la versión paramétrica del *t*-SNE estudiada en la presente tesis doctoral, se plantea mejorar su implementación para mejorar el entrenamiento de las redes neuronales profundas, por ejemplo, haciendo uso de otro tipo de función de activación como podría ser la llamada *rectified linear unit* (ReLU) (Goodfellow *et al.*, 2016) o utilizando la técnica denominada *BatchNorm* (Ioffe y Szegedy, 2015). De esta forma, seguramente se mejorará la eficiencia.

Otra posible e interesante línea de investigación, que puede enriquecer mucho el trabajo desarrollado, consiste en comparar la novedosa metodología aquí propuesta con las diferentes estrategias encontradas en la literatura.

Por otra parte, las principales limitaciones de esta tesis son que las condiciones ambientales no fueron consideradas en el estudio y que no se trabajó con datos desequilibrados, convirtiéndose ambas limitaciones en otras líneas de trabajo futuras de interés.

Capítulo 9

Compendio de artículos publicados

Publicaciones que conforman la tesis doctoral.

Received: 3 June 2019 | Revised: 17 December 2019 | Accepted: 2 February 2020

DOI: 10.1002/stc.2533

RESEARCH ARTICLE

WILEY

Vibration-based detection and classification of structural changes using principal component analysis and *t*-distributed stochastic neighbor embedding

David Agis[1] | **Diego A. Tibaduiza**[2] | **Francesc Pozo**[1]

[1]Control, Modeling, Identification and Applications (CoDAlab), Department of Mathematics, Escola d'Enginyeria de Barcelona Est, Universitat Politècnica de Catalunya, Campus Diagonal-Besòs, Barcelona, Spain

[2]Departamento de Ingeniería Eléctrica y Electrónica, Universidad Nacional de Colombia, Bogotá, Colombia

Correspondence
Francesc Pozo, Control, Modeling, Identification and Applications (CoDAlab), Department of Mathematics, Escola d'Enginyeria de Barcelona Est (EEBE), Universitat Politècnica de Catalunya (UPC), Campus Diagonal-Besòs (CDB), Eduard Maristany 16, Barcelona 08019, Spain.
Email: francesc.pozo@upc.edu

Funding information
Generalitat de Catalunya / Agència de Gestió d'Ajuts Universitaris i de Recerca, Grant/Award Number: 2017 SGR 388; Agencia Estatal de Investigación (AEI), Ministerio de Economía, Industria y Competitividad (MINECO), Fondo Europeo de Desarrollo Regional (FEDER) / Secretaría de Estado de Investigación, Desarrollo e Innovación, Grant/Award Number: DPI2017- 82930-C2-1-R

Summary

This paper describes a structural health monitoring strategy to detect and classify structural changes in structures that can be equipped with sensors. The proposed approach is based on the *t*-distributed stochastic neighbor embedding (*t*-SNE), a nonlinear technique that can represent the local structure of high-dimensional data collected from multiple sensors in a plane or spatial representation. We propose the following basic steps for the detection and classification. First, the raw data are preprocessed: We scale the data using the mean-centered group scaling and apply principal component analysis to reduce the dimensionality of the scaled data. Second, *t*-SNE is applied to represent the scaled and reduced data as points in a plane, defining a cluster for each structural state. Finally, the current structure to be diagnosed is associated with a cluster (or structural state) using three different strategies: (a) the smallest point-centroid distance; (b) the majority voting; and (c) the sum of the inverse distances. The combination of *t*-SNE with our preprocessing and the three proposed classification strategies significantly improves the quality of the clusters that represent different structural states. We evaluate the performance of our method using experimental data from an aluminum plate instrumented with piezoelectric transducers. Results are presented in the time domain, and they reveal the high classification accuracy and strong performance of this method, with a percentage of correct decisions close to 100% in several scenarios.

KEYWORDS

classification, detection, principal component analysis (PCA), structural changes, structural health monitoring (SHM), t-distributed stochastic neighbor embedding (t-SNE)

1 | INTRODUCTION

Structural health monitoring (SHM) is an essential process for engineering structures: It verifies the correct performance of the structure and determines whether it needs maintenance. The healthy state of the structure must remain between the specified limits or threshold; however, these limits may change due to the aging of the structure and its use, or due to the environmental and operational conditions. Therefore, in SHM systems, it is important to detect and classify structural changes, which helps to improve safety and reduce maintenance costs. If damage is detected and classified just as it occurs, some action may be taken before a human and/or economic disaster occurs, thereby reducing the probability of

accidents and costs of inspection and maintenance. SHM has been applied in countless structures such as buildings,[1,2] wind turbines,[3,4] and aircrafts.[5,6] A review of the state-of-the-art literature reveals that SHM is a very active research area.

To monitor the state of the structure, data are collected from multiple sensors. This sensor network is placed along with the structure. The signals extracted from multiple sensors are gathered in a high-dimensional dataset, which contains a large volume of data because of continuous measurements of the monitoring system. Several methods have been proposed for the management of high-dimensional, big, and complex data. Among these methods, plane or spatial representation techniques stand out, as they can help to represent data using an intuitive interface that allows people to easily detect natural clusters, identify hidden patterns, and so forth.[7] Plane or spatial representation techniques are also somehow related to dimensionality reduction. Dimensionality reduction is the process of reducing the dimension of the original data keeping the most important intrinsic information.[8] One of the previously proposed methods of dimensionality reduction is *t*-distributed stochastic neighbor embedding (*t*-SNE) a technique developed by L. van der Maaten and G. Hinton,[9] which represents the local structure of original high-dimensional data in a low-dimensional space (e.g., a simple scatter plot). This technique detects patterns by identifying clusters based on the similarity of data points. *t*-SNE is widely used in the literature for dimensionality reduction, classification, pattern recognition, or visualization and compression of big datasets. Although *t*-SNE has been applied in several fields, this is one of the first approaches that uses *t*-SNE in the field of SHM.

In this study, we propose an SHM strategy to detect and classify structural changes using two-step data integration (type *E* unfolding[10] and the so-called mean-centered group scaling (MCGS), data transformation using principal component analysis (PCA), and two-step data reduction combining PCA and *t*-SNE. PCA is a common technique that is mainly used for dimensionality reduction or feature extraction in the field of pattern recognition[11]; moreover, it can also be applied to detect and classify structural changes or faults.[12] In our study, the PCA model will help to detect different types of damage, not only the *healthy* structures. In some cases, however, we observe that using only the first few principal components does not help with visual grouping, clustering, or separation. For this reason, we propose to detect damage or faults using the combination of PCA and *t*-SNE. Hence, we use the following basic steps for detection and classification: (a) first, we scale the collected data using MCGS, because of different scales and magnitudes in the measurements; (b) then, we apply PCA to obtain a better representation of the original data; thus, we reduce the dimensionality of the scaled data and then project the scaled data into the vectorial space spanned by the principal components; and (c) finally, we apply *t*-SNE to the projected data to represent these points in a plane. We will show that, compared with the PCA, the quality of the clusters related to different structural states is significantly improved. Specifically, the current structure to be diagnosed will then be associated with a structural state using three different strategies: (a) the smallest point-centroid distance (when a single actuation phase is considered); (b) majority voting; and (c) sum of the inverse distances (when several actuation phases are combined). Therefore, in this study, *t*-SNE is used (in combination with particular data integration, data transformation, and data reduction) for the first time in the field of SHM in a time-based approach. In comparison with previous strategies found in the literature, this novel method can yield the best detection and classification of structural changes, thus leading to the best performance.

We evaluate the proposed method for the detection and classification of structural changes using experimental data from an aluminum plate instrumented with piezoelectric transducers (PZTs) attached to its surface. Because guided wave propagation-based SHM strategies have proven their ability to adequately identify defects in structures,[13-16] in our study, we have also considered the paradigm of guided waves. In this paradigm, the structure is excited by a signal, and the response is measured to create a baseline pattern. When a new structure must be diagnosed, it must be excited by the same signal, and the response is measured and compared with the baseline pattern. Results show a high classification accuracy and strong performance of this method, with a percentage of correct decisions close to 100% in several scenarios. We must highlight that the environmental conditions were not considered in the present study, as it will be a topic for further developments.

The remainder of this paper is structured as follows. Section 2 describes how we collect and preprocess the baseline data, reduce the global dimension of the data, and create the clusters using *t*-SNE. The damage detection and classification procedure for a structure that must be diagnosed is presented in Section 3. The experimental case studies are described in Section 4. In Section 5, the results are shown. Finally, in Section 6, some conclusions are drawn.

2 | DATA PREPROCESSING AND CLUSTERING: BASELINE DATA

Contributions of our study include the methods of data preprocessing: how the data are collected, arranged, scaled, transformed, and reduced. In the following subsections, data preprocessing is presented in sufficient detail, so that the

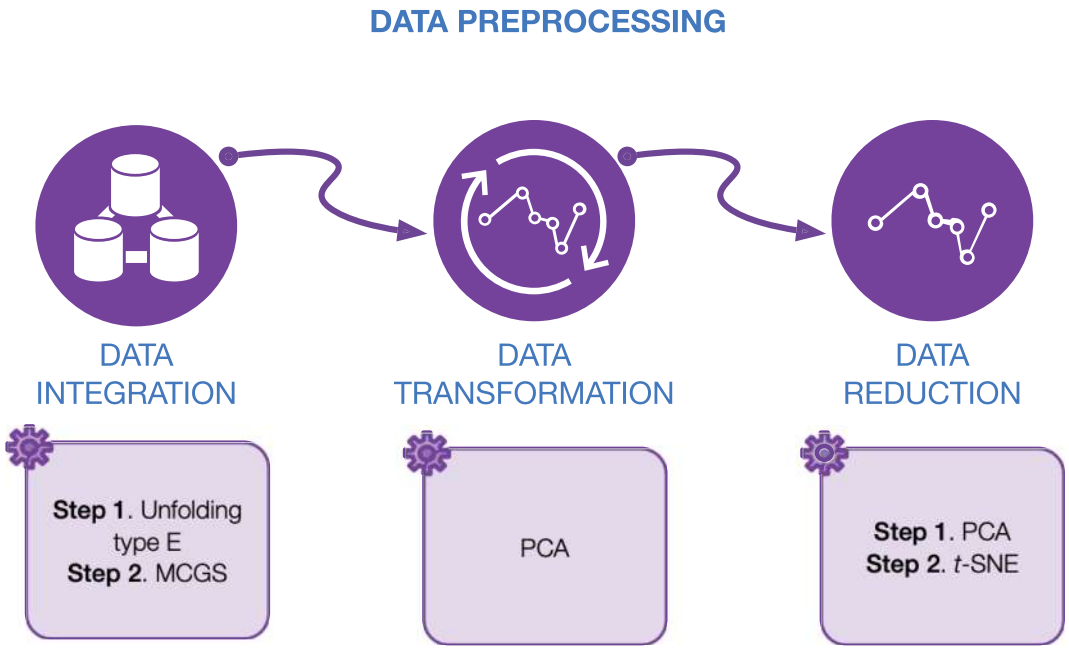

FIGURE 1 Preprocessing is divided into three stages: data integration (including unfolding and scaling), data transformation, and data reduction (PCA and *t*-SNE). MCGS, mean-centered group scaling; PCA, principal component analysis; *t*-SNE, t-distributed stochastic neighbor embedding

proposed approach can be easily reproduced. The preprocessing is divided into three stages: data integration (Section 2.1), data transformation (Section 2.2), and data reduction (Section 2.3). Figure 1 illustrates these three stages. Finally, data are organized in clusters in Section 2.4.

2.1 | Data integration

In this study, data integration is defined as combining different response signals (measured by different sources during multiple observations) into a single and unified view. In our case, this unified view will be represented by a matrix. Section 2.1.1 presents the unfolding of the raw data (measured by the sensors) that are naturally stored as a three-dimensional matrix. Section 2.1.2 describes the standardization of these data.

2.1.1 | Type *E* unfolding

The collected data include different response signals measured by sensors on a vibrating structure. Multiple observations of these responses are measured under different structural states. A matrix that collects all observations under different structural states is defined as follows:

$$\mathbf{X} = \left(x_{i,l}^{k,j}\right) = \begin{bmatrix} x_{1,1}^{1,1} & \cdots & x_{1,1}^{1,L} & x_{1,1}^{2,1} & \cdots & x_{1,1}^{2,L} & \cdots & x_{1,1}^{N,1} & \cdots & x_{1,1}^{N,L} \\ \vdots & \ddots & \vdots & \vdots & \ddots & \vdots & \ddots & \vdots & \ddots & \vdots \\ x_{n_1,1}^{1,1} & \cdots & x_{n_1,1}^{1,L} & x_{n_1,1}^{2,1} & \cdots & x_{n_1,1}^{2,L} & \cdots & x_{n_1,1}^{N,1} & \cdots & x_{n_1,1}^{N,L} \\ x_{1,2}^{1,1} & \cdots & x_{1,2}^{1,L} & x_{1,2}^{2,1} & \cdots & x_{1,2}^{2,L} & \cdots & x_{1,2}^{N,1} & \cdots & x_{1,2}^{N,L} \\ \vdots & \ddots & \vdots & \vdots & \ddots & \vdots & \ddots & \vdots & \ddots & \vdots \\ x_{n_2,2}^{1,1} & \cdots & x_{n_2,2}^{1,L} & x_{n_2,2}^{2,1} & \cdots & x_{n_2,2}^{2,L} & \cdots & x_{n_1,2}^{N,1} & \cdots & x_{n_2,2}^{N,L} \\ \vdots & \ddots & \vdots & \vdots & \ddots & \vdots & \ddots & \vdots & \ddots & \vdots \\ x_{1,E}^{1,1} & \cdots & x_{1,E}^{1,L} & x_{1,E}^{2,1} & \cdots & x_{1,E}^{2,L} & \cdots & x_{1,E}^{N,1} & \cdots & x_{1,E}^{N,L} \\ \vdots & \ddots & \vdots & \vdots & \ddots & \vdots & \ddots & \vdots & \ddots & \vdots \\ x_{n_E,E}^{1,1} & \cdots & x_{n_E,E}^{1,L} & x_{n_E,E}^{2,1} & \cdots & x_{n_E,E}^{2,L} & \cdots & x_{n_E,E}^{N,1} & \cdots & x_{n_E,E}^{N,L} \end{bmatrix} = \begin{bmatrix} \mathbf{X}_1 \\ \mathbf{X}_2 \\ \vdots \\ \mathbf{X}_E \end{bmatrix} \tag{1}$$

$$= \left[\mathbf{X}^1 \middle| \mathbf{X}^2 \middle| \cdots \middle| \mathbf{X}^N \right] \in \mathcal{M}_{(n_1+\cdots+n_E)\times(N\cdot L)}(\mathbb{R}), \tag{2}$$

where $N \in \mathbb{N}$ is the number of sensors and $k = 1, \ldots, N$ identifies the sensor that is measuring; $L \in \mathbb{N}$ is the number of components in each signal and $j = 1, \ldots, L$ indicates the $j-$th measurement; $E \in \mathbb{N}$ is the number of different structural states that are considered and $l = 1, \ldots, E$ represents the structural state that is been measured. Finally, n_l, $l = 1, \ldots, E$ is the number of observations per structural state and $i = 1, \ldots, n_l$ is the ith observation related to the lth structural state. Note that matrix $\mathbf{X}$ in Equation (1) is formed by E horizontal blocks, $\mathbf{X}_l$, $l = 1, \ldots, E$, where each block is related to a different structural state. Meanwhile, matrix $\mathbf{X}$ can also be viewed as formed by N vertical blocks, $\mathbf{X}^k$, $k = 1, \ldots, N$, where each block is related to a different sensor. Notably, matrix $\mathbf{X}$ in Equation (1) is a particular unfolded version of a three-dimensional $(n_1 + \cdots + n_E) \times N \times L$ data matrix, where the first dimension is related to the multiple observations, the second dimension is related to the sensors in the sensor network, and the third dimension is time. To handle three-dimensional matrices, several approaches have been proposed; the most widely adopted ones are based on the unfolding of these matrices. According to Westerhuis *et al.*,[10] there are six alternative ways of arranging a three-dimensional data matrix, which affect the performance of the overall strategy. In our study, out of the six possible unfolded matrices, we have considered type E in the classification proposed by Westerhuis *et al.*[10] The choice of type E unfolding simplifies the study of the variability among samples, because we compile the information related to the sensor measurements and their variations over time.

2.1.2 | Mean-centered group scaling

We consider two main reasons for the scaling or standardization of the raw data in matrix $\mathbf{X}$ in Equation (1): first, to process data with different magnitudes that come from different sensors and second, to simplify the computations of the data transformation in Section 2.2 using PCA. How the raw data are scaled may severely affect the overall performance of the subsequent methods that have to be applied.[17] Some strategies consider each column vector in matrix $\mathbf{X}$ as an independent entity, and each element in the column vector is *normalized* by subtracting the mean of all the elements in the column and by dividing by the standard deviation of the same set of data. Therefore, in this case—that can be defined as *column scaling*—the mean of each column is zero and its standard deviation is one. A second strategy[17]—the so-called group scaling—considers the nature of the vertical blocks, where all measures come from the same sensor. In this case, each element in the block is normalized by subtracting the mean of all the elements in the block and by dividing by the standard deviation of the same set of data. The main drawback of this approach is that the mean of each column is no longer zero, and its standard deviation is no longer one. As a practical solution to this drawback, Pozo *et al.*[17] suggest the mean-centered version of the group scaling (MCGS), where the mean of each column is zero again; however, we cannot guarantee that the standard deviation of each column is one. Hence, in our study, we apply MCGS to matrix $\mathbf{X}$ in Equation (1) and obtain a scaled matrix $\check{\mathbf{X}}$.

2.2 | Data transformation

In the current framework, data transformation is understood as an application of a particular mathematical function to each row of the scaled matrix $\check{\mathbf{X}}$. Because the final goal is dimensionality reduction, the transformation that we use in our study is PCA.

Thanks to the choice of the MCGS, we can compute the variance-covariance matrix of $\check{\mathbf{X}}$ in a compact way as

$$\mathbf{C}_{\check{\mathbf{X}}} = \frac{1}{n-1}\check{\mathbf{X}}^\top\check{\mathbf{X}} \in \mathcal{M}_{(N\cdot L)\times(N\cdot L)}(\mathbb{R}). \tag{3}$$

The vectorial subspaces in the PCA model are defined by eigenvectors ρ_k, $k = 1, \ldots, N \cdot L$, associated with the eigenvalues λ_k, $k = 1, \ldots, N \cdot L$, ordered in decreasing order. The matrix

$$\mathbf{P} = \left[\rho_1 \ \rho_2 \ \cdots \ \rho_{N\cdot L} \right] \in \mathcal{M}_{(N\cdot L)\times(N\cdot L)}(\mathbb{R})$$

is the so-called PCA *model* and contains, written as columns, their corresponding eigenvectors ρ_k, $k = 1, \ldots, N \cdot L$. These vectors are known as the principal components. Finally, the transformation is calculated as a matrix-to-matrix multiplication:

$$\mathbf{T} = \check{\mathbf{X}}\mathbf{P} \in {}_{(n_1+\cdots+n_E)\times(N\cdot L)}(\mathbb{R}).$$

2.3 | Data reduction

In our study, we use two approaches to data reduction. First, we apply PCA in Section 2.3.1 to represent the scaled matrix $\check{\mathbf{X}}$ in a new vectorial space with a reduced dimension and without a significant loss of information. Second, we apply *t*-SNE in Section 2.3.2 as a two-dimensional representation technique. These two methods are combined to reduce the data complexity, as well as to reduce the computational time and effort.

2.3.1 | Principal component analysis

The eigenvectors of the variance-covariance matrix in Equation (3) define the PCA model. The eigenvalues define the partial variance of each principal component. When the *column scaling* is applied to matrix $\mathbf{X}$ in Equation (1)—this is not the case in our study—the trace of the variance–covariance matrix is equal to the number of columns of $\check{\mathbf{X}}$, that is, $N \cdot L$. This means that the first $\ell \in \mathbb{N}$ principal components retain a proportion of the variance given by $(\lambda_1 + \cdots + \lambda_\ell)/(N \cdot L)$. However, when the MCGS is applied to scale the raw data in matrix $\mathbf{X}$ in Equation (1), the trace of the variance–covariance matrix $\mathbf{C}_{\check{\mathbf{X}}}$ is no longer necessarily equal to $N \cdot L$. Therefore, the proportion of the variance directed along the first ℓ principal components is given by

$$\frac{\lambda_1 + \cdots + \lambda_\ell}{\lambda_1 + \cdots + \lambda_\ell + \cdots + \lambda_{N \cdot L}}.$$

In this study, we use PCA to reduce the dimensionality of the scaled dataset $\check{\mathbf{X}}$ by selecting a reduced (but still significant) number $\ell < N \cdot L$ of principal components. Specifically, the number of principal components $\ell \in \mathbb{N}$ is chosen so that the proportion of the variance retained is at least 95%.

We perform the dimensionality reduction using the reduced PCA model:

$$\mathbf{P}_\ell = \begin{bmatrix} \rho_1 & \rho_2 & \cdots & \rho_\ell \end{bmatrix} \in \mathcal{M}_{(N \cdot L) \times \ell}(\mathbb{R}). \tag{4}$$

The scaled dataset $\check{\mathbf{X}}$ is then projected into the vectorial space spanned by the first ℓ principal components through the premultiplication of $\mathbf{P}_\ell$ by $\check{\mathbf{X}}$. Specifically,

$$\mathbf{T}_\ell = \check{\mathbf{X}}\mathbf{P}_\ell \in \mathcal{M}_{n \times \ell}(\mathbb{R}). \tag{5}$$

P_ℓ in Equation (4) has been defined as the reduced PCA model that includes multiple observations under different structural states. Meanwhile, $\mathbf{T}_\ell$ in Equation (5) is the projection of the scaled dataset $\check{\mathbf{X}}$ into the subspace spanned by the reduced PCA model.

2.3.2 | *t*-distributed stochastic neighbor embedding

t-SNE is an enhanced modification of the so-called stochastic neighbor embedding (SNE).[18] Compared with SNE, *t*-SNE is much easier to optimize. Moreover, *t*-SNE produces better plane or spatial representations of the original data, because it reduces the tendency to crowd points in the center of the distribution. The improvements of *t*-SNE over SNE can be partially explained by the cost function that is different in two aspects: (a) *t*-SNE uses a symmetrized version of the SNE cost function with simpler gradients and (b) *t*-SNE uses a Student's *t*-distribution, instead of a Gaussian, to compute the similarity between two points in the low-dimensional space.

Given a collection of ν high-dimensional data points

$$\mathcal{X} = \left\{ \mathbf{x}^i \in \mathbb{R}^D \mid i = 1, \ldots, \nu, \ \nu, D \in \mathbb{N} \right\}, \tag{6}$$

the objective is to find a collection of low-dimensional map points $\mathcal{Y} = \{\mathbf{y}^i \in \mathbb{R}^d \mid i = 1, \ldots, \nu, \ \nu, d \in \mathbb{N}\}$ that form a representation that preserves, as much as possible, the local structure of the original data $\mathcal{X}$. Typical values for d are 2 (*plane* representation) or 3 (*spatial* representation), where $d \ll D$.

To preserve local similarities of the original data $\mathcal{X}$, *t*-SNE first transforms the high-dimensional Euclidean distances between data points $\mathbf{x}^i$ and $\mathbf{x}^j$ into conditional probabilities by centering a Gaussian distribution at $\mathbf{x}^i$, computing the density of $\mathbf{x}^j$ under this Gaussian distribution, and re-normalizing:

$$p_{j|i} = \exp\left(\frac{-\|\mathbf{x}^i - \mathbf{x}^j\|_2^2}{2\sigma_i^2}\right) \Bigg/ \sum_{\substack{l=1 \\ l \neq i}}^{\nu} \exp\left(\frac{-\|\mathbf{x}^i - \mathbf{x}^l\|_2^2}{2\sigma_i^2}\right), \quad i, j = 1, \ldots, \nu, \ \ i \neq j, \tag{7}$$

where $\|\mathbf{x}^i - \mathbf{x}^j\|_2^2 / \left(2\sigma_i^2\right)$ (scaled squared Euclidean distance or *affinity*) is the dissimilarity between data points $\mathbf{x}^i$ and $\mathbf{x}^j$. The variance of the Gaussian distribution, σ_i^2, is calculated automatically. Because only pairwise similarities between data points are of interest, t-SNE establishes $p_{i|i} = 0$. This conditional probability measures the similarity of $\mathbf{x}^j$ to $\mathbf{x}^i$. If two data points are close together, $p_{j|i}$ will be large. However, if two data points are separated, $p_{j|i}$ will be small.

Then, by symmetrizing the conditional probability in Equation (7), t-SNE defines the *pseudo*-joint probability as

$$\begin{aligned} p_{ij} &= \left(p_{j|i} + p_{i|j}\right)/(2\nu), \quad i, j = 1, \ldots, \nu, \quad i \neq j, \\ p_{ii} &= 0. \end{aligned}$$

The *pseudo*-joint probability also measures the pairwise similarity between data points $\mathbf{x}^i$ and $\mathbf{x}^j$. Hence, we define the similarity matrix $\mathcal{P} \in \mathcal{M}_{\nu\times\nu}(\mathbb{R})$ for the high-dimensional data points as $\mathcal{P} = \left(p_{ij}\right)_{i,j=1,\ldots,\nu}$.

Once the similarity matrix for the data points $\mathcal{X}$ in Equation (6) is obtained, we also define the similarity matrix $\mathcal{Q} \in \mathcal{M}_{\nu\times\nu}(\mathbb{R})$ for the map points $\mathcal{Y}$. We build matrix $\mathcal{Q}$ following the same idea as for the similarity matrix $\mathcal{P}$ regarding the original data points. The only difference is that we use, for matrix $\mathcal{Q}$, a re-normalized Student's t-distribution with one degree of freedom and $\sigma_i^2 = \frac{1}{2}$ for all i, instead of a Gaussian distribution:

$$q_{ij} = \frac{\left[1 + \|\mathbf{y}^i - \mathbf{y}^j\|_2^2\right]^{-1}}{\sum_{k=1}^{\nu}\sum_{\substack{l=1 \\ l\neq k}}^{\nu}\left[1 + \|\mathbf{y}^k - \mathbf{y}^l\|_2^2\right]^{-1}}, \quad i, j = 1, \ldots, \nu, \quad i \neq j, \tag{8}$$

$$q_{ii} = 0, \tag{9}$$

where q_{ij} represents the local structure of the data points in the low-dimensional space.

The goal is to select the map points such that the two similarity matrices, $\mathcal{P}$ and $\mathcal{Q}$, are as similar as possible. The similarity between these two matrices will be defined in terms of the Kullback–Leibler (KL) divergence. The KL divergence between the *pseudo*-joint probability distributions $\mathcal{P}$ and $\mathcal{Q}$ measures the *distance* between the two similarity matrices, and it can be defined as[9,18,19]

$$C = \mathcal{D}_{KL}\left(\mathcal{P}\|\mathcal{Q}\right) = \sum_{i=1}^{\nu}\sum_{\substack{j=1 \\ j\neq i}}^{\nu} p_{ij} \log\left(p_{ij}/q_{ij}\right). \tag{10}$$

Therefore, minimizing the KL divergence reduces the error between these two matrices. Moreover, to minimize the cost function C, the gradient descent method is used: $\partial C/\partial \mathbf{y}^i$. Gradient descent is an iterative optimization algorithm; therefore, it updates the map point $\mathbf{y}^i$ at each step.

More details can be found in the original t-SNE paper.[9]

2.4 | Clustering effect

In Section 2.3.1, the dimensionality reduction has been performed using PCA. Specifically, $n = n_1 + \cdots + n_E$ observations under E different structural states (the rows of matrix $\mathbf{X}$ in Equation 1), which may be seen as $N \cdot L-$dimensional vectors, are projected and transformed into $\ell-$dimensional vectors. This reduction of the dimension of the original data is performed with a small loss of information (less than 5%), and it is also expected that ℓ is much smaller than $N \cdot L$.

A second dimensionality reduction is applied to the projected data in matrix $\mathbf{T}_\ell$ in Equation (5) using t-SNE, as presented in Section 2.3.2. Let us define

$$\mathbf{x}^i = \mathbf{e}_i^\top \mathbf{T}_\ell = \mathbf{e}_i^\top \breve{\mathbf{X}} \mathbf{P}_\ell \in \mathbb{R}^\ell, \quad i = 1, \ldots, n$$

as the ith row of matrix $\mathbf{T}_\ell$ in Equation (5). Vector $\mathbf{e}_i \in \mathbb{R}^n$ is the ith element of the canonical basis. Let us also define

$$\mathcal{X} = \left\{\mathbf{x}^i \in \mathbb{R}^\ell \mid i = 1, \ldots, n\right\} \tag{11}$$

as a collection of high-dimensional data points. The objective is to find a collection of two-dimensional map points $\mathcal{Y} = \{\mathbf{y}^i \in \mathbb{R}^2 \mid i = 1, \ldots, n\}$ that represent the original set $\mathcal{X}$ with no explicit loss of information and preserving the local structure of this set. After the application of t-SNE, we expect to observe E clusters related to E different structural states.

These clusters are formed by the map points $\{\mathbf{y}^1, \dots, \mathbf{y}^{n_1}\} \subset \mathcal{Y}$, related to the *first* structural state; $\{\mathbf{y}^{n_1+1}, \dots, \mathbf{y}^{n_1+n_2}\} \subset \mathcal{Y}$, related to the *second* structural state; and so on. Finally, $\{\mathbf{y}^{n-n_{E-1}-n_E+1}, \dots, \mathbf{y}^{n-n_E}\} \subset \mathcal{Y}$ are related to the *penultimate* structural state, and $\{\mathbf{y}^{n-n_E+1}, \dots, \mathbf{y}^{n}\} \subset \mathcal{Y}$ are related to the *last* structural state.

3 | VIBRATION-BASED DAMAGE DETECTION AND CLASSIFICATION PROCEDURE: STRUCTURE TO DIAGNOSE

In Section 2.4, we have described how the original observations under different structural states define a set of clusters on a plane. In this section, we present the vibration-based damage detection and classification procedure for a structure that must be diagnosed.

For damage detection and classification, we need a single observation of the current structure to diagnose it. The collected data include different response signals measured by the same number of sensors N and the same number of components in each signal L, as in Equation (1). When these measures are obtained, we construct a new data vector $\mathbf{z}$:

$$\mathbf{z}^\top = \left[z^{1,1} \ \dots \ z^{1,L} \middle| z^{2,1} \ \dots \ z^{2,L} \middle| \dots \middle| z^{N,1} \ \dots \ z^{N,L} \right] \in \mathbb{R}^{N \cdot L}. \tag{12}$$

3.1 | Scaling (MCGS)

Before the collected data (coming from the structure to be diagnosed) are projected into the space spanned by the ℓ principal components, we must scale the row vector $\mathbf{z}^\top$ to define a scaled row vector $\check{\mathbf{z}}^\top$:

$$\check{z}^{k,j} = \frac{z^{k,j} - \mu^{k,j}}{\sigma^k}, \quad k = 1, \dots, N, \quad j = 1, \dots, L, \tag{13}$$

where $\mu^{k,j}$ is the arithmetic mean of all the elements in the $[(k-1)L + j]-$th column of matrix $\mathbf{X}$ in Equation (1)—that is, the jth column of the vertical block $\mathbf{X}^k$ in Equation (2), and σ^k is the standard deviation of all the elements in the vertical block $\mathbf{X}^k$ in Equation (2) relative to the mean value μ^k (the arithmetic mean of all the elements in the vertical block $\mathbf{X}^k$ in Equation 2).

3.2 | Projection (PCA)

The projection of the scaled row vector $\check{\mathbf{z}}^\top \in \mathbb{R}^{N \cdot L}$ into the space spanned by the first ℓ principal components in $\mathbf{P}_\ell$ is calculated as a vector-to-matrix multiplication:

$$\mathbf{x}^{n+1} = \check{\mathbf{z}}^\top \cdot \mathbf{P}_\ell \in \mathbb{R}^\ell.$$

Notably, the $N \cdot L-$dimensional vector, which contains the collected data (coming from the structure to be diagnosed), is now transformed into an $\ell-$dimensional vector. We add this new point to dataset $\mathcal{X}$ in Equation (11) to define a new set:

$$\mathcal{X}' = \mathcal{X} \cup \left\{\mathbf{x}^{n+1}\right\} = \left\{\mathbf{x}^i \in \mathbb{R}^\ell \mid i = 1, \dots, n, n+1\right\}. \tag{14}$$

3.3 | *t*-SNE and final classification

We apply t-SNE to the $\ell-$dimensional dataset $\mathcal{X}'$ in Equation (14) to find a collection of two-dimensional map points $\mathcal{Y}' = \{\mathbf{y}^i \mid i = 1, \dots, n, n+1\}$ that represent the original set $\mathcal{X}$ with no explicit loss of information and preserving the local structure of this set. Moreover, we include the map point $\mathbf{y}^{n+1}$ associated with the data point $\mathbf{x}^{n+1}$. We expect to observe the same E clusters related to E different structural states. As in Section 2.4, these clusters are formed by the map points $\{\mathbf{y}^1, \dots, \mathbf{y}^{n_1}\} \subset \mathcal{Y}$ related to the first structural state; $\{\mathbf{y}^{n_1+1}, \dots, \mathbf{y}^{n_1+n_2}\} \subset \mathcal{Y}$ related to the *second* structural state, and so on.

For each cluster, we compute its centroid: the mean of the values of the data points in the cluster. For instance, the centroid associated with the first structural state is

$$\mathcal{Y}_1 := \frac{1}{n_1} \sum_{i=1}^{n_1} \mathbf{y}^i = \frac{\mathbf{y}^1 + \dots + \mathbf{y}^{n_1}}{n_1} \in \mathbb{R}^2.$$

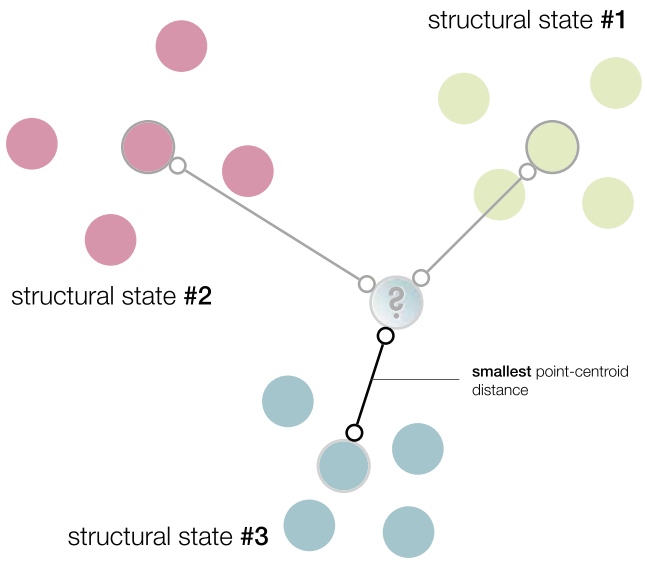

FIGURE 2 The current structure to diagnose is associated with the structural state with the smallest point-centroid distance

In general, the centroid associated with the lth structural state, $l = 1, \dots, E$, is the point of the plane defined as

$$\mathcal{Y}_l := \frac{1}{n_l}\sum_{i=1}^{n_l}\mathbf{y}^{\left(\sum_{j=0}^{l-1} n_j\right)+i} \in \mathbb{R}^2, \quad l = 1, \dots, E, \tag{15}$$

where $n_0 = 0$. Therefore, the current structure to diagnose is associated with the lth structural state if

$$l = \arg\min_{l=1,\dots,E} \|\mathcal{Y}_l - \mathbf{y}^{n+1}\|_2,$$

that is, if the minimum distance between $\mathbf{y}^{n+1}$ and each centroid corresponds to the Euclidean distance between $\mathbf{y}^{n+1}$ and $\mathcal{Y}_l$. We call this approach the smallest point-centroid distance (see Figure 2).

A flowchart of the proposed approach and how it is applied is given in Figure 3.

4 | CASE STUDIES: ALUMINUM PLATE WITH FOUR PZTS

4.1 | Experimental set-up

In this section, we consider a square aluminum plate with an area of 1,600 cm^2 (40×40 cm and a thickness of 0.2 cm) instrumented with four PZTs to demonstrate the reliability of the vibration-based method of damage detection and classification presented in Sections 2 and 3. The PZT discs are attached to the surface; their precise location is shown in Figure 4a. Assuming that the origin of coordinates is placed in the lower left corner of the plate in Figure 4a, the piezoelectric sensors are installed at these coordinates (units in centimeters):

- first PZT (S1) at (20, 35);
- second PZT (S2) at (35, 20);
- third PZT (S3) at (20, 5); and
- fourth PZT (S4) at (5, 20).

These PZTs can work both in the actuator mode (exciting the plate with the burst signal in Figure 5, thus producing a mechanical vibration) and in the sensor mode (detecting a time-varying mechanical response). It is worth recalling that the distance between the four sensors is not the same. For example, the distance between the centers of Sensor 1 and Sensor 4 and the distance between the centers of Sensor 1 and Sensor 2 is equal ($15\sqrt{2} \approx 21.21$ cm). However, the distance between the centers of Sensor 1 and Sensor 3 is larger (30 cm).

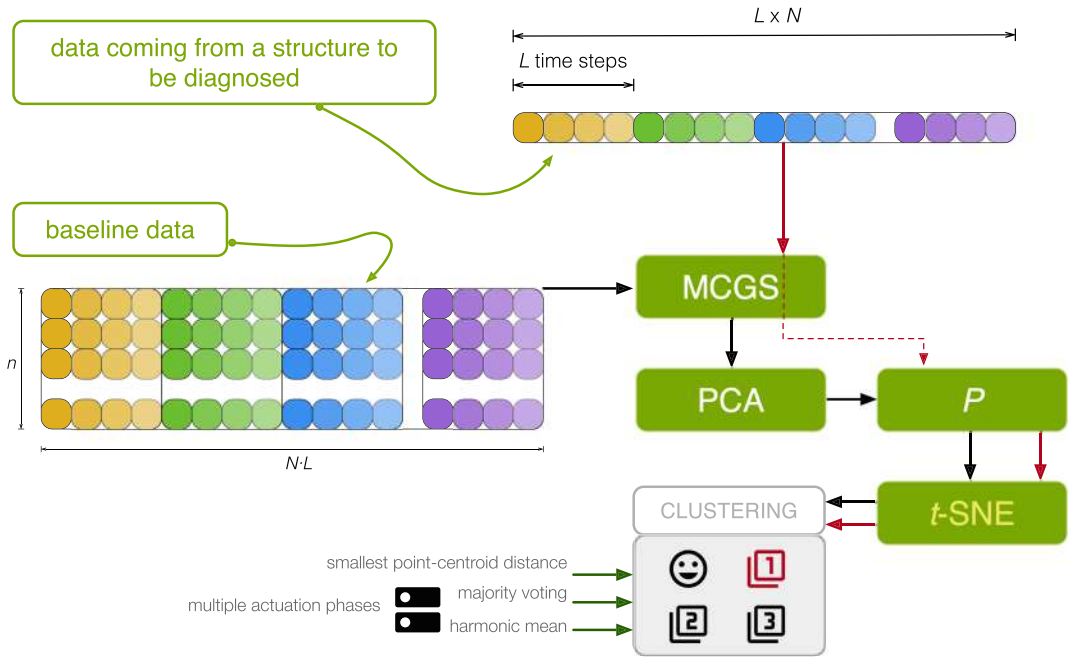

FIGURE 3 Flowchart of the proposed approach. Data coming from a structure are first scaled and then projected into the PCA model. Finally, *t*-SNE is applied to create the clusters that will be used in the vibration-based detection and classification of structural changes. MCGS, mean-centered group scaling; PCA, principal component analysis; *t*-SNE, t-distributed stochastic neighbor embedding

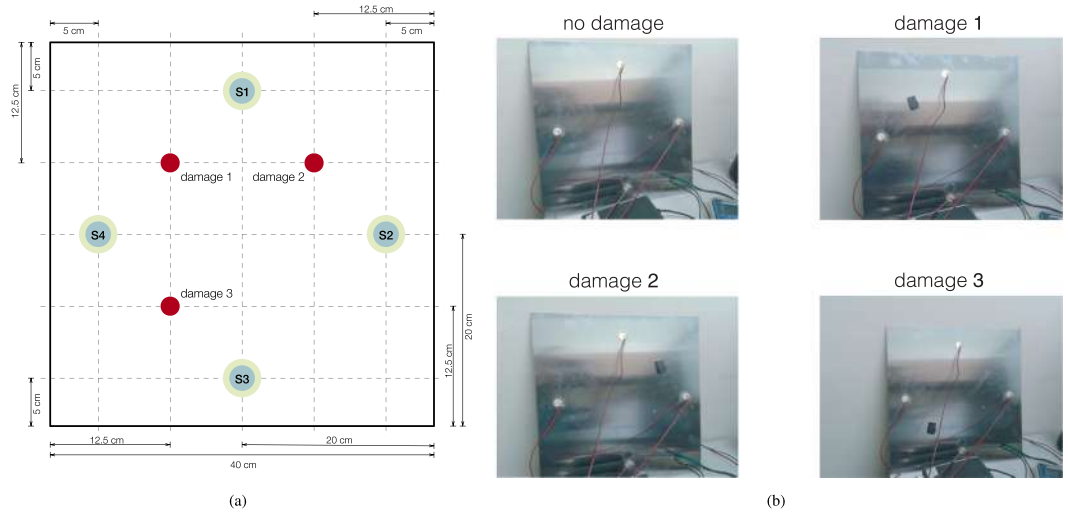

FIGURE 4 (a) Aluminum plate instrumented with four piezoelectric sensors (S1, S2, S3, and S4); (b) aluminum plate with four piezoelectric transducers and in four different structural states

We add a mass of 17.2916 g to simulate the damage (in a nondestructive way) in the aluminum plate. This mass is a magnet attached to both sides of the plate. We use this kind of damage to change the properties of the structure (because aluminum is a nonmagnetic metal) and to produce changes in the propagated wave. Thus, we obtain different scenarios for validating the proposed method. The location of the mass defines each damage. These locations are as follows (units in centimeters):

- Damage 1 at (12.5, 27.5);
- Damage 2 at (27.5, 27.5);
- Damage 3 at (12.5, 12.5).

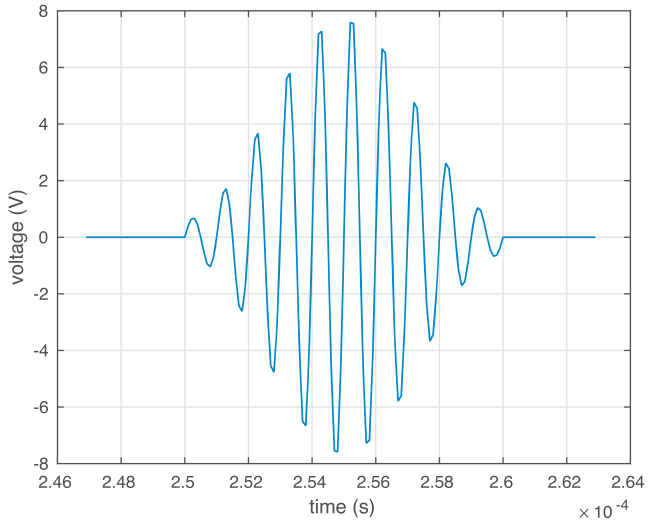

FIGURE 5 In the actuator mode, this burst signal is applied to the piezoelectric transducers to produce a mechanical vibration

Consequently, $E = 4$ structural states are considered here:

- the first structural state corresponds to the healthy state of the structure: the square aluminum plate with no damage;
- the second, third, and fourth structural states correspond to the plate with a mass added at the positions indicated in Figure 4a as Damage 1, Damage 2, and Damage 3, respectively.

The aluminum plate is isolated from the vibration and noise in the laboratory, as shown in Figure 4b.

4.2 | Scenarios and actuation phases

The experimental setup includes three different scenarios to determine the performance of the method under the presence of white Gaussian noise, filters, and considering the length of the wire from the digitizer to the sensors:

- **Scenario 1**. The signals are acquired using a short wire (0.5 m) from the digitizer to the sensors, and these signals are filtered with a Savitzky–Golay[20] filter algorithm after adding white Gaussian noise. The filter is applied to smoothen the data.
- **Scenario 2**. The nonfiltered signals are acquired using a short wire (0.5 m) from the digitizer to the sensors.
- **Scenario 3**. The signals are acquired using a long wire (2.5 m) from the digitizers to the sensors. Signals are also filtered with the Savitzky–Golay algorithm.

In this way, we can observe the effect of the following parameters on the performance of our method: using short and long wires, adding white Gaussian noise to the measured signals, and using a Savitzky–Golay filter in the detection and classification process.

As mentioned in Section 4.1, we use four PZTs (S1, S2, S3, and S4) to excite the aluminum plate and collect the measured response. This sensor network works in what we call *actuation phases*. In each actuation phase, a single PZT is used as an actuator (active sensor: the PZT excites the structure with the burst signal in Figure 5), and the rest of the PZTs are used as sensors (passive sensors: PZTs measure signals). Therefore, we have as many *actuation phases* as *sensors*:

- **Actuation Phase 1**. S1 is used as the actuator. S2, S3, and S4 are used as sensors.
- **Actuation Phase 2**. S2 is used as the actuator. S1, S3, and S4 are used as sensors.
- **Actuation Phase 3**. S3 is used as the actuator. S1, S2, and S4 are used as sensors.
- **Actuation Phase 4**. S4 is used as the actuator. S1, S2, and S3 are used as sensors.

It is very common in the literature—when using the sensor data fusion as in Vitola *et al.*[21,22]—to merge the data that come from different actuation phases in a single data matrix. In this study, we also use the approach with a single data matrix; however, we additionally examine the case where each actuation phase has a classifier, in Section 4.5.

4.3 | Actuation phases and data integration

Given a particular scenario (as the three defined in Section 4.2), we obtain four matrices $\mathbf{X}[\varphi], \quad \varphi = 1, \ldots, 4$ (one for each actuation phase). Each matrix $\mathbf{X}[\varphi], \quad \varphi = 1, \ldots, 4$, is organized as follows:

- $n_1 = n_2 = n_3 = n_4 = 25$ observations or experiments are performed for each structural state. Consequently, each matrix $\mathbf{X}[\varphi], \quad \varphi = 1, \ldots, 4$, consists of 100 rows (i.e., $n_1+n_2+n_3+n_4 = 25{\cdot}4$). Specifically, the first 25 rows represent the structure with no damage, the next 25 rows are experiments where damage 1 is present in the structure, and so on.
- For each actuation phase $\varphi, \quad \varphi = 1, \ldots, 4$, we measure $N = 3$ PZTs working as sensors during $L = 60,000$ time instants. Therefore, the number of columns of matrix $\mathbf{X}[\varphi], \quad \varphi = 1, \ldots, 4$, is equal to $N \cdot L = 3 \cdot 60,000 = 180,000$.

Therefore, the matrix that collects all observations under the four different structural states is (see Equation 1; here, $E = 4$)

$$\mathbf{X}[\varphi] = \left(x[\varphi]_{i,l}^{k,j} \right) \in \mathcal{M}_{100\times 180000}(\mathbb{R}). \tag{16}$$

The damage detection and classification procedure introduced in Sections 2 and 3 can be applied to each matrix $\mathbf{X}[\varphi], \quad \varphi = 1, \ldots, 4$, in Equation (16), thereby leading to one classification per actuation phase. However, we can also use the horizontal concatenation of the four matrices $\mathbf{X}[\varphi], \quad \varphi = 1, \ldots, 4$, to obtain the matrix

$$\mathbf{X}[1,2,3,4] = \left[\mathbf{X}[1] \ \mathbf{X}[2] \ \mathbf{X}[3] \ \mathbf{X}[4] \right] \in \mathcal{M}_{100\times(4\cdot 180000)}(\mathbb{R}) = \mathcal{M}_{100\times 720000}(\mathbb{R}). \tag{17}$$

If matrix $\mathbf{X}[1,2,3,4]$ in Equation (17) is used for the damage detection and classification procedure introduced in Sections 2 and 3 (this allows us to analyze the data from all actuation phases simultaneously), we obtain a single classifier that combines these four phases. Finally, we can also use the separate classifiers obtained for each actuation phase: when each actuation phase casts a vote and the final decision is based on the four actuation phases. These strategies will be explained in Section 4.5.

4.4 | $\kappa-$fold nonexhaustive leave-p-out cross-validation

We evaluate the proposed approach by comparing *test* data (the new experiments in *unknown* state under the same conditions) with *baseline* data (data from the structure under different structural states).

For clarity, let us write $\mathbf{X}[\Phi]$ to refer to both matrix $\mathbf{X}[\varphi]$ in Equation (16) and matrix $\mathbf{X}[1,2,3,4]$ in Equation (17). Some of the rows in $\mathbf{X}[\Phi]$ will be used as the baseline data to build the model and the clusters ($\upsilon = 5$ rows per structural state), and the remaining rows are used for the validation. Specifically, we will perform five iterations ($\kappa = 5$) of a nonexhaustive leave-p-out cross-validation, where $p = \sum_{i=1}^{E} (n_i - \upsilon) = n_1 + n_2 + n_3 + n_4 - \upsilon \cdot E = 80$, to estimate the overall accuracy and avoid overfitting. For each structural state $l = 1, \ldots, E$, we define permutation σ_l:

$$\begin{aligned} \sigma_l : \{1, 2, \ldots, n_l\} &\to \{1, 2, \ldots, n_l\}, \\ i &\to \sigma_l(i). \end{aligned}$$

In this particular case, $n_1 = n_2 = n_3 = n_4 = 25$. Therefore, in the first iteration, we use the following matrix as baseline data to build the model:

$$\mathrm{X} = \mathbf{S}^{\top} \cdot \mathbf{X}[\Phi], \tag{18}$$

$$\mathbf{S} = \left[\mathbf{e}_{\sigma_1(1)} \ \cdots \ \mathbf{e}_{\sigma_1(5)} \middle| \mathbf{e}_{n_1+\sigma_2(1)} \ \cdots \ \mathbf{e}_{n_1+\sigma_2(5)} \middle| \cdots \middle| \mathbf{e}_{n_1+n_2+n_3+\sigma_4(1)} \ \cdots \ \mathbf{e}_{n_1+n_2+n_3+\sigma_4(5)} \right], \tag{19}$$

where $\mathbf{e}_j \in \mathbb{R}^{n_1+n_2+n_3+n_4} = \mathbb{R}^{100}$ is the jth element of the canonical basis of the real vector space $\mathbb{R}^{n_1+n_2+n_3+n_4} = \mathbb{R}^{100}$ and $\mathbf{S} \in \mathcal{M}_{(n_1+n_2+n_3+n_4)\times(\upsilon\cdot E)}(\mathbb{R})$ is the *selector* matrix. Matrix X in Equation (18) has been built by randomly selecting $\upsilon = 5$ rows per structural state. The $\sum_{i=1}^{E} (n_i - \upsilon) = 80$ rows of matrix $\mathbf{X}[\Phi]$ that are not used to build the model are used for the validation.

In the ith iteration, $i = 1, \ldots, \kappa$, we use the following matrix as baseline data to build the model:

$$\mathrm{X} = \mathbf{S}^{\top} \cdot \mathbf{X}[\Phi], \tag{20}$$

$$\mathbf{S} = \left[\mathbf{e}_{\sigma_1(5(i-1)+1)} \ \cdots \ \mathbf{e}_{\sigma_1(5(i-1)+5)} \middle| \mathbf{e}_{n_1+\sigma_2(5(i-1)+1)} \ \cdots \ \mathbf{e}_{n_1+\sigma_2(5(i-1)+5)} \middle| \cdots \middle| \mathbf{e}_{n_1+n_2+n_3+\sigma_4(5(i-1)+1)} \ \cdots \ \mathbf{e}_{n_1+n_2+n_3+\sigma_4(5(i-1)+5)} \right], \quad (21)$$

where $\mathbf{e}_j$ is the jth element of the canonical basis and $\mathbf{S}$ is the *selector* matrix. Because 80 rows of matrix $\mathbf{X}[\Phi]$ will be used for the validation step in $\kappa = 5$ iterations, the sum of all the elements in the *confusion matrices* that we will present in Section 5 is equal to $\left(\sum_{i=1}^{E}(n_i - \upsilon)\right) \cdot \kappa = 400$.

4.5 | Damage detection and classification

In this section, we present two strategies for damage detection and classification. These two strategies are as follows:

(1) the classification is based on a single matrix: $\mathbf{X}[1], \mathbf{X}[2], \mathbf{X}[3], \mathbf{X}[4]$, or $\mathbf{X}[1, 2, 3, 4]$, as defined in Equations (16) and (17), respectively, with $\kappa-$fold nonexhaustive leave-p-out cross-validation;
(2) the classification is based on the four matrices $\mathbf{X}[1], \mathbf{X}[2], \mathbf{X}[3]$, and $\mathbf{X}[4]$, defined in Equation (16), for the four actuation phases, with $\kappa-$fold nonexhaustive leave-p-out cross-validation. Each actuation phase will cast a vote to determine the final decision.

In the first strategy, we follow the next seven steps:

- **Step 1**. The data in matrix X are scaled using MCGS to define a new matrix $\check{\mathrm{X}}$.
- **Step 2**. PCA is applied to $\check{\mathrm{X}}$ to obtain the PCA model $\mathbf{P}$.
- **Step 3**. The number $\ell \in \mathbb{N}$ of principal components is chosen so that the proportion of variance explained is at least 95%. Therefore, the reduced PCA model is $\mathbf{P}_\ell$.
- **Step 4**. A observation $\mathbf{z}^\top \in \mathbb{R}^{3\cdot 60000} = \mathbb{R}^{180000}$ (for $\mathbf{X}[1], \mathbf{X}[2], \mathbf{X}[3]$, and $\mathbf{X}[4]$) or $\mathbf{z}^\top \in \mathbb{R}^{4\cdot 180000} = \mathbb{R}^{720000}$ (for $\mathbf{X}[1, 2, 3, 4]$) of the current structure to diagnose is needed. Then, vector $\mathbf{z}^\top$ is scaled as in Equation (13) to define $\check{\mathbf{z}}^\top$.
- **Step 5**. Dataset $\mathcal{X}'$ is defined as $\mathcal{X}' = \{\mathbf{x}^i \in \mathbb{R}^\ell \mid i = 1, \ldots, 21\}$, where

$$\begin{aligned} \mathbf{x}^i &= \mathbf{e}_i^\top \check{\mathrm{X}} \mathbf{P}_\ell, \quad i = 1, \ldots, 20, \\ \mathbf{x}^{21} &= \check{\mathbf{z}}^\top \mathbf{P}_\ell. \end{aligned}$$

  Subsequently, t-SNE is applied to this $\ell-$dimensional dataset $\mathcal{X}'$ to find a collection of two-dimensional map points $\mathcal{Y}' = \{\mathbf{y}^i \in \mathbb{R}^2 \mid i = 1, \ldots, 21\}$.
- **Step 6**. $E = 4$ clusters are obtained and are related to the $E = 4$ different structural states. These clusters are formed by the map points: $\{\mathbf{y}^1, \ldots, \mathbf{y}^5\} \subset \mathcal{Y}$, related to the *first* structural state; $\{\mathbf{y}^6, \ldots, \mathbf{y}^{10}\} \subset \mathcal{Y}$, related to the *second* structural state; $\{\mathbf{y}^{11}, \ldots, \mathbf{y}^{15}\}$, related to the *third* structural state; and $\{\mathbf{y}^{16}, \ldots, \mathbf{y}^{20}\} \subset \mathcal{Y}$, related to the *fourth* structural state.
  Centroid $\mathcal{Y}_l, \quad l = 1, \ldots, E$, associated with the lth structural state is computed as in Equation (15).
- **Step 7**. Finally, the current structure to diagnose is associated with the lth structural state if

$$l = \arg \min_{l=1,\ldots,E} \|\mathcal{Y}_l - \mathbf{y}^{21}\|_2.$$

In the second strategy, we follow Step 1 to Step 6 (as above) for the four matrices $\mathbf{X}[\varphi], \quad \varphi = 1, \ldots, 4$, related to the four actuation phases. With the information provided by the four actuation phases, we consider several approaches to finally classify the structure that must be diagnosed. One of these approaches, the majority voting, is widely used in standard fusion schemes,[23] as well as *weighted majority vote* or *soft voting*. For the case studies in this work, the majority voting will be used, as well as an approach based on the sum of the inverse distances between the centroids and the map point, which is somehow related to a weighted majority vote. Here are the details of both approaches:

- **Majority voting**. In this case, the strategy of the smallest point-centroid distance is applied four times, one per the actuation phase. Therefore, four classifications are obtained for a single structure to diagnose. Specifically, each actuation phase acts as a *classifier*. Figure 6 illustrates this idea for the three actuation phases.
  The current structure to diagnose, in the φth actuation phase, $\varphi = 1, \ldots, 4$, is associated with the l_φth structural state if

$$l_\varphi = \arg \min_{l=1,\ldots,E} \|\mathcal{Y}_l^\varphi - \mathbf{y}_\varphi^{21}\|_2. \quad (22)$$

It is worth remembering that $\mathbf{y}_{\varphi}^{21} \in \mathbb{R}^2$ is the map point associated with the observation of the current structure to diagnose. The structure is finally classified according to the most repeated classification. That is, the current structure to diagnose is associated with the lth structural state if $l = \text{mode}\{l_1, l_2, l_3, l_4\}$, in the case of a unimodal set. In the case of a bimodal set, if the two modal values are l_α and l_β, the current structure to diagnose is associated with the lth structural state if

$$l = \arg \min_{l \in \{l_\alpha, l_\beta\}} \sum_{\varphi=1}^{4} \| \mathcal{Y}_l^{\varphi} - \mathbf{y}_{\varphi}^{21} \|_2.$$

Finally, if the set $\{l_1, l_2, l_3, l_4\}$ is a set with no mode, the structure is associated with the lth structural state if

$$l = \arg \min_{l=1,\ldots,E} \sum_{\varphi=1}^{4} \| \mathcal{Y}_l^{\varphi} - \mathbf{y}_{\varphi}^{21} \|_2.$$

- **Sum of the inverse distances**. In this case, for a given structural state, we sum the inverse of the distances between the centroids $\mathcal{Y}_l^{\varphi}$ and the map point $\mathbf{y}_{\varphi}^{21}$, for all the actuation phases $\varphi = 1, \ldots, 4$. The assigned structural state is the

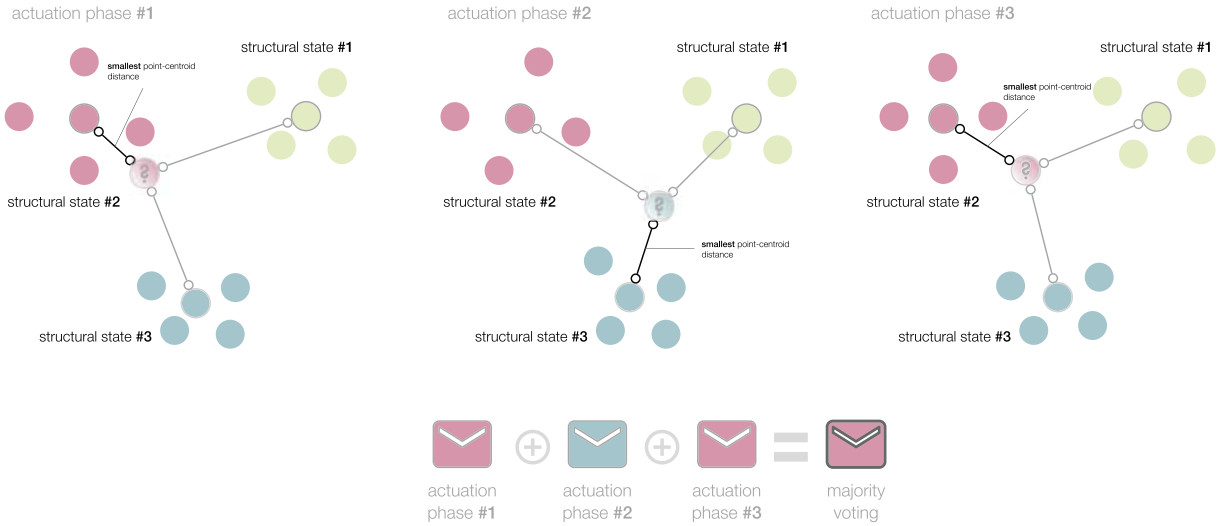

FIGURE 6 In the majority voting, the strategy of the smallest point-centroid distance is performed per actuation phase. The current structure to diagnose is associated with the most voted structural state

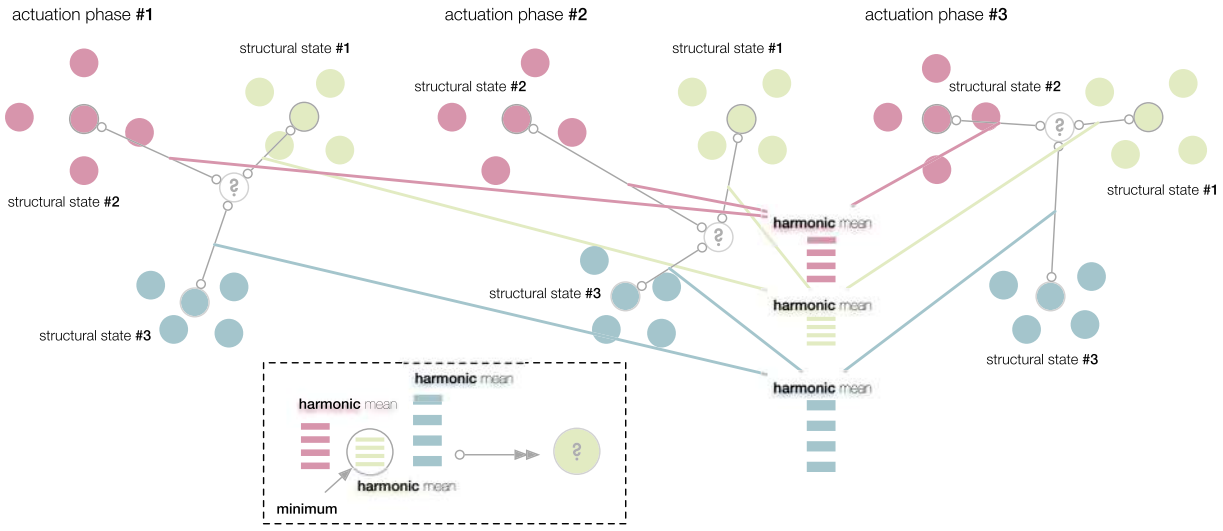

FIGURE 7 In the sum of the inverse distances approach, the current structure to diagnose is associated with the structural state with the minimum harmonic mean of the distances between the centroids (the points with a gray stroke) and the map point (the points with a question mark)

one that obtains the highest sum. Specifically, the current structure to diagnose is associated with the lth structural state if

$$l = \arg \max_{l=1,\dots,E} \sum_{\varphi=1}^{4} \frac{1}{\|\mathcal{Y}_l^{\varphi} - \mathbf{y}_{\varphi}^{21}\|_2}.$$

Notably, the arguments of the maxima of the sum of the inverse distances is equivalent to the arguments of the minima of the harmonic mean of these distances. Figure 7 illustrates this idea for the three actuation phases. Specifically, for a given structural state, the harmonic mean of the distances between the centroids $\mathcal{Y}_l^{\varphi}$ and the map point $\mathbf{y}_{\varphi}^{21}$ for all the actuation phases $\varphi = 1, \dots, 4$ is

$$\frac{1}{\frac{1}{4}\sum_{\varphi=1}^{4} \frac{1}{\|\mathcal{Y}_l^{\varphi} - \mathbf{y}_{\varphi}^{21}\|_2}}.$$

Therefore,

$$l = \arg \max_{l=1,\dots,E} \sum_{\varphi=1}^{4} \frac{1}{\|\mathcal{Y}_l^{\varphi} - \mathbf{y}_{\varphi}^{21}\|_2} = \arg \min_{l=1,\dots,E} \frac{1}{\frac{1}{4}\sum_{\varphi=1}^{4} \frac{1}{\|\mathcal{Y}_l^{\varphi} - \mathbf{y}_{\varphi}^{21}\|_2}}.$$

Mehta *et al.*[24] also use the harmonic distance to define a pattern classification technique similar to the k-nearest neighbor classifier.

5 | RESULTS

The results of damage detection and classification (introduced in Sections 2 and 3 and detailed in Sections 4.3–4.5) for the aluminum plate are presented in terms of the confusion matrices for the scenarios defined in Section 4.2. We present the results for each scenario in a different section. Specifically, Section 5.1 presents the results for Scenario 1. Section 5.2 and Section 5.3 present the results for Scenario 2 and Scenario 3, respectively. In the three scenarios, four different structural states have been considered. The first structural state corresponds to the healthy state of the structure: the square aluminum plate with no damage (denoted as $D0$). The second, third, and fourth structural states correspond to the plate with an added mass at the positions indicated in Figures 4a and 4b (denoted as $D1$, $D2$, and $D3$, respectively).

To validate the method of damage detection and classification from Sections 4.3–4.5, we will perform five iterations ($\kappa = 5$) of a nonexhaustive leave-p-out cross-validation, where $p = 80$, as described in Section 4.4. At each iteration, we have considered 80 observations according to the following distribution: 20 observations per structural state ($D0$, $D1$, $D2$, and $D3$). Because 80 observations have been used for the validation step in $\kappa = 5$ iterations, the sum of all the elements in the confusion matrices that we will present in Sections 5.1, 5.2, and 5.3 is equal to $5 \cdot 80 = 400$.

Hence, for the three scenarios, we present five different confusion matrices:

- **Actuation Phase 1** and **Actuation Phase 3**. Damage detection and classification are applied to a single matrix, $\mathbf{X}[1]$ or $\mathbf{X}[3]$, as in Equation (16), using the smallest point-centroid distance.
- **Actuation Phases 1–4**. Damage detection and classification are applied to a single matrix: the horizontal concatenation of the four matrices $X[\varphi], \quad \varphi = 1, \dots, 4$, namely, $\mathbf{X}[1, 2, 3, 4]$, as in Equation (17), using the smallest point-centroid distance.
- **Majority voting**. Damage detection and classification are applied to the four matrices: $X[\varphi], \ \varphi = 1, \dots, 4$. Each actuation phase casts a vote, and a final decision is taken using the majority voting (Section 4.5).
- **Sum of the inverse distances**. Damage detection and classification are applied to the four matrices: $X[\varphi], \ \varphi = 1, \dots, 4$. Each actuation phase casts a vote, and a final decision is taken based on the maximum sum of the inverse distances (Section 4.5).

Finally, in some cases, to compare the performance of the current approach to damage detection and classification, we have included confusion matrices of a similar approach. The approach that is used to compare the performance of t-SNE relies on the same strategy for data integration (Section 2.1) and data transformation (Section 2.2). The difference is that the clusters are created using PCA, instead of t-SNE.

True \ Predicted	Actuation phase 1				Actuation phase 3			
	*D*0	*D*1	*D*2	*D*3	*D*0	*D*1	*D*2	*D*3
*D*0	96	0	2	2	99	0	0	1
*D*1	0	100	0	0	0	100	0	0
*D*2	0	0	100	0	1	0	98	1
*D*3	0	0	0	100	0	0	0	100

Note. *D*0: healthy state of the structure; *D*1, *D*2, and *D*3: added masses at the positions indicated in Figures 4a and 4b.

TABLE 1 Confusion matrix of the application of the *t*-distributed stochastic neighbor embedding-based damage detection and classification procedure presented in Sections 2 and 3 to the case of the aluminum plate (Scenario 1) described in Section 4.1, for the Actuation Phases 1 and 3

True \ Predicted	Actuation phase 1				Actuation phase 3			
	*D*0	*D*1	*D*2	*D*3	*D*0	*D*1	*D*2	*D*3
*D*0	78	0	0	22	100	0	0	0
*D*1	0	100	0	0	0	100	0	0
*D*2	0	0	100	0	2	0	78	20
*D*3	0	0	0	100	0	0	0	100

Note. *D*0: healthy state of the structure; *D*1, *D*2, and *D*3: added masses at the positions indicated in Figures 4a and 4b.

TABLE 2 Confusion matrix of the application of the principal component analysis-based damage detection and classification procedure to the case of the aluminum plate (Scenario 1) described in Section 4.1, for the Actuation Phases 1 and 3

TABLE 3 Confusion matrix of the application of the *t*-distributed stochastic neighbor embedding-based damage detection and classification procedure presented in Sections 2 and 3 to the case of the aluminum plate (Scenario 1) described in Section 4.1, when the four actuation phases are used simultaneously

True \ Predicted	Phases 1–4				Majority voting				Inverse distances			
	*D*0	*D*1	*D*2	*D*3	*D*0	*D*1	*D*2	*D*3	*D*0	*D*1	*D*2	*D*3
*D*0	100	0	0	0	100	0	0	0	100	0	0	0
*D*1	0	100	0	0	0	100	0	0	0	100	0	0
*D*2	0	0	100	0	0	0	100	0	0	0	100	0
*D*3	0	0	0	100	0	0	0	100	0	0	0	100

Note. *D*0: healthy state of the structure; *D*1, *D*2, and *D*3: added masses at the positions indicated in Figures 4a and 4b.

5.1 | Scenario 1

In this section, we present the results for Scenario 1. In this scenario, a short wire has been used, and the measured signals are filtered with a Savitzky–Golay algorithm. Tables 1 and 3 show the five confusion matrices. When the decision is based on a single actuation phase (Table 1), the overall accuracy is quite good. Specifically, 396 and 397 observations out of 400 cases have been correctly classified in Actuation Phases 1 and 3, respectively (which corresponds to an overall accuracy of 99% and 99.25%, respectively). When the four actuation phases are used simultaneously (Actuation Phases 1–4, Equation 17, the majority voting and the sum of the inverse distances), we achieve an overall accuracy of 100%, as shown in Table 3.

In this scenario, which is the most advantageous, the PCA-based damage detection and classification also perform well. However, the overall accuracy is reduced to 94.5% (Table 2). This is the first indication that the clusters created with *t*-SNE have a better quality compared with the clusters created with PCA.

5.2 | Scenario 2

In this section, we present the results for Scenario 2. In this case, a short wire has been used, but the measured signals were not filtered. Tables 4 and 6 show the five confusion matrices. When the decision is based on a single actuation phase (Table 4), the overall accuracy is quite remarkable. Specifically, for Actuation Phase 1, 382 observations out of 400 have been correctly classified (which corresponds to an overall accuracy of 95.5%). For Actuation Phase 3, when the four actuation phases are used simultaneously (Actuation Phases 1–4, Equation 17), the majority voting and the sum of the inverse distances), an overall accuracy of 100% is achieved, as shown in Table 6.

Moreover, in this case, the results of the *t*-SNE based damage detection and classification are compared with those of the PCA-based method. In particular, in Actuation Phase 1, 289 observations out of 400 have been correctly classified

TABLE 4 Confusion matrix of the application of the *t*-distributed stochastic neighbor embedding-based damage detection and classification procedure presented in Sections 2 and 3 to the case of the aluminum plate (Scenario 2) described in Section 4.1, for the Actuation Phases 1 and 3

True \ Predicted	Actuation phase 1				Actuation phase 3			
	*D*0	*D*1	*D*2	*D*3	*D*0	*D*1	*D*2	*D*3
*D*0	82	6	12	0	100	0	0	0
*D*1	0	100	0	0	0	100	0	0
*D*2	0	0	100	0	0	0	100	0
*D*3	0	0	0	100	0	0	0	100

*Note.D*0: healthy state of the structure; *D*1, *D*2, and *D*3: added masses at the positions indicated in Figures 4a and 4b.

TABLE 5 Confusion matrix of the application of the principal component analysis-based damage detection and classification procedure to the case of the aluminum plate (Scenario 2) described in Section 4.1, for the Actuation Phases 1 and 3

True \ Predicted	Actuation phase 1				Actuation phase 3			
	*D*0	*D*1	*D*2	*D*3	*D*0	*D*1	*D*2	*D*3
*D*0	51	8	40	1	100	0	0	0
*D*1	4	76	20	0	0	100	0	0
*D*2	26	2	70	2	0	0	100	0
*D*3	4	0	4	92	0	0	0	100

*Note. D*0: healthy state of the structure; *D*1, *D*2, and *D*3: added masses at the positions indicated in Figures 4a and 4b.

TABLE 6 Confusion matrix of the application of the *t*-distributed stochastic neighbor embedding-based damage detection and classification procedure presented in Sections 2 and 3 to the case of the aluminum plate (Scenario 2) described in Section 4.1, when the four actuation phases are used simultaneously

True \ Predicted	Phases 1–4				Majority voting				Inverse distances			
	*D*0	*D*1	*D*2	*D*3	*D*0	*D*1	*D*2	*D*3	*D*0	*D*1	*D*2	*D*3
*D*0	100	0	0	0	100	0	0	0	100	0	0	0
*D*1	0	100	0	0	0	100	0	0	0	100	0	0
*D*2	0	0	100	0	0	0	100	0	0	0	100	0
*D*3	0	0	0	100	0	0	0	100	0	0	0	100

*Note. D*0: healthy state of the structure; *D*1, *D*2, and *D*3: added masses at the positions indicated in Figures 4a and 4b.

(Table 5). This corresponds to an overall accuracy of 72.25%. The *t*-SNE-based damage detection and classification (with an overall accuracy of 95.5%) outperforms the PCA-based approach. Moreover, the false-positive rate (FPR)—defined as the ratio of false positives to the total number of negatives—is $49/100 = 49\%$, which is unsatisfactory. Similarly, the false-negative rate (FNR)—the ratio of false negatives to the total number of positives—is $34/300 = 11.3\%$. To compute the FNR, the three different types of damage (*D*1, *D*2, and *D*3) are considered as a single category (the opposite of the healthy state of the structure).

5.3 | Scenario 3

In this section, we present the results for Scenario 3. In the two previous scenarios, a short wire was used. However, in this case, the signals are acquired using a 2.5 m long wire. Tables 7 and 8 show the five confusion matrices. When the decision is based on a single actuation phase (Table 7), the overall accuracy significantly decreases compared with Scenario 1 and Scenario 2. Specifically, 244 and 280 observations have been correctly classified in the Actuation Phases 1 and 3, respectively (which represents an overall accuracy of 61% and 70%, respectively). For Actuation Phase 1, the FPR is 50%, and the FNR is 16%: Both values are unacceptable.

The potential of the approaches where the four actuation phases are used can be observed in this last scenario (see Table 8):

- When the four actuation phases are merged in a single matrix (as in Equation 17), 354 observations out of 400 are correctly classified; this represents an overall accuracy of 88.5%, an FPR of 14%, and an FNR of 4%.
  When each actuation phase casts a vote, and a final decision is taken using the majority voting, the overall accuracy is increased to 91.25%. The FPR is reduced to 2%, and the FNR is slightly increased to 6%.

True \ Predicted	Actuation phase 1				Actuation phase 3			
	*D*0	*D*1	*D*2	*D*3	*D*0	*D*1	*D*2	*D*3
*D*0	50	6	19	25	93	1	3	3
*D*1	19	66	11	4	16	50	23	11
*D*2	14	3	73	10	5	19	70	6
*D*3	15	9	21	55	0	23	10	67

Note. *D*0: healthy state of the structure; *D*1, *D*2, and *D*3: added masses at the positions indicated in Figures 4a and 4b.

TABLE 7 Confusion matrix of the application of the *t*-distributed stochastic neighbor embedding-based damage detection and classification procedure presented in Sections 2 and 3 to the case of the aluminum plate (Scenario 3) described in Section 4.1, for the Actuation Phases 1 and 3

True \ Predicted	Phases 1–4				Majority voting				Inverse distances			
	*D*0	*D*1	*D*2	*D*3	*D*0	*D*1	*D*2	*D*3	*D*0	*D*1	*D*2	*D*3
*D*0	86	1	7	6	98	0	0	2	99	0	1	0
*D*1	8	88	4	0	12	85	2	1	1	99	0	0
*D*2	1	8	89	2	6	2	90	2	1	1	95	3
*D*3	3	4	2	91	0	3	5	92	1	2	2	95

Note. *D*0: healthy state of the structure; *D*1, *D*2, and *D*3: added masses at the positions indicated in Figures 4a and 4b.

TABLE 8 Confusion matrix of the application of the *t*-distributed stochastic neighbor embedding-based damage detection and classification procedure presented in Sections 2 and 3 to the case of the aluminum plate (Scenario 3) described in Section 4.1, when the four actuation phases are used simultaneously

	Accuracy	FPR	FNR
Actuation phase 1	61.0%	50.0%	16.0%
Actuation phase 3	70.0%	7.0%	7.0%
Phases 1-4	88.5%	14.0%	4.0%
Majority voting	91.3%	2.0%	6.0%
Inverse distances	97.0%	1.0%	1.0%

Abbreviations: FNR, false-negative rate; FPR, false-positive rate.

TABLE 9 Overall accuracy, FPR, and FNR of the application of the *t*-distributed stochastic neighbor embedding-based damage detection and classification procedure presented in Sections 2 and 3 to the case of the aluminum plate (Scenario 3) described in Section 4.1, when the four actuation phases are used separately and simultaneously

- Finally, when each actuation phase casts a vote, and a final decision is taken using the maximum sum of the inverse distances, the overall accuracy increases to 97%. FPR and FNR are significantly reduced to 1% and 1%, respectively.

Table 9 summarizes the values for the overall accuracy, FPR, and FNR in this scenario.

5.4 | General comments

According to the results presented in Sections 5.1–5.3, it is better to make a decision considering all of the actuation phases (assembling these phases or using them to cast a vote) rather than working with the phases separately. Moreover, the results reveal the strong performance of the sum of the inverse distances strategy as compared with the majority voting or the horizontal concatenation of the four actuation phases. The majority voting outperforms the horizontal concatenation of the four actuation phases, but it cannot accurately classify damage *D*1 (Scenario 3, Table 8). In contrast, the sum of the inverse distances strategy classifies the practical totality of the kinds of damage that we have considered. In general, the healthy state of the structure is confused with a damaged structure only in a few cases. Similarly, the damaged structure is identified as a structure with no damage in a very limited number of observations. In general, the performance of the proposed method is satisfactory when the signals are acquired using a short wire, with or without adding white Gaussian noise. In these two cases, if using PCA as a preprocessing step, the noise is canceled. The third scenario presents the worst case, because it used a long cable (2.5 m) from the digitizers to the sensors. In this scenario, the signals were badly digitized (because of the impedance of the cable, the low voltage of the stimulus, and other experimental characteristics). Therefore, we observe that the use of a long cable from the digitizer to the sensors affects the quality of detection and classification. However, combining the four actuation phases and the sum of the inverse distances strategy, we can obtain very accurate results.

6 | CONCLUSIONS

In this study, we proposed an SHM strategy for detection and classification of structural changes using two-step data integration (type *E* unfolding and MCGS), data transformation using PCA, and two-step data reduction combining PCA

and *t*-SNE. We evaluated the proposed approach using experimental data. In general, the obtained results show that the performance of the proposed method is very satisfactory, given its high classification accuracy. The performance is very good and similar in all the datasets. In the case studies, we obtain very accurate results regardless of adding white Gaussian noise, because PCA cancels the noise. However, the use of a long wire (2.5 m) from the digitizers to the sensors reduces the quality of detection and classification. Moreover, we can obtain accurate results by combining the four actuation phases and the sum of the inverse distances strategy. Results also show that the quality of the two-dimensional clusters created with *t*-SNE is better than the quality of the equivalent two-dimensional clusters created only with PCA; thus, *t*-SNE improves the classification. Therefore, the *t*-SNE-based damage detection and classification significantly outperforms the PCA-only-based approach. Some aspects to highlight in the proposed method are as follows. First, the *t*-SNE technique has been extended and adapted to the field of SHM to detect and classify structural changes. Second, our method classifies the current state of the structure using data-driven analysis (i.e., using the data collected from the structure under different structural states) and without the use of complex mathematical models. Third, our results show that it is better to make a decision considering all of the actuation phases (assembling these phases or using them to cast a vote) rather than working with the phases separately. Fourth, our findings show the strong performance of the sum of the inverse distances strategy compared with the majority voting or the horizontal concatenation of the four actuation phases. Fifth, the majority voting outperforms the horizontal concatenation of the four actuation phases. Finally, in general, the healthy state of the structure is confused with a damaged structure only in a few cases; similarly, a damaged structure is identified as a structure with no damage in a very limited number of observations. Regarding the possible fields of application, similar aluminum plates have been used to represent parts of a plane (wings or fuselage). We think that we can also apply this approach to detect damage and faults in wind turbines. In general, there is no prescribed field of application: If a sensor network can be installed in a structure, and several actuation phases can be considered, the proposed approach can be a priori implemented. In future work, we plan to apply the proposed method to different environmental and operational conditions to determine its effectiveness, as well as to handle imbalanced data. Besides, we aim to investigate the parametric version of *t*-SNE.

ACKNOWLEDGEMENTS

This work has been partially funded by the Spanish Agencia Estatal de Investigación (AEI), Ministerio de Economía, Industria y Competitividad (MINECO), by the Fondo Europeo de Desarrollo Regional (FEDER) through the research project DPI2017-82930-C2-1-R, and by the Generalitat de Catalunya through the research project 2017 SGR 388. We gratefully acknowledge the support of NVIDIA Corporation that donated the Titan Xp GPU used for this research. We thank the Universitat Politècnica de Catalunya (UPC) for the predoctoral fellowship to D. Agis.

ORCID

David Agis https://orcid.org/0000-0002-7283-6902
Diego A. Tibaduiza https://orcid.org/0000-0002-4498-596X
Francesc Pozo https://orcid.org/0000-0001-8958-6789

REFERENCES

1. Raju KS, Pratap Y, Sahni Y, Babu MN. Implementation of a WSN system towards SHM of civil building structures. In: 2015 IEEE 9th International Conference on Intelligent Systems and Control (ISCO); 2015; Coimbatore, India:1-7.
2. Blanco H, Boffill Y, Lombillo I, Villegas L. An integrated structural health monitoring system for determining local/global responses of historic masonry buildings. *Struct Control Health Monit*. 2018;25(8):e2196.
3. Ciang CC, Lee J-R, Bang H-J. Structural health monitoring for a wind turbine system: A review of damage detection methods. *Meas Sci Technol*. 2008;19(12):122001.
4. Loh C-H, Loh KJ, Yang Y-S, Hsiung W-Y, Huang Y-T. Vibration-based system identification of wind turbine system. *Struct Control Health Monit*. 2017;24(3):e1876.
5. Nisha M. Structural health monitoring of aircraft wing using wireless network. *Int J Technol Explor Learn*. 2014;3(1):341-343.
6. Ochôa P, Groves RM, Benedictus R. Systematic multiparameter design methodology for an ultrasonic health monitoring system for full-scale composite aircraft primary structures. *Struct Contr Health Monit*. 2019;26:e2340.
7. Ward MO, Grinstein G, Keim D. *Interactive Data Visualization: Foundations, Techniques, and Applications*. Boca Raton, FL, USA: CRC Press; 2015.
8. Tenenbaum JB, De Silva V, Langford JC. A global geometric framework for nonlinear dimensionality reduction. *Science*. 2000;290(5500):2319-2323.

9. van der Maaten L, Hinton G. Visualizing data using t-SNE. *J Machine Learn Res*. 2008;9:2579-2605.
10. Westerhuis JA, Kourti T, MacGregor JF. Comparing alternative approaches for multivariate statistical analysis of batch process data. *J Chemomet J Chemomet Soc*. 1999;13(3-4):397-413.
11. Mujica L, Rodellar J, Fernandez A, Güemes A. Q-statistic and T2-statistic PCA-based measures for damage assessment in structures. *Struct Health Monit*. 2011;10(5):539-553.
12. Vidal Y, Pozo F, Tutivén C. Wind turbine multi-fault detection and classification based on scada data. *Energies*. 2018;11(11):3018.
13. Sikdar S, Kundu A, Jurek M, Ostachowicz W. Nondestructive analysis of debonds in a composite structure under variable temperature conditions. *Sensors*. 2019;19(16):3454.
14. Yan J, Jin H, Sun H, Qing X. Active monitoring of fatigue crack in the weld zone of bogie frames using ultrasonic guided waves. *Sensors*. 2019;19(15):3372.
15. Cho H, Hasanian M, Shan S, Lissenden CJ. Nonlinear guided wave technique for localized damage detection in plates with surface-bonded sensors to receive lamb waves generated by shear-horizontal wave mixing. *NDT E Int*. 2019;102:35-46.
16. Jiménez AA, Muñoz CQG, Márquez FPG. Dirt and mud detection and diagnosis on a wind turbine blade employing guided waves and supervised learning classifiers. *Reliab Eng Syst Safety*. 2019;184:2-12.
17. Pozo F, Vidal Y, Salgado Ó. Wind turbine condition monitoring strategy through multiway PCA and multivariate inference. *Energies*. 2018;11(4):749.
18. Hinton GE, Roweis ST. Stochastic Neighbor Embedding. In: Becker, S, Thrun, S, & Obermayer, K, eds. *Advances in Neural Information Processing Systems 15*. 2003:857-864. Cambridge MA, USA: MIT Press. http://papers.nips.cc/paper/2276-stochastic-neighbor-embedding.pdf
19. Min R. A non-linear dimensionality reduction method for improving nearest neighbour classification. *Ph.D. Thesis*: University of Toronto; 2005.
20. Orfanidis SJ. *Introduction to Signal Processing*. Upper Saddle River, NJ, USA: Prentice-Hall, Inc.; 1995.
21. Vitola J, Pozo F, Tibaduiza DA, Anaya M. A sensor data fusion system based on *k*-nearest neighbor pattern classification for structural health monitoring applications. *Sensors*. 2017;17(2):417.
22. Vitola J, Pozo F, Tibaduiza DA, Anaya M. Distributed piezoelectric sensor system for damage identification in structures subjected to temperature changes. *Sensors*. 2017;17(6):1252.
23. Tardy B, Inglada J, Michel J. Assessment of optimal transport for operational land-cover mapping using high-resolution satellite images time series without reference data of the mapping period. *Remote Sens*. 2019;11(9):1047.
24. Mehta S, Shen X, Gou J, Niu D. A new nearest centroid neighbor classifier based on *k* local means using harmonic mean distance. *Information*. 2018;9(9):234.

How to cite this article: Agis D, Tibaduiza DA, Pozo F. Vibration-based detection and classification of structural changes using principal component analysis and *t*-distributed stochastic neighbor embedding. *Struct Control Health Monit*. 2020;27:e2533. https://doi.org/10.1002/stc.2533

sensors

MDPI

Article

A Frequency-Based Approach for the Detection and Classification of Structural Changes Using *t*-SNE †

David Agis and Francesc Pozo *

Control, Modeling, Identification and Applications (CoDAlab), Department of Mathematics, Escola d'Enginyeria de Barcelona Est (EEBE), Universitat Politècnica de Catalunya (UPC), Campus Diagonal-Besòs (CDB), Eduard Maristany, 16, 08019 Barcelona, Spain; david.agis@upc.edu

* Correspondence: francesc.pozo@upc.edu; Tel.: +34-934-137-316

† This paper is an extended version of our paper published in International Conference on Structural Engineering Dynamics (ICEDyn 2019).

Received: 24 October 2019; Accepted: 20 November 2019; Published: 21 November 2019

Abstract: This work presents a structural health monitoring (SHM) approach for the detection and classification of structural changes. The proposed strategy is based on *t*-distributed stochastic neighbor embedding (*t*-SNE), a nonlinear procedure that is able to represent the local structure of high-dimensional data in a low-dimensional space. The steps of the detection and classification procedure are: (i) the data collected are scaled using mean-centered group scaling (MCGS); (ii) then principal component analysis (PCA) is applied to reduce the dimensionality of the data set; (iii) *t*-SNE is applied to represent the scaled and reduced data as points in a plane defining as many clusters as different structural states; and (iv) the current structure to be diagnosed will be associated with a cluster or structural state based on three strategies: (a) the smallest point-centroid distance; (b) majority voting; and (c) the sum of the inverse distances. The combination of PCA and *t*-SNE improves the quality of the clusters related to the structural states. The method is evaluated using experimental data from an aluminum plate with four piezoelectric transducers (PZTs). Results are illustrated in frequency domain, and they manifest the high classification accuracy and the strong performance of this method.

Keywords: classification detection; principal component analysis (PCA); structural changes; structural health monitoring (SHM); *t*-distributed stochastic neighbor embedding (*t*-SNE)

1. Introduction

Structural health monitoring (SHM) is a crucial process for engineering structures because it checks the correct behavior of the structure and determines whether it needs some type of maintenance. The healthy state of the structure has to remain between the specified limits or threshold, but these limits may change due to the aging of the structure and its use, or due to the environmental and operational conditions (EOC). Hence, in SHM systems, detection and classification of structural changes are essential in order to know the current state of the structure for security and to reduce costs of inspection and maintenance. If damage is detected and classified precisely at the time it occurs, some action may be taken before a human and/or economic disaster occurs, thus reducing the probability of accidents and the maintenance costs. SHM has been applied in many structures such as wind turbines [1–3], buildings [4,5], and aircraft [6,7], among others, and a review of the state-of-the-art manifests that SHM is a very active research field.

With the goal of obtaining information about the state of the structure, data are collected by a sensor network, which is placed along the structure. The information obtained from multi-sensor signals

creates a high-dimensional data set with a large volume of data due to continuous measurements of the monitoring system. Various methods have been proposed for the handling of high-dimensional, big, and complex data. Among these methods, plane or spatial representation techniques stick out as they offer a way to handle this type of data by means of an interface that allows an easy detection of natural clusters, identifying hidden patterns, et cetera [8]. Plane or spatial representation techniques are also somehow related to dimensionality reduction. Dimensionality reduction is the mechanism of reducing the dimension of the original data, while keeping mostly the same intrinsic information [9]. One of the proposed dimensionality reduction methods in the literature is *t*-distributed stochastic neighbor embedding (*t*-SNE), a technique developed by L. van der Maaten and G. Hinton [10], which is able to represent the local structure of original high-dimensional data in a low-dimensional space (for example, a simple 2-D plot). This technique detects patterns by identifying clusters based on similarity of data points. *t*-SNE is widely used in the literature as a dimensionality reduction technique, as a classification or pattern recognition method, or as a visualization and compression method of big data sets, but although *t*-SNE has been applied in several applications, this is one of the first approaches of *t*-SNE in the field of SHM [11].

In the present approach, *t*-SNE is applied in the frequency domain. In the field of SHM and condition monitoring (CM) this is sometimes common, and the combination of time-frequency domain is also used. Some examples are Tsogka et al. [12], who propose a novel vibration-based SHM method for damage detection in the frequency domain, which illustrates its practical application in the case of a historic bell tower. Xu et al. [13] propose a clustering method based on ensemble empirical mode decomposition and affinity propagation for bearing performance degradation assessment. To prove the superiority of the approach, the proposed methodology is compared to various popular clustering methods and commonly used time-domain indicators. The results show that the proposed method outperforms these popular clustering methods and time-domain indicators. Cheng et al. [14] propose a multisensory data-driven health degradation monitoring system by using a generalized multiclass support vector machine. In this method, multidimensional feature extraction is implemented in the time domain, frequency domain, and time-frequency domain.

In this work, a SHM strategy for detection and classification of structural changes based on a two-step data integration (type *E* unfolding [15] and the so-called mean-centered group scaling (MCGS)), data transformation using PCA, and a two-step data reduction combining PCA and *t*-SNE has been proposed. PCA is an extensively used technique that is mainly used for dimensionality reduction or feature extraction in the framework of pattern recognition [16], and it can be applied differently to detect and classify structural changes or faults [17]. In some cases, however, it can be observed that the projection into the first principal components does not allow a visual grouping, clustering, or separation. For this reason, we propose the damage or fault detection based on the combination of PCA and *t*-SNE. As a consequence, the basic steps of the detection and classification procedure that we apply are: (i) the data collected, in the frequency domain, are first scaled using MCGS due to the different scales and magnitudes in the measurements; (ii) then PCA is applied to obtain a better representation of the original data, by reducing the dimensionality of the scaled data and projecting the scaled data into the vectorial space spanned by the principal components; and (iii) *t*-SNE is finally applied to the projected data to represent these points as points in a plane. It will be shown that, with respect to the time domain, the quality of the clusters related to the different structural states is significantly improved. More precisely, the current structure to be diagnosed will then be associated with a structural state based on three different strategies: (i) the smallest point-centroid distance, i.e., when a single actuation phase is considered; (ii) majority voting; and (iii) sum of the inverse distances, i.e., when several actuation phases are combined. Therefore, in this work, *t*-SNE is used, in combination with a particular data integration, data transformation, and data reduction, for the first time in the field of SHM in a frequency-based approach. In comparison to previous

strategies found in the literature, this novel method is able to yield a best detection and classification of structural changes, thus leading to a best performance.

The proposed method for the detection and classification of structural changes is assessed using experimental data from a plate with four piezoelectric transducers (PZTs). Since guided wave propagation-based SHM strategies have proven their ability to adequately identify defects in structures [18–21], in the present work, we have also considered the paradigm of guided waves. In this paradigm, the structure is excited by a signal and the response is measured to create a baseline pattern. When a new structure has to be diagnosed, it has to be excited by the exact same signal and the response is measured and compared with the baseline pattern. Results reveal the high classification accuracy and the strong performance of this methodology, with a percentage of correct decisions of about 100% in various scenarios. In the present work, the environmental conditions were not considered, as it will be the topic for further developments.

The structure of the paper is as follows: Section 2 describes the objective of *t*-SNE and how the plane or spatial representation is obtained. Section 3 includes how the baseline data are collected and pre-processed, how the global dimension of the data is reduced, and how the clusters are created using *t*-SNE. The damage detection and classification procedure of a structure that has to be diagnosed is presented in Section 4. The experimental case study is described in Section 5. In Section 6, the results are shown. Finally, in Section 7, some conclusions are drawn.

2. *t*-Distributed Stochastic Neighbor Embedding (*t*-SNE)

2.1. The Objective of t-SNE

t-SNE is an improved variation of the technique so-called stochastic neighbor embedding (SNE) [22]. With respect to SNE, *t*-SNE is much easier to optimize and yields better plane or spatial representations of the high-dimensional data, since it reduces the tendency to crowd points in the center of the distribution (the so-called *crowding problem*). Part of the enhancements of *t*-SNE with respect to SNE are due to the fact that the cost function used by *t*-SNE differs from the one used by SNE in two features: (i) *t*-SNE uses a symmetrized version of the SNE cost function with simpler gradients; and (ii) *t*-SNE uses a Student's *t*-distribution, instead of a Gaussian, to calculate the similarity between two points in the low-dimensional space.

Given a collection of high-dimensional data points:

$$\mathcal{X} = \{\mathbf{x}^1, \ldots, \mathbf{x}^\nu\} \subset \mathbb{R}^D, \quad \nu, D \in \mathbb{N}, \tag{1}$$

the aim is to find a collection of low-dimensional map points

$$\mathcal{Y} = \{\mathbf{y}^1, \ldots, \mathbf{y}^\nu\} \subset \mathbb{R}^d, \quad d \in \mathbb{N}$$

that form a faithful representation of the original points $\{\mathbf{x}^1, \ldots, \mathbf{x}^\nu\}$ in a lower-dimensional space. Typical values for d are 2 (*plane* representation) or 3 (*spatial* representation), where $d \ll D$. By saying *faithful* representation, we mean that the points $\{\mathbf{y}^1, \ldots, \mathbf{y}^\nu\}$ in the lower-dimensional space preserve, as much as possible, the local structure of the original data $\mathcal{X}$.

2.2. Pairwise Similarities

To preserve local similarities of the original data $\mathcal{X}$ by this embedding, *t*-SNE first converts the high-dimensional Euclidean distances between data points $\mathbf{x}^i$ and $\mathbf{x}^j$ into conditional probabilities by

centering a Gaussian distribution at $\mathbf{x}^i$, computing the density of $\mathbf{x}^j$ under this Gaussian distribution, and renormalizing:

$$p_{j|i} = \frac{\exp\left(\frac{-\|\mathbf{x}^i - \mathbf{x}^j\|_2^2}{2\sigma_i^2}\right)}{\sum\limits_{\substack{l=1 \\ l\neq i}}^{\nu} \exp\left(\frac{-\|\mathbf{x}^i - \mathbf{x}^l\|_2^2}{2\sigma_i^2}\right)}, \quad i,j = 1,\ldots,\nu,\ i \neq j, \tag{2}$$

where $\frac{\|\mathbf{x}^i - \mathbf{x}^j\|_2^2}{2\sigma_i^2}$ (*affinity or scaled squared Euclidean distance*) is the dissimilarity between data points $\mathbf{x}^i$ and $\mathbf{x}^j$. The variance of the Gaussian distribution, σ_i^2, is computed automatically. Since only pairwise similarities between data points are of interest, t-SNE imposes $p_{i|i} = 0$. This conditional probability measures the similarity of $\mathbf{x}^j$ to $\mathbf{x}^i$. If two data points are close, $p_{j|i}$ will be large. However, if two data points are far, $p_{j|i}$ will be small.

Then, by symmetrizing the conditional probability in Equation (2), the joint probability is defined as follows:

$$p_{ij} = \frac{p_{j|i} + p_{i|j}}{2\nu}, \quad i,j = 1,\ldots,\nu,\ i \neq j,$$
$$p_{ii} = 0.$$

The joint probability also measures the pairwise similarity between data points $\mathbf{x}^i$ and $\mathbf{x}^j$. As a result, let us define the similarity matrix $\mathcal{P} \in \mathcal{M}_{\nu\times\nu}(\mathbb{R})$ for the high-dimensional data points as $\mathcal{P} = \left(p_{ij}\right)_{i,j=1,\ldots,\nu}$.

When the similarity matrix for the data points $\mathcal{X}$ in Equation (1) is obtained, t-SNE also defines the similarity matrix $\mathcal{Q} \in \mathcal{M}_{\nu\times\nu}(\mathbb{R})$ for the map points $\mathcal{Y}$. Essentially, we build matrix $\mathcal{Q}$ following the same idea as for the similarity matrix $\mathcal{P}$ with respect to original data points. The one and only difference is that we use for matrix $\mathcal{Q}$ a renormalized Student's t-distribution with one degree of freedom and $\sigma_i^2 = \frac{1}{2}$ for all i, instead of a Gaussian distribution:

$$q_{ij} = \frac{\frac{1}{1 + \|\mathbf{y}^i - \mathbf{y}^j\|_2^2}}{\sum\limits_{k=1}^{\nu}\sum\limits_{\substack{l=1 \\ l\neq k}}^{\nu} \frac{1}{1 + \|\mathbf{y}^k - \mathbf{y}^l\|_2^2}}, \quad i,j = 1,\ldots,\nu,\ i \neq j, \tag{3}$$

$$q_{ii} = 0, \tag{4}$$

where q_{ij} represents the local structure of the data points in the low-dimensional space.

2.3. Comparing Similarity Matrices: Cost Function

The goal is to select the map points so that the two similarity matrices, $\mathcal{P}$ and $\mathcal{Q}$, are as similar as possible. The similarity between these two matrices will be defined in terms of the Kullback–Leibler (KL) divergence. The KL divergence between the joint probability distributions $\mathcal{P}$ and $\mathcal{Q}$ is a measure of the *distance* between the two similarity matrices, and it can be defined as [10,22,23]:

$$\mathcal{C} = \mathcal{D}_{KL}\left(\mathcal{P}\|\mathcal{Q}\right) = \sum_{i=1}^{\nu}\sum_{\substack{j=1 \\ j\neq i}}^{\nu} p_{ij} \log\left(\frac{p_{ij}}{q_{ij}}\right). \tag{5}$$

Therefore, minimizing the KL divergence reduces the *distance* between these two matrices. And to minimize the cost function $\mathcal{C}$, the gradient descent method is used: $\frac{\partial \mathcal{C}}{\partial \mathbf{y}^i}$. It is worth noting that the gradient descent is an iterative optimization algorithm and therefore it updates the map point $\mathbf{y}^i$ at each step.

For more details, see the original *t*-SNE paper [10].

3. Data Collection, Pre-Processing, and Clustering: Baseline Data

3.1. Data Collection and Pre-Processing

The data collected are made up of different response signals measured, in the time domain, by sensors on a vibrating structure. Multiple realizations of these responses are measured, under different structural states. Coming up next, these responses signals are transformed into the frequency domain using the fast Fourier transform (FFT) algorithm, and features are extracted from the spectrum to reduce the data dimension, dividing by two and adding one to the number of components in each signal. A matrix which collects all the realizations under different structural states in the frequency domain is defined as:

$$\mathbf{X} = \left(x_{i,l}^{k,j}\right) = \left[\begin{array}{ccc|c|ccc} x_{1,1}^{1,1} & \cdots & x_{1,1}^{1,L} & \cdots & x_{1,1}^{N,1} & \cdots & x_{1,1}^{N,L} \\ \vdots & \ddots & \vdots & \ddots & \vdots & \ddots & \vdots \\ x_{n_1,1}^{1,1} & \cdots & x_{n_1,1}^{1,L} & \cdots & x_{n_1,1}^{N,1} & \cdots & x_{n_1,1}^{N,L} \\ \hline x_{1,2}^{1,1} & \cdots & x_{1,2}^{1,L} & \cdots & x_{1,2}^{N,1} & \cdots & x_{1,2}^{N,L} \\ \vdots & \ddots & \vdots & \ddots & \vdots & \ddots & \vdots \\ x_{n_2,2}^{1,1} & \cdots & x_{n_2,2}^{1,L} & \cdots & x_{n_2,2}^{N,1} & \cdots & x_{n_2,2}^{N,L} \\ \hline \vdots & \ddots & \vdots & \ddots & \vdots & \ddots & \vdots \\ \hline x_{1,E}^{1,1} & \cdots & x_{1,E}^{1,L} & \cdots & x_{1,E}^{N,1} & \cdots & x_{1,E}^{N,L} \\ \vdots & \ddots & \vdots & \ddots & \vdots & \ddots & \vdots \\ x_{n_E,E}^{1,1} & \cdots & x_{n_E,E}^{1,L} & \cdots & x_{n_E,E}^{N,1} & \cdots & x_{n_E,E}^{N,L} \end{array}\right] \tag{6}$$

$$= \left[\begin{array}{c} \mathbf{X}_1 \\ \hline \mathbf{X}_2 \\ \hline \vdots \\ \hline \mathbf{X}_E \end{array}\right] \in \mathcal{M}_{(n_1+\cdots+n_E)\times(N\cdot L)}(\mathbb{R}), \tag{7}$$

$$= \left[\begin{array}{c|c|c|c} \mathbf{X}^1 & \mathbf{X}^2 & \cdots & \mathbf{X}^N \end{array}\right], \tag{8}$$

where $N \in \mathbb{N}$ is the number of sensors and $k = 1, \ldots, N$ identifies the sensor that is measuring; $L \in \mathbb{N}$ is the number of components in each signal and $j = 1, \ldots, L$ indicates the j-th measurement in the frequency domain; $E \in \mathbb{N}$ is the number of different structural states that are considered and $l = 1, \ldots, E$ represents the structural state that is been measured; and finally, n_l, $l = 1, \ldots, E$, is the number of realizations per structural state and $i = 1, \ldots, n_l$ is the i-th realization related to the l-th structural state. Note that matrix $\mathbf{X}$ in Equation (7) is formed by E horizontal blocks, $\mathbf{X}_l$, $l = 1, \ldots, E$, each one of them related to the different structural states. At the same time, this matrix $\mathbf{X}$ can also be viewed as formed by N vertical blocks, $\mathbf{X}^k$, $k = 1, \ldots, N$, each one of them related to the different sensors. Due to the different scales and magnitudes in the measurements, the matrix $\mathbf{X}$ in Equation (7) is rescaled using MCGS, which is suggested by Pozo et al. [24].

3.2. Dimensionality Reduction

One of the main reasons of using the MCGS is that the covariance matrix of matrix $\check{\mathbf{X}}$, i.e., the scaled data set, can be computed in a very simple way as:

$$\mathbf{C}_{\check{\mathbf{X}}} = \frac{1}{n-1}\check{\mathbf{X}}^{\top}\check{\mathbf{X}} \in \mathcal{M}_{(N\cdot L)\times(N\cdot L)}(\mathbb{R}). \tag{9}$$

The eigenvectors ρ_k, $k = 1, \ldots, N \cdot L$, and eigenvalues λ_k, $k = 1, \ldots, N \cdot L$, of the covariance matrix $\mathbf{C}_{\check{\mathbf{X}}}$ define the subspaces in the PCA model. The eigenvalues λ_k are then ordered in decreasing order as

$$\lambda_1 \geq \lambda_2 \geq \cdots \geq \lambda_{N\cdot L},$$

and the matrix $\mathbf{P} \in \mathcal{M}_{(N\cdot L)\times(N\cdot L)}(\mathbb{R})$ contains, written as columns, their corresponding eigenvectors ρ_k. These eigenvectors are known as the principal components. The eigenvalues define the partial variance of each eigenvector. When the *column scaling* is applied to matrix $\mathbf{X}$ in Equation (7), although not not the case of this paper, we have that the trace of the covariance matrix $\mathbf{C}_{\check{\mathbf{X}}}$, which is the sum of the eigenvalues, is equal to the number of columns of $\mathbf{X}$, that is, $N \cdot L$. This means that the proportion of the variance directed along the first $\ell \in \mathbb{N}$ principal components is given by $\dfrac{\lambda_1 + \cdots + \lambda_\ell}{N \cdot L}$. However, when the MCGS is applied to scale the raw data in matrix $\mathbf{X}$ in Equation (7), the trace of the covariance matrix $\mathbf{C}_{\check{\mathbf{X}}}$ is no longer necessarily equal to $N \cdot L$. As a consequence, the proportion of the variance explained by the first ℓ principal components is given by:

$$\frac{\lambda_1 + \cdots + \lambda_\ell}{\lambda_1 + \cdots + \lambda_{N\cdot L}}.$$

In this work, we use PCA to reduce the dimensionality of the scaled data set $\check{\mathbf{X}}$ by selecting a reduced, but still significant, number $\ell = D < N \cdot L$ of principal components. This dimensionality reduction is performed through the reduced matrix

$$\mathbf{P}_\ell = \mathbf{P}_D = \begin{bmatrix} \rho_1 & \rho_2 & \cdots & \rho_\ell \end{bmatrix} \in \mathcal{M}_{(N\cdot L)\times\ell}(\mathbb{R}), \tag{10}$$

which is composed by the concatenation of the eigenvectors ρ_k related to the highest eigenvalues. Matrix $\mathbf{P}_\ell = \mathbf{P}_D$ in Equation (10) is the *model* or *PCA model*. The scaled data set $\check{\mathbf{X}}$ is then projected into the vectorial space spanned by the $\ell = D$ first principal components through the premultiplication of $\mathbf{P}_\ell$ by $\check{\mathbf{X}}$. More precisely,

$$\mathbf{T}_\ell = \mathbf{T}_D = \check{\mathbf{X}}\mathbf{P}_\ell \in \mathcal{M}_{n\times\ell}(\mathbb{R}). \tag{11}$$

P_ℓ in Equation (10) has been defined as the PCA model that includes multiple realizations under different structural states. At the same time, $\mathbf{T}_\ell$ in Equation (11) is the projection of the scaled data set $\check{\mathbf{X}}$ into the subspace spanned by the PCA model. The number of principal components $\ell = D \in \mathbb{N}$ is chosen so that the proportion of the variance explained is greater than or equal to 95%.

3.3. Clustering Effect

In Section 3.2, the dimensionality reduction has been performed. More precisely, n realizations under different structural states (the rows of matrix $\mathbf{X}$ in Equation (7)), that may be seen as $N \cdot L-$dimensional vectors, are projected and transformed into $\ell = D-$dimensional vectors. This reduction of the dimension

of the original data is performed with a small loss of information, less than 5%, and it is also expected that ℓ is much smaller than $N \cdot L$.

A second transformation is performed to the projected data in matrix $\mathbf{T}_\ell$ in Equation (11) using the t-SNE presented in Section 2. Let us define

$$\mathbf{x}^i = \mathbf{e}_i^\top \mathbf{T}_\ell = \mathbf{e}_i^\top \check{\mathbf{X}} \mathbf{P}_\ell \in \mathbb{R}^\ell, \; i = 1, \ldots, n$$

as the i-th row of matrix $\mathbf{T}_\ell$ in Equation (11). The vector $\mathbf{e}_i \in \mathbb{R}^n$ is the i-th element of the canonical basis. Let us also define

$$\mathcal{X} = \{\mathbf{x}^1, \ldots, \mathbf{x}^n\} \subset \mathbb{R}^\ell \tag{12}$$

as a collection of high-dimensional data points. The objective is to find a collection of $2-$dimensional map points

$$\mathcal{Y} = \{\mathbf{y}^1, \ldots, \mathbf{y}^n\} \subset \mathbb{R}^2$$

that represent the original set $\mathcal{X}$ with no explicit loss of information and preserving the local structure of this set. After the application of t-SNE, we expect E clusters to be observed, related to the E different structural states. These clusters are formed by the map points:

$$\begin{aligned}
\{\mathbf{y}^1, \ldots, \mathbf{y}^{n_1}\} &\subset \mathcal{Y}, \text{related to the } \textit{1st} \text{ structural state;} \\
\{\mathbf{y}^{n_1+1}, \ldots, \mathbf{y}^{n_1+n_2}\} &\subset \mathcal{Y}, \text{related to the } \textit{2nd} \text{ structural state;} \\
\{\mathbf{y}^{n_1+n_2+1}, \ldots, \mathbf{y}^{n_1+n_2+n_3}\} &\subset \mathcal{Y}, \text{related to the } \textit{3rd} \text{ structural state;} \\
&\vdots \\
\{\mathbf{y}^{n-n_{E-1}-n_E+1}, \ldots, \mathbf{y}^{n-n_E}\} &\subset \mathcal{Y}, \text{related to the } \textit{penultimate} \text{ structural state; and} \\
\{\mathbf{y}^{n-n_E+1}, \ldots, \mathbf{y}^{n}\} &\subset \mathcal{Y}, \text{related to the } \textit{last} \text{ structural state.}
\end{aligned} \tag{13}$$

4. Damage Detection and Classification Procedure: Structure to Diagnose

In Section 3.3, we have seen how the original realizations under different structural states are finally projected on a plane to define a set of clusters. In this section, we will present the damage detection and classification procedure of a structure that has to be diagnosed.

A single realization of the current structure to diagnose is needed. The data collected are made up, in this case, of different response signals measured by the same number of sensors N and the same number of components in each signal L, as in Equation (7). When these measures are obtained and they are transformed into the frequency domain, a new data vector $\mathbf{z}$ is constructed:

$$\mathbf{z}^\top = \left[\begin{array}{ccc|c|ccc} z^{1,1} & \cdots & z^{1,L} & \cdots & z^{N,1} & \cdots & z^{N,L} \end{array} \right] \in \mathbb{R}^{N \cdot L}.$$

4.1. Scaling (MCGS)

Before the collected data coming from the structure to diagnose is projected into the space spanned by the principal components, the row vector $\mathbf{z}^\top$ has to be scaled to define a scaled row vector $\check{\mathbf{z}}^\top$:

$$\check{z}^{k,j} = \frac{z^{k,j} - \mu^{k,j}}{\sigma^k}, \quad k = 1, \ldots, N, \; j = 1, \ldots, L, \tag{14}$$

where $\mu^{k,j}$ is the arithmetic mean of all the elements in the $[(k-1)L+j]$-th column of matrix $\mathbf{X}$ in Equation (6) i.e., the j-th column of the vertical block $\mathbf{X}^k$ in Equation (8); and σ^k is the standard deviation of all the elements in the vertical block $\mathbf{X}^k$ in Equation (8) with respect to the mean value μ^k (the arithmetic mean of all the elements in the vertical block $\mathbf{X}^k$ in Equation (8)).

4.2. Projection (PCA)

The projection of the scaled row vector $\check{\mathbf{z}}^\top \in \mathbb{R}^{N\cdot L}$ into the space spanned by the ℓ first principal components in $\mathbf{P}_\ell$ is performed through the following vector to matrix multiplication:

$$\mathbf{x}^{n+1} = \check{\mathbf{z}}^\top \cdot \mathbf{P}_\ell \in \mathbb{R}^\ell.$$

It is worth noting that the $N \cdot L-$dimensional vector that contains the collected data coming from the structure to be diagnosed in now transformed into an $\ell-$dimensional vector. This new point will be added to the data set $\mathcal{X}$ in Equation (12) to define a new set:

$$\mathcal{X}' = \mathcal{X} \cup \{\mathbf{x}^{n+1}\} = \{\mathbf{x}^1, \ldots, \mathbf{x}^n, \mathbf{x}^{n+1}\} \subset \mathbb{R}^\ell. \tag{15}$$

4.3. t-SNE and Final Classification

t-SNE is applied to the $\ell-$dimensional data set $\mathcal{X}'$ in Equation (15) to find a collection of $2-$dimensional map points:

$$\mathcal{Y}' = \{\mathbf{y}^1, \ldots, \mathbf{y}^n, \mathbf{y}^{n+1}\} \subset \mathbb{R}^2$$

that represent the original set $\mathcal{X}$ with no explicit loss of information and preserving the local structure of this set, as well as including the map point $\mathbf{y}^{n+1}$ associated to the data point $\mathbf{x}^{n+1}$. The same E clusters have to be observed, related to the E different structural states. As in Section 3.3, these clusters are formed by the map points in Equation (13).

For each cluster, we compute its centroid, that is, the mean of the values of the points of data in the cluster. For instance, the centroid associated with the first structural state is:

$$\mathcal{Y}_1 := \frac{1}{n_1}\sum_{i=1}^{n_1} \mathbf{y}^i = \frac{\mathbf{y}^1 + \cdots + \mathbf{y}^{n_1}}{n_1} \in \mathbb{R}^2,$$

whereas the centroid associated with the second structural state is:

$$\mathcal{Y}_2 := \frac{1}{n_2}\sum_{i=1}^{n_2} \mathbf{y}^{n_1+i} = \frac{\mathbf{y}^{n_1+1} + \cdots + \mathbf{y}^{n_1+n_2}}{n_2} \in \mathbb{R}^2.$$

In general, the centroid associated with the l-th structural state, $l = 1, \ldots, E$, is the point of the plane defined as

$$\mathcal{Y}_l := \frac{1}{n_l}\sum_{i=1}^{n_l} \mathbf{y}^{\left(\sum_{j=0}^{l-1} n_j\right)+i} \in \mathbb{R}^2,\ l = 1, \ldots, E, \tag{16}$$

where $n_0 = 0$. Therefore, the current structure to diagnose is associated to the l-th structural state if

$$l = \arg\min_{l=1,\ldots,E} \|\mathcal{Y}_l - \mathbf{y}^{n+1}\|_2,$$

that is, if the minimum distance between $\mathbf{y}^{n+1}$ and each one of the centroids corresponds to the Euclidean distance between $\mathbf{y}^{n+1}$ and $\mathcal{Y}_l$. We call this approach the smallest point-centroid distance (see Figure 1).

A flowchart of the proposed approach and how it is applied is given in Figure 2.

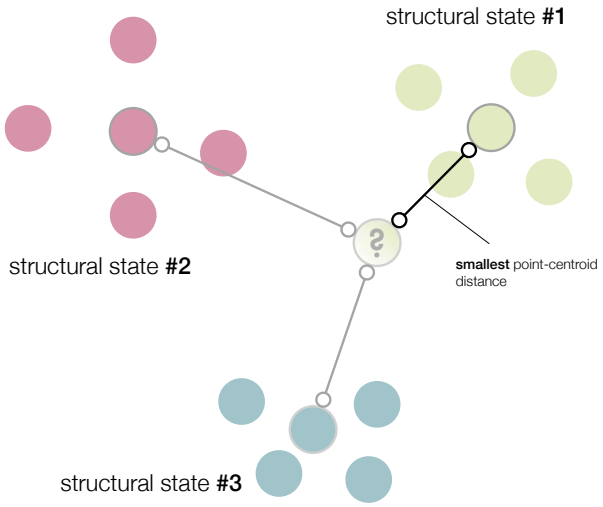

Figure 1. The current structure to diagnose is associated to the structural state with the smallest point-centroid distance.

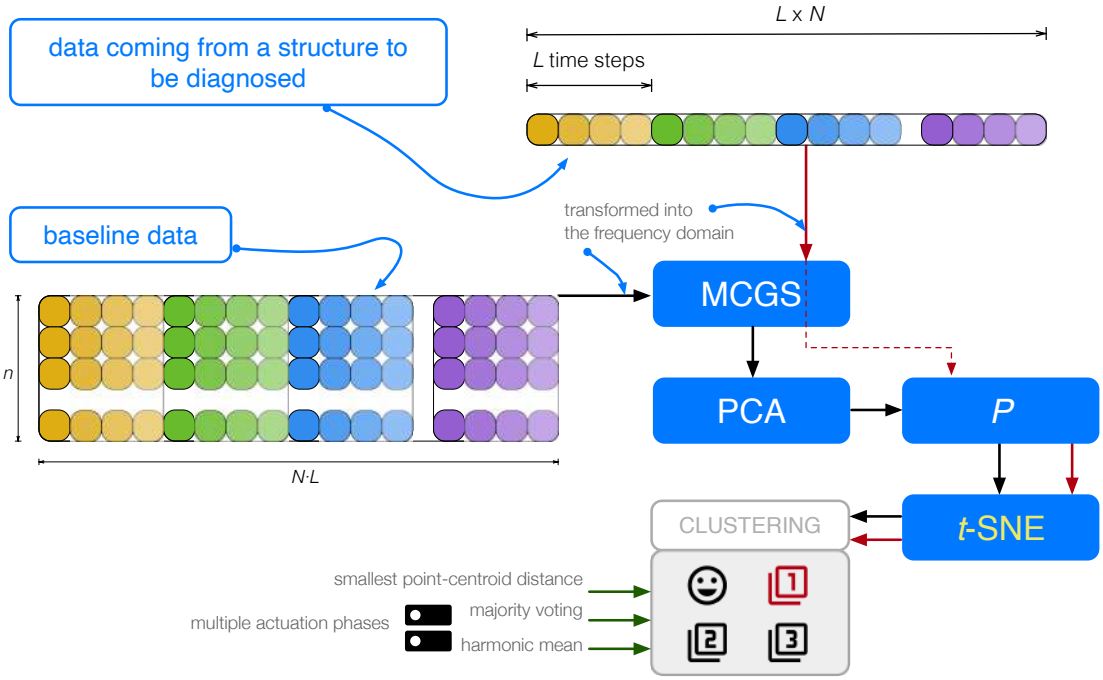

Figure 2. Flowchart of the proposed approach. Data coming from a structure are first transformed into the frequency domain and scaled, and then projected into the principal component analysis (PCA) model. Finally, *t*-distributed stochastic neighbor embedding (*t*-SNE) is used to create the clusters that will be used in the detection and classification of structural changes. MCGS = mean-centered group scaling.

5. Case Study: Aluminum Plate with Four PZTs

5.1. Structure

In this section, a square aluminum plate with an area of 1600 cm^2 (40 cm $\times$ 40 cm, and a thickness of 0.2 cm) and instrumented with four PZTs is considered to demonstrate the reliability of the damage detection and classification methodology introduced in Sections 3 and 4. The piezoelectric transducer discs are attached to the surface and their location is shown in Figure 3. Assuming that the lower left corner of the plate in Figure 3 represents the origin of coordinates, the PZTs are installed at these positions (units in centimeters):

- PZT1 at $(20, 35)$
- PZT2 at $(35, 20)$
- PZT3 at $(20, 5)$
- PZT4 at $(5, 20)$

These PZTs are able to work both in actuator mode and in sensor mode. In actuator mode, the burst signal in Figure 4 is applied to the PZTs, and they produce a mechanical vibration; and in sensor mode, they detect time varying mechanical response. It is worth keeping in mind that the distance between the four sensors is not the same. More precisely, for example, the distance between sensor 1 and sensor 2 and the distance between sensor 1 and sensor 4 is equal. However, the distance between sensor 1 and sensor 3 is relatively larger.

A 17.2916 grams mass is added to simulate the damage, in a non-destructive way, in the aluminum plate. This mass is an attached magnet in both sides of the plate, since aluminum is non-magnetic metal. This kind of damage is used to change the properties of the structure and to produce changes in the propagated wave, therefore providing different scenarios for validating the proposed method. The location of the mass defines each damage. These locations are (units in centimeters):

- damage 1 at $(12.5, 27.5)$
- damage 2 at $(27.5, 27.5)$
- damage 3 at $(12.5, 12.5)$

$E = 4$ structural states are considered here:

- the first structural state corresponds to the healthy state of the structure, that is, the square aluminum plate with no damage;
- the second, third, and fourth structural states correspond to the plate with an added mass at the positions indicated in Figure 3 as damage 1, damage 2, and damage 3, respectively.

The aluminum plate is isolated from the vibration and noise that could affect the laboratory, as can be observed in Figure 5.

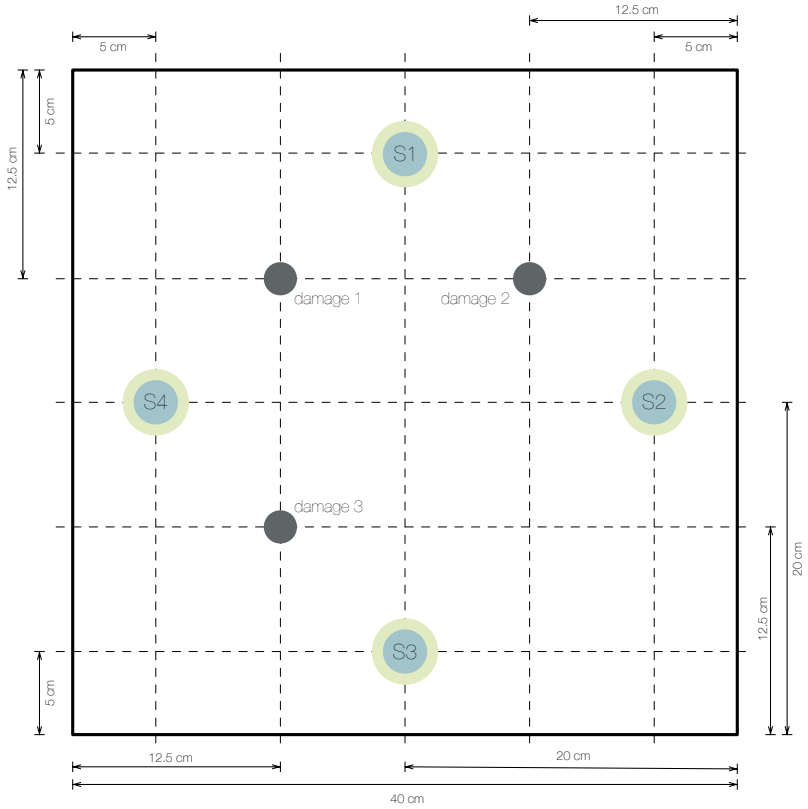

Figure 3. Aluminum plate instrumented with four piezoelectric sensors (*S*1, *S*2, *S*3, and *S*4).

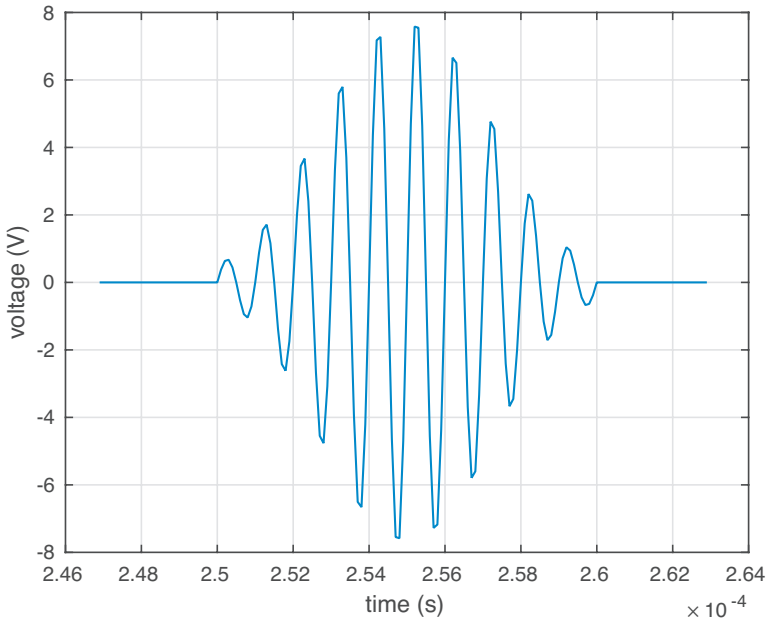

Figure 4. In actuator mode, this burst signal is applied to the piezoelectric transducers (PZTs) to produce a mechanical vibration.

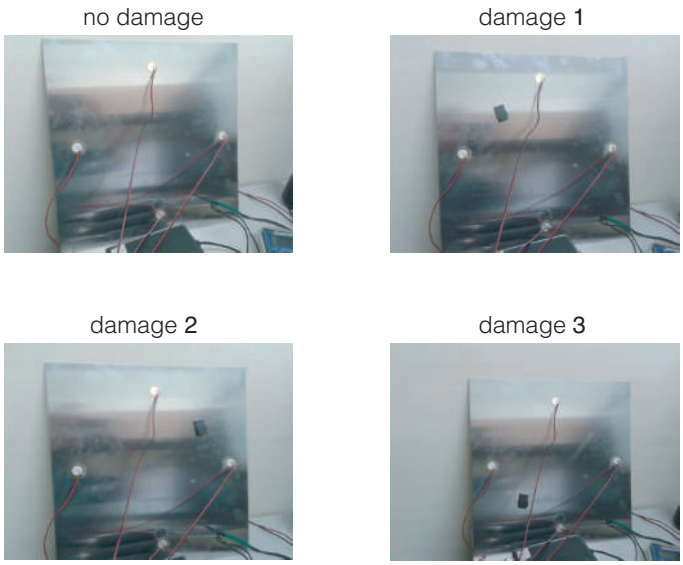

Figure 5. Aluminum plate with four PZTs and with four different structural states.

5.2. Scenarios and Actuation Phases

The experimental setup includes three different scenarios to determine the behavior of the methodology under the presence of white Gaussian noise, filters, and with respect to the length of the wire that is used from the digitizer to the sensors:

- **Scenario 1**. The signals are obtained using a short wire (0.5 m) from the digitizer to the PZTs, and these signals are filtered with a Savitzky–Golay (SG) [25] filter algorithm after adding white Gaussian noise. The filter is applied for the intention of smoothing the data.
- **Scenario 2**. The signals are obtained using a short wire (0.5 m) from the digitizer to the PZTs, but these signals are not filtered.
- **Scenario 3**. The signals are obtained using a long wire (2.5 m) from the digitizers to the PZTs. Signals are also filtered with the SG algorithm.

In this manner, we can observe the effect of the attenuation with short and long wires, the effect of adding white Gaussian noise to the measured signals, and the effect of the use of a SG filter in the detection and classification procedure.

As stated in Section 5.1, four PZTs (PZT1, PZT2, PZT3, and PZT4) are used to excite the aluminum plate and collect the measured response. This sensor network works in what we call *actuation phases*. In each actuation phase, a single PZT is used as an actuator (active sensor: the PZT excites the structure with a given excitation signal), and the rest of the PZTs are used as sensors (passive sensors: PZTs measure signals). Therefore, we have as many *actuation phases* as *sensors*:

- **Actuation phase 1**. PZT1 is used as the actuator, and PZT2, PZT3, and PZT4 are used as sensors.
- **Actuation phase 2**. PZT2 is used as the actuator, and PZT1, PZT3, and PZT4 are used as sensors.
- **Actuation phase 3**. PZT3 is used as the actuator, and PZT1, PZT2, and PZT4 are used as sensors.
- **Actuation phase 4**. PZT4 is used as the actuator, and PZT1, PZT2, and PZT3 are used as sensors.

It is very common in the literature, when using a sensor data fusion as in J. Vitola et al. [26,27], to merge the data that come from the different actuation phases in a single data matrix. In this paper, the approach with a single data matrix is also considered, but the case where each actuation phase is used as a classifier is additionally examined in Section 5.5.

5.3. Data Collection

Given a particular scenario, as the three defined in Section 5.2, four matrices $\mathbf{X}[\varphi],\ \varphi = 1,\ldots,4$, one for each actuation phase, are obtained. Each matrix $\mathbf{X}[\varphi],\ \varphi = 1,\ldots,4$, is organized as follows:

- $n_1 = n_2 = n_3 = n_4 = 25$ experiments or realizations are performed for each structural state. Consequently, each matrix $\mathbf{X}[\varphi],\ \varphi = 1,\ldots,4$, consists of 100 rows, that is $n_1 + n_2 + n_3 + n_4 = 25 \cdot 4$. More precisely, the first 25 rows represent the structure with no damage, the next 25 are realization where damage 1 is present in the structure, and so on.
- For each actuation phase $\varphi,\ \varphi = 1,\ldots,4$, we measure $N = 3$ PZTs working as sensors during 60000 time instants. Then, these measurements are transformed into the frequency domain. Therefore, the number of columns of matrix $\mathbf{X}[\varphi],\ \varphi = 1,\ldots,4$, is equal to $N \cdot L = 3 \cdot ((60000/2) + 1) = 90003$.

Therefore, the matrix that collects all the realizations under the four different structural states in the frequency domain is (see Equation (6): here $L = 30001$ and $E = 4$):

$$\mathbf{X}[\varphi] = \left(x[\varphi]_{i,l}^{k,j}\right) \in \mathcal{M}_{100\times 90003}(\mathbb{R}). \tag{17}$$

The damage detection and classification procedure introduced in Sections 3 and 4 can be applied to each one of the matrices $\mathbf{X}[\varphi],\ \varphi = 1,\ldots,4$, in Equation (17), thus leading to one classification per actuation phase. But we can also use the horizontal concatenation of the four matrices $\mathbf{X}[\varphi],\ \varphi = 1,\ldots,4$, to obtain the matrix:

$$\mathbf{X}[1,2,3,4] = \Big[\mathbf{X}[1]\,\mathbf{X}[2]\,\mathbf{X}[3]\,\mathbf{X}[4]\Big] \in \mathcal{M}_{100\times(4\cdot 90003)}(\mathbb{R}) = \mathcal{M}_{100\times 360012}(\mathbb{R}). \tag{18}$$

If matrix $\mathbf{X}[1,2,3,4]$ in Equation (18) is used for the damage detection and classification procedure introduced in Sections 3 and 4, which this allows analyzation of the information of all the actuation phases at one time, a single classification is obtained that combines these four phases. Finally, we can also use the separate classification obtained for each actuation phase so that each actuation phase casts a vote thus leading to a final decision based on the four actuation phases. These strategies will be explained in detail in Section 5.5.

5.4. $\kappa-$Fold Non-Exhaustive Leave-p-Out Cross Validation

The analysis of the proposed approach is done by comparing *test* data, i.e., the new experiments in *unknown* state under the same conditions, with *baseline* data, which is data from the structure under different structural states. To this end, we use the $\kappa-$fold non-exhaustive leave-p-out cross validation described in the subsequent paragraphs.

For the sake of clarity, let us write $\mathbf{X}[\Phi]$ to refer to both matrix $\mathbf{X}[\varphi]$ in Equation (17) and matrix $\mathbf{X}[1,2,3,4]$ in Equation (18). Some of the rows in $\mathbf{X}[\Phi]$ will be used as the baseline data to build the model and the clusters, i.e., $v = 5$ rows per structural state, and the rest of the rows are used for the validation. More precisely, we will perform five iterations ($\kappa = 5$) of a non-exhaustive leave-p-out cross validation, where $p = \sum_{i=1}^{E}(n_i - v) = n_1 + n_2 + n_3 + n_4 - v \cdot E = 80$, to estimate the overall accuracy and avoid overfitting. Let us define, for each structural state $l = 1,\ldots,E$, the permutation σ_l:

$$\begin{aligned} \sigma_l : \{1,2,\ldots,n_l\} &\to \{1,2,\ldots,n_l\} \\ i &\to \sigma_l(i) \end{aligned}$$

In this particular case, $n_1 = n_2 = n_3 = n_4 = 25$. Therefore, in the first iteration, the baseline data to build the model are the matrix:

$$\mathbf{X} = \mathbf{S}^\top \cdot \mathbf{X}[\Phi], \tag{19}$$

$$\mathbf{S} = \left[\mathbf{e}_{\sigma_1(1)} \ \cdots \ \mathbf{e}_{\sigma_1(5)} \middle| \mathbf{e}_{n_1+\sigma_2(1)} \ \cdots \ \mathbf{e}_{n_1+\sigma_2(5)} \middle| \cdots \middle| \mathbf{e}_{n_1+n_2+n_3+\sigma_4(1)} \ \cdots \ \mathbf{e}_{n_1+n_2+n_3+\sigma_4(5)} \right], \tag{20}$$

where $\mathbf{e}_j \in \mathbb{R}^{n_1+n_2+n_3+n_4} = \mathbb{R}^{100}$ is the j-th element of the canonical basis of the real vector space $\mathbb{R}^{n_1+n_2+n_3+n_4} = \mathbb{R}^{100}$, and $\mathbf{S} \in \mathcal{M}_{(n_1+n_2+n_3+n_4)\times(v\cdot E)}(\mathbb{R})$ is the *selector* matrix. Basically, matrix $\mathbf{X}$ in Equation (19) has been built by randomly selecting $v = 5$ rows per structural state. The $\sum_{i=1}^{E}(n_i - v) = 80$ rows of matrix $\mathbf{X}[\Phi]$ that are not used to build the model are used for the validation.

In the i-th iteration, $i = 1, \ldots, \kappa$, the baseline data to build the model are the matrix:

$$\begin{aligned}
&\mathbf{X} = \mathbf{S}^\top \cdot \mathbf{X}[\Phi], \\
&\mathbf{S} = \Big[\mathbf{e}_{\sigma_1(5(i-1)+1)} \ \cdots \ \mathbf{e}_{\sigma_1(5(i-1)+5)} \Big| \mathbf{e}_{n_1+\sigma_2(5(i-1)+1)} \ \cdots \ \mathbf{e}_{n_1+\sigma_2(5(i-1)+5)} \Big| \cdots \\
&\qquad \cdots \Big| \ \mathbf{e}_{n_1+n_2+n_3+\sigma_4(5(i-1)+1)} \quad \cdots \quad \mathbf{e}_{n_1+n_2+n_3+\sigma_4(5(i-1)+5)} \ \Big]
\end{aligned}$$

where, as in Equation (19), $\mathbf{e}_j \in \mathbb{R}^{n_1+n_2+n_3+n_4} = \mathbb{R}^{100}$ is the j-th element of the canonical basis of the real vector space $\mathbb{R}^{n_1+n_2+n_3+n_4} = \mathbb{R}^{100}$ and, as in Equation (20), $\mathbf{S} \in \mathcal{M}_{(n_1+n_2+n_3+n_4)\times(v\cdot E)}(\mathbb{R})$ is the *selector* matrix. Since $\sum_{i=1}^{E}(n_i - v) = 80$ rows of matrix $\mathbf{X}[\Phi]$ will be used for the validation step and with respect to $\kappa = 5$ iterations, the sum of all the elements in the *confusion matrices* that we will present in Section 6 is equal to $\left(\sum_{i=1}^{E}(n_i - v)\right) \cdot \kappa = 400$.

5.5. Application of the Damage Detection and Classification Procedure

In this section, two strategies are presented to apply the damage detection and classification procedure. These two strategies are:

(1) the classification is based on a single matrix: $\mathbf{X}[1], \mathbf{X}[2], \mathbf{X}[3], \mathbf{X}[4]$ or $\mathbf{X}[1,2,3,4]$, as defined in Equations (17) and (18), respectively, with $\kappa-$fold non-exhaustive leave-p-out cross validation;

(2) the classification is based on the four matrices $\mathbf{X}[1], \mathbf{X}[2], \mathbf{X}[3]$ and $\mathbf{X}[4]$, defined in Equation (17), with respect to the four actuation phases, with $\kappa-$fold non-exhaustive leave-p-out cross validation. Each actuation phase will cast a vote and a final decision is taken.

In the first case, in a succinct way, the following seven steps are performed:

- **Step 1**. The data in matrix $\mathbf{X}$ are scaled using MCGS to define a new matrix $\check{\mathbf{X}}$.
- **Step 2**. PCA is applied to $\check{\mathbf{X}}$ to obtain the PCA model $\mathbf{P}$.
- **Step 3**. The number $\ell = D \in \mathbb{N}$ of principal components is chosen so that the proportion of variance explained is greater than or equal to 95%. Therefore, the reduced PCA model is $\mathbf{P}_\ell$.
- **Step 4**. A realization $\mathbf{z}^\top \in \mathbb{R}^{3\cdot 30001} = \mathbb{R}^{90003}$ —for $\mathbf{X}[1], \mathbf{X}[2], \mathbf{X}[3]$ and $\mathbf{X}[4]$— or $\mathbf{z}^\top \in \mathbb{R}^{4\cdot 90003} = \mathbb{R}^{360012}$ —for $\mathbf{X}[1,2,3,4]$— of the current structure to diagnose is needed. Then, vector $\mathbf{z}^\top$ is scaled as in Equation (14) to define $\check{\mathbf{z}}^\top$.
- **Step 5**. The data points set $\mathcal{X}$ is defined as:

$$\mathcal{X}' = \{\mathbf{x}^1, \ldots, \mathbf{x}^{20}, \mathbf{x}^{21}\} \subset \mathbb{R}^\ell,$$

where

$$\mathbf{x}^i = \mathbf{e}_i^\top \check{\mathbf{X}} \mathbf{P}_\ell,\ i = 1, \ldots, 20,$$
$$\mathbf{x}^{21} = \check{\mathbf{z}}^\top \mathbf{P}_\ell.$$

Subsequently, t-SNE is applied to this $\ell-$dimensional data set $\mathcal{X}'$ to find a collection of $2-$dimensional map points:

$$\mathcal{Y}' = \{\mathbf{y}^1, \ldots, \mathbf{y}^{20}, \mathbf{y}^{21}\} \subset \mathbb{R}^2.$$

- **Step 6**. $E = 4$ clusters are obtained, that are related to the $E = 4$ different structural states. These clusters are formed by the map points:

$$\{\mathbf{y}^1, \ldots, \mathbf{y}^5\} \subset \mathcal{Y}, \text{related to the } \textit{1st} \text{ structural state;}$$
$$\{\mathbf{y}^6, \ldots, \mathbf{y}^{10}\} \subset \mathcal{Y}, \text{related to the } \textit{2nd} \text{ structural state;}$$
$$\{\mathbf{y}^{11}, \ldots, \mathbf{y}^{15}\} \subset \mathcal{Y}, \text{related to the } \textit{3rd} \text{ structural state;}$$
$$\{\mathbf{y}^{16}, \ldots, \mathbf{y}^{20}\} \subset \mathcal{Y}, \text{related to the } \textit{4th} \text{ structural state.}$$

The centroid $\mathcal{Y}_l$, $l = 1, \ldots, E$, associated with the l-th structural state is computed as in Equation (16).

- **Step 7**. Finally, the current structure to diagnose is associated to the l-th structural state if

$$l = \arg \min_{l=1,\ldots,E} \|\mathcal{Y}_l - \mathbf{y}^{21}\|_2.$$

In the second case, we follow **Step 1** to **Step 6** above for the four matrices $\mathbf{X}[\varphi]$, $\varphi = 1, \ldots, 4$, related to the four actuation phases. With the information provided by the four actuation phases, several approaches can be considered to finally classify the structure that has to be diagnosed. One of these approaches, majority voting, is widely used in standard fusion schemes [28], as well as weighted majority vote or soft voting. For our case of the small aluminum plate, the majority voting will be used, as well as an approach based on the sum of the inverse distances between the centroids and the map point, which is somehow related to a weighted majority vote. Here are the details of both approaches:

- **Majority voting**. In this case, the strategy of the smallest point-centroid distance is performed four times, one per actuation phase. Therefore, four classifications are obtained for a single structure to diagnose. More precisely, each actuation phase acts as a *classifier*. Figure 6 illustrates this idea with respect to three actuation phases.

  The current structure to diagnose, in the φ-th actuation phase, $\varphi = 1, \ldots, 4$, is associated to the l_φ-th structural state if

$$l_\varphi = \arg \min_{l=1,\ldots,E} \|\mathcal{Y}_l^\varphi - \mathbf{y}_\varphi^{21}\|_2.$$

  It is worth remembering that $\mathbf{y}_\varphi^{21} \in \mathbb{R}^2$ is the map point associated to the realization of the current structure to diagnose. The structure is finally classified according to the most repeated classification. That is, the current structure to diagnose is associated to the l-th structural state if

$$l = \text{mode}\{l_1, l_2, l_3, l_4\},$$

in the case of a unimodal set. In the case of a bi-modal set, if the two modal values are l_α and l_β, the current structure to diagnose is associated to the l-th structural state if

$$l = \arg \min_{l \in \{l_\alpha, l_\beta\}} \sum_{\varphi=1}^{4} \| \mathcal{Y}_l^\varphi - \mathbf{y}_\varphi^{21} \|_2.$$

Finally, if the set $\{l_1, l_2, l_3, l_4\}$ is a set with no mode, the structure is associated to the l-th structural state if

$$l = \arg \min_{l=1,\ldots,E} \sum_{\varphi=1}^{4} \| \mathcal{Y}_l^\varphi - \mathbf{y}_\varphi^{21} \|_2.$$

- **Sum of the inverse distances**. In this case, for a given structural state, we sum the inverse of the distances between the centroids $\mathcal{Y}_l^\varphi$ and the map point $\mathbf{y}_\varphi^{21}$, for all the actuation phases $\varphi = 1, \ldots, 4$. The assigned structural state is the one that obtains the highest sum. More precisely, the current structure to diagnose is associated to the l-th structural state if

$$l = \arg \max_{l=1,\ldots,E} \sum_{\varphi=1}^{4} \frac{1}{\| \mathcal{Y}_l^\varphi - \mathbf{y}_\varphi^{21} \|_2}.$$

It is worth remarking that the arguments of the maxima of the sum of the inverse distances is equivalent to the arguments of the minima of the harmonic mean of these distances. More precisely, for a given structural state, the harmonic mean of the distances between the centroids $\mathcal{Y}_l^\varphi$ and the map point $\mathbf{y}_\varphi^{21}$, for all the actuation phases $\varphi = 1, \ldots, 4$ is

$$\frac{1}{\frac{1}{4} \sum_{\varphi=1}^{4} \frac{1}{\| \mathcal{Y}_l^\varphi - \mathbf{y}_\varphi^{21} \|_2}}.$$

Therefore,

$$l = \arg \max_{l=1,\ldots,E} \sum_{\varphi=1}^{4} \frac{1}{\| \mathcal{Y}_l^\varphi - \mathbf{y}_\varphi^{21} \|_2} = \arg \min_{l=1,\ldots,E} \frac{1}{\frac{1}{4} \sum_{\varphi=1}^{4} \frac{1}{\| \mathcal{Y}_l^\varphi - \mathbf{y}_\varphi^{21} \|_2}}.$$

S. Mehta et al. [29] also uses the harmonic distance to define a pattern classification technique similar to k-nearest neighbors classifier.

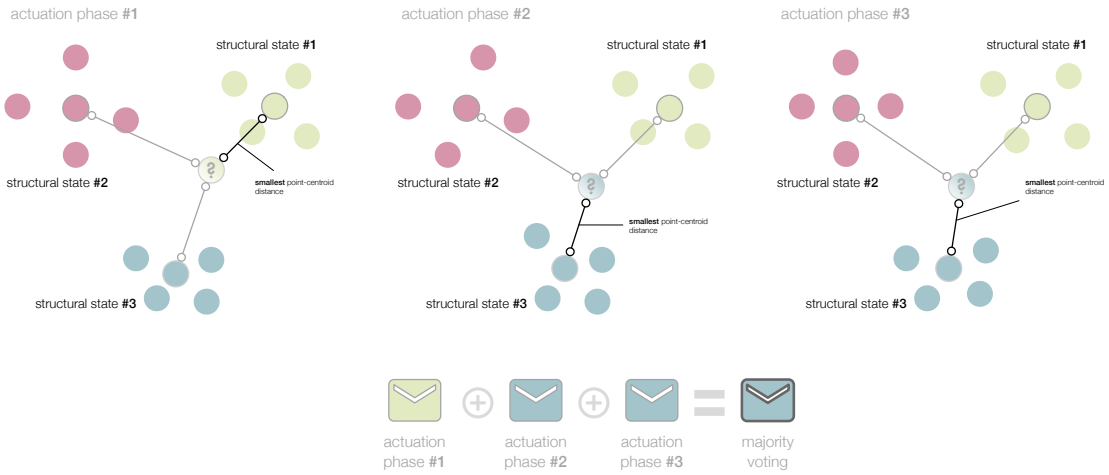

Figure 6. In the majority voting, the strategy of the smallest point-centroid distance is performed per actuation phase. The current structure to diagnose is associated to the most voted structural state.

6. Results

In this section, the results of the application of the damage detection and classification procedure, introduced in Sections 3 and 4 and detailed in Sections 5.3–5.5, to the aluminum plate are presented in terms of the confusion matrices and with respect to the scenarios defined in Section 5.2. The results for each scenario are presented in a different section. More precisely, in Section 6.1 the results with respect to **Scenario 1** are presented. Equivalently, Sections 6.2 and 6.3 present the results with respect to **Scenario 2** and **Scenario 3**, respectively. In the three scenarios, four different structural states have been considered:

- the first structural state corresponds to the healthy state of the structure, that is, the square aluminum plate with no damage, noted as $D0$;
- the second, third, and fourth structural states correspond to the plate with an added mass at the positions indicated in Figures 3 and 5, noted as $D1$, $D2$, and $D3$, respectively.

To validate the damage detection and classification detailed in Sections 5.3–5.5, we will perform five iterations ($\kappa = 5$) of a non-exhaustive leave-p-out cross validation, where $p = 80$, as described in Section 5.4. At each iteration, a total of 80 realizations have been considered, according to the following distribution: 20 realization per structural state ($D0, D1, D2$, and $D3$). Since 80 realizations have been used for the validation step and with respect to $\kappa = 5$ iterations, the sum of all the elements in the confusion matrices that we will present in Sections 6.1–6.3 is equal to $5 \cdot 80 = 400$.

Again, for the three scenarios, seven different confusion matrices are presented:

- **Actuation phase 1**. The damage detection and classification procedure is applied to a single matrix, $\mathbf{X}[1]$, as in Equation (17), using the smallest point-centroid distance.
- **Actuation phase 2**. The damage detection and classification procedure is applied to a single matrix, $\mathbf{X}[2]$, as in Equation (17), using the smallest point-centroid distance.
- **Actuation phase 3**. The damage detection and classification procedure is applied to a single matrix, $\mathbf{X}[3]$, as in Equation (17), using the smallest point-centroid distance.
- **Actuation phase 4**. The damage detection and classification procedure is applied to a single matrix, $\mathbf{X}[4]$, as in Equation (17), using the smallest point-centroid distance.

- **Actuation phases 1–4**. The damage detection and classification procedure is applied to a single matrix, i.e., the horizontal concatenation of the four matrices $X[\varphi],\ \varphi = 1,\ldots,4$, $\mathbf{X}[1,2,3,4]$, as in Equation (18), using the smallest point-centroid distance.
- **Majority voting**. The damage detection and classification procedure is applied to the four $X[\varphi]$, $\varphi = 1,\ldots,4$. Each actuation phase casts a vote, and a final decision is taken based on majority voting (Section 5.5).
- **Sum of the inverse distances**. The damage detection and classification procedure is applied to the four $X[\varphi],\ \varphi = 1,\ldots,4$. Each actuation phase casts a vote and a final decision is taken based on the maximum sum of the inverse distances (Section 5.5).

Finally, in some cases, and with the purpose of comparing the performance of the current damage detection and classification approach, confusion matrices in the frequency and time domains have been included.

As an illustrating example, we have included in Figure 7 the clusters formed by the different structural states described in this section and in the case of Scenario 3. In this figure, the diamond represents the structure to diagnose. It can be clearly observed how the diamond is close to the cluster related to damage 3.

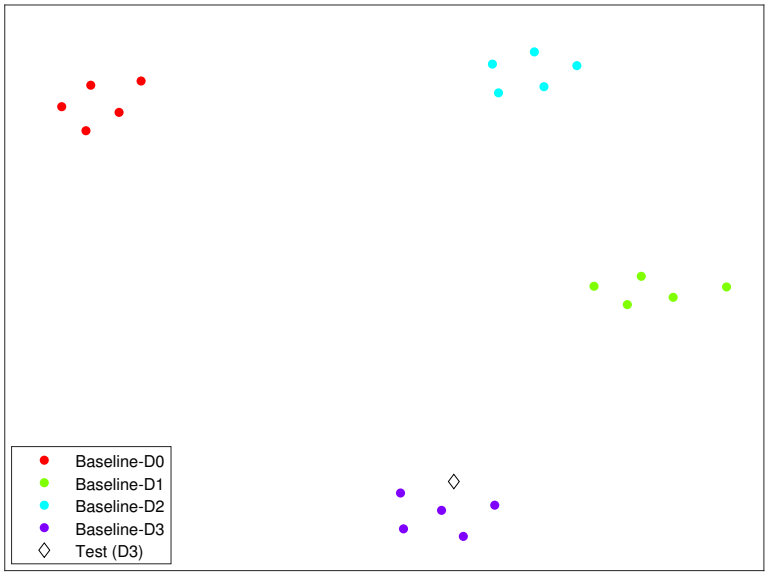

Figure 7. Clusters formed by the different structural states described in Section 6, for Scenario 3. The diamond represents the structure to diagnose.

6.1. Scenario 1

In this section, the results with respect to **Scenario 1** are presented. It is worth noting that, in this scenario, a short wire has been used, and the measured signals are filtered with a SG algorithm. The seven confusion matrices can be found in Tables 1 and 2. When the decision is based on a single actuation phase (Table 1), the overall accuracy is quite good. More precisely, with 397 in the actuation phase 1, 399 in the actuation phase 2, 395 in the actuation phase 3, and 397 in the actuation phase 4, realizations have been correctly classified out of 400 cases, which represents an overall accuracy of 99.25%, 99.75%, 98.75%, and 99.25%, respectively. When the four actuation phases are used at the same time (actuation phases 1–4, Equation (18), majority voting, and sum of the inverse distances), an overall accuracy of 99–100% is achieved, as it can be observed from Table 2.

Table 1. Confusion matrix of the application of the *t*-SNE based damage detection and classification procedure presented in Sections 3 and 4 to the case of the aluminum plate in **Scenario 1**, in the **frequency domain**. Rows represent true values, while columns represent predicted values.

	Actuation Phase 1				**Actuation Phase** 2				**Actuation Phase** 3				**Actuation Phase** 4			
	D0	***D1***	***D2***	***D3***	***D0***	***D1***	***D2***	***D3***	***D0***	***D1***	***D2***	***D3***	***D0***	***D1***	***D2***	***D3***
*D*0	97	0	2	1	100	0	0	0	100	0	0	0	100	0	0	0
*D*1	0	100	0	0	0	100	0	0	0	100	0	0	0	100	0	0
*D*2	0	0	100	0	0	0	100	0	3	0	96	1	0	0	98	2
*D*3	0	0	0	100	0	0	1	99	1	0	0	99	0	0	1	99

*D*0 (healthy state of the structure); *D*1, *D*2, and *D*3 (added masses at the positions indicated in Figures 3 and 5).

Table 2. Confusion matrix of the application of the *t*-SNE based damage detection and classification procedure presented in Sections 3 and 4 to the case of the aluminum plate in **Scenario 1**, when the four actuation phases are used at the same time, in the **frequency domain**. Rows represent true values, while columns represent predicted values.

	Phases 1–4				**Majority Voting**				**Inverse Distances**			
	D0	***D1***	***D2***	***D3***	***D0***	***D1***	***D2***	***D3***	***D0***	***D1***	***D2***	***D3***
*D*0	100	0	0	0	100	0	0	0	100	0	0	0
*D*1	0	99	1	0	0	100	0	0	0	100	0	0
*D*2	1	0	99	0	0	0	100	0	0	0	100	0
*D*3	0	0	0	100	0	0	0	100	0	0	0	100

*D*0 (healthy state of the structure); *D*1, *D*2, and *D*3 (added masses at the positions indicated in Figures 3 and 5).

6.2. Scenario 2

In this section, the results with respect to **Scenario 2** are presented. In this case, a short wire has been used but the measured signals are not filtered. The seven confusion matrices can be found in Tables 3 and 4. When the decision is based on a single actuation phase (Table 3), the overall accuracy is very remarkable. More precisely, with respect to actuation phase 1, 2, and 3, 400 realizations have been correctly classified out of 400 cases, which represents an overall accuracy of 100%. With respect to actuation phase 4, 399 realizations have been correctly classified out of 400 cases, that is to say, an overall accuracy of 99.75%. When the four actuation phases are used at the same time (actuation phases 1–4, Equation (18), majority voting, and sum of the inverse distances), an overall accuracy of 100% is achieved, as it can be observed from Table 4.

Table 3. Confusion matrix of the application of the *t*-SNE based damage detection and classification procedure presented in Sections 3 and 4 to the case of the aluminum plate in **Scenario 2**, in the **frequency domain**. Rows represent true values, while columns represent predicted values.

	Actuation Phase 1				**Actuation Phase** 2				**Actuation Phase** 3				**Actuation Phase** 4			
	D0	***D1***	***D2***	***D3***	***D0***	***D1***	***D2***	***D3***	***D0***	***D1***	***D2***	***D3***	***D0***	***D1***	***D2***	***D3***
*D*0	100	0	0	0	100	0	0	0	100	0	0	0	100	0	0	0
*D*1	0	100	0	0	0	100	0	0	0	100	0	0	0	100	0	0
*D*2	0	0	100	0	0	0	100	0	0	0	100	0	0	0	100	0
*D*3	0	0	0	100	0	0	0	100	0	0	0	100	0	0	1	99

*D*0 (healthy state of the structure); *D*1, *D*2, and *D*3 (added masses at the positions indicated in Figures 3 and 5).

Table 4. Confusion matrix of the application of the *t*-SNE based damage detection and classification procedure presented in Sections 3 and 4 to the case of the aluminum plate in **Scenario 2**, when the four actuation phases are used at the same time, in the **frequency domain**. Rows represent true values, while columns represent predicted values.

	Phases 1–4				**Majority Voting**				**Inverse Distances**			
	D0	***D1***	***D2***	***D3***	***D0***	***D1***	***D2***	***D3***	***D0***	***D1***	***D2***	***D3***
D0	100	0	0	0	100	0	0	0	100	0	0	0
D1	0	100	0	0	0	100	0	0	0	100	0	0
D2	0	0	100	0	0	0	100	0	0	0	100	0
D3	0	0	0	100	0	0	0	100	0	0	0	100

D0 (healthy state of the structure); *D1*, *D2*, and *D3* (added masses at the positions indicated in Figures 3 and 5).

6.3. Scenario 3

The results with respect to **Scenario 3** are finally presented in this section. In the two previous scenarios, a short wire was used. However, in this case, the signals are acquired using a 2.5 m long wire. Tables 5 and 6 include the seven confusion matrices. When the decision is based on a single actuation phase (Table 5), the overall accuracy is quite good, too. More precisely, with 384 in the actuation phase 1, 395 in the actuation phase 2, 395 in the actuation phase 3, and 398 in the actuation phase 4, realizations have been correctly classified, which represents an overall accuracy of 96%, 98.75%, 98.75%, and 99.5%, respectively. When the four actuation phases are used at the same time (actuation phases 1–4, Equation (18), majority voting, and sum of the inverse distances), an overall accuracy of 99.5–100% is achieved, as it can be observed from Table 6.

Table 5. Confusion matrix of the application of the *t*-SNE based damage detection and classification procedure presented in Sections 3 and 4 to the case of the aluminum plate in **Scenario 3**, in the **frequency domain**. Rows represent true values, while columns represent predicted values.

	Actuation Phase 1				**Actuation Phase 2**				**Actuation Phase 3**				**Actuation Phase 4**			
	D0	***D1***	***D2***	***D3***	***D0***	***D1***	***D2***	***D3***	***D0***	***D1***	***D2***	***D3***	***D0***	***D1***	***D2***	***D3***
D0	98	2	0	0	99	0	1	0	100	0	0	0	100	0	0	0
D1	6	90	2	2	0	99	1	0	0	95	5	0	1	99	0	0
D2	1	1	97	1	0	1	97	2	0	0	100	0	0	0	100	0
D3	0	1	0	99	0	0	0	100	0	0	0	100	0	0	1	99

D0 (healthy state of the structure); *D1*, *D2*, and *D3* (added masses at the positions indicated in Figures 3 and 5).

Table 6. Confusion matrix of the application of the *t*-SNE based damage detection and classification procedure presented in Sections 3 and 4 to the case of the aluminum plate in **Scenario 3**, when the four actuation phases are used at the same time, in the **frequency domain**. Rows represent true values, while columns represent predicted values.

	Phases 1–4				**Majority Voting**				**Inverse Distances**			
	D0	***D1***	***D2***	***D3***	***D0***	***D1***	***D2***	***D3***	***D0***	***D1***	***D2***	***D3***
D0	100	0	0	0	100	0	0	0	100	0	0	0
D1	0	99	0	1	0	100	0	0	0	100	0	0
D2	0	1	99	0	0	0	100	0	0	0	100	0
D3	0	0	0	100	0	0	0	100	0	0	0	100

D0 (healthy state of the structure); *D1*, *D2*, and *D3* (added masses at the positions indicated in Figures 3 and 5).

The potential of the approaches where the four actuation phases are used can be observed in this last scenario, see Table 6:

- When the four actuation phases are merged in a single matrix as in Equation (18), 398 realizations have been correctly classified out of 400 cases, which represents an overall accuracy of 99.5%.
- When each actuation phase casts a vote and a final decision is taken based on majority voting, the overall accuracy is increased to 100%.
- Finally, when each actuation phase casts a vote and a final decision is taken based on the maximum sum of the inverse distances, the overall accuracy is increased to 100%, too.

In addition, in this scenario, the results in the frequency domain are compared to those in the time domain [11]. In the time domain, when the decision is based on a single actuation phase (Table 7), with 244 in the actuation phase 1, 398 in the actuation phase 2, 280 in the actuation phase 3, and 277 in the actuation phase 4, realizations have been correctly classified out of 400 cases. This represents an overall accuracy of 61%, 99.5%, 70%, and 69.25%, respectively. Clearly, the strategy in the frequency domain, i.e., the overall accuracy fluctuates between 96% and 99.5%, outperforms the approach in the time domain. In addition, the false positive rate (FPR), i.e., the number of false positives with respect to the total number of negatives, and the false negative rate (FNR), i.e., the number of false negatives with respect to the total number of positives, are clearly unsatisfactory in the time domain. However, FPR and FNR are significantly reduced to values close to 0% in the frequency domain. It is worth noting that in the computation of the FNR, the three different types of damage $D1$, $D2$, and $D3$ are considered as a single category, just the opposite of the healthy state of the structure. In the time domain, when the four actuation phases are used at the same time (Table 8), the overall accuracy is of 88.5% in actuation phases 1–4, of 91.25% in majority voting, and of 97% in sum of the inverse distances, whereas the overall accuracy is increased to 99.5%, 100%, and 100%, respectively, in the frequency domain. At the same time, FPR and FNR are reduced to 0% in the frequency domain, while they are slightly increased in the time domain. All this is an indication of the better quality of the clusters created in the frequency domain than the ones created in the time domain. Table 9 summarizes the values for the overall accuracy, the FPR, and the FNR in this scenario and in the time and frequency domains.

Table 7. Confusion matrix of the application of the *t*-SNE based damage detection and classification procedure presented in Sections 3 and 4 to the case of the aluminum plate in textbfScenario 3, in the **time domain**. Rows represent true values, while columns represent predicted values.

	Actuation Phase 1				**Actuation Phase** 2				**Actuation Phase** 3				**Actuation Phase** 4			
	D0	***D1***	***D2***	***D3***	***D0***	***D1***	***D2***	***D3***	***D0***	***D1***	***D2***	***D3***	***D0***	***D1***	***D2***	***D3***
*D*0	50	6	19	25	100	0	0	0	93	1	3	3	53	21	1	25
*D*1	19	66	11	4	0	100	0	0	16	50	23	11	17	61	2	20
*D*2	14	3	73	10	0	1	98	1	5	19	70	6	5	3	76	16
*D*3	15	9	21	55	0	0	0	100	0	23	10	67	10	3	0	87

*D*0 (healthy state of the structure); *D*1, *D*2, and *D*3 (added masses at the positions indicated in Figures 3 and 5).

Table 8. Confusion matrix of the application of the *t*-SNE based damage detection and classification procedure presented in Sections 3 and 4 to the case of the aluminum plate in **Scenario 3**, when the four actuation phases are used at the same time, in the **time domain**. Rows represent true values, while columns represent predicted values.

	Phases 1–4				**Majority voting**				**Inverse distances**			
	D0	***D1***	***D2***	***D3***	***D0***	***D1***	***D2***	***D3***	***D0***	***D1***	***D2***	***D3***
*D*0	86	1	7	6	98	0	0	2	99	0	1	0
*D*1	8	88	4	0	12	85	2	1	1	99	0	0
*D*2	1	8	89	2	6	2	90	2	1	1	95	3
*D*3	3	4	2	91	0	3	5	92	1	2	2	95

*D*0 (healthy state of the structure); *D*1, *D*2, and *D*3 (added masses at the positions indicated in Figures 3 and 5).

Table 9. Overall accuracy, false positive rate (FPR) and false negative rate (FNR) of the application of the *t*-SNE-based damage detection and classification procedure presented in Sections 3 and 4 to the case of the aluminum plate in **Scenario 3**, when the four actuation phases are used separately and at the same time, in both domains, time and frequency.

	Accuracy		**FPR**		**FNR**	
	Time	**Frequency**	**Time**	**Frequency**	**Time**	**Frequency**
Actuation phase 1	61.0%	96.0%	50.0%	2.0%	16.0%	2.3%
Actuation phase 2	99.5%	98.8%	0.0%	1.0%	0.0%	0.0%
Actuation phase 3	70.0%	98.8%	7.0%	0.0%	7.0%	0.0%
Actuation phase 4	69.3%	99.5%	47.0%	0.0%	10.7%	0.3%
Phases 1-4	88.5%	99.5%	14.0%	0.0%	4.0%	0.0%
Majority voting	91.3%	100.0%	2.0%	0.0%	6.0%	0.0%
Inverse distances	97.0%	100.0%	1.0%	0.0%	1.0%	0.0%

6.4. General Comments

The results presented in Sections 6.1–6.3 reveal that it is better to make a decision considering all of the actuation phases (assembling theses phases or using them to cast a vote) rather than working with the phases separately. On the other hand, the results also show that both strategies majority voting and sum of the inverse distances slightly outperform the horizontal concatenation of the four actuation phases in the frequency domain. However, in the time domain (**Scenario 3**, Table 8), the results reveal (i) the strong performance of the sum of the inverse distances strategy, which clearly classifies the practical totality of the kinds of damage that we have considered, compared to majority voting or the horizontal concatenation of the four actuation phases; and (ii) that the majority voting outperforms the horizontal concatenation of the four actuation phases, but it cannot completely classify damage *D*1.

It is worth noting that, in general, the healthy state of the structure is confused with the structure with damage in just a few cases. Similarly, the structure with damage is identified as a structure with no damage in a very limited number of realizations.

In general, the performance of the proposed methodology is very satisfactory when the signals are acquired using a short wire, with or without adding white Gaussian noise. In these two cases, using PCA as a pre-processing step, the noise is canceled. The third scenario presents the worst case because it used a long cable (2.5 m) from the digitizers to the sensors. In this scenario, the signals were badly digitized due to the impedance of the cable, the low voltage of the stimulus, and other experimental features. Therefore, it can be observed that the use of a long cable from the digitizer to the sensors affects in the detection and classification method. However, combining the four actuation phases with

(i) the sum of the inverse distances strategy, in the time domain; or
(ii) the majority voting strategy or the sum of the inverse distances strategy, in the frequency domain,

very accurate results can be obtained.

It should be noted that, in general, it is better to work in the frequency domain than in the time domain because the obtained results are significantly improved, as it can be clearly observed in the third scenario.

7. Conclusions

In this work, a SHM strategy for detection and classification of structural changes based on a two-step data integration (type *E* unfolding and MCGS), data transformation using PCA, and a two-step data reduction combining PCA and *t*-SNE has been proposed. The proposed approach is evaluated using experimental data. In general, the results obtained show that the performance of the proposed methodology is very satisfactory, given its high classification accuracy; and its behavior is very good and similar in all the data sets.

In the case study, very accurate results are obtained with or without adding white Gaussian noise, since PCA cancels the noise. However, the use of a long wire (2.5 m) from the digitizers to the sensors negatively affects the detection and classification method. But combining the four actuation phases with the sum of the inverse distances strategy, in the time domain, and with the majority voting strategy or the sum of the inverse distances strategy, in the frequency domain, accurate results can be obtained. Results also show that the quality of the two-dimensional clusters created with *t*-SNE in the frequency domain is better than the quality of the two-dimensional clusters created with *t*-SNE in the time domain, thus leading to a better classification. Therefore, the strategy in the frequency domain significantly outperforms the approach in the time domain.

Some aspects to highlight in the proposed methodology are: the *t*-SNE technique has been extended and adapted to the field of SHM, in the detection and classification of structural changes; the method classifies the current state of the structure by means of a data-driven analysis, that is, using collected data from the structure under different structural states and without the use of complex mathematical models; it is better to make a decision considering all of the actuation phases (assembling theses phases or using them to cast a vote) rather than working with the phases separately; both strategies, majority voting and sum of the inverse distances, slightly outperform the horizontal concatenation of the four actuation phases in the frequency domain; in the time domain, sum of the inverse distances strategy outperforms majority voting, and this last strategy outperforms the horizontal concatenation of the four actuation phases; it is better to work in the frequency domain than in the time domain because better results are obtained; and finally, in general, the healthy state of the structure is confused with the structure with damage in just a few cases, and similarly, the structure with damage is identified as a structure with no damage in a very limited number of realizations. With respect to the possible fields of application, similar aluminum plates have been used to represent parts of a plane (wings or fuselage). We think that we can also apply this approach for the damage and fault detection of wind turbines. In general, there is no a prescribed field of application: if a sensor network can be installed in a structure, and several actuation phases can be considered, the proposed approach can be implemented a priori.

As a future work, we plan to develop further the proposed method for different EOC to determine its effectiveness, as well as to handle imbalanced data. In addition, we aim to investigate the parametric version of *t*-SNE.

Author Contributions: D.A. and F.P. developed the idea and designed the exploration framework; D.A. developed the algorithms; F.P. supervised the results of the validation; D.A. and F.P. drafted the manuscript.

Funding: This work has been partially funded by the Spanish Agencia Estatal de Investigación (AEI) - Ministerio de Economía, Industria y Competitividad (MINECO), and the Fondo Europeo de Desarrollo Regional (FEDER) through

the research project DPI2017-82930-C2-1-R; and by the Generalitat de Catalunya through the research project 2017 SGR 388.

Acknowledgments: We gratefully acknowledge the support of NVIDIA Corporation with the donation of the Titan Xp GPU used for this research. We thank the Universitat Politècnica de Catalunya (UPC) for pre-doctoral fellowship (to David Agis). We also thank Jaime Vitola and Diego A. Tibaduiza for useful discussions with respect to the experimental set-up.

Conflicts of Interest: The authors declare no conflict of interest.

Nomenclature

$\mathcal{X}$	High-dimensional data set.
$\mathcal{X}'$	High-dimensional data set including the data point to diagnose.
$\mathcal{Y}$	Low-dimensional map points.
$\mathcal{Y}'$	Low-dimensional map points including the map point to diagnose.
$\mathcal{Y}_l$	Centroid associated with the l-th structural state.
$\mathcal{P}$	Similarity matrix for the high-dimensional data points.
$\mathcal{Q}$	Similarity matrix for the low-dimensional map points.
$\mathcal{C}$	KL divergence.
η	Learning rate.
$\alpha(t)$	Momentum term at iteration t.
p	Perplexity.
$\mathbf{X}$	Matrix that collects all the realizations under different structural states.
$\check{\mathbf{X}}$	Scaled original —in the frequency domain— data matrix.
N	Number of sensors.
L	Number of components in each signal.
E	Number of different structural states.
$\mathbf{C}_{\check{\mathbf{X}}}$	Covariance matrix of $\check{\mathbf{X}}$.
λ_k	Eigenvalues.
ρ_k	Eigenvectors.
Λ	Eigenvalues in a diagonal matrix.
$\mathbf{P}$	PCA model (full case).
$\mathbf{P}_\ell$	PCA model (reduced).
$\mathbf{T}$	Projection of the scaled data set $\check{\mathbf{X}}$ into the subspace spanned by the PCA model.
$\mathbf{e}_i$	i-th element of the canonical basis.
$\mathbf{z}$	Current original —in the frequency domain— data vector to diagnose.
$\check{\mathbf{z}}$	Current scaled original —in the frequency domain— data vector to diagnose.
φ	φ-th actuation phase.
$\mathbf{S}$	Selector matrix

Abbreviations

CM	Condition monitoring
EOC	Environmental and operational conditions
FFT	Fast Fourier transform
FNR	False negative rate
FPR	False positive rate
KL	Kullback-Leibler
MCGS	Mean-centered group scaling
PCA	Principal component analysis

PZT	Piezoelectric transducer
SG	Savitzky–Golay
SHM	Structural health monitoring
SNE	Stochastic neighbor embedding
t-SNE	*t*-distributed stochastic neighbor embedding

References

1. Rolfes, R.; Zerbst, S.; Haake, G.; Reetz, J.; Lynch, J.P. Integral SHM-system for offshore wind turbines using smart wireless sensors. In Proceedings of the 6th International Workshop on Structural Health Monitoring, Stanford, CA, USA, 11–13 September 2007; pp. 11–13.
2. Ciang, C.C.; Lee, J.R.; Bang, H.J. Structural health monitoring for a wind turbine system: A review of damage detection methods. *Meas. Sci. Technol.* **2008**, *19*, 122001. [CrossRef]
3. Loh, C.H.; Loh, K.J.; Yang, Y.S.; Hsiung, W.Y.; Huang, Y.T. Vibration-based system identification of wind turbine system. *Struct. Control Health Monit.* **2017**, *24*, e1876. [CrossRef]
4. Raju, K.S.; Pratap, Y.; Sahni, Y.; Babu, M.N. Implementation of a WSN system towards SHM of civil building structures. In Proceedings of the IEEE 9th International Conference on Intelligent Systems and Control (ISCO), Coimbatore, India, 9–10 January 2015; pp. 1–7.
5. Blanco, H.; Boffill, Y.; Lombillo, I.; Villegas, L. An integrated structural health monitoring system for determining local/global responses of historic masonry buildings. *Struct. Control Health Monit.* **2018**, *25*, e2196. [CrossRef]
6. Nisha, M. Structural health monitoring of aircraft wing using wireless network. *Int. J. Technol. Explor. Learn. Www. Ijtel. Org Struct* **2014**, *3*, 341–343.
7. Ochôa, P.; Groves, R.M.; Benedictus, R. Systematic multiparameter design methodology for an ultrasonic health monitoring system for full-scale composite aircraft primary structures. *Struct. Control Health Monit.* **2019**, *26*, e2340. [CrossRef]
8. Ward, M.O.; Grinstein, G.; Keim, D.*Interactive Data Visualization: Foundations, Techniques, and Applications*; AK Peters/CRC Press: Boca Raton, FL, USA, 2015.
9. Tenenbaum, J.B.; De Silva, V.; Langford, J.C. A global geometric framework for nonlinear dimensionality reduction. *Science* **2000**, *290*, 2319–2323. [CrossRef]
10. van der Maaten, L.; Hinton, G. Visualizing data using t-SNE. *J. Mach. Learn. Res.* **2008**, *9*, 2579–2605.
11. Agis, D.; Pozo, F. Detection and classification of structural changes using t-distributed stochastic neighbor embedding. In Proceedings of the International Conference on Structural Engineering Dynamics, Viana do Castelo, Portugal, 24–26 June 2019; pp. 1–10.
12. Tsogka, C.; Daskalakis, E.; Comanducci, G.; Ubertini, F. The stretching method for vibration-based structural health monitoring of civil structures. *Comput. Aided Civ. Infrastruct. Eng.* **2017**, *32*, 288–303. [CrossRef]
13. Xu, F.; Song, X.; Tsui, K.L.; Yang, F.; Huang, Z. Bearing performance degradation assessment based on ensemble empirical mode decomposition and affinity propagation clustering. *IEEE Access* **2019**, *7*, 54623–54637. [CrossRef]
14. Cheng, Y.; Zhu, H.; Hu, K.; Wu, J.; Shao, X.; Wang, Y. Multisensory data-driven health degradation monitoring of machining tools by generalized multiclass support vector machine. *IEEE Access* **2019**, *7*, 47102–47113. [CrossRef]
15. Westerhuis, J.A.; Kourti, T.; MacGregor, J.F. Comparing alternative approaches for multivariate statistical analysis of batch process data. *J. Chemom. A J. Chemom. Soc.* **1999**, *13*, 397–413. [CrossRef]
16. Mujica, L.; Rodellar, J.; Fernandez, A.; Güemes, A. Q-statistic and T2-statistic PCA-based measures for damage assessment in structures. *Struct. Health Monit.* **2011**, *10*, 539–553. [CrossRef]
17. Vidal, Y.; Pozo, F.; Tutivén, C. Wind turbine multi-fault detection and classification based on SCADA data. *Energies* **2018**, *11*, 3018. [CrossRef]
18. Sikdar, S.; Kundu, A.; Jurek, M.; Ostachowicz, W. Nondestructive analysis of debonds in a composite structure under variable temperature conditions. *Sensors* **2019**, *19*, 3454. [CrossRef]
19. Yan, J.; Jin, H.; Sun, H.; Qing, X. Active monitoring of fatigue crack in the weld zone of bogie frames using ultrasonic guided waves. *Sensors* **2019**, *19*, 3372. [CrossRef]

20. Cho, H.; Hasanian, M.; Shan, S.; Lissenden, C.J. Nonlinear guided wave technique for localized damage detection in plates with surface-bonded sensors to receive Lamb waves generated by shear-horizontal wave mixing. *NDT E Int.* **2019**, *102*, 35–46. [CrossRef]
21. Jiménez, A.A.; Muñoz, C.Q.G.; Márquez, F.P.G. Dirt and mud detection and diagnosis on a wind turbine blade employing guided waves and supervised learning classifiers. *Reliab. Eng. Syst. Saf.* **2019**, *184*, 2–12. [CrossRef]
22. Hinton, G.; Roweis, S.T. Stochastic neighbor embedding. *Adv. Neural Inf. Process. Syst.* **2003**, 15, 857–864.
23. Min, R. *A Non-Linear Dimensionality Reduction Method for Improving Nearest Neighbour Classification*; University of Toronto: Toronto, ON, Canada, 2005.
24. Pozo, F.; Vidal, Y.; Salgado, Ó. Wind turbine condition monitoring strategy through multiway PCA and multivariate inference. *Energies* **2018**, *11*, 749. [CrossRef]
25. Orfanidis, S.J. *Introduction to Signal Processing*; Prentice-Hall, Inc.: Upper Saddle River, NJ, USA, 1995.
26. Vitola, J.; Pozo, F.; Tibaduiza, D.A.; Anaya, M. A sensor data fusion system based on *k*-nearest neighbor pattern classification for structural health monitoring applications. *Sensors* **2017**, *17*, 417. [CrossRef]
27. Vitola, J.; Pozo, F.; Tibaduiza, D.A.; Anaya, M. Distributed piezoelectric sensor system for damage identification in structures subjected to temperature changes. *Sensors* **2017**, *17*, 1252. [CrossRef] [PubMed]
28. Tardy, B.; Inglada, J.; Michel, J. Assessment of optimal transport for operational land-cover mapping using high-resolution satellite images time series without reference data of the mapping period. *Remote Sens.* **2019**, *11*, 1047. [CrossRef]
29. Mehta, S.; Shen, X.; Gou, J.; Niu, D. A new nearest centroid neighbor classifier based on *k* local means using harmonic mean distance. *Information* **2018**, *9*, 234. [CrossRef]

sensors

MDPI

Article

Vibration-Based Structural Health Monitoring Using Piezoelectric Transducers and Parametric *t*-SNE

David Agis and Francesc Pozo *

Control, Modeling, Identification, and Applications (CoDAlab), Department of Mathematics, Escola d'Enginyeria de Barcelona Est (EEBE), Universitat Politècnica de Catalunya (UPC), Campus Diagonal-Besòs (CDB), Eduard Maristany, 16, 08019 Barcelona, Spain; david.agis@upc.edu

* Correspondence: francesc.pozo@upc.edu; Tel.: +34-934-137-316

Received: 12 February 2020; Accepted: 17 March 2020; Published: 19 March 2020

Abstract: In this paper, we evaluate the performance of the so-called parametric *t*-distributed stochastic neighbor embedding (P-*t*-SNE), comparing it to the performance of the *t*-SNE, the non-parametric version. The methodology used in this study is introduced for the detection and classification of structural changes in the field of structural health monitoring. This method is based on the combination of principal component analysis (PCA) and P-*t*-SNE, and it is applied to an experimental case study of an aluminum plate with four piezoelectric transducers. The basic steps of the detection and classification process are: (i) the raw data are scaled using mean-centered group scaling and then PCA is applied to reduce its dimensionality; (ii) P-*t*-SNE is applied to represent the scaled and reduced data as 2-dimensional points, defining a cluster for each structural state; and (iii) the current structure to be diagnosed is associated with a cluster employing two strategies: (a) majority voting; and (b) the sum of the inverse distances. The results in the frequency domain manifest the strong performance of P-*t*-SNE, which is comparable to the performance of *t*-SNE but outperforms *t*-SNE in terms of computational cost and runtime. When the method is based on P-*t*-SNE, the overall accuracy fluctuates between 99.5% and 99.75%.

Keywords: classification; detection; parametric *t*-distributed stochastic neighbor embedding (P-*t*-SNE); piezoelectric transducers (PZTs); principal component analysis (PCA); structural health monitoring (SHM); vibration-based SHM

1. Introduction

In structural health monitoring (SHM), an important process for engineering structures, many methods have been applied for damage detection. In [1], the use of the Treed Gaussian Process model—a class of powerful switching response surface model—is illustrated in the context of the SHM of bridges. In [2], a SHM methodology, based on the system-identification techniques, is proposed to quantify the structural degradation in laminated composite booms used in satellite application. In [3], it is casted SHM in the context of statistical pattern recognition, and damage or structural changes are detected using two techniques based on time series analysis. In [4], three optimization-algorithm based support vector machines for damage detection in SHM are presented, which are expected to help engineers to process high-dimensional data.

Real-world datasets usually have high dimensionality, and their dimensionality may need to be reduced to facilitate data processing. Dimensionality reduction is the process of reducing the number of high-dimensional variables by obtaining a low-dimensional set of variables. This reduced representation must correspond to the intrinsic information of the data. Dimensionality reduction is very important, because it alleviates undesired properties of high-dimensional spaces, such as "the curse of dimensionality" [5]. In the literature, various dimensionality reduction methods have been

proposed: (i) linear methods, such as principal component analysis (PCA) [6,7] and linear discriminant analysis (LDA) [8,9], and (ii) nonlinear methods, such as isometric mapping (ISOMAP) [10,11] and the non-parametric version of t-distributed stochastic neighbor embedding (t-SNE) [12].

In general, real-world data are likely to be highly nonlinear. Therefore, unsupervised nonlinear dimensionality reduction techniques are widely used in many applications for pattern recognition or classification [13,14], visualization [15,16], and compression [17] of big datasets. Among these types of techniques, t-SNE is extensively adopted. However, this method is not designed to support the incorporation of out-of-sample data—that is, the embedding of new data. To avoid this problem, the so-called parametric t-SNE (P-t-SNE) method [18] was proposed. This method uses a neural network (NN) to learn an explicit parametric mapping function from a high-dimensional data space to a low-dimensional space. Thus, P-t-SNE can incorporate out-of-sample data. Another advantage of P-t-SNE is that it can be applied to large-scale datasets, while t-SNE can only be applied to datasets with a size not greater than the order of thousands.

To address the above-mentioned problems of t-SNE, in this work, we propose a strategy that combines PCA and P-t-SNE to detect and classify damage to structures to diagnose. This combination is much better than a combination of PCA with t-SNE: the proposed method achieves similar embedding performance but with a much lower computational cost and runtime. This was confirmed by our experimental results on an aluminum plate instrumented with four piezoelectric transducers (PZTs). Therefore, the aims of this paper are (i) to compare two approaches (P-t-SNE versus t-SNE) and (ii) to identify the advantages of the parametric version. To do this, we will use scenarios 1 and 3 from [19], because these two scenarios are two extreme cases. In addition, we will approach the damage detection and classification problem in the frequency domain, as recommended in the same paper [19]. The final classification of the current state of the structure is based on two different voting systems: the so-called majority voting and the sum of the inverse distances [19].

The contributions of this study are summarized in the following list. These contributions mainly refer to the data preprocessing, divided into three parts: data integration, data transformation, and data reduction.

1. Data preprocessing: Data integration. According to [20], there are six different ways to arrange the raw data collected by multiple sensors that collected measurements for several seconds in different experiments. The type of integration of raw data affects the posterior analysis. In this work, we have considered type-E unfolding.
2. Data preprocessing: Data normalization. The second step, before data transformation, is the data normalization. We perform the mean-centered group scaling (MCGS), as detailed in [21].
3. Data preprocessing: Data transformation. We build the PCA model ($\mathbf{P}$) so that the normalized data $\check{\mathbf{X}}$ are transformed into the projected data $\mathbf{T} = \check{\mathbf{X}}\mathbf{P}$. Notably, matrices $\check{\mathbf{X}}$ and $\mathbf{T}$ have equal dimensions; hence, no reduction is performed at this stage.
4. Data preprocessing: Data reduction (phase I). We use PCA for the data reduction. The number of principal components $\ell \in \mathbb{N}$ is chosen so that the proportion of the variance explained is greater than or equal to 95%.
5. Data preprocessing: Data reduction (phase II). We now propose P-t-SNE, avoiding the limitations of t-SNE, as a second phase to reduce the dimensionality from ℓ to 2. This is one of the first approaches that use P-t-SNE in the field of SHM.
6. Data postprocessing: Classification. For the classification, we propose the majority voting and the sum of the inverse distances, where each actuation phase casts a vote.

As a summary, the contribution of the present work is, precisely, the combination of existing preprocessing methods with a very promising approach: P-t-SNE.

The remainder of this paper is structured as follows. In Section 2, we present the P-t-SNE method. Section 3 describes the preprocessing of the baseline data, reduction of the global dimension of the data, and creation of the clusters using P-t-SNE. Section 4 describes the damage diagnosis procedure.

Subsequently, the application of the proposed method is presented in Section 5. Section 6 shows the results. Finally, Section 7 provides our conclusions.

2. Parametric t-SNE (P-t-SNE)

The non-parametric version of t-SNE has a huge computational cost of optimization: to map new data, the optimization has to run for the complete set again. To avoid the heavy optimization of the t-SNE, the P-t-SNE was proposed. P-t-SNE is an unsupervised dimensionality reduction technique that learns a parametric mapping between the high-dimensional data space and the low-dimensional latent space, preserving the local structure of the data in the latent space as well as possible.

In the P-t-SNE method, the mapping $f : X \rightarrow Y$ from the high-dimensional space X to the low-dimensional space Y is parameterized through a feed-forward NN with weights W. The NN is trained in such a way that it retains the local structure of the data in the low-dimensional space. There are two main stages in the training procedure:

1. Pretraining with a restricted Boltzmann machine (RBM). RBM is used to construct a pretrained P-t-SNE network. The main aim of the pretraining stage is to define an initialization of the model parameters for the next stage.
2. Fine-tuning using the cost function of P-t-SNE. In this stage, the weights of the pretrained NN are fine-tuned in such a way that the NN preserves the local structure of the data in the low-dimensional space. In the feed-forward NN, term q_{ij} [12,19] of the t-SNE is adapted as follows:

$$q_{ij} = \frac{\left[1 + \|f(x_i|W) - f(x_j|W)\|^2/\alpha\right]^{-(\alpha+1)/2}}{\sum_{k \neq l} \left[1 + \|f(x_k|W) - f(x_l|W)\|^2/\alpha\right]^{-(\alpha+1)/2}},$$

where α denotes the degrees of freedom of the Student's t-distribution.

Restricted Boltzmann Machine

In this section, a short introduction to RBM [22,23] is given.

An RBM is a two-layer stochastic NN. This network consists of a visible, or input, layer (visible nodes **v**) and a hidden layer (hidden nodes **h**). Values of the nodes are normally Bernoulli-distributed. Each visible node is connected to all hidden nodes using weighted connections, but there are no intra-layer connections. The structure of the RBM is illustrated in Figure 1.

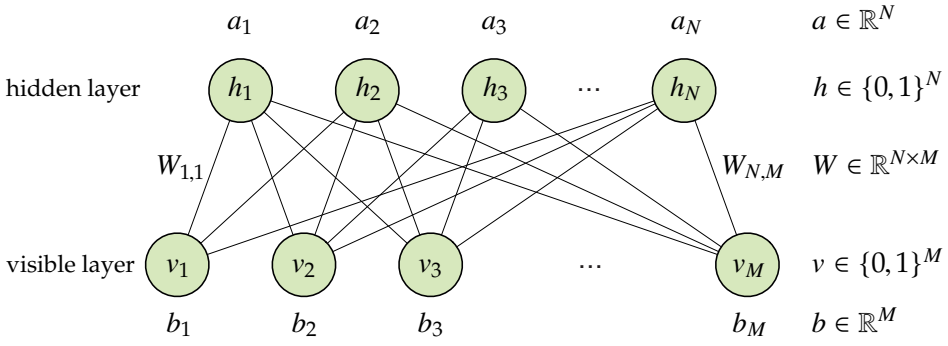

Figure 1. Structure of the RBM.

Boltzmann distribution is specified by the energy function $E(\mathbf{v}, \mathbf{h})$, and this distribution gives the joint distribution over all nodes, $P(\mathbf{v}, \mathbf{h})$:

$$E(\mathbf{v}, \mathbf{h}) = -\sum_{i,j} W_{ij} v_i h_j - \sum_i b_i v_i - \sum_j a_j h_j,$$
$$P(\mathbf{v}, \mathbf{h}) = \frac{\exp(-E(\mathbf{v}, \mathbf{h}))}{\sum_{\mathbf{v},\mathbf{h}} \exp(-E(\mathbf{v}, \mathbf{h}))},$$

where W_{ij} is the weight of the connection between a visible node v_i and a hidden node h_j; and b_i and a_j are the biases of visible and hidden nodes, respectively. Moreover, conditional probabilities $P(v_i = 1|\mathbf{h})$ and $P(h_j = 1|\mathbf{v})$ are given by the sigmoid function:

$$P(v_i = 1|\mathbf{h}) = \frac{1}{1 + \exp(-\sum_j W_{ij} h_j - b_i)}, \quad (1)$$
$$P(h_j = 1|\mathbf{v}) = \frac{1}{1 + \exp(-\sum_i W_{ij} v_i - a_j)}. \quad (2)$$

The RBM can calculate the values of visible nodes from the values of hidden nodes by Equation (1); similarly, the RBM can calculate the values of hidden nodes from the visible nodes by Equation (2).

The model parameters W, b, and a are learned so that the marginal distribution over the visible nodes under model $P_{\text{model}}(\mathbf{v})$ is close to the true distribution of data, $P_{\text{data}}(\mathbf{v})$. In particular, the RBM uses the Kullback–Leibler (KL) divergence to measure the distance between the true distribution $P_{\text{data}}(\mathbf{v})$ and the distribution based on the model $P_{\text{model}}(\mathbf{v})$. The gradient of the KL divergence with respect to W_{ij} is given by

$$\frac{\partial \text{KL}(P_{\text{data}}||P_{\text{model}})}{\partial W_{ij}} = \mathbb{E}[v_i h_j]_{P_{\text{data}}} - \mathbb{E}[v_i h_j]_{P_{\text{model}}},$$

where $\mathbb{E}[v_i h_j]_{P_{\text{data}}}$ is the expected value under the true distribution, and $\mathbb{E}[v_i h_j]_{P_{\text{model}}}$ is the expected value under the model distribution.

However, the model expectation, $\mathbb{E}[v_i h_j]_{P_{\text{model}}}$, cannot be computed analytically. To avoid computing the model, we follow an approximation: the gradient of a slightly different objective function that is called contrastive divergence (CD) [24]. The CD measures how the model distribution gets away from the true distribution of data through $\text{KL}(P_{\text{data}}||P_{\text{model}}) - \text{KL}(P_1||P_{\text{model}})$, where $P_1(\mathbf{v})$ is the distribution over the visible nodes because the RBM can run for one iteration (that is, one Gibbs sweep) when initialized according to the true distribution. Using standard gradient descent techniques, the CD can be minimized efficiently:

$$\mathbb{E}[v_i h_j]_{P_{\text{data}}} - \mathbb{E}[v_i h_j]_{P_1}.$$

The second term, $\mathbb{E}[v_i h_j]_{P_1}$, is estimated from the samples obtained using Gibbs sampling.

3. Baseline Data: Preprocessing and Clustering

In this section, data preprocessing is presented briefly, because a more detailed description can be found in [19]. The preprocessing has three stages: data integration (Section 3.1), data transformation (Section 3.2), and data reduction (Section 3.3). Subsequently, data are organized in clusters in Section 3.4.

3.1. Data Integration: Unfolding and Scaling

The collected data contain different response signals measured by sensors on a vibrating structure in the time domain. Under different structural states, multiple observations of these responses are measured. Then, using the fast Fourier transform (FFT) algorithm, these response signals are transformed into the frequency domain. All these observations in the frequency domain are collected in a matrix that is defined as follows:

$$\mathbf{X} = \left(x_{i,j}^{k,l}\right) = \left[\begin{array}{ccc|ccc|c|ccc} x_{1,1}^{1,1} & \cdots & x_{1,1}^{1,L} & x_{1,1}^{2,1} & \cdots & x_{1,1}^{2,L} & \cdots & x_{1,1}^{K,1} & \cdots & x_{1,1}^{K,L} \\ \vdots & \ddots & \vdots & \vdots & \ddots & \vdots & \ddots & \vdots & \ddots & \vdots \\ x_{n_1,1}^{1,1} & \cdots & x_{n_1,1}^{1,L} & x_{n_1,1}^{2,1} & \cdots & x_{n_1,1}^{2,L} & \cdots & x_{n_1,1}^{K,1} & \cdots & x_{n_1,1}^{K,L} \\ \hline x_{1,2}^{1,1} & \cdots & x_{1,2}^{1,L} & x_{1,2}^{2,1} & \cdots & x_{1,2}^{2,L} & \cdots & x_{1,2}^{K,1} & \cdots & x_{1,2}^{K,L} \\ \vdots & \ddots & \vdots & \vdots & \ddots & \vdots & \ddots & \vdots & \ddots & \vdots \\ x_{n_2,2}^{1,1} & \cdots & x_{n_2,2}^{1,L} & x_{n_2,2}^{2,1} & \cdots & x_{n_2,2}^{2,L} & \cdots & x_{n_2,2}^{K,1} & \cdots & x_{n_2,2}^{K,L} \\ \hline \vdots & \ddots & \vdots & \vdots & \ddots & \vdots & \ddots & \vdots & \ddots & \vdots \\ \hline x_{1,J}^{1,1} & \cdots & x_{1,J}^{1,L} & x_{1,J}^{2,1} & \cdots & x_{1,J}^{2,L} & \cdots & x_{1,J}^{K,1} & \cdots & x_{1,J}^{K,L} \\ \vdots & \ddots & \vdots & \vdots & \ddots & \vdots & \ddots & \vdots & \ddots & \vdots \\ x_{n_J,J}^{1,1} & \cdots & x_{n_J,J}^{1,L} & x_{n_J,J}^{2,1} & \cdots & x_{n_J,J}^{2,L} & \cdots & x_{n_J,J}^{K,1} & \cdots & x_{n_J,J}^{K,L} \end{array}\right] \in \mathcal{M}_{(n_1+\cdots+n_J)\times(K\cdot L)}(\mathbb{R}), \tag{3}$$

where $K \in \mathbb{N}$ is the number of sensors and $k = 1, \ldots, K$ identifies the sensor that is measuring; $L \in \mathbb{N}$ is the number of components in each signal and $l = 1, \ldots, L$ indicates the l-th measurement in the frequency domain; $J \in \mathbb{N}$ is the number of different structural states that are considered and $j = 1, \ldots, J$ represents the structural state that is measured; finally, n_j, $j = 1, \ldots, J$, is the number of observations per structural state and $i = 1, \ldots, n_j$ is the i-th observation related to the j-th structural state.

Matrix $\mathbf{X}$ in Equation (3) is a particular unfolded version of a 3-dimensional $(n_1 + \cdots + n_J) \times K \times L$ data matrix, where the first dimension is observation, the second dimension is sensor, and the third dimension is time. Numerous approaches have been proposed to handle 3-dimensional matrices. The most widely adopted approaches are based on the unfolding of these matrices. There are six alternative ways of arranging a 3-dimensional data matrix [20] that affect the performance of the overall strategy, and we have considered type E in this work, because type-E unfolding simplifies the study of variability among samples.

Matrix $\mathbf{X}$ in Equation (3) is rescaled through MCGS [21] because of the different magnitudes and scales in the measurements.

3.2. Data Transformation

Data transformation means applying a particular mathematical function. The transformation that we apply in this study is PCA, because the final aim is dimensionality reduction. We build the PCA model, $\mathbf{P}$, so that the normalized data $\mathbf{X}$ using MCGS, $\check{\mathbf{X}}$, are transformed to the projected data $\mathbf{T} = \check{\mathbf{X}}\mathbf{P}$. Notably, matrices $\check{\mathbf{X}}$ and $\mathbf{T}$ have equal dimensions; hence, no reduction is performed at this stage.

3.3. Data Reduction: PCA and P-t-SNE

In this work, we use two methods of data reduction. On the one hand, we apply PCA to represent the normalized matrix $\check{\mathbf{X}}$ in a new space with reduced dimensions and without a significant loss of information. On the other hand, we apply P-t-SNE as a 2-dimensional representation technique. These two approaches are combined to reduce the data complexity, computational effort, and time.

3.4. Clustering Effect

The first dimensionality reduction is performed using PCA. Specifically, for $n = n_1 + \cdots + n_J$ observations, the rows of matrix $\mathbf{X}$ in Equation (3) under J different structural states are projected and transformed into a lower-dimensional space.

Next, the second dimensionality reduction is applied to the projected and transformed data using P-*t*-SNE. The aim is to find a collection of 2-dimensional points that represent the projected and transformed data by PCA with no explicit loss of information and preserve the local structure of this dataset. After the application of P-*t*-SNE, we expect to observe J clusters related to J different structural states.

As mentioned at the beginning of Section 3, see [19] for more details on these stages.

4. Structure to Diagnose: Damage Detection and Classification Procedure

In this section, we describe the vibration-based damage detection and classification procedure to diagnose a new structure.

For damage detection and classification, a single observation of the current structure is required to diagnose it. The collected data are composed of different response signals measured by K sensors and L components in each signal, as in Equation (3). When these measures are obtained in the frequency domain, we build a new data vector $\mathbf{z}$:

$$\mathbf{z}^\top = \left[\begin{array}{ccc|ccc|c|ccc} z^{1,1} & \cdots & z^{1,L} & z^{2,1} & \cdots & z^{2,L} & \cdots & z^{K,1} & \cdots & z^{K,L} \end{array} \right] \in \mathbb{R}^{K \cdot L}.$$

4.1. Scaling (MCGS)

First, we have to scale the row vector $\mathbf{z}^\top$ to define a scaled row vector $\check{\mathbf{z}}^\top$:

$$\check{z}^{k,l} = \frac{z^{k,l} - \mu^{k,l}}{\sigma^k}, \quad k = 1, \ldots, K, \; l = 1, \ldots, L, \tag{4}$$

where $\mu^{k,l}$ is the arithmetic mean of all the elements in the $[(k-1)L + l]$-th column of matrix $\mathbf{X}$ in Equation (3) (that is, the l-th column of the k-th sensor) and σ^k is the standard deviation of all measurements of the k-th sensor relative to the mean value μ^k (the arithmetic mean of all the measurements of the k-th sensor).

4.2. Projection (PCA)

The scaled row vector $\check{\mathbf{z}}^\top \in \mathbb{R}^{K \cdot L}$ is projected into the space spanned by the first ℓ principal components in $\mathbf{P}_\ell$ through the vector-to-matrix multiplication:

$$\mathbf{x}^{n+1} = \check{\mathbf{z}}^\top \cdot \mathbf{P}_\ell \in \mathbb{R}^\ell.$$

Notably, the vector containing the data of the structure to be diagnosed initially has dimension $K \cdot L$ but later dimension ℓ. We add this new point to the projected and transformed data by PCA ($\mathcal{X} = \{\mathbf{x}^1, \ldots, \mathbf{x}^n\} \subset \mathbb{R}^\ell$) to define a new set:

$$\mathcal{X}' = \{\mathbf{x}^1, \ldots, \mathbf{x}^n\} \cup \{\mathbf{x}^{n+1}\} = \{\mathbf{x}^1, \ldots, \mathbf{x}^n, \mathbf{x}^{n+1}\} \subset \mathbb{R}^\ell, \tag{5}$$

where

$$\mathbf{x}^i = \mathbf{e}_i^\top \check{\mathbf{X}} \mathbf{P}_\ell, \; i = 1, \ldots, n$$

and $\mathbf{e}_i \in \mathbb{R}^n$ is the i-th element of the canonical basis. The network is trained with $\{\mathbf{x}^1, \ldots, \mathbf{x}^n\}$. Then, $\{\mathbf{x}^{n+1}\}$ will be passed through the trained network.

4.3. P-t-SNE and Final Classification

Finally, we apply P-*t*-SNE to the ℓ-dimensional set $\mathcal{X}'$ in Equation (5) to find a collection of 2-dimensional map points $\mathcal{Y}' = \{\mathbf{y}^1, \ldots, \mathbf{y}^n, \mathbf{y}^{n+1}\} \subset \mathbb{R}^2$ that represent the original set $\mathcal{X} = \{\mathbf{x}^1, \ldots, \mathbf{x}^n\} \subset \mathbb{R}^\ell$ (the data projected and transformed by PCA) with no explicit loss of information and retaining the local structure of this set. Furthermore, the map point $\mathbf{y}^{n+1}$, associated with the data point $\mathbf{x}^{n+1}$, is included. That is, the embedded data are constructed applying the trained network: input $\mathcal{X}'$ and output $\mathcal{Y}'$. We expect to observe the same J clusters related to the J different structural states.

For each cluster, we calculate its centroid: the mean of the values of the data points in the cluster. For instance, the centroid associated with the first structural state is

$$\mathcal{Y}'_1 := \frac{1}{n_1} \sum_{i=1}^{n_1} \mathbf{y}^i = \frac{\mathbf{y}^1 + \cdots + \mathbf{y}^{n_1}}{n_1} \in \mathbb{R}^2.$$

In general, the centroid associated with the j-th structural state, $j = 1, \ldots, J$, is the 2-dimensional point defined as

$$\mathcal{Y}'_j := \frac{1}{n_j} \sum_{i=1}^{n_j} \mathbf{y}^{\left(\sum_{m=0}^{j-1} n_m\right)+j} \in \mathbb{R}^2, \; j = 1, \ldots, J, \tag{6}$$

where $n_0 = 0$. As a result, the current structure to diagnose is associated with the j-th structural state if

$$j = \arg \min_{j=1,\ldots,J} \|\mathcal{Y}'_j - \mathbf{y}^{n+1}\|_2,$$

that is, if the minimum distance between $\mathbf{y}^{n+1}$ and each centroid corresponds to the Euclidean distance between $\mathcal{Y}'_j$ and $\mathbf{y}^{n+1}$. We call this approach the smallest point-centroid distance (see Figure 2).

The proposed procedure is shown in Figure 3.

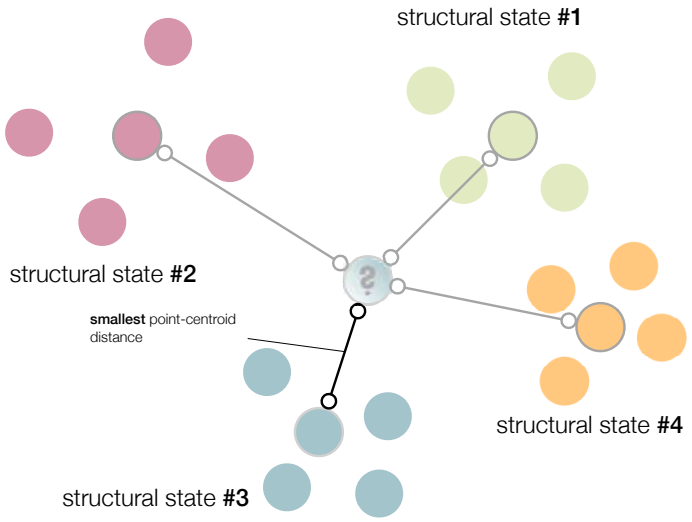

Figure 2. Current structure to diagnose is associated with the structural state with the smallest point-centroid distance.

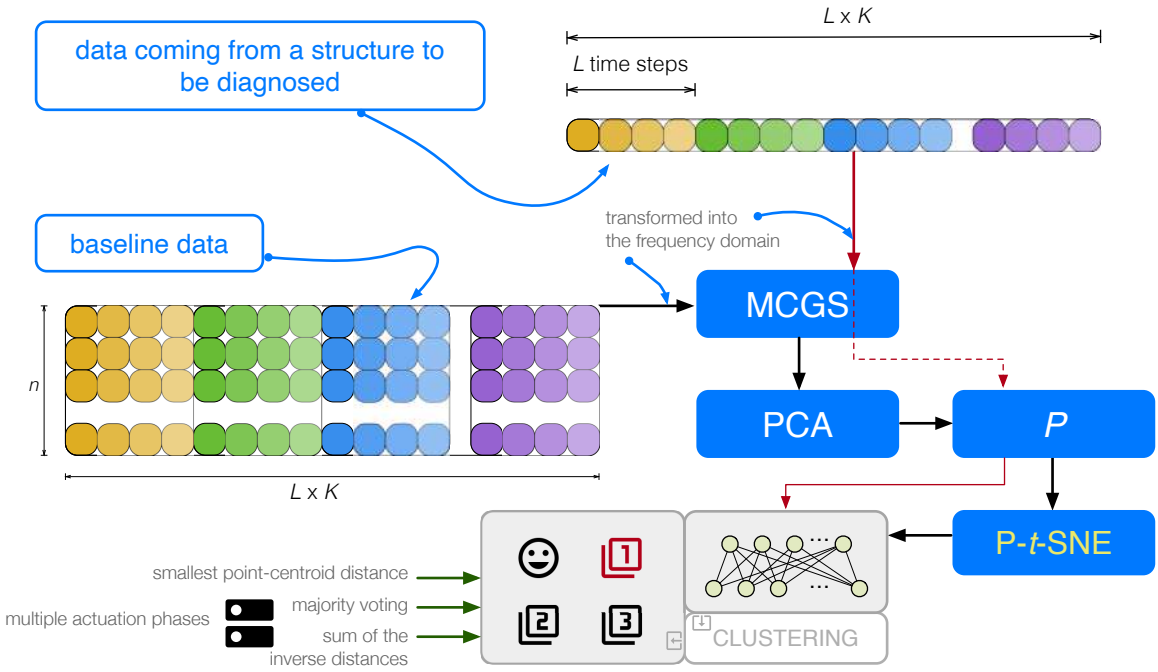

Figure 3. Flowchart of the proposed procedure. Data coming from a structure are first scaled by MCGS and then projected into the PCA model. Finally, P-*t*-SNE is applied to generate the clusters that will be used in the vibration-based detection and classification of structural changes.

5. Application of the SHM System on an Aluminum Plate with Four PZTs

In this study, we reuse the structure and experiment from [19]. Therefore, we can use this structure as a benchmark to compare our results.

5.1. Structure

A square aluminum plate was manufactured to demonstrate the accuracy of the vibration-based method of damage detection and classification presented in Sections 3 and 4. The dimension of the plate is $40 \times 40 \times 0.2$ cm. The plate is instrumented with four PZTs and a mass of 17.2916 g is introduced to simulate the damage in a non-destructive way, producing changes in the propagated wave (see Figure 4a). Each PZT can work in two modes: excite the aluminum plate (actuator mode) with a burst signal or detect a time-varying mechanical response (sensor mode). The location of the mass defines each damage, and $J = 4$ structural states are considered: healthy state and three different types of damage (Figure 4b). The plate is isolated from the vibration and noise in the laboratory (Figure 4b).

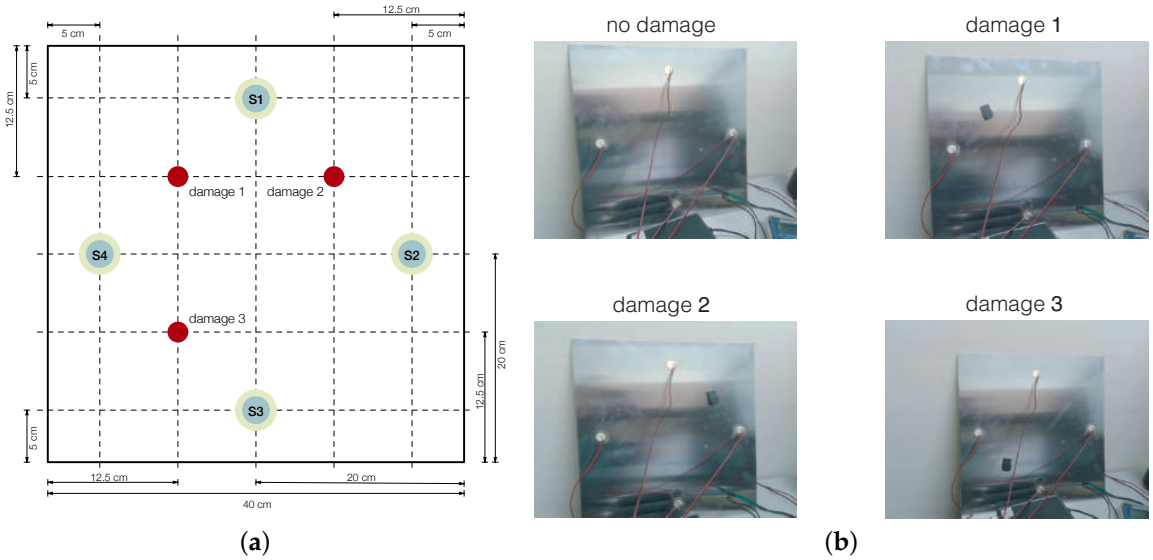

Figure 4. (**a**) Aluminum plate with four piezoelectric sensors (S1, S2, S3, and S4); (**b**) the four structural states considered.

5.2. Scenarios and Actuation Phases

Unlike [19], in this study, the experimental setup includes only two scenarios (the two extreme cases) to determine the performance of the proposed method:

- **Scenario 1**. The signals are obtained using a short wire (0.5 m) from the digitizer to the piezoelectric sensors. Next, the Savitzky–Golay [25] algorithm is used to filter these signals after adding white Gaussian noise. This filter is used to smoothen the data.
- **Scenario 2**. The signals are obtained using a long wire (2.5 m) from the digitizers to the piezoelectric sensors. Signals are also filtered with the Savitzky–Golay algorithm.

As discussed in Section 5.1, there are four PZTs (S1, S2, S3, and S4) that excite the plate and collect the measured signal. This sensor network works in what we call actuation phases. In each actuation phase, a PZT is used as an actuator (which excites the plate with the burst signal), and the rest of the PZTs are used as sensors (which measure signals). Therefore, we have as many actuation phases as sensors: in actuation phase 1, S1 is used as the actuator and the rest of PZTs are used as sensors; in actuation phase 2, S2 is used as the actuator and the rest of PZTs are used as sensors; and so on.

5.3. Data Collection

Given a certain scenario, as the two defined in Section 5.2, four matrices $\mathbf{X}[\varphi]$, $\varphi = 1, \ldots, 4$, are obtained, one for each actuation phase. Each matrix $\mathbf{X}[\varphi]$, $\varphi = 1, \ldots, 4$, is constructed as follows:

- $n_1 = n_2 = n_3 = n_4 = 25$ observations are performed for each of the four structural states. Therefore, each matrix $\mathbf{X}[\varphi]$, $\varphi = 1, \ldots, 4$, contains 100 rows: $n_1 + n_2 + n_3 + n_4 = 25 \cdot 4$. Specifically, the first 25 rows represent the healthy state, the next 25 are observations with damage 1, and so on.
- For each actuation phase φ, $\varphi = 1, \ldots, 4$, $K = 3$ PZTs working as sensors are measured during 60000 time instants. Next, these measurements are transformed into the frequency domain. As a result, the number of columns of matrix $\mathbf{X}[\varphi]$, $\varphi = 1, \ldots, 4$, is equal to $K \cdot L = 3 \cdot ((60000/2) + 1) = 90003$.

Therefore, the matrix that collects all observations under the different structural states in the frequency domain is as follows (see Equation (3); here, $L = 30001$ and $J = 4$):

$$\mathbf{X}[\varphi] = \left(x[\varphi]_{i,j}^{k,l}\right) \in \mathcal{M}_{100\times 90003}(\mathbb{R}). \tag{7}$$

The damage detection and classification method described in Sections 3 and 4 can be applied to each matrix $\mathbf{X}[\varphi]$, $\varphi = 1, \ldots, 4$, in Equation (7), leading to one classification per actuation phase. Then, we will use these four classifications to obtain a final decision based on the four actuation phases. This strategy will be detailed in Section 5.5.

5.4. κ-Fold Nonexhaustive Leave-p-Out Cross-Validation

The proposed approach is evaluated by comparing test data (the new observations in unknown state under the same conditions) with baseline data (data from the structure under the four different structural states). For that purpose, the κ-fold nonexhaustive leave-p-out cross-validation [19] is used. Hence, the sum of all elements in the confusion matrices that are presented in Section 6 is equal to 400. We use the notation $\mathbf{\mathfrak{X}}$ to represent the matrix that is used as the baseline to build the model. Matrix $\mathbf{\mathfrak{X}}$ has 20 rows: five for each structural state.

5.5. Damage Detection and Classification

The strategy for damage detection and classification is as follows: the classification will be based on the four matrices $\mathbf{X}[1], \mathbf{X}[2], \mathbf{X}[3]$, and $\mathbf{X}[4]$, defined in Equation (7), with κ-fold nonexhaustive leave-p-out cross-validation. Each actuation phase will cast a vote that will determine the final classification.

In this strategy, the next steps are followed:

- **Step 1**. The data matrix $\mathbf{\mathfrak{X}}$ is scaled by MCGS, obtaining matrix $\breve{\mathbf{\mathfrak{X}}}$.
- **Step 2**. PCA is applied to matrix $\breve{\mathbf{\mathfrak{X}}}$, obtaining the PCA model $\mathbf{P}$.
- **Step 3**. The reduced PCA model $\mathbf{P}_\ell$ is chosen such that the proportion of variance explained is at least 95%.
- **Step 4**. An observation $\mathbf{z}^\top \in \mathbb{R}^{3\cdot 30001} = \mathbb{R}^{90003}$ of the current structure-to-diagnose is needed. Then, $\mathbf{z}^\top$ is scaled by Equation (4) to obtain $\breve{\mathbf{z}}^\top$, which is projected into the space spanned by the first ℓ principal components in $\mathbf{P}_\ell$.
- **Step 5**. Dataset $\mathcal{X}' = \{\mathbf{x}^1, \ldots, \mathbf{x}^{20}\} \cup \{\mathbf{x}^{21}\} = \{\mathbf{x}^1, \ldots, \mathbf{x}^{20}, \mathbf{x}^{21}\} \subset \mathbb{R}^\ell$ is defined by Equation (5). The network is trained with $\{\mathbf{x}^1, \ldots, \mathbf{x}^{20}\}$. Then, $\{\mathbf{x}^{21}\}$ will be passed through the trained network.
- **Step 6**. P-t-SNE is applied to $\mathcal{X}'$ to find a set of 2-dimensional points: $\mathcal{Y}' = \{\mathbf{y}^1, \ldots, \mathbf{y}^{20}, \mathbf{y}^{21}\} \subset \mathbb{R}^2$. Thus, the embedded data are constructed using the trained network: input $\mathcal{X}'$ and output $\mathcal{Y}'$.
- **Step 7**. $J = 4$ clusters are obtained, one per structural state. These clusters are formed by the 2-dimensional points: $\{\mathbf{y}^1, \ldots, \mathbf{y}^5\} \subset \mathcal{Y}'$, related to the healthy state; $\{\mathbf{y}^6, \ldots, \mathbf{y}^{10}\} \subset \mathcal{Y}'$, related to damage 1; $\{\mathbf{y}^{11}, \ldots, \mathbf{y}^{15}\} \subset \mathcal{Y}'$, related to damage 2; and $\{\mathbf{y}^{16}, \ldots, \mathbf{y}^{20}\} \subset \mathcal{Y}'$, related to damage 3. Centroid $\mathcal{Y}'_j$, $j = 1, \ldots, J$, associated with the j-th structural state is calculated by Equation (6).
- **Step 8**. With the information given by the four actuation phases, the structure that must be diagnosed is finally classified considering two approaches: majority voting and sum of the inverse distances. For details of both approaches, see [19].

6. Results

In this section, confusion matrices summarize the results of the damage detection and classification method presented in Sections 3 and 4 and detailed in Sections 5.3–5.5. The results for each scenario are shown in different subsections. Four different structural states are considered in both scenarios:

- The healthy state ($D0$)—the aluminum plate with no damage;
- Three states with damage ($D1$, $D2$, and $D3$)—the aluminum plate with an added mass at the positions indicated in Figure 4.

Five iterations ($\kappa = 5$) of a nonexhaustive leave-p-out cross-validation, with $p = 80$, are performed to validate the damage detection and classification method. At each iteration, 80 observations are considered: 20 observations per structural state ($D0, D1, D2$, and $D3$). Therefore, the sum of all elements in the confusion matrices is equal to $5 \cdot 80 = 400$.

Two different confusion matrices are shown for each of the two scenarios:

- **Majority voting**. The damage detection and classification method is applied to the four matrices $\mathbf{X}[\varphi],\ \varphi = 1, \ldots, 4$. Each actuation phase emits a vote, and the final classification is made by the majority voting [19].
- **Sum of the inverse distances**. The damage detection and classification method is applied to the four matrices $\mathbf{X}[\varphi],\ \varphi = 1, \ldots, 4$. Each actuation phase emits a vote, and the final classification is made using the maximum sum of the inverse distances [19].

Finally, we have included the confusion matrices for t-SNE, to compare its performance with P-t-SNE.

6.1. Scenario 1

In this section, we describe the results for **Scenario 1** from Section 5.2. Tables 1 and 2 show the four confusion matrices. The green background cells correspond to observations that are correctly classified, while the red background cells represent the misclassifications. The color intensity (green or red) is related to the proportion of correct or wrong decisions.

With P-t-SNE and the majority voting (Table 1), the overall accuracy is very good. Specifically, 398 out of 400 observations have been correctly classified, which corresponds to the overall accuracy of 99.5%. With t-SNE, the overall accuracy is 100% (Table 1).

Using the sum of the inverse distances (Table 2) for the P-t-SNE-based damage detection and classification, 399 out of 400 observations have been correctly classified; hence, the overall accuracy is 99.75%. For t-SNE, 400 out of 400 observations have been correctly classified (100% accuracy).

Furthermore, other metrics are calculated. The most common metrics for choosing the best solution in a binary classification problem are as follows:

- *Accuracy*, defined as the proportion of true results among the total number of cases examined.
- *Precision* or *positive predictive value* (PPV) that attempts to answer the question "what proportion of positive identifications is actually correct?".
- *Sensitivity* or *true positive rate* (TPR) that measures the proportion of actual positives that are correctly identified as such.
- F_1 *score*, defined as the harmonic mean of PPV and TPR.
- *Specificity* or *true negative rate* (TNR) that measures the proportion of actual negatives that are correctly identified as such.

These metrics are easy to calculate for binary and multiclass classification problems [26]. When the classification problem is multiclass, as in the current work, according to [27,28], the result is the average obtained by adding the result of each class and dividing over the total number of classes.

In all cases (P-t-SNE, t-SNE, the majority voting, and the sum of the inverse distances), these five metrics vary between 99.5% and 100% (Tables 3 and 4).

As can be seen, both parametric and non-parametric approaches obtain practically the same results. However, P-t-SNE dramatically reduces the processing time: it decreases from 40 min and 15 s (t-SNE) to 2 min and 34 s (P-t-SNE) on an Intel Core i7 4.20 GHz computer with 32 GB RAM. Using P-t-SNE, a decision is made in just a few milliseconds. The reduced time (2 min and 34 s) includes both the pretraining and the fine-tuning of the NN, as well as the classification of the current state of the structure. The total computational cost of P-t-SNE is reduced by approximately 94% compared with t-SNE.

Table 1. Confusion matrix of the application of P-*t*-SNE and *t*-SNE damage detection and classification method presented in Sections 3 and 4: scenario 1 and the majority voting approach.

Predicted / True	P-*t*-SNE				*t*-SNE			
	***D*0**	***D*1**	***D*2**	***D*3**	***D*0**	***D*1**	***D*2**	***D*3**
*D*0	100	0	0	0	100	0	0	0
*D*1	0	100	0	0	0	100	0	0
*D*2	0	0	100	0	0	0	100	0
*D*3	0	0	2	98	0	0	0	100

[1] *D*0: healthy state of the structure; *D*1, *D*2, and *D*3: added masses at the positions indicated in Figure 4.

Table 2. Confusion matrix of the application of P-*t*-SNE and *t*-SNE damage detection and classification method presented in Sections 3 and 4: scenario 1 and the sum of the inverse distances approach.

Predicted / True	P-*t*-SNE				*t*-SNE			
	***D*0**	***D*1**	***D*2**	***D*3**	***D*0**	***D*1**	***D*2**	***D*3**
*D*0	100	0	0	0	100	0	0	0
*D*1	0	100	0	0	0	100	0	0
*D*2	0	0	99	1	0	0	100	0
*D*3	0	0	0	100	0	0	0	100

[1] *D*0: healthy state of the structure; *D*1, *D*2, and *D*3: added masses at the positions indicated in Figure 4.

Table 3. Accuracy, PPV, TPR, F_1 score, and TNR of the application of P-*t*-SNE and *t*-SNE damage detection and classification method presented in Sections 3 and the 4: scenario 1 and the majority voting approach.

	P-*t*-SNE	*t*-SNE
Accuracy	99.8%	100.0%
PPV	99.5%	100.0%
TPR	99.5%	100.0%
F_1 score	99.5%	100.0%
TNR	99.8%	100.0%

Table 4. Accuracy, PPV, TPR, F_1 score, and TNR of the application of P-*t*-SNE and *t*-SNE damage detection and classification method presented in Sections 3 and 4: scenario 1 and the sum of the inverse distances approach.

	P-*t*-SNE	*t*-SNE
Accuracy	99.9%	100.0%
PPV	99.8%	100.0%
TPR	99.8%	100.0%
F_1 score	99.7%	100.0%
TNR	99.9%	100.0%

6.2. Scenario 2

In this section, we describe the results for Scenario 2 from Section 5.2. Tables 5 and 6 show the four confusion matrices.

With P-*t*-SNE and the majority voting (Table 5), the overall accuracy is also very good. Specifically, 398 out of 400 observations have been correctly classified; this corresponds to the overall accuracy of 99.5%. With *t*-SNE and the majority voting, the overall accuracy is 100% (Table 5).

Using the maximum sum of the inverse distances to take a final decision (Table 6) with P-*t*-SNE, 399 out of 400 observations have been correctly classified (the overall accuracy of 99.75%). With *t*-SNE, 400 out of 400 observations have been correctly classified (the overall accuracy of 100%).

In the non-parametric approach, using the majority voting and the sum of the inverse distances, the five metrics presented in Section 6.1 achieve 100%. In contrast, in the parametric approach, these metrics slightly decrease (between 0.1% and 0.5%, see Tables 7 and 8).

Again, as in scenario 1, parametric and non-parametric methods obtain similar results. However, as before, the P-*t*-SNE approach dramatically reduces the processing time: from 42 min and 1 s (*t*-SNE) to 2 min and 32 s (P-*t*-SNE). As in the previous scenario, the total computational cost of P-*t*-SNE is reduced by approximately 94% compared with *t*-SNE.

Table 5. Confusion matrix of the application of P-*t*-SNE and *t*-SNE damage detection and classification method presented in Sections 3 and 4: scenario 2 and the majority voting approach.

Predicted / True	P-*t*-SNE				*t*-SNE			
	***D*0**	***D*1**	***D*2**	***D*3**	***D*0**	***D*1**	***D*2**	***D*3**
*D*0	100	0	0	0	100	0	0	0
*D*1	1	99	0	0	0	100	0	0
*D*2	1	0	99	0	0	0	100	0
*D*3	0	0	0	100	0	0	0	100

[1] *D*0: healthy state of the structure; *D*1, *D*2, and *D*3: added masses at the positions indicated in Figure 4.

Table 6. Confusion matrix of the application of P-*t*-SNE and *t*-SNE damage detection and classification method presented in Sections 3 and 4: scenario 2 and the sum of the inverse distances approach.

Predicted / True	P-*t*-SNE				*t*-SNE			
	***D*0**	***D*1**	***D*2**	***D*3**	***D*0**	***D*1**	***D*2**	***D*3**
*D*0	100	0	0	0	100	0	0	0
*D*1	1	99	0	0	0	100	0	0
*D*2	0	0	100	0	0	0	100	0
*D*3	0	0	0	100	0	0	0	100

[1] *D*0: healthy state of the structure; *D*1, *D*2, and *D*3: added masses at the positions indicated in Figure 4.

Table 7. Accuracy, PPV, TPR, F_1 score, and TNR of the application of P-*t*-SNE and *t*-SNE damage detection and classification method presented in Sections 3 and 4: scenario 2 and the majority voting approach.

	P-*t*-SNE	*t*-SNE
Accuracy	99.8%	100.0%
PPV	99.5%	100.0%
TPR	99.5%	100.0%
F_1 score	99.5%	100.0%
TNR	99.8%	100.0%

Table 8. Accuracy, PPV, TPR, F_1 score, and TNR of the application of P-*t*-SNE and *t*-SNE damage detection and classification method presented in Sections 3 and 4: scenario 2 and the sum of the inverse distances approach.

	P-*t*-SNE	*t*-SNE
Accuracy	99.9%	100.0%
PPV	99.8%	100.0%
TPR	99.8%	100.0%
F_1 score	99.7%	100.0%
TNR	99.9%	100.0%

6.3. Repeatability

We use error bars to give the reader a general idea of the uncertainty in the results. Figure 5 shows the mean of each structural state with error bars representing the standard error. As it can be seen both in Figure 5 and in Tables 9–12, the standard error is very small, when we repeat the procedure 10 times.

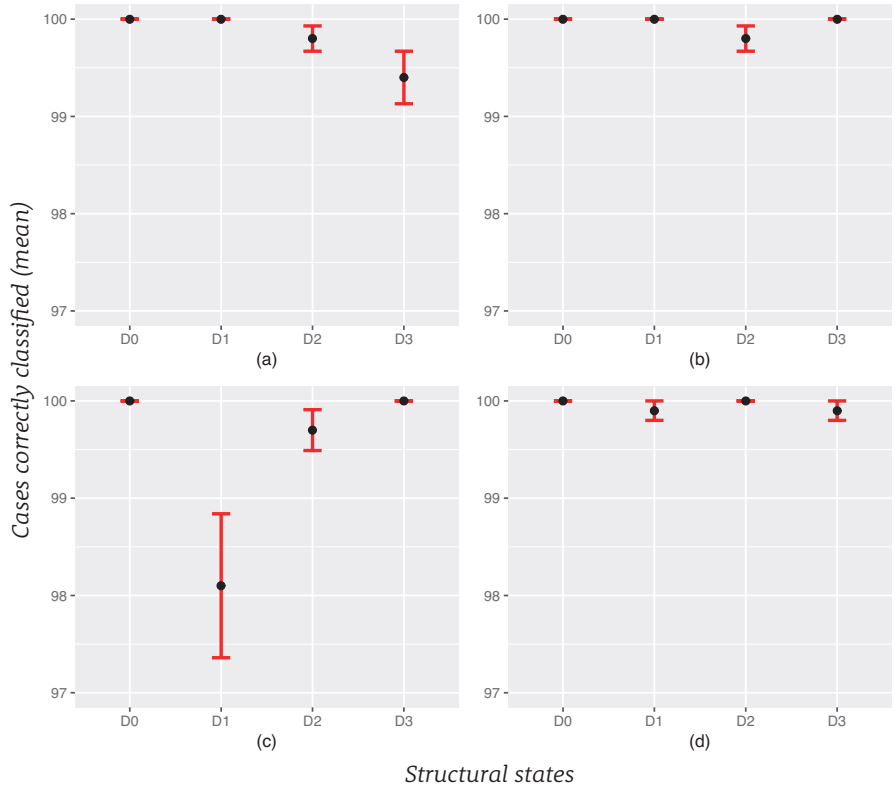

Figure 5. Repeatability of the SHM strategy (10 times), graphs with error bars: (**a**) scenario 1 and majority voting approach; (**b**) scenario 1 and sum of the inverse distances approach; (**c**) scenario 2 and majority voting approach; (**d**) scenario 2 and sum of the inverse distances approach. *D*0: healthy state of the structure; *D*1, *D*2, and *D*3: added masses at the positions indicated in Figure 4.

Table 9. Repeatability of the SHM strategy (10 times): scenario 1 and majority voting approach. *D*0: healthy state of the structure; *D*1, *D*2, and *D*3: added masses at the positions indicated in Figure 4.

	***D*0**	***D*1**	***D*2**	***D*3**
Mean	100.00	100.00	99.80	99.40
Standard deviation	0.00	0.00	0.42	0.84
Standard error	0.00	0.00	0.13	0.27

Table 10. Repeatability of the SHM strategy (10 times): scenario 1 and sum of the inverse distances approach. *D*0: healthy state of the structure; *D*1, *D*2, and *D*3: added masses at the positions indicated in Figure 4.

	***D*0**	***D*1**	***D*2**	***D*3**
Mean	100.00	100.00	99.80	100.00
Standard deviation	0.00	0.00	0.42	0.00
Standard error	0.00	0.00	0.13	0.00

Table 11. Repeatability of the SHM strategy (10 times): scenario 2 and majority voting approach. *D*0: healthy state of the structure; *D*1, *D*2, and *D*3: added masses at the positions indicated in Figure 4.

	***D*0**	***D*1**	***D*2**	***D*3**
Mean	100.00	98.10	99.70	100.00
Standard deviation	0.00	2.33	0.67	0.00
Standard error	0.00	0.74	0.21	0.00

Table 12. Repeatability of the SHM strategy (10 times): scenario 2 and sum of the inverse distances approach. $D0$: healthy state of the structure; $D1$, $D2$, and $D3$: added masses at the positions indicated in Figure 4.

	***D*0**	***D*1**	***D*2**	***D*3**
Mean	100.00	99.90	100.00	99.90
Standard deviation	0.00	0.32	0.00	0.32
Standard error	0.00	0.10	0.00	0.10

7. Conclusions

In this paper, we proposed an SHM strategy for the detection and classification of structural changes combining PCA and P-*t*-SNE. We evaluated the proposed method with experimental data. The obtained results show that its performance is very good, given its high classification accuracy. In addition, we have compared the parametric version of *t*-SNE with the non-parametric version.

According to the results shown in Sections 6.1 and 6.2, the performance is very satisfactory and similar in both approaches: P-*t*-SNE and *t*-SNE. However, in terms of processing time, it is better to make a decision considering the P-*t*-SNE-based damage detection and classification rather than working with the *t*-SNE-based method: although the non-parametric approach slightly outperforms the parametric approach, the parametric approach can reduce the total computational cost by approximately 94%. Hence, P-*t*-SNE can classify a current structure in just a few milliseconds. This is the first indication that P-*t*-SNE is better compared with the *t*-SNE. Other advantages of using P-*t*-SNE are as follows:

1. P-*t*-SNE can handle large-scale datasets, while *t*-SNE can only handle datasets with a size not greater than the order of thousands.
2. The *t*-SNE method requires an extremely large computational cost for the optimization: to map a new data sample, the optimization has to run for the whole dataset again. However, P-*t*-SNE can learn from the training data and be applied when a new observation arises; hence, it can work with real-time observations. Therefore, the parametric approach can make inferences about new samples to be diagnosed without having to recalculate everything; the model predicts on out-of-sample data.

Based on the foregoing, and seeing the strong performance of the P-*t*-SNE-based approach, we conclude that it is better to work with the parametric version of *t*-SNE than with the non-parametric version.

Many possible fields of application exist. For example, in aeronautics, parts of an airplane (wings or fuselage) can be simulated with similar aluminum plates; for wind turbines, this methodology can be applied to detect damage and faults. In general, if a sensor network can be installed in a structure, and various actuation phases can be defined, the proposed approach can be considered.

In our future work, we contemplate to apply the proposed methodology to handle imbalanced data, as well as to determine its effectiveness in different environmental and operational conditions.

Author Contributions: D.A. and F.P. developed the idea and designed the exploration framework; D.A. developed the algorithms; F.P. supervised the results of the validation; D.A. and F.P. drafted the manuscript. All authors have read and agreed to the published version of the manuscript.

Funding: This research has been partially funded by the Spanish Agencia Estatal de Investigación (AEI)—Ministerio de Economía, Industria y Competitividad (MINECO), by the Fondo Europeo de Desarrollo Regional (FEDER) through the research project DPI2017-82930-C2-1-R, and by the Generalitat de Catalunya through the research project 2017 SGR 388.

Acknowledgments: We thank the Universitat Politècnica de Catalunya (UPC) for predoctoral fellowship (to David Agis).

Conflicts of Interest: The authors declare no conflict of interest. The funders had no role in the design of the study; in the collection, analyses, or interpretation of data; in the writing of the manuscript, or in the decision to publish the results.

Abbreviations

The following abbreviations are used in this manuscript:

CD	contrastive divergence
FFT	fast Fourier transform
ISOMAP	isometric mapping
KL	Kullback–Leibler
LDA	linear discriminant analysis
MCGS	mean-centered group scaling
NN	neural network
PCA	principal component analysis
PPV	positive predictive value
P-*t*-SNE	parametric *t*-distributed stochastic neighbor embedding
PZT	piezoelectric transducers
RBM	restricted Boltzmann machine
SHM	structural health monitoring
TNR	true negative rate
TPR	true positive rate
t-SNE	*t*-distributed stochastic neighbor embedding

References

1. Worden, K.; Cross, E. On switching response surface models, with applications to the structural health monitoring of bridges. *Mech. Syst. Sig. Process.* **2018**, *98*, 139–156. [CrossRef]
2. Liu, Y.; Kim, S.B.; Chattopadhyay, A.; Doyle, D. Application of system-identification techniques to health monitoring of on-orbit satellite boom structures. *J. Spacecraft Rockets* **2011**, *48*, 589–598. [CrossRef]
3. Sohn, H.; Farrar, C.R.; Hunter, N.F.; Worden, K. Structural health monitoring using statistical pattern recognition techniques. *J. Dyn. Sys. Meas. Control* **2001**, *123*, 706–711. [CrossRef]
4. Gui, G.; Pan, H.; Lin, Z.; Li, Y.; Yuan, Z. Data-driven support vector machine with optimization techniques for structural health monitoring and damage detection. *KSCE J. Civ. Eng.* **2017**, *21*, 523–534. [CrossRef]
5. Jimenez, L.O.; Landgrebe, D.A. Supervised classification in high-dimensional space: geometrical, statistical, and asymptotical properties of multivariate data. *IEEE Trans. Syst. Man Cybern. Part C Appl. Rev.* **1998**, *28*, 39–54. [CrossRef]
6. Tibaduiza, D.; Mujica, L.; Rodellar, J. Damage classification in structural health monitoring using principal component analysis and self-organizing maps. *Struct. Control Health Monit.* **2013**, *20*, 1303–1316. [CrossRef]
7. Caggiano, A. Tool wear prediction in Ti-6Al-4V machining through multiple sensor monitoring and PCA features pattern recognition. *Sensors* **2018**, *18*, 823. [CrossRef] [PubMed]
8. Sharma, A.; Paliwal, K.K.; Onwubolu, G.C. Class-dependent PCA, MDC and LDA: A combined classifier for pattern classification. *Pattern Recognit.* **2006**, *39*, 1215–1229. [CrossRef]
9. Elvira, M.; Iáñez, E.; Quiles, V.; Ortiz, M.; Azorín, J.M. Pseudo-online BMI based on EEG to detect the appearance of sudden obstacles during walking. *Sensors* **2019**, *19*, 5444. [CrossRef] [PubMed]
10. Jeong, M.; Choi, J.H.; Koh, B.H. Isomap-based damage classification of cantilevered beam using modal frequency changes. *Struct. Control Health Monit.* **2014**, *21*, 590–602. [CrossRef]
11. Ullah, S.; Jeong, M.; Lee, W. Nondestructive inspection of reinforced concrete utility poles with ISOMAP and random forest. *Sensors* **2018**, *18*, 3463. [CrossRef] [PubMed]
12. Van Der Maaten, L.; Hinton, G.E. Visualizing data using t-SNE. *J. Mach. Learn. Res.* **2008**, *9*, 2579–2605.
13. Zhang, X.; Gou, L.; Li, Y.; Feng, J.; Jiao, L. Gaussian process latent variable model based on immune clonal selection for SAR target feature extraction and recognition. *J. Infrared Millim. Waves* **2013**, *32*, 231–236. [CrossRef]
14. Kebede, T.M.; Djaneye-Boundjou, O.; Narayanan, B.N.; Ralescu, A.; Kapp, D. Classification of malware programs using autoencoders based deep learning architecture and its application to the microsoft malware classification challenge (big 2015) dataset. In Proceedings of the 2017 IEEE National Aerospace and Electronics Conference (NAECON), Dayton, OH, USA, 27–30 June 2017.

15. Li, Y.; Wang, Y.; Zi, Y.; Zhang, M. An enhanced data visualization method for diesel engine malfunction classification using multi-sensor signals. *Sensors* **2015**, *15*, 26675–26693. [CrossRef]
16. Balamurali, M.; Melkumyan, A. *t*-SNE based visualisation and clustering of geological domain. In Proceedings of the International Conference on Neural Information Processing, Kyoto, Japan, 16–21 October 2016.
17. Peng, Z.; Cao, C.; Liu, Q.; Pan, W. Human walking pattern recognition based on KPCA and SVM with ground reflex pressure signal. *Math. Probl. Eng.* **2013**, *2013*. [CrossRef]
18. Van Der Maaten, L. Learning a parametric embedding by preserving local structure. In Proceedings of the 12th International Conference on Artificial Intelligence and Statistics, Clearwater, FL, USA, 16–19 April 2009.
19. Agis, D.; Pozo, F. A frequency-based approach for the detection and classification of structural changes using t-SNE. *Sensors* **2019**, *19*, 5097. [CrossRef]
20. Westerhuis, J.A.; Kourti, T.; MacGregor, J.F. Comparing alternative approaches for multivariate statistical analysis of batch process data. *J. Chemom. A J. Chemom. Soc.* **1999**, *13*, 397–413. [CrossRef]
21. Pozo, F.; Vidal, Y.; Salgado, Ó. Wind turbine condition monitoring strategy through multiway PCA and multivariate inference. *Energies* **2018**, *11*, 749. [CrossRef]
22. Smolensky, P. Information processing in dynamical systems: foundations of harmony theory. In *Parallel Distributed Processing: Explorations in the Microstructure of Cognition, Foundations*; Rumelhart, D.E., McClelland, J.L., Eds.; MIT Press: Cambridge, MA, USA, 1986; Volume 1, pp. 194–281.
23. Hinton, G.E. A practical guide to training restricted Boltzmann machines. In *Neural Networks: Tricks of the Trade*; Springer: Berlin, Germany, 2012; pp. 599–619.
24. Hinton, G.E. Training products of experts by minimizing contrastive divergence. *Neural Comput.* **2002**, *14*, 1771–1800. [CrossRef]
25. Orfanidis, S.J. *Introduction to Signal Processing*; Prentice-Hall, Inc.: Upper Saddle River, NJ, USA, 1995.
26. Hossin, M.; Sulaiman, M. A review on evaluation metrics for data classification evaluations. *Int. J. Data Min. Knowl. Manage. Process* **2015**, *5*, 1–11.
27. Krüger, F. Activity, Context, and Plan Recognition with Computational Causal Behaviour Models. Ph.D. Thesis, University of Rostock, Mecklenburg, Germany, 26 September 2016.
28. Hameed, N.; Hameed, F.; Shabut, A.; Khan, S.; Cirstea, S.; Hossain, A. An intelligent computer-aided scheme for classifying multiple skin lesions. *Computers* **2019**, *8*, 62. [CrossRef]

Apéndice A

Factor de impacto y categoría de las revistas

Revista	**JCR 2019 y cuartil**	**Categoría**
Structural Control and Health Monitoring	3.499	
	Q1 (12/64)	**Instruments & Instrumentation**
	Q1 (13/63)	Construction & Building Technology
	Q1 (20/134)	Civil Engineering
Sensors	3.275	
	Q1 (15/64)	**Instruments & Instrumentation**
	Q2 (22/86)	Analytical Chemistry
	Q2 (77/266)	Electrical & Electronic Engineering

Revista	**SJR 2019 y cuartil**	**Categoría**
Structural Control and Health Monitoring	1.484	
	Q1	**Civil & Structural Engineering**
	Q1	Building & Construction
	Q1	Mechanics of Materials
Sensors	0.653	
	Q1	**Instrumentation**
	Q2	Analytical Chemistry
	Q2	Electrical & Electronic Engineering

Revista	**CiteScore 2019 y percentil**	**Categoría**
Structural Control and Health Monitoring	6.2	
	90 % (31/310)	**Civil & Structural Engineering**
	91 % (16/174)	Building & Construction
	87 % (47/367)	Mechanics of Materials
Sensors	5.0	
	87 % (17/129)	**Instrumentation**
	71 % (35/119)	Analytical Chemistry
	78 % (147/670)	Electrical & Electronic Engineering

Apéndice B

Contribución del doctorando

La contribución del doctorando David Agis Cherta en los tres artículos que constituyen la presente tesis doctoral fue la revisión sistemática de la literatura, el desarrollo de la idea, el diseño del marco de exploración, el desarrollo de la metodología propuesta, la selección de los algoritmos matemáticos adecuados para clasificar los diferentes estados estructurales, la realización de todos los análisis, la evaluación de los resultados, la redacción de los artículos, las correcciones requeridas por los revisores de las revistas y la presentación y discusión de los resultados en congresos.

Apéndice C

Otros trabajos

En este Apéndice, se presentan dos artículos en los cuales el doctorando participó como coautor, pero que no forman parte del compendio de artículos de esta tesis doctoral. También se presentan tres trabajos presentados en conferencias:

Artículo 1:

 Agis, D.; Vidal, Y.; Pozo, F. Damage diagnosis for offshore fixed wind turbines. *Renewable energy and power quality journal* 2019, 17(10), 366-370. Esta publicación en revista salió del **Trabajo 1 presentado en conferencia:**

Damage diagnosis for offshore fixed wind turbines, ICREPQ'19 Tenerife, España, 10-12 Abril 2019.

Artículo 2:

 Tibaduiza, D.A.; Gómez, R.C.; Pedraza, C.; Agis, D.; Pozo, F. Damage identification in structural health monitoring: A brief review from its implementation to the use of data-driven applications. *Sensors* 2020, 20(3), 733.

Trabajo 2 presentado en conferencia:

Detection and classification of structural changes using t-distributed stochastic neighbor embedding, ICEDyn'19 Viana do Castelo, Portugal, 24-26 Junio 2019.

Trabajo 3 presentado en conferencia:

Vibration-based structural health monitoring using piezoelectric transducers and parametric t-SNE, EACS'20 Varsovia, Polonia, 12-15 Julio 2020 (trabajo aceptado, pero no presentado, ya que se pospone al 2021 por el COVID-19).

17th International Conference on Renewable Energies and Power Quality(ICREPQ'19)
Tenerife, Spain, 10th to 12th April, 2019
Renewable Energy and Power Quality Journal (RE&PQJ)
ISSN 2172-038 X, Volume No.17, July 2019

Damage diagnosis for offshore fixed wind turbines

D. Agis[1], Y. Vidal[1], and F. Pozo[1]

[1]Mathematics Department,
Control, Modeling, Identification and Applications,
Escola d'Enginyeria de Barcelona Est
[1] Universitat Politècnica de Catalunya,
Campus Diagonal-Besòs, 08019 Barcelona (Spain)
Phone number:+0034934137309, e-mail: {**david.agis, yolanda.vidal, francesc.pozo**}**@upc.edu**

Abstract. This paper proposes a damage diagnosis strategy to detect and classify different type of damages in a laboratory offshore-fixed wind turbine model. The proposed method combines an accelerometer sensor network attached to the structure with a conceived algorithm based on principal component analysis (PCA) with quadratic discriminant analysis (QDA).

The paradigm of structural health monitoring can be undertaken as a pattern recognition problem (comparison between the data collected from the healthy structure and the current structure to diagnose given a known excitation). However, in this work, as the strategy is designed for wind turbines, only the output data from the sensors is used but the excitation is assumed unknown (as in reality is provided by the wind).

The proposed methodology is tested in an experimental laboratory tower modeling an offshore-fixed jacked-type wind turbine. The obtained results show the reliability of the proposed approach.

Key words

Damage diagnosis, structural health monitoring, wind turbine.

1. Introduction

Wind energy is one of the best fuel sources since it is clean, relatively cheap and inexhaustible. In order to increase the energy produced by these means, more and more wind farms have been installed in the sea. Taking into account the location of wind turbines and the conditions of the sea, new problems arise, since inspection and maintenance work becomes more difficult. To reduce the enormous logistic and maintenance costs as well as to minimize turbine downtime, wind turbines must be continuously monitored. Among all the monitoring systems, two systems can be highlighted: structural health monitoring (SHM) and condition monitoring (CM). On one hand, a structural health monitoring system verifies the mechanical state of the structure to ensure its proper functioning and determines whether the wind turbine needs some kind of maintenance. On the other hand, a condition monitoring system is able to detect faults in the sensors and/or actuators systems. Traditionally, condition monitoring for WTs has focused on two widely-used methods: vibration analysis and oil monitoring [1]. Therefore, the capability to detect wind turbine damage and faults is crucial to decrease the cost of wind energy [2], [3]. SHM and damage detection have been widely studied in recent years. A review of the state-of-the-art revealed that damage detection is a very active field, but there is not a universal optimum method for it.

This work proposes a complete methodology for damage detection and classification in a laboratory offshore-fixed wind turbine model. The strategy combines: (i) the use of an accelerometer sensor network attached to the structure; (ii) the use of principal component analysis (PCA) as a pre-processing step to both reduce the dimensionality of the data and extract features; and (iii) a quadratic discriminant analysis (QDA). It should be noted that PCA has been widely used in the field of SHM either as the single strategy [4] or in combination with univariate [5] and multivariate [6] hypothesis testing. Furthermore, methods based on principal component analysis (PCA) have also proven its capability to build WT fault detection strategies [7], [3], [8]. However, QDA is most commonly used in medicine [9], [10] and genomics [11], [12], as a classifier or as a pattern-recognition method. A recent application of QDA in WT fault detection is proposed by [13] where an approach for detecting and diagnosing the delamination in wind turbine blades is proposed.

As in [14], it is supposed that the only available excitation of the WTs is the wind turbulence, so the input excitation is assumed to be unknown. Therefore, the scheme of the proposed method can be summarized in the following steps: (i) the wind excitation is simulated as a Gaussian white noise and the data coming from the WT is collected using a set of accelerometers. It is worth remarking that only output data will be used to detect damage; (ii) the raw data is pre-processed using group-scaling to simplify the computation of the principal components; (iii) PCA is selected as a technique to reduce the dimensionality of the data and the computing time of the next step; finally, (iv) the quadratic discriminant analysis (QDA) is used as a classifier. In the end, 10-fold crossvalidation technique

is employed to estimate the overall accuracy and to avoid over-fitting. In order to validate the proposed approach in this work, the damage detection strategy is applied to different types of predefined damage in a small-scale structure —an experimental laboratory tower modeling an offshore-fixed jacked-type wind turbine—. The results that have been obtained for these predefined damages are included and discussed to demonstrate the reliability of the proposed approach.

The structure of the paper is as follows. We first present the scaled wind turbine model, together with the two types of damage that are introduced at the jacket support and the sensors placed in the tower and jacket. We then present the damage diagnosis strategy that includes how data is collected, reshaped and auto scaled. Subsequently, both PCA and QDA are briefly described. Finally, the main results are summarized and discussed and some conclusions are drawn.

2. Laboratory Tower Definition

A. Structure

The real structure used in this work is a scaled WT tower model, see Figure 1. This structure is 2.7 m high and it is composed, mainly, of three parts:

1) Jacket support, it is a lattice structure composed with several bars, all of them joined with bolts with a torque of 12 Nm.
2) Tower, composed of three sections joined with bolts.
3) Nacelle, modeled in this experiment by the top beam of 1 m long and 0.6 m width and a modal shaker located at one edge of the beam.

The shaker simulates the nacelle mass and the environmental effects of the wind over the whole structure. The vibration needed to excite the structure is created by applying an electrical signal to the shaker (Gaussian white noise).

B. Damages

Two types of damage are introduced at the jacket support:

(a) a 5 mm crack in one of the bars; and
(b) loosening one of the bolts in the jacket.

Also a healthy replica of the studied bar has been considered. The proposed strategy should be able to detect and classify the studied faults, but also be robust to the replacement of one bar by a new healthy one (avoiding false alarms).

C. Sensors

To analyze the structural response, eight triaxial accelerometers are placed in the tower and jacket. The method used to find the optimum location and amount of these sensors is given in [15]. Thus, data from 24 sensors is collected. The nomenclature used for each sensor is given in Table I.

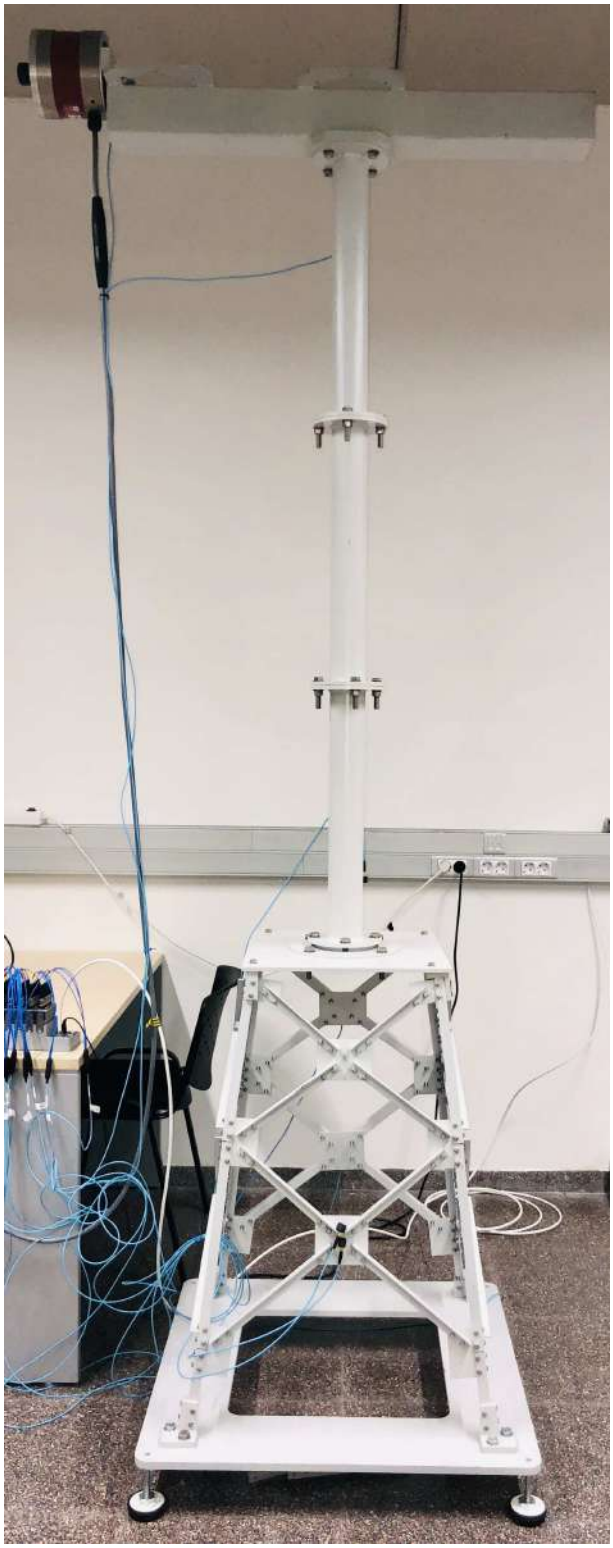

Fig. 1. WT scaled tower model used in the experimental tests (off-shore fixed jacked-type platform).

3. Damage diagnosis strategy

A. Data collection

The time window for each experimental test is 60 seconds with a sampling frequency of 1651.6129 Hz. Thus,

TABLE I

NOMENCLATURE USED TO REFER TO EACH AVAILABLE SENSOR. NOTE THAT $i = 1, \ldots, 8$, AS THERE ARE EIGHT ACCELEROMETERS.

	Sensor
A_i^x	Acceleration in x-direction for accelerometer number i
A_i^y	Acceleration in y-direction for accelerometer number i
A_i^z	Acceleration in z-direction for accelerometer number i

each experiment obtains $1651.6129 \times 60 = 99097$ data measurements from each of the 24 sensors. Given the k-th experimental test, the data is initially stored in a matrix $\mathbf{Y}^{(k)} \in \mathcal{M}_{24\times 99097}(\mathbb{R})$ such that

$$\mathbf{Y}^{(k)} = \begin{pmatrix} y_{1,1}^{(k)} & y_{1,2}^{(k)} & \cdots & y_{1,99097}^{(k)} \\ y_{2,1}^{(k)} & y_{2,2}^{(k)} & \cdots & y_{2,99097}^{(k)} \\ \vdots & \vdots & \ddots & \vdots \\ y_{24,1}^{(k)} & y_{24,2}^{(k)} & \cdots & y_{24,99097}^{(k)} \end{pmatrix}, \quad (1)$$

where the number of rows is given by the number of sensors and the number of columns is equal to the number of time stamps in each experimental test. Note that data in the first row is related to sensor A_1^x, data in the second row is related to sensor A_1^y, third row is related to A_1^z, fourth row to A_2^x, and so on and so forth. Finally, the matrix is reshaped, by concatenating its rows, to form a row-vector with $99097 \times 24 = 2378328$ components. That is, from each experimental test, a row-vector $z^{(k)} \in \mathcal{M}_{1\times 2378328}(\mathbb{R})$ is obtained such that

$$z^{(k)} = (z_1^{(k)}, \ldots, z_j^{(k)}, \ldots, z_{24}^{(k)}) \in \mathcal{M}_{1\times(99097\cdot 24)}(\mathbb{R}) \quad (2)$$

where

$$z_j^{(k)} = (y_{j,1}^{(k)}, \ldots, y_{j,99097}^{(k)}) \in \mathcal{M}_{1\times 99097}(\mathbb{R}),\ j = 1, \ldots, 24. \quad (3)$$

In this work, a total of 25 experimental tests are conducted. In particular:

(i) 10 tests with the original healthy bar.
(ii) 5 tests with the replica bar.
(iii) 5 tests with the 5 mm crack damaged bar.
(iv) 5 tests with an unlocked bolt in the jacket.

The data from all the experimental tests is stored in a matrix $\mathbf{Z} \in \mathcal{M}_{25\times 2378328}$, where each row, $k = 1, \ldots, 25$, is given by the row-vector $z^{(k)}$ as defined in Equation (2):

$$\mathbf{Z} = \begin{pmatrix} z^{(1)} \\ \vdots \\ z^{(k)} \\ \vdots \\ z^{(25)} \end{pmatrix} \in \mathcal{M}_{25\times(99097\cdot 24)}(\mathbb{R}). \quad (4)$$

B. Data reshape (Sample Size and Power Analysis)

The input dataset, $\mathbf{Z}$, consists of a matrix with a small number of experimental tests, only 25, and a large number of data measurements, 99097×24. When a small sample size is used in data analysis, this might be insufficient to detect wind turbine damages. For this reason, we propose to reshape the matrix $\mathbf{Z}$ in order to increase the statistical power, by means of increasing the number of experimental tests. In addition, with this reshaping, the time window for each sample is reduced from 60 to 1.46 seconds. Therefore, leading to a fault detection time reduction. Thus, we reshape the matrix $\mathbf{Z}$ as follows: for each row and sensor, we split the 99097 time stamps to 41 subsets of 2417 time instants. Therefore, we get a total of 41 experimental tests with 2417 data measurements for each original row and sensor:

$$\mathbf{x}_j^{(k)} = \begin{pmatrix} z_{j,1}^{(k)} & \cdots & z_{j,2417}^{(k)} \\ z_{j,2418}^{(k)} & \cdots & z_{j,4834}^{(k)} \\ \vdots & \ddots & \vdots \\ z_{j,96681}^{(k)} & \cdots & z_{j,99097}^{(k)} \end{pmatrix} \in \mathcal{M}_{41\times 2417}(\mathbb{R}), \quad (5)$$

where $z_{j,i}^{(k)},\ j = 1, \ldots, 24,\ i = 1, \ldots, 99097$ is defined as the i-th component of the vector $z_j^{(k)}$ defined in Equation (3). Equivalently,

$$z_{j,i}^{(k)} = y_{j,i}^{(k)},\ j = 1, \ldots, 24,\ i = 1, \ldots, 99097.$$

Similarly, matrix $\mathbf{x}_j^{(k)}$ can be defined as

$$\left(\mathbf{x}_j^{(k)}\right)_{mn} = z_{j,2417\cdot(m-1)+n}^{(k)},$$

where $m = 1, \ldots, 41$ and $n = 1, \ldots, 2417$.

Then, the measurements are arranged in a matrix $\mathbf{X} \in \mathcal{M}_{(41\cdot 25)\times(2417\cdot 24)}(\mathbb{R}) = \mathcal{M}_{1025\times 58008}(\mathbb{R})$:

$$\mathbf{X} = \begin{pmatrix} \mathbf{x}_1^{(1)} & \cdots & \mathbf{x}_j^{(1)} & \cdots & \mathbf{x}_{24}^{(1)} \\ \mathbf{x}_1^{(2)} & \cdots & \mathbf{x}_j^{(2)} & \cdots & \mathbf{x}_{24}^{(2)} \\ \vdots & \ddots & \vdots & \ddots & \vdots \\ \mathbf{x}_1^{(25)} & \cdots & \mathbf{x}_j^{(25)} & \cdots & \mathbf{x}_{24}^{(25)} \end{pmatrix}. \quad (6)$$

It is to be assumed that larger sample sizes will improve data analysis.

C. Autoscaling

The main reason to autoscale the raw data is to simplify the computations for the multiway PCA decomposition. Autoscaling uses column-wise mean-centering followed by division of each column by the standard deviation of that column of matrix $\mathbf{X}$. The result is that each column of the new autoscaled matrix, $\tilde{\mathbf{X}}$, has a mean of zero and a standard deviation of one. The fact that $\tilde{\mathbf{X}}$ is a mean-centered matrix simplifies the empirical covariance matrix computation, needed for the PCA decomposition.

D. Principal component analysis and quadratic discriminant analysis

Recall that, before using a classifier, the data must be processed to obtain the most suitable features. In this work, after the autoscaling step, multiway PCA is selected as the main objective is to reduce computing time for the quadratic discriminant analysis classifier. In this work, only the first 30 components of the PCA decomposition are used as they account for 75% of the variance. Thus, the transformed coordinates of the $\tilde{\mathbf{X}}$ data in the new basis given by the first 30 principal components are used as features by the QDA strategy.

It is beyond the purpose of this work to give a detailed explanation of the QDA approach. An excellent tutorial about the basic background needed to understand the discriminant analysis classifier is given in [16]. However, it is important to recall that it is assumed that the measurements from each class are normally distributed. Unlike linear discriminant analysis (DA) however, in QDA there is no assumption that the covariance of each of the classes is identical. When the normality assumption is true, the best possible test for the hypothesis that a given measurement is from a given class is the likelihood ratio test. Thus, in a nutshell, the QDA classifier models the likelihood of each class as a Gaussian distribution, and then uses the posterior distributions to estimate the class for a given test point [17]. The Gaussian parameters for each class can be estimated from training points with maximum likelihood estimation. In this work, the one-sample Kolmogorov-Smirnov test, see [18], is used to test the normality of the data. The null hypothesis is that the data comes from a standard normal distribution, against the alternative that it does not come from such a distribution. The test fails to reject the null hypothesis at a 5% significance level. Furthermore, we confirm the test decision by visually comparing the empirical cumulative distribution function to the standard normal (Gaussian) one, see Figure 2.

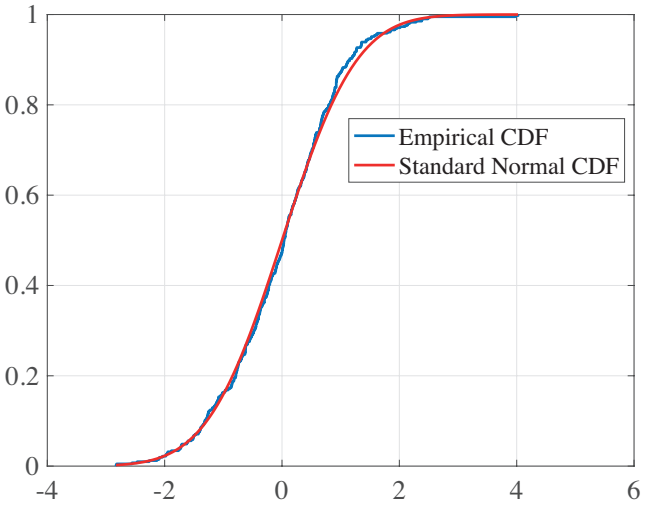

Fig. 2. Empirical cumulative distribution function.

Finally, in this work, the 10-fold crossvalidation technique has been employed to estimate the overall accuracy and to avoid over-fitting.

4. Results and discussion

Table II summarizes the results obtained from the proposed strategy. It presents not only the overall accuracy, but also the training time and prediction speed, as both parameters are critical in real application. Notice that the obtained prediction speed allows this methodology to be deployed for online (real-time) condition monitoring in WTs.

TABLE II
SUMMARY OF THE OBTAINED RESULTS.

Accuracy (%)	95.2
Training time (s)	9.5
Prediction speed (obs/s)	7300

Besides, a comprehensive decomposition of the error between the true classes and the predicted classes is shown by means of the so called confusion matrix, see Figure 3. In these matrices, each row represents the instances in a true class while each column represents the instances in a predicted class (by the classifier). In particular, first row (and first column) is labeled as 0 and corresponds to the healthy case. Next labels (for rows and columns) correspond to the replica bar (label 1), the 5 mm crack (label 2), and the unlocked bolt (label 3). From the confusion matrix the following issues can be highlighted. The healthy class has a true positive rate (TPR), that is percentage of correctly classified instances, of 90% and a false negative rate (FNR), that is percentage of incorrectly classified instances, of 10%. It is noteworthy that the 5 mm crack damage has a TPR of 99% and the unlocked bolt damage has a TPR of 100%.

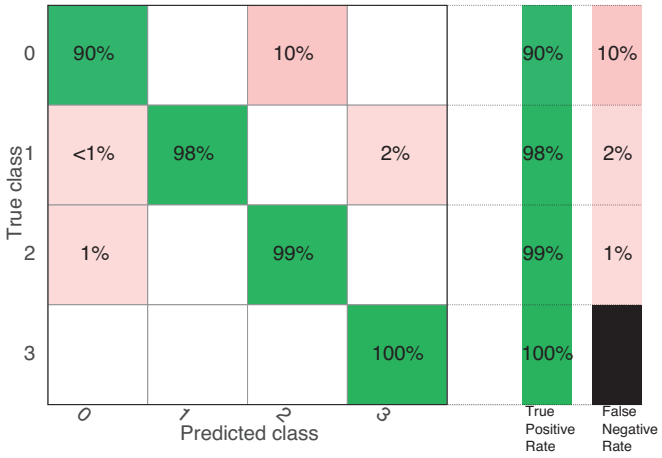

Fig. 3. Confusion matrix.

5. Conclusions and future work

This work has proposed a damage detection and classification strategy and tested it in a laboratory WT model. The results show a 95.2% overall accuracy. The immediate future work is to develop further the proposed strategy for different environmental and operational conditions which could be modeled by using different amplitudes for the white noise excitation.

Acknowledgement

This work has been partially funded by the Spanish Ministerio de Economía, Industria y Competitividad (MINECO) through the research project DPI2014-58427-C2-1-R; by the Spanish Agencia Estatal de Investigación (AEI) - Ministerio de Economía, Industria y Competitividad (MINECO), and the Fondo Europeo de Desarrollo Regional (FEDER) through the research project DPI2017-82930-C2-1-R; and by the Generalitat de Catalunya through the research project 2017 SGR 388. We gratefully acknowledge the support of NVIDIA Corporation with the donation of the Titan Xp GPU used for this research. We thank the Universitat Politècnica de Catalunya (UPC) for pre-doctoral fellowship (to D. A.).

References

[1] P. Tchakoua, R. Wamkeue, M. Ouhrouche, F. Slaoui-Hasnaoui, T. A. Tameghe, and G. Ekemb, "Wind turbine condition monitoring: State-of-the-art review, new trends, and future challenges," *Energies*, vol. 7, no. 4, pp. 2595–2630, 2014.

[2] F. Pozo, Y. Vidal, and Ó. Salgado, "Wind turbine condition monitoring strategy through multiway pca and multivariate inference," *Energies*, vol. 11, no. 4, p. 749, 2018.

[3] F. Pozo and Y. Vidal, "Damage and fault detection of structures using principal component analysis and hypothesis testing," in *Advances in Principal Component Analysis*, pp. 137–191, Springer, 2018.

[4] L. Mujica, J. Rodellar, A. Fernandez, and A. Güemes, "Q-statistic and t2-statistic pca-based measures for damage assessment in structures," *Structural Health Monitoring*, vol. 10, no. 5, pp. 539–553, 2011.

[5] L. Mujica, M. Ruiz, F. Pozo, J. Rodellar, and A. Güemes, "A structural damage detection indicator based on principal component analysis and statistical hypothesis testing," *Smart materials and structures*, vol. 23, no. 2, p. 025014, 2013.

[6] F. Pozo, I. Arruga, L. E. Mujica, M. Ruiz, and E. Podivilova, "Detection of structural changes through principal component analysis and multivariate statistical inference," *Structural Health Monitoring*, vol. 15, no. 2, pp. 127–142, 2016.

[7] Y. Wang, X. Ma, and P. Qian, "Wind turbine fault detection and identification through pca-based optimal variable selection," *IEEE Transactions on Sustainable Energy*, 2018.

[8] P. F. Odgaard and J. Stoustrup, "Gear-box fault detection using time-frequency based methods," *Annual Reviews in Control*, vol. 40, pp. 50–58, 2015.

[9] R. S. Ryback, M. J. Eckardt, R. R. Rawlings, and L. S. Rosenthal, "Quadratic discriminant analysis as an aid to interpretive reporting of clinical laboratory tests," *Jama*, vol. 248, no. 18, pp. 2342–2345, 1982.

[10] G. Zonta, G. Anania, B. Fabbri, A. Gaiardo, S. Gherardi, A. Giberti, N. Landini, C. Malagù, L. Scagliarini, and V. Guidi, "Preventive screening of colorectal cancer with a device based on chemoresistive sensors," *Sensors and Actuators B: Chemical*, vol. 238, pp. 1098–1101, 2017.

[11] M. Q. Zhang, "Identification of protein coding regions in the human genome by quadratic discriminant analysis," *Proceedings of the National Academy of Sciences*, vol. 94, no. 2, pp. 565–568, 1997.

[12] L. Zhang and L. Luo, "Splice site prediction with quadratic discriminant analysis using diversity measure," *Nucleic Acids Research*, vol. 31, no. 21, pp. 6214–6220, 2003.

[13] A. Arcos Jiménez, C. Q. Gómez Muñoz, and F. P. García Márquez, "Machine learning for wind turbine blades maintenance management," *Energies*, vol. 11, no. 1, p. 13, 2017.

[14] F. Pozo and Y. Vidal, "Wind turbine fault detection through principal component analysis and statistical hypothesis testing," *Energies*, vol. 9, no. 1, p. 3, 2015.

[15] E. Zugasti Uriguen, *Design and validation of a methodology for wind energy structures health monitoring*. PhD thesis, Universitat Politècnica de Catalunya, 2014.

[16] A. Tharwat, "Linear vs. quadratic discriminant analysis classifier: a tutorial," vol. 3, p. 145, 01 2016.

[17] J. Friedman, T. Hastie, and R. Tibshirani, *The elements of statistical learning*, vol. 1. Springer series in statistics New York, NY, USA:, 2001.

[18] F. J. Massey Jr, "The kolmogorov-smirnov test for goodness of fit," *Journal of the American statistical Association*, vol. 46, no. 253, pp. 68–78, 1951.

sensors

MDPI

Review

Damage Identification in Structural Health Monitoring: A Brief Review from its Implementation to the Use of Data-Driven Applications

Diego A. Tibaduiza Burgos [1,*], Ricardo C. Gomez Vargas [1,2], Cesar Pedraza [3], David Agis [4] and Francesc Pozo [4]

1 Departamento de Ingeniería Eléctrica y Electrónica, Universidad Nacional de Colombia, Cra 45 No. 26-85, Bogotá 111321, Colombia; rcgomezv@unal.edu.co
2 Escuela de Tecnologías de la información y la comunicación, Politécnico Grancolombiano Institución Universitaria, Bogotá 111321, Colombia
3 Departamento de Ingeniería de Sistemas e Industrial, Universidad Nacional de Colombia, Cra 45 No. 26-85, Bogotá 111321, Colombia; capedrazab@unal.edu.co
4 Control, Modeling, Identification and Applications (CoDAlab), Departament de Matemàtiques, Escola d'Enginyeria de Barcelona Est (EEBE), Universitat Politècnica de Catalunya (UPC), Campus Diagonal-Besòs (CDB), Eduard Maristany, 16, 08019 Barcelona, Spain; david.agis@upc.edu (D.A.); francesc.pozo@upc.edu (F.P.)
* Correspondence: dtibaduizab@unal.edu.co; Tel.: +57-1-316-5000 (ext. 11103)

Received: 8 November 2019; Accepted: 20 January 2020; Published: 29 January 2020

Abstract: The damage identification process provides relevant information about the current state of a structure under inspection, and it can be approached from two different points of view. The first approach uses data-driven algorithms, which are usually associated with the collection of data using sensors. Data are subsequently processed and analyzed. The second approach uses models to analyze information about the structure. In the latter case, the overall performance of the approach is associated with the accuracy of the model and the information that is used to define it. Although both approaches are widely used, data-driven algorithms are preferred in most cases because they afford the ability to analyze data acquired from sensors and to provide a real-time solution for decision making; however, these approaches involve high-performance processors due to the high computational cost. As a contribution to the researchers working with data-driven algorithms and applications, this work presents a brief review of data-driven algorithms for damage identification in structural health-monitoring applications. This review covers damage detection, localization, classification, extension, and prognosis, as well as the development of smart structures. The literature is systematically reviewed according to the natural steps of a structural health-monitoring system. This review also includes information on the types of sensors used as well as on the development of data-driven algorithms for damage identification.

Keywords: data-driven algorithms; damage identification; structural health monitoring; sensors

1. Introduction

Ensuring the proper performance of all elements in a structure is a priority for designers and users. In most cases, continuous monitoring can detect damages at an early stage can prevent potential accidents and catastrophes that result from inadequate inspection or damages to the evaluation process. Structural health monitoring (SHM) involves the use of continuous monitoring using sensors that are permanently attached to the structure, together with algorithms related to the damage-identification

process. There are several advantages associated with the use of an SHM system, some of which are listed below:

- the continuous monitoring of the structure since sensors are a part of it;
- the possibility of real-time damage detection;
- the possibility of using sensor or actuator networks;
- robust data analysis that can provide relevant information about the damage;
- an automated inspection process to reduce the number of unnecessary maintenance tasks, thereby improving the economic benefits; and
- operational and environmental evaluation conditions.

Although SHM is still a developing area—as evidenced by the rapid increase in the number of research works and publications—research has been ongoing for the past 23 years [1]. Both the benefits in the above list and the advances in computation and data science applications motivate the continually rising interest in structural health-monitoring applications.

Different levels of damage diagnosis in SHM were proposed by Rytter [2]. These levels are defined on the basis of the information that can be obtained during the damage identification process. In general, *damage detection* is the first level of damage diagnosis and can provide information about irregular behavior of the structure that, in some cases, can be regarded as possible damage [3]. After damage detection, damage localization (Where is the damage?), damage classification (What kind of damage does the structure have? damage extention) and damage prognosis (What is the remaining useful life of the system?) are considered, as shown in Figure 1.

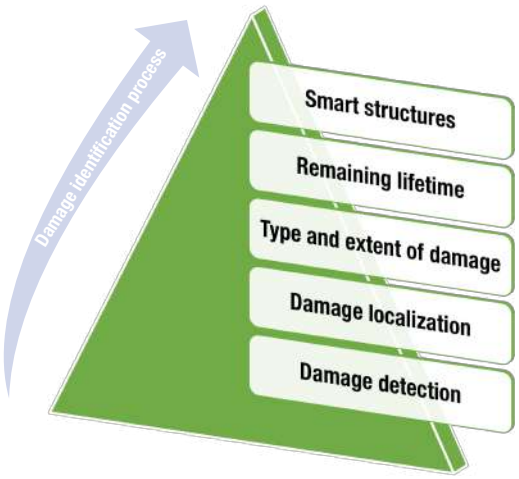

Figure 1. Damage identification levels.

Different algorithms and methodologies have been developed for each level of the damage identification process, including the management of historical information on the functioning of the structure, and they often use different sensors and actuators, materials, and configurations. Some of the works available in the literature have focused on problems related to a single level of SHM [4], a specific application [5], a specific technique [6], or a certain type of sensor for inspection [7]. For example, at the level of damage detection, aspects such as sensor locations and the use of wireless sensor networks [8] as well as the use of specific kinds of sensors or sensor networks, such as microelectromechanical systems (MEMS) [9], accelerometers, optical fibers [10], vibration sensors [11], and pressure-based sensors [12] have been addressed. Similarly, this level has been tackled using different techniques, as shown throughout this review. Neural networks [13–15], modal analysis [16], bio-inspired algorithms [17], non-probabilistic methodologies [18], and time series analysis [19–21] are among the main techniques that are used. The autonomy of SHM systems has also been addressed through the possible ways

in which they obtain energy [22]. Other works have examined the use of mechanical energy from different sources, such as thermal energy, wind energy, solar energy, electromagnetic sources, or hlRF antennas [23].

Other state-of-the-art reviews have concentrated on SHM applications in different areas, such as the aeronautical industry [22], wind generation [24], civil engineering applications [25], and naval engineering [26]. It is also possible to find review papers that are oriented toward the development of SHM methodologies with guided waves [27,28] and the use or integration of the Internet of Things (IoT) [29] in SHM applications.

This review is focused on the use of data-driven methodologies for all levels of the damage-identification process. This work is organized as follows: Section 2 is devoted to the description of the SHM process, including different approaches to analyzing SHM systems and the variables that are identified in the operational and environmental conditions that affect damage identification. In Section 3, the SHM process and its implementation are described. The implementation of SHM is included in Section 4, along with information about some of the elements of SHM systems such as data acquisition, sensors and actuators, and preprocessing strategies. This section also presents works on the decision-making process. Finally, conclusions drawn from the reviewed literature are summarized in Section 5.

2. Description of the SHM Processes

Several definitions have been used to define damage; however, one of the most accepted definitions was given by Farrar and Worden [30]:

> "Damage is defined as changes to the material and/or geometric properties of these systems, including changes to the boundary conditions and system connectivity, which adversely affect the system's performance."

This definition indirectly implies that all SHM applications, including online monitoring, require an adequate sensor network system to evaluate possible changes in the structure that can affect its proper performance. Usually, the sensibility of the SHM system is associated with good interaction between the structure and the sensors. For this reason, it is very important to select appropriate sensors to be installed by considering the material of the structure to inspect, the variables to sense or measure, and the information to obtain for damage identification.

For SHM applications, increasing the reliability of the forecasts or predictions and the damage identification process is a fundamental task in the implementation of these approaches in the industry. Therefore, the number of false positives detected because of noise or the acquisition process must be minimized. For this purpose, some reliability indices have been proposed. For instance, reliability analysis has been based on the estimated distributions of dead, live, and wind loads in long-span bridges [31].

Failures caused by inconsistencies between the capturing techniques, the information of the sensors, the processing of the information captured, and the analysis of data for the forecast can affect the results obtained from the algorithms or the methodologies used in the damage-identification process [17,32].

In SHM, several current approaches to evaluating the integrity of a structure at any moment under different operating conditions are based on measuring changes in the mechanical, physical, or chemical behavior of the structures under inspection. As illustrated in the following sections, various techniques have been implemented to capture and analyze information from a sensor network that is installed and used for continuous monitoring. As discussed later in this paper, the analysis carried out in some of the current methodologies not only aims to identify possible existing damages but also is used in the development of forecasts about the future behavior of the inspected materials and structures.

In general, SHM developments can be classified into two large groups [30]: *model-based* approaches and *data-driven* approaches. In the first type of approach, theoretical information or data acquired from

the structure are used to build a mathematical or physical model to predict the behavior of a structure in different scenarios and with different variations in operational and environmental conditions. Model-based approaches make frequent use of finite element analysis (FEA) [33]. The second approach to damage identification relies on the analysis of data acquired directly from the structure. In general, this analysis can be performed under the pattern recognition paradigm [30]: that is, data obtained from the healthy structure are used to build a pattern and data from the structure during the inspection process are used to determine its current state by comparing some features obtained from the inspection data with the baseline. Both types of methods—model-based and data-based—can be applied at every level of the damage-identification process in Figure 1. This means that, currently, there are different strategies that consider a single level or multiple levels of the damage-identification process. Implementation at particular levels delivers specific results that may be the end of the process, depending on the application. It is also possible, for example, to build a solution of which the intended scope is limited to the detection and location of damages. In other cases, the expected scope is related to the implementation of the first four levels, thus determining the remaining useful life of the structure under inspection. However, it is clear that all levels present an incremental approximation since the implementation of a particular level requires the performance of the previous levels in the pyramid in Figure 1.

In terms of applications, different engineering associations and events perform analyses of SHM benchmarks, which present a set of solutions applicable to specific scenarios, such as the American Society of Civil Engineerings with the IASC-ASCE SHM Benchmark Study [34], and the international association for bridge maintenance and safety (IABMAS) conference decisions in Kyoto at 2014 with the benchmarks from the University of Central Florida and the Drexel University , and other studies that guide the instrumentation of civil structures. Similarly, other works, such as that in Reference [35], have developed a classification scheme for benchmarking methods in use that include simulation and implementation.

Since structures are subjected to operational and environmental variations during their use, it is necessary to consider these variables in the damage-identification process. In fact, these variations can be regarded as a disturbance in some SHM algorithms and need to be considered in order to reduce the possibility of a poor identification process. The subsequent sections provide a brief review of some works that have addressed operational and environmental conditions. All these works have been arranged using the four-step approach presented by Farrar [36].

3. SHM Implementation

Farrar [36] suggested that SHM developments must comply with economic, environmental, operational, and temporary restrictions, among others. These factors must be analyzed before proposing an SHM system as a solution. From this point of view, some works and considerations focused on these topics are summarized here.

3.1. Economic Justification

Before undertaking the development and application of a structural inspection scheme, it is important to ensure that the solution reached is coherent with respect to (i) the resources it will require; (ii) the response time; (iii) the margin of error that is allowed; and, in general, (iv) compliance with the operational conditions and constraints in the application of this kind of scheme.

Most applications of damage-detection schemes can reduce maintenance costs and the frequency of inspections. These detection schemes result in an increase in the remaining lifetime of the structures. For example, in the aeronautical industry, the utility of SHM is reflected by the reduced periodical revision times, the increased availability and safety of aircraft, and the decreased costs of scheduled repairs [37].

Industries such as power generation have reported substantial costs associated with the repair of turbines. These expenses are significantly increased in offshore platforms [38]. Therefore, the use of SHM as a tool to prevent sudden damage yields essential benefits in this industry [39].

One of the challenges associated with the use of SHM applications in industries is the initial cost of implementing the technology and of ensuring its overall reliability. In this context, the developments such as new transducers and low-cost sensor networks for inspecting large structures, together with the benefits gained by these low-cost sensors compared with the cost of visual supervision and traditional inspection methods in applications such as the inspection of civil structures [40], have resulted in the rapid expansion of the use of SHM. As stated previously, this expansion has been mainly driven by the economic advantages of its use and its fast implementation [41], with the clear and direct consequence of money saved in the long term.

3.2. Operational and Environmental Conditions

Structures in operation are subjected to the influence of operational and environmental conditions. These conditions affect the structures causing degradation, aging, and damage [42]; they are also the cause of possible false detections in SHM systems, due to the sensitivity of the methods to operational and environmental variables (EOVs) [43,44]. For that reason, the influence of these variables must be considered in the development of a reliable SHM system [45].

Reducing the influence of operating and environmental conditions presents excellent opportunities in industries such as aeronautics, in which significant advances that reduce failures of the SHM system have been generated by solutions such as the reduction in environmental noise during data acquisition through the use of transducers with low-frequency digital–analog converters [46], combined with transmission systems based on fibers that reduce the noise in the transmission [47]. Damage detection and classification approaches that consider the effect of temperature with multivariate analysis are available in the literature. These approaches combine, for instance, the use of principal component analysis (PCA) and machine learning (ML) [48] or PCA and self-organizing maps (SOM) [49]. Other approaches consider different elements, such as the influence of the viscoelastic material properties of the adhesives used by sensors on SHM applications [50], the influence of temperature and surface wetting on the ultrasonic waves used for damage detection [51], and the relationship between feature extraction and data fusion. Proposed solutions include the use of sensor data fusion, PCA, and self-organizing maps to compensate for the undesirable effect of temperature on damage detection and classification [49], the use of optimal baseline subtraction [52], and the effect of elevated temperatures on the adhesive layers of piezoelectric transducers (PZTs). Other works have examined the effects of temperature on baseline impedance profiles and the use of a small subset of baseline profiles for certain critical temperatures to estimate baseline profiles for a given ambient temperature through interpolation [53]. Finally, the use of local density in self-organizing maps has also been considered for two-level clustering as a methodology to compensate for the effects of temperature [54] or the effects of extreme aeronautical environments on the use of wireless sensors for SHM [55].

Structures such as those used for marine platforms, which are exposed to variable environmental conditions, have shown failures in their systems of damage detection and location. In this context, Prendergast et al. [56] presented an analysis of the variation in eigenfrequencies of turbines under progressive scour. The work reported by Zhou et al. [57] demonstrated an SHM approach for marine platforms that accounted for the variability of the ocean environment, vibration, corrosion, marine currents, and the effects of collisions modeled using a transfer matrix. Their approach enabled the calculation of changes in the form of the structure and the differentiation of possible failures. Other closely related works have presented dynamic models of the behavior of this type of structure; these models include the relationship between ocean currents under the ocean and wind currents on the surface, which may affect the analysis of the captured data [39]. Oliveira et al. [58] show the

implementation of modal analysis in turbines based on vibration, building strategies to reduce the influence of EOVs through statistical analysis.

In applications of SHM for civil structures, such as bridges or other buildings, the moving loads that affect these structures play a fundamental role in the determination of their lifetime. The use of vibration characteristics of vehicular bridges, which are analyzed as a source of vibration, has also been explored. For instance, methods such as mode shape as damage-detection indicator have been applied to analyze the behavior of a bridge [59]. Other proposals in this kind of structure seek to increase the reliability of operational modal analysis (OMA) concerning external phenomena, such as vibration [60], or the performance of estuaries in seismic areas [61].

Rainieri et al. [42] show the application of the second-order blind identification method (SOBI) to predict variations in natural frequencies, which makes it possible to compensate for the environmental influence on the use of OMA, this being a limitation of the PCA analysis. The implementation carried out requires a relatively low computational effort and obtaining a linear model between natural frequencies and unknown EOV sources.

3.3. Damage Definition

When using damag- detection techniques that are noninvasive and use sensors that are permanently installed on the structure, which is the case in SHM, the influence of the operation of the structure must be taken into account. This means that a small change in the structure can be detected as a different signal by the sensors, and the final result of the analysis can lead to a greater frequency of misclassification. In this case, the characterization of the behavior of the structure under different conditions and the definition of the influence of the operating conditions are critical tasks in the implementation of a reliable SHM system. It is very important to differentiate between a *normal* or an *acceptable* state and *damage* to determine whether the current state should be reported. Different studies have been carried out in this framework, with subjects ranging from the comparison of material [62] to the realization of failure models of structures.

The work in Reference [63] presents a list of modeling techniques for determining the existence of damage; they are based on the use of the smoothed finite element method (SFEM), focus on detection techniques based on high-frequency inputs, and use a number of tools for the definition of a fault.

3.4. Limitations

SHM has limitations associated with the capture and processing of data, the use of statistical models, and the interpretation of the results. As a consequence, ad hoc schemes must be generated for different SHM applications. Determining the limits of the application as well as the tools and the techniques involved can increase the certainty of the prediction.

Studies associated with nonlinear analysis methods have been reported in different works [64,65]. Similarly, methodological limitations caused by the propagation of linear excitation signals were described in Reference [66].

The inspection of structures using stationary cameras is an SHM practice that is widely used for civil structures. These procedures present challenges with respect to locating an optimal site at which to place the camera [67]. This problem, sometimes, is dealt with by using moving video systems. The work in Reference [68] introduced a solution to the limitations in the instrumentation of large civil structures. The proposed solution combined the use of georeferenced visual inspection systems with the use of technology such as the linear variable differential transducer (LVDT) and laser Doppler vibrometer (LDV).

Among the most important damage detection issues with any technique is its reliability, which is indispensable. Multiple works have reviewed this topic with respect to SHM [69–71]. Errors at the detection level have hindered the inclusion of SHM in industries such as the automotive and aeronautics sectors [72] and other mission-critical applications [73].

4. SHM Implementation Steps

From a general point of view, the implementation of an SHM system requires four steps: (i) the definition of the sensor/actuator system to attach to the structure; (ii) the data acquisition system; (iii) the preprocessing step; and (iv) the development of statistical models. These four steps are represented in a pyramid in Figure 2. These steps allow for the generation of solutions to challenges in the different levels of the damage-identification process (Figure 1). An additional level can even be included to consider *smart* solutions in which the previous levels are evaluated to determine the best combination of multiple configurations to produce an optimal solution to the damage-identification task.

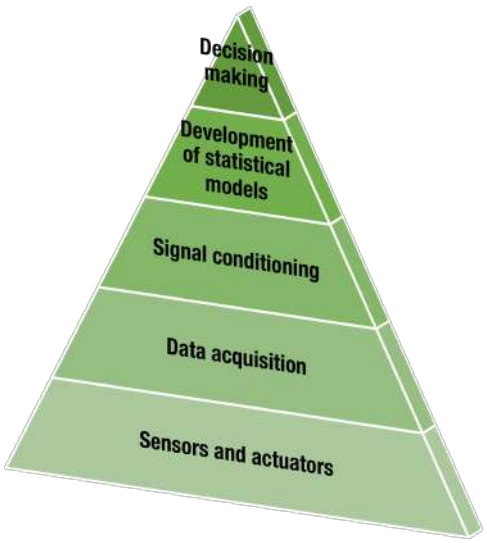

Figure 2. Development steps as a part of an structural health-monitoring (SHM) solution.

The lowest level in the pyramid in Figure 2, labeled "Sensor and actuator", defines the first part of the hardware that will be used. The sensor/actuator system must be selected considering, among other factors, the type of variables to measure, the constraints related to physical or environmental conditions, and the type of information to obtain. As stated previously, this level corresponds to the definition of the type of sensor to be used, the configuration of the sensor network, and the possible actuators, if required [74]. These configurations must agree with aspects such as maximum operating frequencies, the extent or size of the damage to be identified, possible locations, characterization, and, in general, the physical limitations of the application.

The next level in the pyramid is related to data acquisition, also known as DAQ. Data acquisition refers to the way in which the signals generated by each sensor are obtained. At this level, some of the SHM system's characteristics, such as cost, mobility, and scalability, need to be considered. The information acquired by the SHM system can be affected by aspects such as sensor configuration, operational and environmental noise, and any other event that differs from the initial setup of the system. Some of these problems must be resolved before performing any analysis on the generated information to generalize the techniques used for classification, identification, or recognition. This step corresponds to signal conditioning or preprocessing, and it can be performed by means of hardware devices, software algorithms, or both. In some cases, data can be corrupted or affected by a lossy transmission. These kinds of problems frequently appear, for instance, in applications that use wireless communication. This is the case for large structures [75]. Consequently, several works have addressed these issues to improve the reliability of data communication.

In most cases, the raw data obtained in the acquisition process require a data reduction step. For this purpose, a discrete wavelet transform (DWT) can reexpress the raw data by means of coefficients that decompose the data into so-called *details* and *coefficients* [76,77]. With this technique,

it is possible to obtain a reduced representation of the original data. Similarly, techniques such as PCA [78] and independent component analysis (ICA) have demonstrated their versatility in this respect by reducing data to a few components by the criteria of the retained variance [79].

The step called "Development of statistical models" includes the use of data analysis tools to determine the existence of abnormalities in the instrumented structure and to characterize the possible sources of these anomalies. This step directly influences the costs of the solution in both economic and computational terms, and it undoubtedly affects the detection, location, and characterization of damages.

As the final step, it is possible to use decision tools that support the intervention processes and to define possible action routes to take. This step, "Decision making", aims to reduce subjectivity in the development of the SHM process and to decrease the number of failures in the methods defined in the previous step. This step is not always considered or contemplated in an SHM solution.

4.1. Sensors and Actuators

From the perspective of SHM, damage detection requires the implementation of a set of sensors of which the main function is to capture information that can be used to determine the state of the structure under analysis [25]. Some inspection schemes use the propagation of a signal that may be produced by an actuator. The inspection schemes also depend on the types of transducers used and the kinds of signals propagated through the structure. As parts of a comprehensive sensor network, these sensors can obtain information from different parts of the specimen or structure under inspection. Similarly, sensor arrays require the use of various sources of excitation. In some cases, the actuators are located as close as possible to the sensors so that a transducer can serve as both an actuator and a sensor. This type of duality is exemplified by piezoelectric arrays [80].

The sensor/actuator system can be classified as *active* or *passive*. This classification depends on the source and whether the signals are propagated through the instrumented structure [81,82].

Passive methods only use sensors to detect variations in the received signals without the use of an external signal. The data obtained from these sensors can be used to detect structural abnormalities produced by the corrosion, deformation, or perforation of the materials [74,83]. Active inspection methods apply a known excitation and evaluate the data of the propagated signal. The excitation depends on the type of sensor and the interaction that is required within the structure.

4.1.1. Excitation Methods

Active inspection methods can be classified as *linear* or *nonlinear* [74], depending on the propagation of the signals. Linear methods include the pitch-catch mode, in which an ultrasonic signal is applied by an actuator and the propagated signal is received by another sensor [84,85]; the pulse-echo technique, in which signal reflections are detected and the same actuator captures the signal that it transmitted [86,87]; and electromechanical impedance spectroscopy (EMIS), which is used mostly with piezoelectric sensors that monitor changes in the structural-mechanical impedance [88]. Other linear methods have also been developed [89,90].

Some linear methods use the propagation of Lamb waves in metal structures [91] with piezoelectric sensor arrays because of their directionality and low dispersion [92]. The propagation of this type of signal is used recurrently in the development of intelligent materials. In Reference [93], the dual optimization on PZT sensors was investigated to decrease the barrier imposed by the requirement of lines of the base (BF-SHM). The method used in the aeronautical industry varies the Lamb wave signals propagated, and an increase in the accuracy and reliability of the systems that use this type of signal was reported. Other works have focused on improvements in the process of identifying damages in structures. For instance, Li et al. [94] used the propagation of Lamb waves in isotropic materials to analyze the probability damage imaging (PDI) to improve the location and identification of damages in these materials.

Studies have also explored the use of nonlinear methods in the analysis of detection techniques that are based on the frequency of the propagated signal. For example, the work described in Reference [95] compared the results of stress experiments performed on different materials, and significant changes in the root-mean-square deviation (RMSD) analysis were found. Other works have aimed to develop multifrequency excitation systems, such as the system presented in Reference [74], in which the heterodyne principle was used to generate the signal to propagate in the structure. This work reported an increase in the probability of detecting small cracks.

Other works have investigated the use of adequate sources of excitation to improve the response of the implementation of SHM systems under environmental conditions. For instance, in Reference [96], arbitrary waves were propagated to reduce the influence of wind on the posterior analysis. As a result, a robust method was proposed for scenarios with noise, pollution, or exposure to adverse environmental conditions. With this type of analysis, works have reported the ability to decrease (relative to traditional methods) the computational load without affecting the detection [97].

4.1.2. Types of Sensors

With the increased use of SHM approaches, new sensors have been developed that can improve the efficiency of detection, location, and characterization systems [25]. These developments aim to simultaneously reduce the power consumption and weight of the system, to resolve installation problems, and to improve operation facilities and the subsequent data analysis. The following subsections describe some of the different sensors used in SHM applications that are oriented toward the inspection of both metallic and composite materials.

The choice and validation of sensors form one of the most important elements in this step. A correctly chosen sensor not only detects damages but also enables damage location, quantification, and classification [98]. Figure 3 describes some criteria to consider when selecting a sensor.

Sensors can be classified according to the physical variable that they sense [99] or the transduction principle on which they are based [98]. Table 1 includes some of these sensors and the variable that is usually inspected. The classification in Table 1 is used hereinafter, with an emphasis on their applications as well as the advantages and disadvantages of each type of sensor.

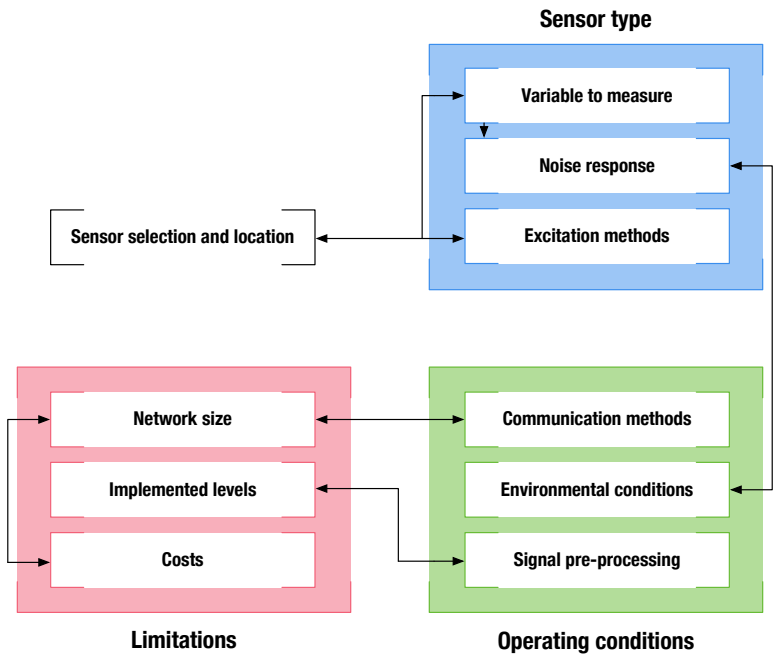

Figure 3. Sensor location and choice.

4.1.3. Piezoelectric Sensors

Piezoelectric materials are built from ceramic and polymers, and they present the direct and inverse piezoelectric effect [100]. This is the reason that these materials are often used to make vibration-based sensors and actuators. The most frequently used materials in piezoelectric sensors are lead zirconate titanate (PZT) and barium titanate ($BaTiO_3$). However, ferroelectric polymers, such as polyvinylidene difluoride (PVDF) and poly(vinylidene-co-trifluoroethylene) (P(VDF-TrFE)), are also used for their high piezoelectric and pyroelectric response levels [101].

An additional advantage of piezoelectric sensors is that they can be manufactured in different shapes, such as rectangular [102], longitudinal [103], and circular [104,105]. These piezoelectric sensors are also flexible and can be adapted to the shape of the structure at their installation locations. With the use of these sensors, it is possible to measure the vibration and to obtain information about different variables, such as deformation [106] or corrosion [107,108]. The literature also includes several applications with a wide range of frequencies, shape adaptation to structures [109], reduced size [110,111], and reduced phase changes [112], among other characteristics.

In terms of methods for inspection, piezoelectric sensors are frequently used in the development of electromechanical impedance (EMI) techniques. These techniques entail the evaluation of changes in the impedance of the sensor. EMI techniques are used in the inspection of civil structures, such as bridges, dams, and transport vehicles in aviation, as well as of trains and ships [113].

Corrosion is an interesting variable to measure and can be inspected using acoustic emission (AE). These sensors are placed in the structure and allow for the evaluation of different types of corrosion [114] as well as some loss of rigidity in the structures [115].

4.1.4. Fiber Optics

Fiber optics are used in applications that require high precision and electromagnetic-interference immunity [116]. The principle underlying fiber optics is based on white-light interference [117], which can relate the absolute shifting of a signal emitted from a light source with any physical variable [118]. This type of sensor is used to measure deformation, temperature, material concentrations, acceleration, rotation, pressure, vibrations, and shifting. For deformation measurements, fiber Bragg grating (FBG) sensors and fiber optics sensors (FOS) are the most used. FBG sensors are used as selective filters of any wavelength [119], while FOS are composed of multimode fibers, have a low cost, and auto-compensate for temperature changes [120]. Deformation can be measured using three different approaches: (i) point sensors or discrete deformation that can locate the deformation [25]; (ii) quasi-distributed deformation sensors—an array of point sensors [121]—and (iii) distributed deformation sensors that can be used to determine a complete profile of deformations [122].

4.1.5. Microelectromechanical Systems (MEMS)

This type of sensor uses miniaturization techniques in its construction [123], and different types of transducers can be combined. These sensors present advantages regarding the costs of implementation and maintenance [124]. It is also possible to take advantage of other attractive features [125], such as their small size [126] or their ability to easily connect to a wireless sensor network [127]. It is even possible to find sensors that use capacitive, inductive, piezoelectric, or optical effects [128,129]. In addition, actuators can be included [130]. In general terms, MEMS consist of the integration of different types of sensors [131].

MEMS are used to measure the magnitude of diverse variables, such as acceleration [127,132], angular velocity (gyroscopes) [133], displacement [134], and deformation [135]. This type of sensor offers high sensitivity [127], responses at low frequencies [136], the measurement of multiple variables, and the integration of communication systems [137]. Because of these factors, the use of MEMS has increased significantly. More precisely, several international research groups are developing a

nanoelectromechanical system (NEMS) in an aim to increase the number of sensors in a structure and to thereby expand the analysis capabilities of existing SHM systems [138].

4.2. Location and Networking

The selection of an appropriate sensor not only depends on the measured variable but also must take into account aspects such as environmental and operational conditions, the number of sensors, the location of the network, and the energy consumption [139,140]. Figure 3 shows some of these aspects to be considered. The selection factors are divided into (a) sensor type; (b) operating conditions; and (c) limitations. In the first case, different elements, such as the variables to measure, the noise response, and the excitation method, are considered. Operating conditions refer to the interaction of the sensor with the structure during its operation. This means that the environmental and operational conditions must be considered when determining the approach to preprocessing the information and when defining the communication methods. Finally, limitations such as costs, implementation requirements, and setup of the sensor network must be considered.

Multiple works have been developed with the objective of determining the best way to locate and interconnect the network of sensors to be used. Decisions on these issues will define the success of data acquisition and will affect the cost of the instrumentation to use.

The work presented in Reference [141] produced a cost–benefit optimization method for the establishment of sensor networks by evaluating two metrics: an optimized benefit–cost ratio and maximized efficiency by complying with operational constraints. The method was applied to the instrumentation of the Pirelli tower in Italy.

Table 1. Sensor types and uses.

Sensor Type	Technology	Variable to Measure	Advantages	Disadvantages	Relevant Features
Piezoelectric	PZT	Acceleration	Low cost	Thermal sensitivity	Used in EMI applications
	PVDF	Deformation [106]	Low price	Aging	Wide range of frequencies [142]
	P(VDF-TrFE)	Corrosion [107,108] Displacement Vibration	Integration possibilities		Shape adaptation [109] Reduced phase changes [112]
Fiber optics	FBG	Deformation [122]	High precision	High price	
	FOS	Acceleration [119] Rotation Pressure Vibrations Shifting	Electromagnetic interference immunity [117] Integration possibilities	Fragility	
Microelectromechanical systems (MEMS)	MEMS	Deformation	Low cost [124]	High-frequency response [136]	
	NEMS [138]	Acceleration [127,132] Gyrometer Displacement [134] Deformation [135] Shifting	Small size [126] Wireless connection [127] Different kinds of sensors and variables [131]	Fragility	

4.3. Data Acquisition

The development of an inspection system depends on the way in which data related to the state of the structure are acquired. In this section, we review the works associated with the way in which excitation signals are generated as well as the selection of sensors; the location and communication of the sensors used; and the acquisition, storage, and transmission of data.

In general, the design of the monitoring system in terms of hardware starts from the definition of the sensor/actuator system—defined according to the previous section—with components that include piezoelectric transducers, microelectromechanical systems, optical fibers, or acoustic sensors [123]. After that, the design of the monitoring system should also take into account additional hardware that will be used to capture, store, and transmit the information. The ability to integrate the hardware in a large sensor network should also be assessed. Several works have addressed these topics. For example, an analysis of a method to determine an efficient sensor distribution in SHM was provided in Reference [143]. In Reference [144], the process of choosing wireless sensors for temperature and pressure measurements was described. In Reference [145], the authors reported a diagnosis related to the acquisition of information and the determination of the types of sensors to be used. Other works have analyzed the location of the sensor network [146,147], the preprocessing of information [148], and the interference of environmental conditions [149].

The general purpose of this step is to provide a signal to the following steps for the analysis of the state of the structure. It is desirable to comply with the requirements for precision, resolution, synchronization, and robustness to environmental and operating conditions [150]. This step is analyzed according to the main components of a data acquisition system: the signal conditioner, the digital–analog converter, and the transmission system.

Data acquisition systems need to be evaluated in the same way, depending on the location at which the information must be processed. This means that there is a difference between the assessment of a system that is required to process these data and the assessment of a system that is only required to capture, store, and transfer these data using different communication methods.

Some authors [20,151–154] have recommended that the following elements be considered for the selection of a DAQ system:

- the evaluation of the required number of inputs and outputs, that is, the number of digital or analog terminals to connect;
- the number of sensors;
- the need for an actuation system;
- the development of a quantified definition of the damage;
- the need for capturing local measurement or using remote sensing;
- the system-level responses—the information that is expected to be processed or preprocessed in the system;
- the possibility of implementing damage identification in an embedded system;
- the integration of feature extraction and statistical modeling algorithms with the sensing system;
- the consistent and retrievable archival of data for long-term monitoring;
- the transmission of information about the system condition to maintenance personnel or control systems;
- the operation of the sensing system with minimal maintenance over long periods of time in order to minimize the cost of the sensing and data acquisition system;
- the power consumption and source for long-term applications; and
- the evaluation of the operational and environmental conditions.

The above factors provide a complete picture of the type of sensor network that is required and the means of acquiring information from these sensor networks. The definition of the operating and environmental conditions to which the system will be exposed is also required: this has been a recurring topic for several authors [155]. This evaluation can reduce these factors when they are implemented by applying certain hardware elements or software strategies. These strategies include the use of interpolation and regression tools [156] to determine and then eliminate the influence of these variables [157]; the use of measurements that are independent of the influence of conditions that have been addressed using mathematical methods, such as singular value decomposition (SVD), PCA, auto-associative neural networks (AANN), factor analysis (FA), or cointegration; and, finally, the use

of variables that are not affected in the short term by changes in environmental conditions [158], as is quite common in the instrumentation of civil structures.

4.4. Signal Conditioning

The measurement systems are exposed to several types of interferences that are produced by the monitoring system itself or by the environment in which the system is operating. Furthermore, the signals collected by the sensors may not have the voltage or power levels required for their analysis, or the signal delivered by the sensors may include unwanted noise in the subsequent analysis. Therefore, it is necessary to process these signals by amplification or attenuation, filtering, compensation, linearization, isolation, or compensation, among other signal-conditioning processes.

Depending on the type of sensor, it is possible to use different elements to satisfy the requirement of one of the steps mentioned above. When implementing signal-conditioning tools in SHM, the interoperability of all elements of the system should be reviewed. Some of the key features to be analyzed are the integration with the rest of the components and the increase in the success of the tool set. Similarly, the flow of information should be examined, and signal degradation, the output voltage levels, and the compatibility with analog-to-digital converters (ADC) should be considered.

In terms of the connectivity between the DAQ and processing devices, some systems offer more than one type of connection for cases of emergency. The following are some of the features that must be considered:

- *Expansion of the generated solution*: In many projects, the increment or adaptability of the created sensor network is required to increase the resolution or to decrease the range of values of a variable. The DAQ system must be able to adapt to these changes.
- *Isolation* should be considered in case of harmful signals for the processing schemes.
- *Bandwidth*: The information content of the sampled signal has to be transmitted with the fewest losses possible. This is achieved with the use of adequate sampling and the allocation of a suitable bandwidth.
- *Calibration* should be performed periodically to avoid failures in the processes of detection, location, or damage characterization.
- *Maintenance* is a relevant feature in continuous inspection systems since correct maintenance decreases the number of failures.

4.5. Preprocessing Step

Once data is acquired and preprocessed by hardware elements, it is possible to perform a preprocessing step, which is an important step for multivariate data analysis. This step allows to reduce random sources of variation in the data set. Since data in SHM can come from different kinds of sensors as was previously explained, there is not a general form to apply in all the cases; from this point of view, it is desireable to explore different methods to determine wich one produces the best results in the final damage-identification process. In general, this is obtained by determining the effectiveness of these techniques in terms of the measure of the separability of the evaluated groups and the accuracy of the classification of the pattern in each case.

These methods are not exclusively for SHM and have been applied in different areas where multivariate analysis is required. Among the main objectives of the preprocessing methods are noise removal, baseline removal, signal alignment, outlier detection, and data normalization. Some of the methods oriented to these aims are as follows:

- wavelet transform (continuous wavelet transform, discrete wavelet transform, and fast wavelet transform)[159,160];
- auto scaling [161,162];
- group scaling [163,164];
- variance scaling [17]; and

- Pareto scaling [165].

Information about each method can be found in the included references.

4.6. Data Reduction and Feature Extraction

The main objective of this step is to reduce the size of the data to analyse and to provide the features to be used in further analysis. Some of the techniques to be used in this step allow to transform the data in a new subspace or a representation by preserving the main features of the original data. Some of the techniques that can be used for feature extraction are as follows:

- Principal Component Analysis (PCA);
- Independent Component Analysis (ICA);
- Latent Sparse Domain Transfer (LSDT);
- Linear Discriminant Analysis (LDA);
- Fast Fourier Transform (FFT);
- Discrete Wavelet Transform (DWT) [166]; and
- Local Discriminant Preservation Projection (LDPP).

4.7. Prognosis Faults in SHM

Fault- or damage-detection systems in SHM work on the basis of the quality of the information capture [167], the analysis of information, the use of statistical tools, and decision making (see Figure 4). If any of these steps are performed incorrectly, the fault- or damage-detection system may present errors that cause unnecessary interventions in the inspected structures (false alarms) or may fail to detect real damages in the structures [168] (missing faults).

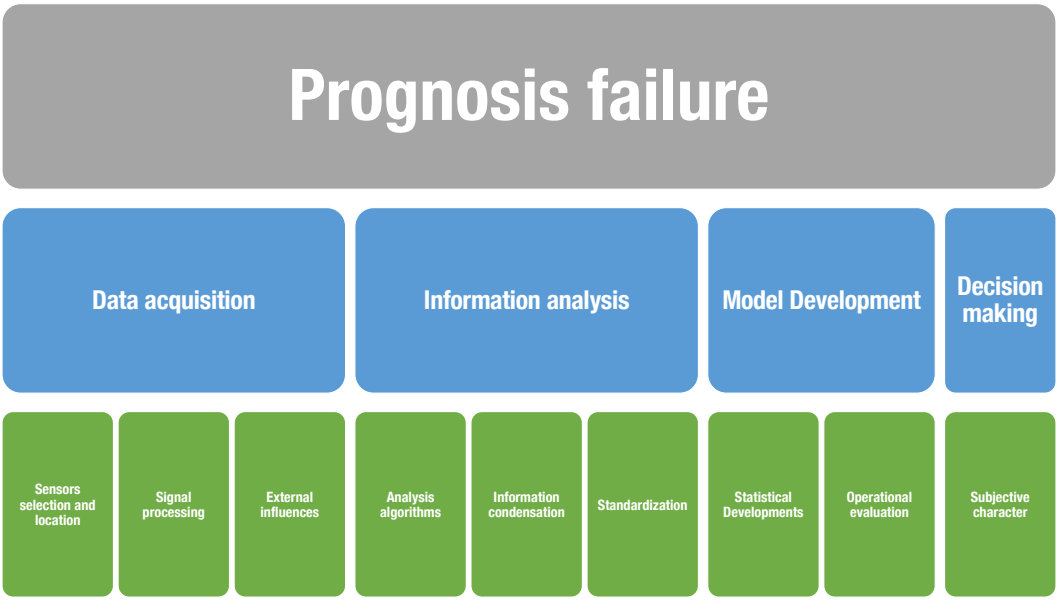

Figure 4. Prognosis failure approaches.

Acquisition errors can result from the selection, location, configuration, or malfunction of the sensors. These failures imply relevant deviations between the signal obtained and the real value of the variable. The main causes of sensor failures are grouped into two types: *soft* and *hard* sensor faults. *Soft* sensor faults include bias, gain, loss of precision, and polarization. In contrast, *hard* sensor failures comprise constant deviations, deviations with noise, and failures due to background noise. In Reference [169], a mathematical analysis of the aforementioned faults was carried out.

Faults related to information processing occur in preprocessing and processing algorithms, condensation, and standardization [170]. Furthermore, the use of statistical tools can introduce errors

to the analysis that, in some cases, lead to false detections. Finally, some errors can be identified in SHM that are associated with the subjectivity that is present in the analysis of the collected information. For instance, in multiple approaches, the levels of detection, location, and sizing include elements of subjective analysis, such as expert judgments.

In general terms, false detections are classified into two large groups: (i) *false positives*, also known as false alarms or type I errors, occur when the SHM system detects a fault or damage but the structure is healthy, and (ii) *false negatives*, also known as missing faults or type II errors, occur when the structure is faulty or damaged but the SHM system classifies it as healthy [170].

4.8. Development of Statistical Models

The use of statistical models has been well accepted in the development of damage-identification methodologies. Some of the works cited in the previous sections considered statistical models in their approach. As a complement to the works addressed above, some additional references are described in the subsequent paragraphs.

Some of these works have approached the fault- or damage-detection problem using multivariate analysis because of a large number of sensors or the use of a sensor network. One multivariate analysis method is PCA. This method has frequently been shown to be useful for data reduction [171], thus offering a great advantage in the analysis of data from sensor networks with a large number of sensor/actuator configurations [172]. However, PCA is only one of multiple methods used for this purpose. Some variations or alternatives include ICA [79,173] and DWT [166,174,175]. They are all very useful tools to re-express raw data in a new reduced version of the data while preserving the relevant information.

More precisely, in damage detection, PCA can be used to change the original data by the corresponding projections of so-called principal components. From the perspective of pattern recognition, data from a healthy state of the structure can be used to define the *healthy pattern*. When the current structure has to be diagnosed, the new measured data can be projected into the PCA or ICA model to obtain so-called *scores*. Figure 5 represents the projection of the first two principal components of a data set in which no damage is present and with three different types of damage. As it is possible to observe that the data from the different structural states are very different; in this case, groups can be distinguished by simple inspection and damage detection can be applied. However, in most of the cases, these groups are mixed and cannot be differentiated in two axes.

The main differences between PCA and ICA are that components in ICA are linearly independent. Therefore, in the latter case, it is not possible to organize the components according to the proportion of the retained variance. This kind of plot is useful for visual analysis or inspection since data from the inspected structure can be analyzed and compared with the data from the healthy structure to determine the presence of damages. The presence of this damage is detected by the *visual* separation of the new data from the current structure to diagnose the data coming from the healthy structure. However, this methodology is useful only if the first two principal components retain a large proportion of the variance. In other cases, the data appear mixed, so it is not possible to detect and classify damages with a single visual inspection. In some of these cases, PCA can be combined with univariate and multivariate hypothesis testing to correctly classify the current state of the structure. Both univariate [3] and multivariate [176] hypothesis testing have been used for damage detection in small-scale structures as well as for fault detection in wind turbines [177–179].

Bayesian approaches have also been studied for damage detection [70] and impact detection. For instance, Morse et al. [69] applied a Bayesian updating (BU) approach and Kalman filter to estimate the location of impact. In general, BU provides a probabilistic prediction of the impact location, so, quantitatively, uncertainties associated with the prediction of the impact are permissible. Flynn and Todd [180] used a formulation of Bayes risk for optimal sensor and actuator placement using different kinds of sensors/actuators. The optimization space was searched by using a genetic algorithm with a time-varying mutation rate.

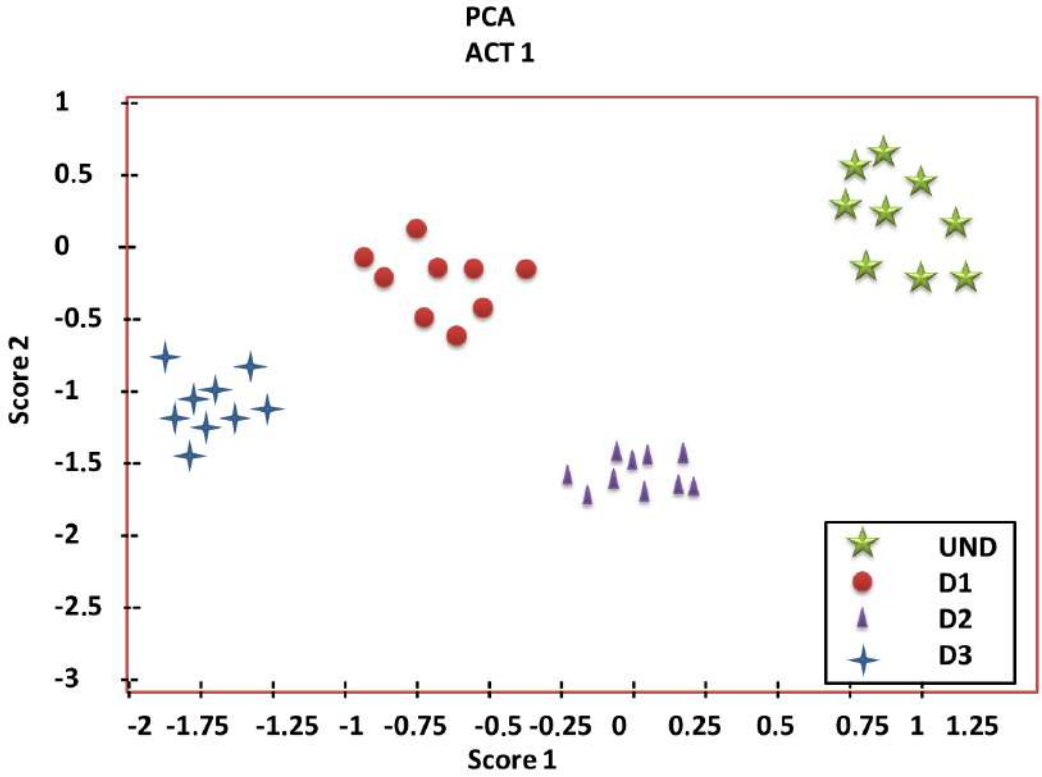

Figure 5. Score 1 versus Score 2.

Anaya et al. [17,181] used both PCA and artificial immune systems (AIS) to detect damages in structures. In the proposed methodology, an active piezoelectric system is used to inspect the structure and to collect the data. The information is encoded by emulating the effect of human immune systems [182] and by considering external elements to be possible damages. This approach defines antibodies as the *detector* of a specific pattern and antigens as the damage condition.

The use of SOM has also been applied for damage detection and classification [183]. SOM are unsupervised neural networks in which training is a blind process that enables the grouping and classification of different kinds of data according to data features. In general, in this kind of methodology, data reduction is performed using techniques such as PCA or DWT and the new components, coefficients, or indices are used as a feature vector; all the results from all the actuation phases are fused into a single vector. This vector acts as the input to train the self-organizing map. When the pattern is built or defined, the same procedure is applied to the structure being tested to evaluate the state of the structure and to determine the presence of damages and their possible classification. As a visualization tool, it is very common to use a cluster map or a U-matrix surface [64]. Figure 6 shows an example of the use of the U-matrix surface; seven structural states are considered in the illustrated classification process: specifically, one healthy structural state and six different damages are included in this plot. Since the methodology requires previous training, the algorithm considers new data with features that differ from those of the data used during training to be a new cluster or a new type of damage.

Machine-learning approaches have also been studied, on their own or in combination with different feature extraction methods [184], as damage detection and classification methodologies. In this kind of approach, in general, PCA is used as a feature-extraction method to define the feature vector to train the machine using several states of the structure. During the test step, data from an unknown structural state are evaluated by the trained machine, and the classification can be performed. Algorithms that are commonly used in machine learning include *k*-nearest neighbor (kNN), decision trees, and support vector machines (SVM).

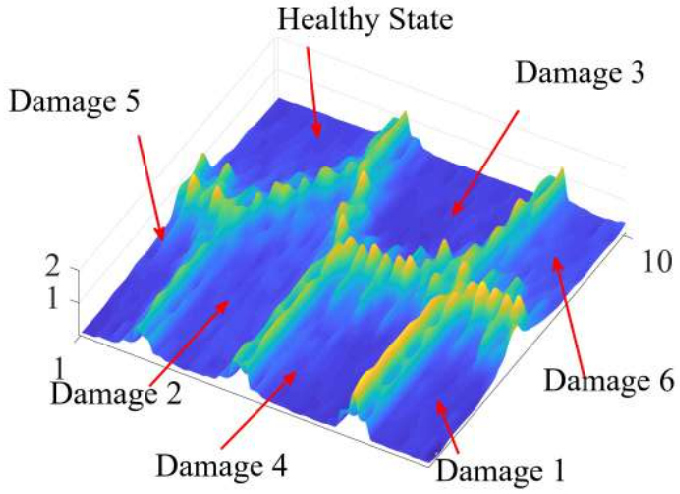

Figure 6. U-matrix surface.

The Gaussian process has also been studied [76] for probabilistic data-driven modeling and structural damage detection methods. In general, data from the structure to be inspected and instrumented with sensors, such as piezoelectric transducers working in pitch-catch mode, provide information that can be pre-processed using a DWT. The details and coefficients of the DWT are subsequently used for the extraction of features, which are simultaneously the input of the Gaussian process. The output of this training—that is, the first step—is the corresponding pattern. In the second step, data from the tested structure are pre-processed as in the first step. Afterward, the features are included in the Gaussian process and a comparison with this pattern is obtained for the classification process. The validation of the methodology can be performed using receiver operating characteristic (ROC) curves to evaluate the effectiveness of the classification.

Nonlinear approaches, such as nonlinear PCA (NLPCA), have also been analyzed for damage detection and classification. Some examples include the combination of the hierarchical version of NLPCA (h-NLPLCA) and machine learning, in which the nonlinear components are used as the feature vector to train different models [185].

Damage progression has also been addressed with the use of piezoceramic arrays [186]: a number of time- and frequency-domain features are derived from existing damage imaging and detection algorithms combined with data-mining algorithms.

In terms of damage localization, damage indices have also been explored [32] as damage indicators and applied to complement PCA to reduce the problems that arise when the two first principal components do not retain a significant proportion of the variance. Two of these indices are the Q-index and the T^2-index, which can be used to determine the contribution of a specific sensor in the sensor network. Subsequently, using triangulation techniques, the potential area or the position of the damage can be defined. One example of the kinds of diagrams that are obtained by the use of contribution plots is shown in Figure 7. This figure shows an example with seven actuation phases, and each phase shows the contribution of each sensor in the sensor network. In this way, localization can be performed by triangulating the sensors with the highest contributions and the piezoelectric used as actuator.

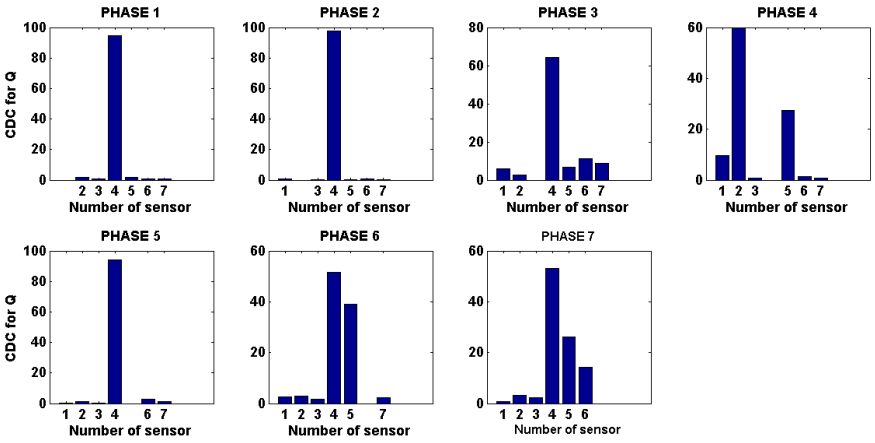

Figure 7. Damage contribution index.

These indices have also been used in damage detection to process data from FBG sensors [187] with good results. Hierarchical clustering (HC) is another supervised method of statistical learning that is commonly used in SHM. As the name suggests, this algorithm collects and groups similar data using a set of distance measures that define the similarity of the data. Commonly, at the detection level, the established parameter is represented by a damaged or undamaged state. HC usually builds a hierarchy of data groups and uses a different function to assign data points to groups. The Euclidean distance and Mahalanobis distance are two popular choices among many that are used for a dissimilarity function [188].

HC has been applied at the detection level for several types of structures. Datteo et al. [189] proposed an HC analysis to obtain a set of clusters based on damage patterns that were found in the experimental data, which were collected from PZT sensors by means of a graphic representation of the information so that the damage could be identified intuitively, both qualitatively and quantitatively. The performance of the proposed approach was tested by three experiments on a full-scale reinforced concrete beam. In another work, Zhou et al. [190] incorporated HC with a method for recognizing artificial immune patterns for the recognition and classification of damage patterns in the health monitoring of an unsupervised structure. The sampled data were classified by an agglomerated hierarchical clustering algorithm. Then, sets of memory cells were trained to imitate the mechanism of learning and immunological recognition. Finally, structural data patterns were judged by the sets of trained memory cells. The results of this work showed that agglomerated hierarchical clustering and incorporated methods could successfully identify the most patterns in the antigen sample data. The work concluded that the unsupervised structural damage-classification algorithm based on HC and artificial immune patterns could produce high-quality memory cells that could effectively identify all types of structural damage patterns. Finally, Sen et al. [188] proposed two data-based techniques—a semi-supervised and supervised learning approach—for the detection of damage in pipelines. The proposed approaches aimed to reduce the number of sensors deployed and to thus reduce maintenance costs. The semi-supervised learning method detected the presence of damages using an algorithm based on hierarchical grouping, and the approach based on supervised learning located damages using multinomial logistic regression. The proposed algorithms were validated by the acquisition of guided ultrasonic wave (GUW) responses from experimental pipelines in a tone capture configuration using low-cost piezoelectric transducers.

Unsupervised statistical methods of learning are also widely used in SHM analysis [191]. One of the reasons is that the algorithms involved are less complex, so they can be used in real-time analysis [192]. These methods were compared with traditional alternatives in works such as the one carried out by McCrory et al. [193], in which three classification techniques were tested—analysis of artificial neural networks (ANN), unsupervised waveform clustering (UWC), and the corrected

measured amplitude ratio (MAR)—in the location and classification of faults in a composite panel of carbon fiber during buckling. This paper reported that UWC and ANN were better classifiers and that their use improved the reliability of the SHM system. Nagarajaiah et al. [194] applied unsupervised methods for the analysis of structures under vibration conditions. The authors used multivariate blind source separation to detect anomalies, and they reported positive results. Despite the stated advantages, unsupervised learning methods are not implemented to the same extent as supervised methods. One reason is the reliability of the obtained results.

Uncertainty quantification has been examined in different fields. One example is the inspection of cultural heritage [195]: in this study, uncertainty reduction was applied to the modal estimation of data from two historical buildings. In Reference [196], uncertainty quantification in OMA was developed for vibration-based analysis. Structural excitations were not directly measured but rather modeled by band-limited white noise processes.

The classification process can be regarded as a binary classification problem. One example is the work in Reference [197], in which possibility theory was introduced to solve a decision-making problem involving conflicting information. The information was modeled as weighted intervals on the basis of importance, and a possibility distribution from the weighted intervals was presented to fuse information with respect to its importance.

4.9. The Decision Level

Decision support systems (DSS) have been used extensively in the analysis of economic, technical, environmental, optimization, and other problems that involve a choice of alternatives [198]. This type of tool is an important component in monitoring and control systems. However, there are few studies on this topic in relation to SHM systems, and most of these works have focused on the monitoring of civil structures.

The research efforts on this matter have involved the implementation of different decision tools to assess the state of the structure. Endsley et al. [199] integrated information from the data banks of the National Bridge Inventory (NBI) with measurements taken from various bridges using nondestructive evaluation (NDE) systems. They unified the information and presented a web application to improve the decision-making processes and to reduce the subjectivity in the interpretation of the data. Sun et al. [200] presented a hybrid system that combined neural network theory and adaptive fuzzy logic to generate a framework for the analysis of heterogeneous signals from various types of sensor networks. The implementation of the hybrid system enabled the evaluation of the type of study to be carried out on each data source in the monitoring scheme. SHM analysis has been used as a test scenario for decision models; Khodaei et al. [201] compared expected utility theory (EUT) with prospect theory (PT) in the estimation of the state of a bridge. Their work showed that the opinions on inspected structures varied because of the subjectivity of the person who analyzed the results.

Different works present proposals related to the management of decisions and decrease of detection failures by defining threshold levels; the work presented in Reference [202] summaries the use of different categories of SHM in the analysis of bridges and civil constructions. This work presents an interesting summary of implementation techniques in the category of SHM implementation related to the definition of limits in the analyzed variables; among them, humidity, vibration, and settlement are found, emphasizing the probabilistic uncertainty quantification models. Bai et al. [203] present a paper oriented to the reduction of false forecasts by evaluating three techniques that use the information generated by fatigue in structures instrumented with Acoustic Emission (AE) sensors. Results of this work show the influence on the definition of threshold levels in the automation of decisions. Deraemaeker et al. [204] present a proposal for decreasing the influence of environmental conditions using filters and definitions of distances on covariance matrices and eigenvalues. As a result of this approach, the high sensitivity of the measurement systems and the efficiency of the definition of thresholds in the reduction of false positives is presented; this study was carried out in civil structures. In Reference [205], a laboratory test is applied to a metallic structure instrumented with piezoelectric

transducers in a system based on electromechanical impedance; a part the analysis shows that threshold levels significantly influence the detection and location of faults.

Very few works on the development of DSS have examined the monitoring of composite and metallic structures. One such work was carried out by Bolognani et al. [206], who implemented a multilevel decision scheme to reduce the costs of processing and instrumentation. The generated method could reduce the risk of errors in evaluation (false positive and negative), increase the profitability of the instrumentation, and unify the results of different information sources. Finally, the work reported by Sabatino et al. [207] focused on the development of a framework that aimed to improve the cost–benefit in the choice of sensing schemes for naval structures. They reported that their framework could decrease the risks associated with choosing the data-processing system to be used.

From the existing studies, a decision level for the analysis of composite materials is presented that would be located in the upper part of Figure 2. The function of this level is focused on the choice and evaluation of the types of processing of data from structures instrumented with different types of sensors.

5. Conclusions

In this review, several elements of the SHM process and its implementation are explored. These elements are the description of the SHM process and the components of SHM implementation, including sensors and actuators, location and networking, data acquisition, signal conditioning, statistical analysis, and decision levels. It is shown that diverse authors have made significant contributions to these achievements. From the presented information, the following general conclusions are drawn:

- The works related to the advances and implementation of SHM systems account for the monitoring requirements of healthy structures in diverse areas of applications, such as civil engineering, aeronautics, transport, and power generation. This research field, which is still developing, presents research opportunities related to methods for sensor selection and location, communication systems, analysis of environmental and operational conditions, reduction of false positives and false negatives, and decision methodologies, among others.
- There has been a considerable increase in the use of SHM systems in operating structures. This increase, together with the emergence of regulations for the operation of systems for monitoring structures, reflects the rapid adoption of SHM in industries such as the automotive and aeronautics sectors and intelligent materials development. As a result, a significant growth in investment, leading to the application of all levels of SHM, is expected.
- Although this paper presents the steps of implementing an SHM system, these steps should be used only as a reference: they can be decomposed or complemented according to the implementation and the intended approach. This is currently a focus that is actively researched to improve the reliability of the elements of the implementation.
- Using data that are directly acquired from sensors installed on the structure is a convenient way to evaluate the current state of a structure. This allows for the continuous measurement of data to monitor applications in real time. However, some problems may arise during the implementation of these SHM approaches. Such challenges include the following:

  (a) Failures in the sensors are possible and can arise from problems during installation or damages to the sensor when the structure is subjected to hard conditional and operational variations. This problem can be solved by the use of faulty sensor detection, similar to damage detection. In some cases, it is possible to reconstruct the signal to avoid false damage detections during the damage-identification process. Similarly, there are some data-driven algorithms that can compensate for the effects of environmental and operational variations; these are required because, as it was explained, environmental and operational variations can change the baseline and can produce false positive damage identification.

(b) Poor use of preprocessing techniques often leads to poor results of the damage-identification process. This problem can be partially solved by the design of robust methodologies.
(c) Some problems are related to storing data and processing the information coming from large structures instrumented with a large number of sensors. In some cases, such problems can be easily solved through a distributed analysis.

Although there are several proposed solutions to the different problems in the task of identifying damage, most of the results are relevant to a specific application and are tested under laboratory conditions. Hence, problems at different levels of the damage-identification process, such as the problems associated with data acquisition and preprocessing, remain open for investigation.

According to the number of publications, one of the least explored topics is the implementation of decision support tools. This document demonstrates the need for such tools in data-driven applications. Some studies have focused on specific cases, but the different alternatives of all the levels explored require an intelligent system that is able to decrease the number of false positives and negatives in the identification process. Its development and implementation will allow for the mixing of different types of information sources and for eliminating the subjectivity of the analysis, among other improvements.

Author Contributions: All authors contributed equally to this work. All authors have read and agreed to the published version of the manuscript.

Funding: This work has been partially funded by the Spanish Agencia Estatal de Investigación (AEI)—Ministerio de Economía, Industria y Competitividad (MINECO), the Fondo Europeo de Desarrollo Regional (FEDER) through the research project DPI2017-82930-C2-1-R and by the Generalitat de Catalunya through the research project 2017 SGR 388.

Acknowledgments: We gratefully acknowledge the support of NVIDIA Corporation with the donation of the Titan Xp GPU used for this research. We thank the Universitat Politècnica de Catalunya (UPC) for predoctoral fellowship (to David Agis).

Conflicts of Interest: The authors declare no conflict of interest.

Abbreviations

The following abbreviations are used in this manuscript:

AANN	Auto-associative neural networks
ADC	Analog-to-digital converters
AE	Acoustic emission
AIS	Artificial immune systems
ANN	Analysis of artificial neural networks
BF-SHM	Baseline-free SHM
BHM	Bridge Health Monitoring
BU	Bayesian updating
DAQ	Data acquisition
DSS	Decision support systems
DWT	Discrete wavelet transform
EMI	Electromechanical impedance
EMIS	Electromechanical impedance spectroscopy
EUT	Expected utility theory
FA	Factor analysis
FBG	Fiber Bragg grating
FDD	Frequency domain decomposition
FEA	Finite element analysis
FOS	Fiber optics sensors
GUW	Guided ultrasonic wave
HC	Hierarchical clustering
h-NLPLCA	Hierarchical nonlinear principal component analysis
ICA	Independent component analysis

IoT	Internet of Things
kNN	*k*-nearest neighbor
LDV	Laser Doppler vibrometer
LVDT	Linear variable differential transducer
MAR	Measured amplitude ratio
MEMS	Microelectromechanical systems
ML	Machine learning
NBI	National Bridge Inventory
NDE	Nondestructive evaluation
NEMS	Nanoelectromechanical system
NLPCA	Nonlinear principal component analysis
OMA	Operational modal analysis
PCA	Principal component analysis
PDI	Probability damage imaging
PT	Prospect theory
PVDF	Polyvinylidene difluoride
P(VDF-TrFE)	Poly(vinylidene-co-trifluoroethylene)
PZT	Piezoelectric transducer
RF	Radio frequency
RMSD	Root-mean-square deviation
ROC	Receiver operating characteristic
SFEM	Smoothed finite element method
SHM	Structural health monitoring
SOM	Self-organizing maps
SVD	Singular value decomposition
UWC	Unsupervised waveform clustering

References

1. Sohn, H.; Farrar, C.R.; Hemez, F.M.; Czarnecki, J.J. *A Review of Structural Health Review of Structural Health Monitoring Literature 1996–2001*; Technical Report; Los Alamos National Laboratory: Los Alamos, NM, USA, 2002.
2. Rytter, A. Vibrational Based Inspection of Civil Engineering Structures. Ph.D. Thesis, Department of Building Technology and Structural Engineering, Aalborg University, Aalborg, Denmark, 1993.
3. Mujica, L.; Ruiz, M.; Pozo, F.; Rodellar, J.; Güemes, A. A structural damage detection indicator based on principal component analysis and statistical hypothesis testing. *Smart Mater. Struct.* **2013**, *23*, 025014. [CrossRef]
4. Ciang, C.C.; Lee, J.R.; Bang, H.J. Structural health monitoring for a wind turbine system: A review of damage detection methods. *Meas. Sci. Technol.* **2008**, *19*, 122001. [CrossRef]
5. Barke, D.; Chiu, W. Structural health monitoring in the railway industry: A review. *Struct. Health Monit.* **2005**, *4*, 81–93. [CrossRef]
6. Carden, E.P.; Brownjohn, J.M. Fuzzy clustering of stability diagrams for vibration-based structural health monitoring. *Comput.-Aided Civ. Infrastruct. Eng.* **2008**, *23*, 360–372. [CrossRef]
7. Lynch, J.P.; Loh, K.J. A summary review of wireless sensors and sensor networks for structural health monitoring. *Shock Vib. Dig.* **2006**, *38*, 91–130. [CrossRef]
8. Noel, A.B.; Abdaoui, A.; Elfouly, T.; Ahmed, M.H.; Badawy, A.; Shehata, M.S. Structural health monitoring using wireless sensor networks: A comprehensive survey. *IEEE Commun. Surv. Tutor.* **2017**, *19*, 1403–1423. [CrossRef]
9. Sabato, A.; Niezrecki, C.; Fortino, G. Wireless MEMS-Based Accelerometer Sensor Boards for Structural Vibration Monitoring: A Review. *IEEE Sens. J.* **2017**, *17*, 226–235. [CrossRef]
10. Pradhan, H.S.; Sahu, P. A survey on the performances of distributed fiber-optic sensors. In Proceedings of the 2015 International Conference on Microwave, Optical and Communication Engineering (ICMOCE), Bhubaneswar, India, 18–20 December 2015; IEEE: Piscataway, NJ, USA, 2015; pp. 243–246.

11. Rothberg, S.; Allen, M.; Castellini, P.; Di Maio, D.; Dirckx, J.; Ewins, D.; Halkon, B.J.; Muyshondt, P.; Paone, N.; Ryan, T.; et al. An international review of laser Doppler vibrometry: Making light work of vibration measurement. *Opt. Lasers Eng.* **2017**, *99*, 11–22. [CrossRef]
12. Sikarwar, S.; Satyendra; Singh, S.; Yadav, B.C. Review on pressure sensors for structural health monitoring. *Photonic Sens.* **2017**, *7*, 294–304. [CrossRef]
13. Amezquita-Sanchez, J.; Adeli, H. Feature extraction and classification techniques for health monitoring of structures. *Sci. Iranica Trans. A Civ. Eng.* **2015**, *22*, 1931.
14. Sofge, D.A. Structural health monitoring using neural network based vibrational system identification. In Proceedings of the ANZIIS'94-Australian New Zealnd Intelligent Information Systems Conference, Brisbane, Australia, 29 November–2 December 1994; IEEE: Piscataway, NJ, USA, 1994; pp. 91–94.
15. Zang, C.; Imregun, M. Structural damage detection using artificial neural networks and measured FRF data reduced via principal component projection. *J. Sound Vib.* **2001**, *242*, 813–827. [CrossRef]
16. Park, J.Y.; Wakin, M.B.; Gilbert, A.C. Modal analysis with compressive measurements. *IEEE Trans. Signal Process.* **2014**, *62*, 1655–1670. [CrossRef]
17. Anaya, M. Design and Validation of a Structural Health Monitoring System Based on Bio-Inspired Algorithms. Ph.D. Thesis, Universitat Politècnica de Catalunya, Barcelona, Spain, 2016.
18. Zonta, D. Sensor data analysis, reduction and fusion for assessing and monitoring civil infrastructures. In *Sensor Technologies for Civil Infrastructures*; Woodhead Publishing: Sawston, UK, 2014; pp. 33–66. [CrossRef]
19. Das, S.; Saha, P.; Patro, S.K. Vibration-based damage detection techniques used for health monitoring of structures: A review. *J. Civ. Struct. Health Monit.* **2016**. [CrossRef]
20. Sohn, H.; Farrar, C.R. Damage diagnosis using time series analysis of vibration signals. *Smart Mater. Struct.* **2001**, *10*, 446–451. [CrossRef]
21. Fassois, S.D.; Kopsaftopoulos, F.P. Statistical Time Series Methods for Vibration Based Structural Health Monitoring. In *CISM International Centre for Mechanical Sciences, Courses and Lectures*; Springer: Vienna, Austria, 2013; pp. 209–264._4. [CrossRef]
22. Le, M.Q.; Capsal, J.F.; Lallart, M.; Hebrard, Y.; Van Der Ham, A.; Reffe, N.; Geynet, L.; Cottinet, P.J. Review on energy harvesting for structural health monitoring in aeronautical applications. *Prog. Aerosp. Sci.* **2015**, *79*, 147–157. [CrossRef]
23. Cao, S.; Li, J. A survey on ambient energy sources and harvesting methods for structural health monitoring applications. *Adv. Mech. Eng.* **2017**, *9*, 1–14. [CrossRef]
24. Li, D.; Ho, S.C.M.; Song, G.; Ren, L.; Li, H. A review of damage detection methods for wind turbine blades. *Smart Mater. Struct.* **2015**, *24*, 033001. [CrossRef]
25. Das, S.; Saha, P. A review of some advanced sensors used for health diagnosis of civil engineering structures. *Measurement* **2018**, *129*, 68–90. [CrossRef]
26. Vendittozzi, C.; Sindoni, G.; Paris, C.; del Marmo, P.P. Application of an FBG sensors system for structural health monitoring and high performance trimming on racing yacht. In Proceedings of the 2011 Fifth International Conference on Sensing Technology, Palmerston North, New Zealand, 28 November–1 December 2011; IEEE: Piscataway, NJ, USA, 2011; pp. 617–622.
27. Mitra, M.; Gopalakrishnan, S. Guided wave based structural health monitoring: A review. *Smart Mater. Struct.* **2016**, *25*, 053001. [CrossRef]
28. Willberg, C.; Duczek, S.; Vivar-Perez, J.; Ahmad, Z. Simulation methods for guided wave-based structural health monitoring: A review. *Appl. Mech. Rev.* **2015**, *67*, 010803. [CrossRef]
29. Tokognon, C.A.; Gao, B.; Tian, G.Y.; Yan, Y. Structural health monitoring framework based on Internet of Things: A survey. *IEEE Internet Things J.* **2017**, *4*, 619–635. [CrossRef]
30. Farrar, C.R.; Worden, K. An introduction to structural health monitoring. *Philos. Trans. R. Soc. A Math. Phys. Eng. Sci.* **2006**, *365*, 303–315. [CrossRef] [PubMed]
31. Catbas, F.N.; Susoy, M.; Frangopol, D.M. Structural health monitoring and reliability estimation: Long span truss bridge application with environmental monitoring data. *Eng. Struct.* **2008**, *30*, 2347–2359. [CrossRef]
32. Tibaduiza, D.A.; Torres-Arredondo, M.A.; Mujica, L.; Rodellar, J.; Fritzen, C.P. A study of two unsupervised data driven statistical methodologies for detecting and classifying damages in structural health monitoring. *Mech. Syst. Signal Process.* **2013**, *41*, 467–484. [CrossRef]
33. Adler, F.; Thorpe, M.J.; Cossel, K.C.; Ye, J. Cavity-enhanced direct frequency comb spectroscopy: Technology and applications. *Annu. Rev. Anal. Chem.* **2010**, *3*, 175–205. [CrossRef]

34. Chen, J. (Ed.) Proceedings of the Second International Workshop on Structural Control: Next Generation of Intelligent Structures. 1996. Available online: http://cwis.usc.edu/dept/civil_eng/structural/welcome.html.(accessed on 28 January 2020)
35. Zhou, L.; Yan, G.; Wang, L.; Ou, J. Review of benchmark studies and guidelines for structural health monitoring. *Adv. Struct. Eng.* **2013**, *16*, 1187–1206. [CrossRef]
36. Farrar, C.R.; Worden, K. *Structural Health Monitoring: A Machine Learning Perspective*; John Wiley & Sons: Hoboken, NJ, USA, 2012.
37. Chen, X.; Bil, C.; Ren, H. Influence of SHM Techniques on Scheduled Maintenance for Aircraft Composite Structures. In Proceedings of the 14th AIAA Aviation Technology, Integration, and Operations Conference, Atlanta, GA, USA, 16–20 June 2014; p. 3264.
38. Lau, B.C.P.; Ma, E.W.M.; Pecht, M. Review of offshore wind turbine failures and fault prognostic methods. In Proceedings of the IEEE 2012 Prognostics and System Health Management Conference (PHM-2012 Beijing), Beijing, China, 23–25 May 2012; IEEE: Piscataway, NJ, USA, 2012, pp. 1–5.
39. Jamalkia, A.; Ettefagh, M.M.; Mojtahedi, A. Damage detection of TLP and Spar floating wind turbine using dynamic response of the structure. *Ocean Eng.* **2016**, *125*, 191–202. [CrossRef]
40. Padmavathy, T.; Bhargava, D.; Venkatesh, P.; Sivakumar, N. Design and development of microstrip patch antenna with circular and rectangular slot for structural health monitoring. *Pers. Ubiquitous Comput.* **2018**, *22*, 883–893. [CrossRef]
41. Hoshyarmanesh, H.; Abbasi, A.; Moein, P.; Ghodsi, M.; Zareinia, K. Design and implementation of an accurate, portable, and time-efficient impedance-based transceiver for structural health monitoring. *IEEE/ASME Trans. Mechatron.* **2017**, *22*, 2809–2814. [CrossRef]
42. Rainieri, C.; Magalhaes, F.; Gargaro, D.; Fabbrocino, G.; Cunha, A. Predicting the variability of natural frequencies and its causes by Second-Order Blind Identification. *Struct. Health Monit.* **2019**, *18*, 486–507. [CrossRef]
43. Reynders, E.; Wursten, G.; de Roeck, G. Output-only structural health monitoring in changing environmental conditions by means of nonlinear system identification. *Struct. Health Monit.* **2014**, *13*, 82–93. [CrossRef]
44. Rainieri, C.; Gargaro, D.; Reynders, E.; Fabbrocino, G. A study on the concurrent influence of liquid content and damage on the dynamic properties of a tank for the development of a modal-based SHM system. *J. Civ. Struct. Health Monit.* **2019**, 1–12. [CrossRef]
45. Isidori, D.; Concettoni, E.; Cristalli, C.; Soria, L.; Lenci, S. Proof of concept of the structural health monitoring of framed structures by a novel combined experimental and theoretical approach. *Struct. Control Health Monit.* **2016**, *23*, 802–824. [CrossRef]
46. Smithard, J.; Rajic, N.; Van Der Velden, S.; Norman, P.; Rosalie, C.; Galea, S.; Mei, H.; Lin, B.; Giurgiutiu, V. An advanced multi-sensor acousto-ultrasonic structural health monitoring system: Development and aerospace demonstration. *Materials* **2017**, *10*, 832. [CrossRef] [PubMed]
47. Bilbao, A.; Hoover, D.; Rice, J.; Chapman, J. Ultra-low power wireless sensing for long-term structural health monitoring. In *Sensors and Smart Structures Technologies for Civil, Mechanical, and Aerospace Systems 2011*; International Society for Optics and Photonics: Bellingham, WA, USA, 2011; Volume 7981, p. 798109.
48. Vitola, J.; Pozo, F.; Tibaduiza, D.; Anaya, M. Distributed piezoelectric sensor system for damage identification in structures subjected to temperature changes. *Sensors* **2017**, *17*, 1252. [CrossRef] [PubMed]
49. Anaya, M.; Tibaduiza, D.A.; Torres-Arredondo, M.A.; Pozo, F.; Ruiz, M.; Mujica, L.E.; Rodellar, J.; Fritzen, C.P. Data-driven methodology to detect and classify structural changes under temperature variations. *Smart Mater. Struct.* **2014**, *23*, 045006. [CrossRef]
50. Boehme, B.; Roellig, M.; Wolter, K.J. Measurement of viscoelastic material properties of adhesives for SHM sensors under harsh environmental conditions. In Proceedings of the 2010 11th International Thermal, Mechanical & Multi-Physics Simulation, and Experiments in Microelectronics and Microsystems (EuroSimE), Bordeaux, France, 26–28 April 2010; IEEE: Piscataway, NJ, USA, 2010; pp. 1–8.
51. Lu, Y.; Michaels, J.E. Feature extraction and sensor fusion for ultrasonic structural health monitoring under changing environmental conditions. *IEEE Sens. J.* **2009**, *9*, 1462–1471.
52. Konstantinidis, G.; Wilcox, P.D.; Drinkwater, B.W. An investigation into the temperature stability of a guided wave structural health monitoring system using permanently attached sensors. *IEEE Sens. J.* **2007**, *7*, 905–912. [CrossRef]

53. Zhou, D.; Kim, J.K.; Ha, D.S.; Quesenberry, J.D.; Inman, D.J. A system approach for temperature dependency of impedance-based structural health monitoring. In *Smart Sensor Phenomena, Technology, Networks, and Systems 2009*; International Society for Optics and Photonics: Bellingham, WA, USA, 2009; Volume 7293, p. 72930U.
54. Arredondo, M.A.T.; Sierra-Pérez, J.; Zenuni, E.; Cabanes, G.; Rodellar, J.; Güemes, A.; Fritzen, C.P. A pattern recognition approach for damage detection and temperature compensation in acousto-ultrasonics. In Proceedings of the EWSHM-7th European Workshop on Structural Health Monitoring, Nantes, France, 8–11 July 2014; pp. 348–354.
55. Wilson, W.C.; Atkinson, G.M. Wireless sensor applications in extreme aeronautical environments. In Proceedings of the IEEE International Conference on Wireless for Space and Extreme Environments, Baltimore, MD, USA, 7–9 November 2013; IEEE: Piscataway, NJ, USA, 2013; pp. 1–6.
56. Prendergast, L.; Reale, C.; Gavin, K. Probabilistic examination of the change in eigenfrequencies of an offshore wind turbine under progressive scour incorporating soil spatial variability. *Mar. Struct.* **2018**, *57*, 87–104. [CrossRef]
57. Zhou, X.; Wang, D.; Duan, M.; Gu, J.; Liu, Y. Numerical study on mode curvature for damage detection of a drilling riser using transfer matrix technique. *Appl. Ocean Res.* **2017**, *63*, 65–75. [CrossRef]
58. Oliveira, G.; Magalhães, F.; Cunha, Á.; Caetano, E. Vibration-based damage detection in a wind turbine using 1 year of data. *Struct. Control Health Monit.* **2018**, *25*, 1–22. [CrossRef]
59. Yamamoto, K.; Miyamoto, R.; Takahashi, Y.; Okada, Y. Experimental Study about the Applicability of Traffic-induced Vibration for Bridge Monitoring. *Eng. Lett.* **2018**, *26*, 276–280.
60. Rainieri, C.; Fabbrocino, G. Development and validation of an automated operational modal analysis algorithm for vibration-based monitoring and tensile load estimation. *Mech. Syst. Signal Process.* **2015**, *60*, 512–534. [CrossRef]
61. Rainieri, C.; Gargaro, D.; Fabbrocino, G.; Maddaloni, G.; Di Sarno, L.; Prota, A.; Manfredi, G. Shaking table tests for the experimental verification of the effectiveness of an automated modal parameter monitoring system for existing bridges in seismic areas. *Struct. Control Health Monit.* **2018**, *25*, 1–19. [CrossRef]
62. Packo, P.; Ambrozinski, L.; Uhl, T. Structure damage modelling for guided waves-based SHM systems testing. In Proceedings of the 2011 Fourth International Conference on Modeling, Simulation and Applied Optimization, Kuala Lumpur, Malaysia, 19–21 April 2011; IEEE: Piscataway, NJ, USA, 2011; pp. 1–6.
63. Gopalakrishnan, S.; Chakraborty, A.; Mahapatra, D.R. *Spectral Finite Element Method: Wave Propagation, Diagnostics and Control in Anisotropic and Inhomogeneous Structures*; Springer Science & Business Media: Berlin, Germany, 2007.
64. Torres-Arredondo, M.A.; Buethe, I.; Tibaduiza, D.A.; Rodellar, J.; Fritzen, C.P. Damage detection and classification in pipework using acousto-ultrasonics and non-linear data-driven modelling. *J. Civ. Struct. Health Monit.* **2013**, *3*, 297–306. [CrossRef]
65. Sinou, J.J. A review of damage detection and health monitoring of mechanical systems from changes in the measurement of linear and non-linear vibrations. In *Mechanical Vibrations: Measurement, Effects and Control*; Nova Science: Hauppauge, NY, USA, 2009; pp. 643–702.
66. Wan, X.; Peter, W.T.; Zhang, X.; Xu, G.; Zhang, Q.; Fan, H.; Mao, Q.; Dong, M.; Wang, C.; Ma, H. Numerical study on static component generation from the primary Lamb waves propagating in a plate with nonlinearity. *Smart Mater. Struct.* **2018**, *27*, 045006. [CrossRef]
67. Yoon, H.; Shin, J.; Spencer, B.F., Jr. Structural displacement measurement using an unmanned aerial system. *Comput.-Aided Civ. Infrastruct. Eng.* **2018**, *33*, 183–192. [CrossRef]
68. Park, J.W.; Moon, D.S.; Yoon, H.; Gomez, F.; Spencer, B.F., Jr.; Kim, J.R. Visual–inertial displacement sensing using data fusion of vision-based displacement with acceleration. *Struct. Control Health Monit.* **2018**, *25*, e2122. [CrossRef]
69. Morse, L.; Khodaei, Z.S.; Aliabadi, M. Reliability based impact localization in composite panels using Bayesian updating and the Kalman filter. *Mech. Syst. Signal Process.* **2018**, *99*, 107–128. [CrossRef]
70. Kim, S.; Frangopol, D.M. Multi-objective probabilistic optimum monitoring planning considering fatigue damage detection, maintenance, reliability, service life and cost. *Struct. Multidiscip. Optim.* **2018**, *57*, 39–54. [CrossRef]
71. Fan, X.P.; Lu, D.G. Reliability prediction of bridges based on monitored data and Bayesian dynamic models. Key Engineering Materials. *Trans Tech Publ.* **2014**, *574*, 77–84.

72. Foote, P. New guidelines for implementation of structural health monitoring in aerospace applications. *SAE Int. J. Aerosp.* **2013**, *6*, 525–533. [CrossRef]
73. Van Dam, J.; Bond, L.J. Economics of online structural health monitoring of wind turbines: Cost benefit analysis. *AIP Conf. Proc.* **2015**, *1650*, 899–908.
74. Baghalian, A.; Tashakori, S.; Senyurek, V.Y.; Unal, M.; McDaniel, D.; Tansel, I.N. Development of comprehensive heterodyne effect based inspection (CHEBI) method for inclusive monitoring of cracks. *Measurement* **2018**, *128*, 89–95. [CrossRef]
75. Zou, Z.; Bao, Y.; Deng, F.; Li, H. An approach of reliable data transmission with random redundancy for wireless sensors in structural health monitoring. *IEEE Sens. J.* **2015**, *15*, 809–818.
76. Torres-Arredondo, M.A.; Tibaduiza-Burgos, D.A. An acousto-ultrasonics approach for probabilistic modelling and inference based on Gaussian processes. *Struct. Control Health Monit.* **2018**, *25*, e2178. [CrossRef]
77. Torres-Arredondo, M.A.; Sierra-Pérez, J.; Tibaduiza, D.A.; McGugan, M.; Rodellar, J.; Fritzen, C.P. Signal-based nonlinear modelling for damage assessment under variable temperature conditions by means of acousto-ultrasonics. *Struct. Control Health Monit.* **2015**, *22*, 1103–1118. [CrossRef]
78. Vitola, J.; Pozo, F.; Tibaduiza, D.; Anaya, M. A sensor data fusion system based on k-nearest neighbor pattern classification for structural health monitoring applications. *Sensors* **2017**, *17*, 417. [CrossRef]
79. Zang, C.; Friswell, M.I.; Imregun, M. Structural damage detection using independent component analysis. *Struct. Health Monit.* **2004**, *3*, 69–83. [CrossRef]
80. Hoshyarmanesh, H.; Ebrahimi, N.; Jafari, A.; Hoshyarmanesh, P.; Kim, M.; Park, H.H. PZT/PZT and PZT/BiT Composite Piezo-Sensors in Aerospace SHM Applications: Photochemical Metal Organic+ Infiltration Deposition and Characterization. *Sensors* **2019**, *19*, 13. [CrossRef]
81. Tashakori, S.; Baghalian, A.; Senyurek, V.Y.; Unal, M.; McDaniel, D.; Tansel, I.N. Implementation of heterodyning effect for monitoring the health of adhesively bonded and fastened composite joints. *Appl. Ocean Res.* **2018**, *72*, 51–59. [CrossRef]
82. Chehami, L.; Moulin, E.; De Rosny, J.; Prada, C.; Chatelet, E.; Lacerra, G.; Gryllias, K.; Massi, F. Nonlinear secondary noise sources for passive defect detection using ultrasound sensors. *J. Sound Vib.* **2017**, *386*, 283–294. [CrossRef]
83. Tashakori, S.; Baghalian, A.; Senyurek, V.Y.; Farhangdoust, S.; McDaniel, D.; Tansel, I.N. Composites Bond Inspection Using Heterodyne Effect and SuRE Methods. *Shock Vib.* **2018**, *2018*, 1361932. [CrossRef]
84. Diamanti, K.; Soutis, C. Structural health monitoring techniques for aircraft composite structures. *Prog. Aerosp. Sci.* **2010**, *46*, 342–352. [CrossRef]
85. Carboni, M.; Gianneo, A.; Giglio, M. A Lamb waves based statistical approach to structural health monitoring of carbon fibre reinforced polymer composites. *Ultrasonics* **2015**, *60*, 51–64. [CrossRef]
86. Senyurek, V. Detection of cuts and impact damage at the aircraft wing slat by using Lamb wave method. *Measurement* **2015**, *67*, 10–23. [CrossRef]
87. Ma, S.; Wu, Z.; Wang, Y.; Liu, K. The reflection of guided waves from simple dents in pipes. *Ultrasonics* **2015**, *57*, 190–197. [CrossRef]
88. Gresil, M.; Yu, L.; Giurgiutiu, V.; Sutton, M. Predictive modeling of electromechanical impedance spectroscopy for composite materials. *Struct. Health Monit.* **2012**, *11*, 671–683. [CrossRef]
89. Baghalian, A.; Tashakori, S.; Senyurek, V.Y.; McDaniel, D.; Fekrmandi, H.; Tansel, I.N. Non-contact quantification of longitudinal and circumferential defects in pipes using the surface response to excitation (SuRE) method. *Int. J. Progn. Health Manag.* **2017**, *8*, 1–8.
90. Baghalian, A.; Tashakori, S.; Soto, J.R.; Senyurek, V.Y.; Tansel, I.N.; Uragun, B. Internal defect detection in hollow cylindrical structures using the Surface Response to Excitation (SuRE) Method. In Proceedings of the 2017 8th International Conference on Recent Advances in Space Technologies (RAST), Istanbul, Turkey, 19–22 June 2017; IEEE: Piscataway, NJ, USA, 2017; pp. 523–527.
91. Marino-Merlo, E.; Bulletti, A.; Giannelli, P.; Calzolai, M.; Capineri, L. Analysis of Errors in the Estimation of Impact Positions in Plate-Like Structure through the Triangulation Formula by Piezoelectric Sensors Monitoring. *Sensors* **2018**, *18*, 3426. [CrossRef]
92. Kudela, P.; Radzienski, M.; Ostachowicz, W.; Yang, Z. Structural Health Monitoring system based on a concept of Lamb wave focusing by the piezoelectric array. *Mech. Syst. Signal Process.* **2018**, *108*, 21–32. [CrossRef]

93. Ha, S.; Lonkar, K.; Mittal, A.; Chang, F.K. Adhesive Layer Effects on PZT-induced Lamb Waves at Elevated Temperatures. *Struct. Health Monit.* **2010**, *9*, 247–256. [CrossRef]
94. Li, R.; Li, H.; Hu, B. Damage Identification of Large Generator Stator Insulation Based on PZT Sensor Systems and Hybrid Features of Lamb Waves. *Sensors* **2018**, *18*, 2745. [CrossRef] [PubMed]
95. Annamdas, V.G.M.; Rizzo, P. Influence of the excitation frequency in the electromechanical impedance method for SHM applications. In *Smart Sensor Phenomena, Technology, Networks, and Systems 2009*; International Society for Optics and Photonics: Bellingham, WA, USA, 2009; Volume 7293, p. 72930V.
96. Martínez, A.; Güemes, J.; Perales, J.; Vega, J. SHM via topological derivative. *Smart Mater. Struct.* **2018**, *27*, 085002. [CrossRef]
97. Liu, G.; Mao, Z.; Todd, M.; Huang, Z. Damage assessment with state–space embedding strategy and singular value decomposition under stochastic excitation. *Struct. Health Monit.* **2014**, *13*, 131–142. [CrossRef]
98. Li, H.; Ou, J. Structural health monitoring: From sensing technology stepping to health diagnosis. *Procedia Eng.* **2011**, *14*, 753–760.
99. Zhang, J.; Sunny, A.I.; Zhang, G.; Tian, G. Feature extraction for robust crack monitoring using passive wireless RFID antenna sensors. *IEEE Sens. J.* **2018**, *18*, 6273–6280. [CrossRef]
100. Barski, M.; Kedziora, P.; Muc, A.; Romanowicz, P. Structural health monitoring (SHM) methods in machine design and operation. *Arch. Mech. Eng.* **2014**, *61*, 653–677. [CrossRef]
101. Kedziora, P.; Barski, M.; Chwal, M. Piezoelectric transducers. Key Engineering Materials. *Trans Tech Publ.* **2013**, *542*, 75–80.
102. Potapov, A.; Polyakov, V.; Syasko, V.; Popov, A.; Kurianova, P. Low-frequency broadband ultrasonic transducers for testing articles manufactured of large-structure and composite materials. Part 1. Complete and partial degeneracy of vibration modes in piezoelectric elements of different geometric shapes. *Russ. J. Nondestruct. Test.* **2015**, *51*, 338–351. [CrossRef]
103. Yu, H.; Quan, Q.; Tian, X.; Li, H. Optimization and Analysis of a U-Shaped Linear Piezoelectric Ultrasonic Motor Using Longitudinal Transducers. *Sensors* **2018**, *18*, 809. [CrossRef] [PubMed]
104. Hedberg, C.; Gazisaeidi, H.; Haller, K.; Mfoumou, E. Design alterations of a high power air transducer. *Jpn. J. Appl. Phys.* **2007**, *46*, 4908. [CrossRef]
105. Mandal, D.D.; Banerjee, S. Identification of breathing type disbonds in stiffened panels using non-linear lamb waves and built-in circular PWT array. *Mech. Syst. Signal Process.* **2019**, *117*, 33–51. [CrossRef]
106. de Castro, B.A.; Baptista, F.G.; Ciampa, F. New Signal Processing Approach for Structural Health Monitoring in Noisy Environments Based on Impedance Measurements. *Measurement* **2019**, *137*. [CrossRef]
107. Chandarana, N.; Lansiaux, H.; Gresil, M. Characterisation of damaged tubular composites by acoustic emission, thermal diffusivity mapping and TSR-RGB projection technique. *Appl. Compos. Mater.* **2017**, *24*, 525–551. [CrossRef]
108. Joseph, R.; Bhuiyan, M.Y.; Giurgiutiu, V. Acoustic emission source modeling in a plate using buried moment tensors. In *Health Monitoring of Structural and Biological Systems 2017*; International Society for Optics and Photonics: Bellingham, WA, USA, 2017; Volume 10170, p. 1017028.
109. Kim, H.; Renteria-Marquez, A.; Islam, M.D.; Chavez, L.A.; Garcia Rosales, C.A.; Ahsan, M.A.; Tseng, T.L.B.; Love, N.D.; Lin, Y. Fabrication of bulk piezoelectric and dielectric BaTiO3 ceramics using paste extrusion 3D printing technique. *J. Am. Ceram. Soc.* **2019**, in press. [CrossRef]
110. Ervin, J.D.; Brei, D.; Van Hoy, C.A.; Mawdsley, J.R.; Halloran, J.W. New fabrication process for active micro-sized metal/ceramic devices. In Proceedings of the ASME Aerospace Division International Mechanical Engineering Congress and Exposition, Atlanta, GA, USA, 17–22 November 1996; pp. 695–702.
111. Salowitz, N.; Guo, Z.; Kim, S.J.; Li, Y.H.; Lanzara, G.; Chang, F.K. Screen printed piezoceramic actuators/sensors microfabricated on organic films and stretchable networks. In *Structural Health Monitoring*; DEStech Publications, Inc.: Lancaster, PA, USA, 2013; pp. 1543–1550.
112. Ruan, J.; Ho, S.C.M.; Patil, D.; Li, M.; Song, G. Wind turbine blade damage detection using an active sensing approach. *Smart Mater. Struct.* **2014**, *23*, 105005. [CrossRef]
113. Budoya, D.E.; Baptista, F.G. A comparative study of impedance measurement techniques for structural health monitoring applications. *IEEE Trans. Instrum. Meas.* **2018**, *67*, 912–924. [CrossRef]
114. Qin, L.; Ren, H.; Dong, B.; Xing, F. Development of technique capable of identifying different corrosion stages in reinforced concrete. *Appl. Acoust.* **2015**, *94*, 53–56. [CrossRef]

115. Talakokula, V.; Bhalla, S.; Gupta, A. Corrosion assessment of reinforced concrete structures based on equivalent structural parameters using electro-mechanical impedance technique. *J. Intell. Mater. Syst. Struct.* **2014**, *25*, 484–500. [CrossRef]
116. Li, W.; Yuan, Y.; Yang, J.; Deng, H.; Yuan, L. In-Fiber Integrated Sensor Array With Embedded Weakly Reflective Joint Surface. *J. Lightwave Technol.* **2018**, *36*, 5663–5668. [CrossRef]
117. Yang, W.; Liu, X.; Lu, W.; Yu, N.; Chen, L.; Zhou, L.; Chang, S. A novel white light interference based AFM head. *J. Lightwave Technol.* **2017**, *35*, 3604–3610. [CrossRef]
118. Schmitt, R.; König, N.; de Araújo, E.M. Surface profile analysis using a fiber optic low-coherence interferometer. In *Optical Measurement Systems for Industrial Inspection VI*; International Society for Optics and Photonics: Bellingham, WA, USA, 2009; Volume 7389, p. 738914.
119. Torres, B.; Payá-Zaforteza, I.; Calderón, P.A.; Adam, J.M. Analysis of the strain transfer in a new FBG sensor for structural health monitoring. *Eng. Struct.* **2011**, *33*, 539–548. [CrossRef]
120. Shehata, E.; Rizkalla, S. Intelligent sensing for innovative bridges. *J. Intell. Mater. Syst. Struct.* **1999**, *10*, 304–313. [CrossRef]
121. Kinet, D.; Mégret, P.; Goossen, K.; Qiu, L.; Heider, D.; Caucheteur, C. Fiber Bragg grating sensors toward structural health monitoring in composite materials: Challenges and solutions. *Sensors* **2014**, *14*, 7394–7419. [CrossRef]
122. Drissi-Habti, M.; Raman, V.; Khadour, A.; Timorian, S. Fiber optic sensor embedment study for multi-parameter strain sensing. *Sensors* **2017**, *17*, 667. [CrossRef]
123. Qiu, Z.; Piyawattanamatha, W. New endoscopic imaging technology based on MEMS sensors and actuators. *Micromachines* **2017**, *8*, 210. [CrossRef]
124. Cochran, E.S.; Lawrence, J.F.; Kaiser, A.; Fry, B.; Chung, A.; Christensen, C. Comparison between low-cost and traditional MEMS accelerometers: A case study from the M7. 1 Darfield, New Zealand, aftershock deployment. *Ann. Geophys.* **2012**, *54*. [CrossRef]
125. Giang, D.H.; Duc, N.; Agnus, G.; Maroutian, T.; Lecoeur, P. Fabrication and characterization of PZT string based MEMS devices. *J. Sci. Adv. Mater. Devices* **2016**, *1*, 214–219. [CrossRef]
126. Dong, L.; Wang, H.; Wang, G.; Qiu, W. A wireless multifunctional monitoring system of tower body running state based on MEMS acceleration sensor. In Proceedings of the 2018 19th International Symposium on Quality Electronic Design (ISQED), Santa Clara, CA, USA, 13–14 March 2018; IEEE: Piscataway, NJ, USA, 2018; pp. 357–363.
127. Zhu, L.; Fu, Y.; Chow, R.; Spencer, B.; Park, J.; Mechitov, K. Development of a high-sensitivity wireless accelerometer for structural health monitoring. *Sensors* **2018**, *18*, 262. [CrossRef]
128. Chang, F.K. *Structural Health Monitoring 2013: A Roadmap to Intelligent Structures: Proceedings of the Ninth International Workshop on Structural Health Monitoring, September 10–12, 2013*; DEStech Publications, Inc.: Lancaster, PA, USA, 2013.
129. Saboonchi, H.; Ozevin, D.; Kabir, M. MEMS sensor fusion: Acoustic emission and strain. *Sens. Actuators A Phys.* **2016**, *247*, 566–578. [CrossRef]
130. Dixit, A.; Bhalla, S. Prognosis of fatigue and impact induced damage in concrete using embedded piezo-transducers. *Sens. Actuators A Phys.* **2018**, *274*, 116–131. [CrossRef]
131. Debéda, H.; Lakhmi, R.; Pommier-Budinger, V.; Lucat, C. Study of free-standing electroded PZT thick-films: From materials to microsystems. Key Engineering Materials. *Trans Tech Publ.* **2014**, *605*, 55–58.
132. Moschas, F.; Stiros, S. Experimental evaluation of the performance of arrays of MEMS accelerometers. *Mech. Syst. Signal Process.* **2019**, *116*, 933–942. [CrossRef]
133. Cooperman, A.M.; Martinez, M.J. MEMS inertial sensors for load monitoring of wind turbine blades. In *Smart Materials and Nondestructive Evaluation for Energy Systems 2015*; International Society for Optics and Photonics: Bellingham, WA, USA, 2015; Volume 9439, p. 94390A.
134. Camacho, J.; Quintero, A.; Ruiz, M.; Villamizar, R.; Mujica, L. Implementation of a piezo-diagnostics approach for damage detection based on PCA in a linux-based embedded platform. *Sensors* **2018**, *18*, 3730. [CrossRef]
135. Tondolo, F.; Cesetti, A.; Matta, E.; Quattrone, A.; Sabia, D. Smart reinforcement steel bars with low-cost MEMS sensors for the structural health monitoring of RC structures. *Constr. Build. Mater.* **2018**, *173*, 740–753. [CrossRef]

136. Sabato, A.; Feng, M.Q.; Fukuda, Y.; Carni, D.L.; Fortino, G. A novel wireless accelerometer board for measuring low-frequency and low-amplitude structural vibration. *IEEE Sens. J.* **2016**, *16*, 2942–2949. [CrossRef]
137. Dai, K.; Huang, Y.; Huang, Z.; Zong, G.; Shi, W. Experimental case studies on wireless and wired sensors. In *Nondestructive Characterization for Composite Materials, Aerospace Engineering, Civil Infrastructure, and Homeland Security 2013*; International Society for Optics and Photonics: Bellingham, WA USA, 2013; Volume 8694, p. 86941N.
138. Ghorbanpour Arani, A.; Abdollahian, M.; Rahmati, A. Nonlocal Piezomagnetoelasticity Theory for Buckling Analysis of Piezoelectric/Magnetostrictive Nanobeams Including Surface Effects. *J. Solid Mech.* **2017**, *9*, 707–729.
139. Moreno-Gomez, A.; Perez-Ramirez, C.A.; Dominguez-Gonzalez, A.; Valtierra-Rodriguez, M.; Chavez-Alegria, O.; Amezquita-Sanchez, J.P. Sensors used in structural health monitoring. *Arch. Comput. Methods Eng.* **2018**, *25*, 901–918. [CrossRef]
140. Farrar, C.R.; Worden, K., An introduction to structural health monitoring. In *New Trends in Vibration Based Structural Health Monitoring*; Springer: Vienna, Austria, 2010; pp. 1–17._1. [CrossRef]
141. Capellari, G.; Chatzi, E.; Mariani, S. Cost–benefit optimization of structural health monitoring sensor networks. *Sensors* **2018**, *18*, 2174. [CrossRef]
142. Jung, K.C.; Chang, S.H. Performance evaluation of smart grid fabrics comprising carbon dry fabrics and PVDF ribbon sensors for structural health monitoring. *Compos. Part B Eng.* **2019**, *163*, 690–701. [CrossRef]
143. Wan, F.; Yu, X.; Yu, Q. Research on Optimal Sensor Placement for Aircraft Structural Health Management. In Proceedings of the 2017 IEEE International Conference on Prognostics and Health Management (ICPHM), Dallas, TX, USA, 19–21 June 2017; IEEE: Piscataway, NJ, USA, 2017; pp. 160–166.
144. Salas, M.; Koerdt, M.; Hübner, M.; Kahali, M.; Lang, W. Material integrated sensors for an optimal baseline selection on a wireless SHM network. In Proceedings of the 2016 IEEE SENSORS, Orlando, FL, USA, 30 October–3 November 2016; IEEE: Piscataway, NJ, USA, 2016; pp. 1–3.
145. Lu, W.; Teng, J.; Wen, R.; Zhu, J.; Li, C. Malfunction diagnosis of sensors based on correlation of measurements. *Meas. Sci. Technol.* **2017**, *28*, 024004. [CrossRef]
146. Bhuiyan, M.Z.A.; Wang, G.; Wu, J.; Cao, J.; Liu, X.; Wang, T. Dependable structural health monitoring using wireless sensor networks. *IEEE Trans. Dependable Secur. Comput.* **2017**, *14*, 363–376. [CrossRef]
147. Li, C.; Teng, Y.; Li, X.; Long, J.; Wang, Z.; Tang, Y. Design of network force balanced accelerometer. In Proceedings of the 2017 2nd International Conference on Frontiers of Sensors Technologies (ICFST), Shenzhen, China, 14–16 April 2017; IEEE: Piscataway, NJ, USA, 2017; pp. 40–44.
148. Ganesan, V.; Das, T.; Rahnavard, N.; Kauffman, J.L. Vibration-based monitoring and diagnostics using compressive sensing. *J. Sound Vib.* **2017**, *394*, 612–630. [CrossRef]
149. Van Buren, K.; Reilly, J.; Neal, K.; Edwards, H.; Hemez, F. Guaranteeing robustness of structural condition monitoring to environmental variability. *J. Sound Vib.* **2017**, *386*, 134–148. [CrossRef]
150. Li, H.N.; Ren, L.; Jia, Z.G.; Yi, T.H.; Li, D.S. State-of-the-art in structural health monitoring of large and complex civil infrastructures. *J. Civ. Struct. Health Monit.* **2016**, *6*, 3–16. [CrossRef]
151. Araujo, A.; García-Palacios, J.; Blesa, J.; Tirado, F.; Romero, E.; Samartín, A.; Nieto-Taladriz, O. Wireless measurement system for structural health monitoring with high time-synchronization accuracy. *IEEE Trans. Instrum. Meas.* **2012**, *61*, 801–810. [CrossRef]
152. Wang, Q.; Su, Z.; Hong, M. Online damage monitoring for high-speed train bogie using guided waves: Development and validation. In Proceedings of the EWSHM-7th European Workshop on Structural Health Monitoring, La Cité, Nantes, France, 8–11 July 2014; pp. 143–150.
153. Linderman, L.E.; Jo, H.; Spencer, B.F. Low-latency data acquisition hardware for real-time wireless sensor applications. *IEEE Sens. J.* **2015**, *15*, 1800–1809. [CrossRef]
154. dos Santos, A.D.F.; da Silva, M.F.M.; de Sales Junior, C.d.S.; de Sousa, M.J.; Fernandes, C.S.; Costa, J.C.W.A. Data Management System for Structural Health Monitoring. *IEEE Lat. Am. Trans.* **2015**, *13*, 1090–1097. [CrossRef]
155. Corbetta, M.; Sbarufatti, C.; Elizabeth, J.; Giglio, M. Removal of temperature-induced strain variations for fatigue crack growth detection in a real aeronautical structure. In Proceedings of the 8th European Workshop on Structural Health Monitoring, EWSHM 2016, Bilbao, Spain, 5–8 July 2016; pp. 900–909.

156. Sohn, H. Effects of environmental and operational variability on structural health monitoring. *Philos. Trans. R. Soc. A Math. Phys. Eng. Sci.* **2006**, *365*, 539–560. [CrossRef]
157. Worden, K.; Cross, E. On switching response surface models, with applications to the structural health monitoring of bridges. *Mech. Syst. Signal Process.* **2018**, *98*, 139–156. [CrossRef]
158. Calleja, R.; Boulal, H.; Gómez-Macpherson, H. An innovative way to handle residues in a no-tillage maize-based system under sprinkler irrigation in southern Spain. *Ital. J. Agron.* **2008**, *3*, 643–644.
159. Quiñones, M.M.; Montejo, L.A.; Jang, S. Experimental and numerical evaluation of wavelet based damage detection methodologies. *Int. J. Adv. Struct. Eng.* **2015**, *7*, 69–80. [CrossRef]
160. Kaloop, M.R.; Hu, J.W. Damage Identification and Performance Assessment of Regular and Irregular Buildings Using Wavelet Transform Energy. *Adv. Mater. Sci. Eng.* **2016**, 6027812. [CrossRef]
161. Perez, J.S. Smart Aeronautical Structures: Development and Experimental Validation of a Structural Health Monitoring System for Damage Detection. Ph.D. Thesis, Universidad Politécnica de Madrid, Madrid, Spain, 2014.
162. Gharibnezhad, F.; Mujica Delgado, L.E.; Rodellar Benedé, J.; Fritzen, C.P. Damage detection using robust fuzzy principal component analysis. In Proceedings of the 6th European Workshop on Structural Health Monitoring, EWSHM 2013, Dresden, Germany, 3–6 July 2013; pp. 1–6.
163. Ruiz, M.; Mujica, L.E.; Sierra, J.; Pozo, F.; Rodellar, J. Multiway principal component analysis contributions for structural damage localization. *Struct. Health Monit.* **2018**, *17*, 1151–1165. [CrossRef]
164. Gharibnezhad, F. Robust Damage Detection in Smart Structures. Ph.D. Thesis, Universitat Politecnica de Catalunya, Barcelona, Spain, 2014.
165. Catbas, F.N. Structural Health Monitoring: Applications and Data Analysis. In *Structural Health Monitoring of Civil Infrastructure Systems*; Woodhead Publishin Limited: Sawston, UK, 2009; pp. 1–39.
166. Taha, M.R.; Noureldin, A.; Lucero, J.; Baca, T. Wavelet transform for structural health monitoring: A compendium of uses and features. *Struct. Health Monit.* **2006**, *5*, 267–295. [CrossRef]
167. Huang, H.B.; Yi, T.H.; Li, H.N. Canonical correlation analysis based fault diagnosis method for structural monitoring sensor networks. *Smart Struct. Syst.* **2016**, *17*, 1031–1053. [CrossRef]
168. Yi, T.H.; Huang, H.B.; Li, H.N. Development of sensor validation methodologies for structural health monitoring: A comprehensive review. *Measurement* **2017**, *109*, 200–214. [CrossRef]
169. Kullaa, J. Detection, identification, and quantification of sensor fault in a sensor network. *Mech. Syst. Signal Process.* **2013**, *40*, 208–221. [CrossRef]
170. Iakovidis, I.; Cross, E.J.; Worden, K. A principled multiresolution approach for signal decomposition. *J. Phys. Conf. Ser.* **2018**, *1106*, 012001. [CrossRef]
171. Mujica Delgado, L.E. A Hybrid Approach of Knowledge-Based Reasoning for Structural Assessment. Ph.D. Thesis, Universitat de Girona, Girona, Spain, 2006.
172. Tibaduiza, D.A.; Mujica, L.E.; Rodellar, J.; Güemes, A. Structural damage detection using principal component analysis and damage indices. *J. Intell. Mater. Syst. Struct.* **2016**, *27*, 233–248. [CrossRef]
173. Ge, Z.; Xie, L.; Kruger, U.; Song, Z. Local ICA for multivariate statistical fault diagnosis in systems with unknown signal and error distributions. *AIChE J.* **2012**, *58*, 2357–2372. [CrossRef]
174. Cazangiu, D.; Bulmaga, M. Aspects regarding to the Design of the Feature Extraction Algorithms used at Structural Health Monitoring Systems. *Res. Sci. Today* **2014**, *7*, 95.
175. Andre, J.; Kiremidjian, A.; Liao, Y.; Georgakis, C.; Rajagopal, R. Structural health monitoring approach for detecting ice accretion on bridge cable using the Haar Wavelet Transform. In *Sensors and Smart Structures Technologies for Civil, Mechanical, and Aerospace Systems 2016*; International Society for Optics and Photonics: Bellingham, WA, USA, 2016; Volume 9803, p. 98030F.
176. Pozo, F.; Arruga, I.; Mujica, L.E.; Ruiz, M.; Podivilova, E. Detection of structural changes through principal component analysis and multivariate statistical inference. *Struct. Health Monit.* **2016**, *15*, 127–142. [CrossRef]
177. Pozo, F.; Vidal, Y. Wind turbine fault detection through principal component analysis and statistical hypothesis testing. *Energies* **2016**, *9*, 3. [CrossRef]
178. Pozo, F.; Vidal, Y.; Serrahima, J. On real-time fault detection in wind turbines: Sensor selection algorithm and detection time reduction analysis. *Energies* **2016**, *9*, 520. [CrossRef]
179. Pozo, F.; Vidal, Y.; Salgado, Ó. Wind turbine condition monitoring strategy through multiway PCA and multivariate inference. *Energies* **2018**, *11*, 749. [CrossRef]

180. Flynn, E.B.; Todd, M.D. A Bayesian approach to optimal sensor placement for structural health monitoring with application to active sensing. *Mech. Syst. Signal Process.* **2010**, *24*, 891–903. [CrossRef]
181. Anaya, M.; Tibaduiza, D.A.; Pozo, F. A bioinspired methodology based on an artificial immune system for damage detection in structural health monitoring. *Shock Vib.* **2015**, *2015*. [CrossRef]
182. Zhang, J.; Hou, Z. Application of Artificial Immune System in Structural Health Monitoring. *J. Struct.* **2014**, *2014*. [CrossRef]
183. Tibaduiza, D.; Mujica, L.; Rodellar, J. Damage classification in structural health monitoring using principal component analysis and self-organizing maps. *Struct. Control Health Monit.* **2013**, *20*, 1303–1316. [CrossRef]
184. Vitola, J.; Vejar, M.A.; Burgos, D.A.T.; Pozo, F. Data-Driven Methodologies for Structural Damage Detection Based on Machine Learning Applications. In *Pattern Recognition-Analysis and Applications*; InTech: London, UK, 2016; pp. 109–126.
185. Tibaduiza, D.; Torres-Arredondo, M.Á.; Vitola, J.; Anaya, M.; Pozo, F. A damage classification approach for structural health monitoring using machine learning. *Complexity* **2018**, *2018*, 5081283. [CrossRef]
186. Mulligan, K.R.; Yang, C.; Quaegebeur, N.; Masson, P. A data-driven method for predicting structural degradation using a piezoceramic array. *Int. J. Progn. Health Manag.* **2013**, *4*, 1–14.
187. Sierra-Pérez, J.; Güemes, A.; Mujica, L.E. Damage detection by using FBGs and strain field pattern recognition techniques. *Smart Mater. Struct.* **2012**, *22*, 025011. [CrossRef]
188. Sen, D.; Aghazadeh, A.; Mousavi, A.; Nagarajaiah, S.; Baraniuk, R.; Dabak, A. Data-driven semi-supervised and supervised learning algorithms for health monitoring of pipes. *Mech. Syst. Signal Process.* **2019**, *131*, 524–537. [CrossRef]
189. Datteo, A.; Lucà, F.; Busca, G. Statistical pattern recognition approach for long-time monitoring of the G.Meazza stadium by means of AR models and PCA. *Eng. Struct.* **2017**, *153*, 317–333. [CrossRef]
190. Zhou, Y.; Jia, X.; Zhang, D.; Yue, L. Unsupervised structural damage classification algorithm based on hierarchical clustering and artificial immune pattern recognition. *J. Shenyang Jianzhu Univ. (Nat. Sci.)* **2014**, 374–378.
191. Momon, S.; Godin, N.; Reynaud, P.; R'Mili, M.; Fantozzi, G. Unsupervised and supervised classification of AE data collected during fatigue test on CMC at high temperature. *Compos. Part A Appl. Sci. Manuf.* **2012**, *43*, 254–260. [CrossRef]
192. Cherkassky, V.; Ma, Y. Another look at statistical learning theory and regularization. *Neural Netw.* **2009**, *22*, 958–969. [CrossRef]
193. McCrory, J.; Al-Jumaili, S.; Crivelli, D.; Pearson, M.; Eaton, M.; Featherston, C.; Guagliano, M.; Holford, K.; Pullin, R. Damage classification in carbon fibre composites using acoustic emission: A comparison of three techniques. *Compos. Part B Eng.* **2015**, *68*, 424–430. [CrossRef]
194. Nagarajaiah, S.; Yang, Y. Modeling and harnessing sparse and low-rank data structure: A new paradigm for structural dynamics, identification, damage detection, and health monitoring. *Struct. Control Health Monit.* **2017**, *24*. [CrossRef]
195. Lorenzoni, F.; Casarin, F.; Caldon, M.; Islami, K.; Modena, C. Uncertainty quantification in structural health monitoring: Applications on cultural heritage buildings. *Mech. Syst. Signal Process.* **2016**, *66*, 268–281. [CrossRef]
196. Li, B. Uncertainty Quantification in Vibration-based Structural Health Monitoring using Bayesian Statistics. Ph.D. Thesis, University of California, Berkeley, CA, USA, 2016.
197. Kim, J.J.; Taha, M.M.R.; Ross, T.J. Binary Damage Classification in SHM Using Possibility Distributions. In Proceedings of the Second International Conference on Vulnerability and Risk Analysis and Management (ICVRAM) and the Sixth International Symposium on Uncertainty, Modeling, and Analysis (ISUMA), Liverpool, UK, 13-16 July 2014.
198. Cappello, C.; Zonta, D.; Glišić, B. Expected utility theory for monitoring-based decision-making. *Proc. IEEE* **2016**, *104*, 1647–1661. [CrossRef]
199. Endsley, A.; Brooks, C.; Harris, D.; Ahlborn, T.; Vaghefi, K. Decision support system for integrating remote sensing in bridge condition assessment and preservation. In *Sensors and Smart Structures Technologies for Civil, Mechanical, and Aerospace Systems 2012*; International Society for Optics and Photonics: Bellingham, WA, USA, 2012; Volume 8345, p. 834548.

200. Sun, D.; Lee, V.C.S.; Lu, Y. An intelligent data fusion framework for structural health monitoring. In Proceedings of the 2016 IEEE 11th Conference on Industrial Electronics and Applications (ICIEA), Hefei, China, 5–7 June 2016; pp. 49–54. [CrossRef]
201. Sharif Khodaei, Z.; Aliabadi, M. A multi-level decision fusion strategy for condition based maintenance of composite structures. *Materials* **2016**, *9*, 790. [CrossRef]
202. Webb, G.T.; Vardanega, P.J.; Middleton, C.R. Categories of SHM deployments: Technologies and capabilities. *J. Bridge Eng.* **2015**, *20*, 04014118. [CrossRef]
203. Bai, F.; Gagar, D.; Foote, P.; Zhao, Y. Comparison of alternatives to amplitude thresholding for onset detection of acoustic emission signals. *Mech. Syst. Signal Process.* **2017**, *84*, 717–730. [CrossRef]
204. Deraemaeker, A.; Worden, K. A comparison of linear approaches to filter out environmental effects in structural health monitoring. *Mech. Syst. Signal Process.* **2018**, *105*, 1–15. [CrossRef]
205. Martowicz, A.; Sendecki, A.; Salamon, M.; Rosiek, M.; Uhl, T. Application of electromechanical impedance-based SHM for damage detection in bolted pipeline connection. *Nondestruct. Test. Eval.* **2016**, *31*, 17–44. [CrossRef]
206. Bolognani, D.; Verzobio, A.; Tonelli, D.; Cappello, C.; Glisic, B.; Zonta, D. An application of Prospect Theory to a SHM-based decision problem. In *Health Monitoring of Structural and Biological Systems 2017*; International Society for Optics and Photonics: Bellingham, WA, USA, 2017; Volume 10170, p. 101702G.
207. Sabatino, S.; Frangopol, D.M. Decision making framework for optimal SHM planning of ship structures considering availability and utility. *Ocean Eng.* **2017**, *135*, 194–206. [CrossRef]

DETECTION AND CLASSIFICATION OF STRUCTURAL CHANGES USING T-DISTRIBUTED STOCHASTIC NEIGHBOR EMBEDDING

Agis, D., Pozo, F.

Control, Modeling, Identification and Applications (CoDAlab), Department of Mathematics, Escola d'Enginyeria de Barcelona Est (EEBE), Universitat Politècnica de Catalunya (UPC), Campus Diagonal-Besòs (CDB), Eduard Maristany, 16, Barcelona 08019, Spain
francesc.pozo@upc.edu

ABSTRACT
This work states a structural health monitoring strategy for detection and classification of structural changes. The proposed approach is based on the so-called t-distributed stochastic neighbor embedding (t-SNE), a non-linear technique that is able to represent the local structure of high-dimensional data that are collected from multi-sensor signals in a simple scatter plot. All data sets were pre-processed using principal component analysis (PCA) to reduce their dimensionality before t-SNE was performed. More precisely, when a structure has to be diagnosed, the collected data from the current structure is projected into the t-SNE scatter plot. Subsequently, a sample of the projected data is compared with the center of the clusters of the pre-recorded damages. The current structure to be diagnosed is then associated with a damage based on the distances of the data to the centroids: the structure is classified based on the smallest point-centroid distance.
The methodology is evaluated using experimental data from an aluminum plate instrumented with piezoelectric transducers (PZTs). Results are presented in time domain, and they reveal the strong performance of t-SNE, with a percentage of correct decisions close to 100%.

KEYWORDS: Damage diagnosis, structural health monitoring, t-distributed stochastic neighbor embedding.

1. INTRODUCTION

Structural health monitoring (SHM) is an essential process for engineering structures because it verifies the correct functioning of the structure and determines whether it needs some kind of maintenance. Therefore, in SHM systems, detection and classification of structural changes are very important in order to know the current state of the structure for safety and to reduce maintenance costs. SHM has been applied in countless structures such as buildings [1], wind turbines [2, 3] and aircraft [4], among others, and a review of the state-of-the-art revealed that SHM is a very active research area.
In order to obtain information about the health state of the structure, data are collected from multi-sensor signals. The information extracted from multi-sensor signals creates a high-dimensional dataset that contains a large volume of data due to continuous measurements of the monitoring system. Several methods have been proposed for management high-dimensional, big and complex data. Among these methods, visualization techniques stand out as offer a way to handle this kind of data by means of an intuitive interface that allows people to easily detect natural clusters, identify hidden patterns, etc. [5]. And among visualization techniques, one of the most used is dimensionality reduction. Dimensionality reduction is the process of reducing the dimension of the original data, by keeping basically the same intrinsic information [6].
In the literature, various dimensionality reduction methods are proposed: (i) linear methods, that focus on keeping dissimilar original data points far apart in the low-dimensional space, such as principal component analysis (PCA) [7, 8, 9, 10, 11] and linear discriminant analysis (LDA) [10, 11]; and (ii) non-linear methods, that focus on keeping similar original data points close together in the low-dimensional space, such as isometric mapping (ISOMAP) [6, 9, 10], kernel PCA [8, 10] and t-distributed stochastic neighbor embedding (t-SNE) [12], among others.
This work proposes a SHM strategy for detection and classification of structural changes based on t-SNE, a technique developed by Laurens van der Maaten and Geoffrey Hinton [12], which is able to represent the local structure

of original high-dimensional data, obtained by the different sensors, in a low-dimensional space (for example a simple scatter plot). In a nutshell, in the low-dimensional space, each original high-dimensional point is represented by a low-dimensional point in such a way that nearby low-dimensional points correspond to similar original high-dimensional points, and distant low-dimensional points correspond to dissimilar original high-dimensional points. That is, this technique finds out patterns by identifying clusters based on similarity of data points. t-SNE has been applied to many real data (in the research area of stem cells [13], in computational linguistics [14], in astrophysics [15], in human genetics [16], etc.), but it should be noted that this is the first time that it has been applied in the field of SHM.

In this study, all data sets are pre-processed using PCA to reduce their dimensionality before t-SNE is performed. More precisely, when a structure has to be diagnosed, the collected data from the current structure is projected into the t-SNE scatter plot. Subsequently, a sample of the projected data is compared with the center of the clusters of the pre-recorded damages. The current structure to be diagnosed is then associated with a damage based on the distances of the data to the centroids: the structure is classified based on the smallest point-centroid distance.

The proposed methodology is evaluated using experimental data from an aluminum plate instrumented with piezoelectric transducers (PZTs) attached to its surface. Results are presented in time domain, and they show the high classification accuracy and the strong performance of t-SNE, with a percentage of correct decisions close to 100%. We must highlight that the environmental conditions were not considered, leaving it for future researches.

The contribution of this paper is that t-SNE is extended and adapted for the first time to the field of structural health monitoring, in detection and classification of structural changes, thanks to the developed methodology.

The structure of the paper is as follows: in Section 2, a brief description of the experimental setup is presented. Section 3 describes the damage classification strategy that is applied to classify the damage in the structure. In Section 4, the results are shown. Section 5, conclusions, closes the paper.

2. DESCRIPTION OF THE EXPERIMENTAL SETUP

2.1. Structure

In this work, an aluminum plate with an area of 40 cm^2 and with four piezoelectric transducers is consider to demonstrate the reliability of the damage detection and classification methodology introduced in Section 3. The location of the PZTs and of the three damages that are added in the structure are shown in Figure 1.

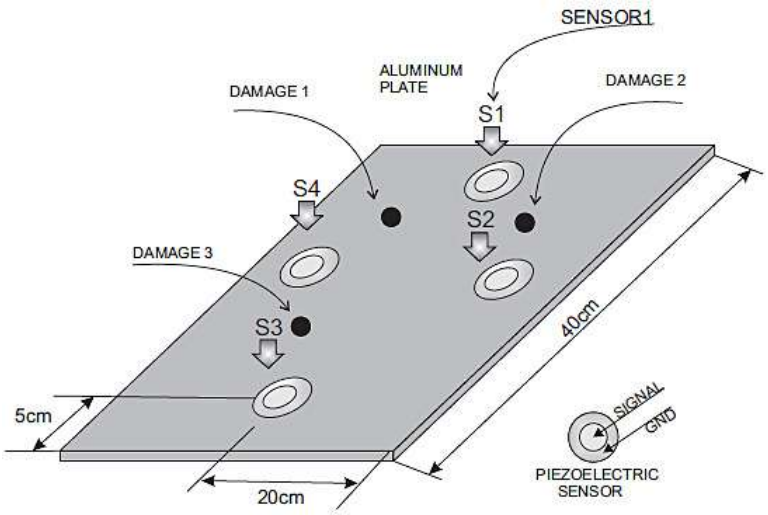

Figure 1 – Aluminum plate instrumented with four piezoelectric sensors. Source: Vitola et al. (2017a) [17].

2.2. Scenarios

The experimental setup includes three different scenarios to determine the behavior of the methodology:

- Scenario 1. The signals are acquired using a short cable (0.5 m) from the digitizer to the sensors, and these signals are filtered with a Golay filter algorithm after adding white Gaussian noise.
- Scenario 2. The signals are acquired using a long cable (2.5 m) to sensors, and signals are filtered with the Golay algorithm.

- Scenario 3. The signals are acquired using a short cable (0.5 m) from the digitizer to the sensors, and these signals are filtered without a Golay filter algorithm.

In this way, we can observe the effect of the attenuation with short and long cables, the effect of adding white Gaussian noise to the measured signals and the effect of the use of a Golay filter in the detection and classification process.

2.3. Sensors

A piezoelectric sensor network is used to excite the aluminum plate and collect the measured response. This sensor network works in several actuation phases. In each actuation phase, a PZT is used as actuator, and the rest of the PZTs are used as sensors. These data are organized in a matrix per actuator.

2.4. Damages

A mass is added to simulate the damage in the aluminum plate. This mass is an attached magnet in both sides of the plate to change its properties and produce changes in the propagated wave. The location of the mass defines each damage or structural state: Damage 1 ($D1$), Damage 2 ($D2$), Damage 3 ($D3$) and no damage ($D0$, healthy plate). Figure 2 shows these four structural states.

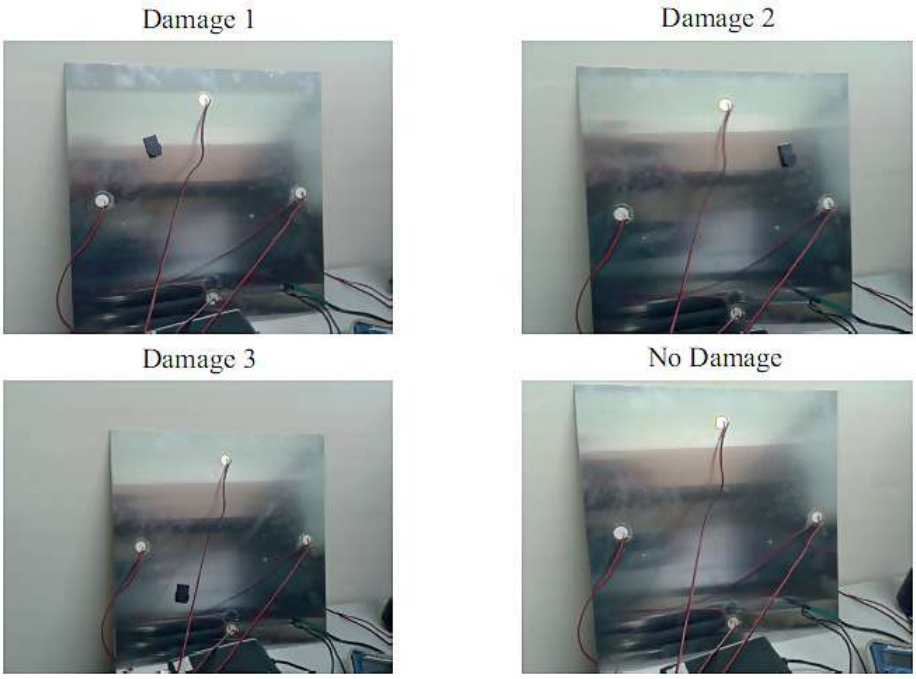

Figure 2 – Aluminum plate with four PZTs and with four different damages. Source: Vitola et al. (2017a) [17].

3. DAMAGE CLASSIFICATION STRATEGY

This work proposes a damage classification strategy that is based on the technique t-distributed stochastic neighbor embedding. This strategy will be described in the following subsections in more detail.

In a few words, all data sets —the data collected from the pristine structure and the new data coming from the structure to be diagnosed in an unknown state— are pre-processed using mean-centered group scaling (MCGS) and principal component analysis. Later, t-SNE is performed. Finally, confusion matrix is obtained from the distances of the data to the centroids associated with each structural state. More precisely, when a structure has to be diagnosed, the collected data from the current structure is projected into the t-SNE scatter plot. Subsequently, a sample of the projected data is compared with the center of the clusters of the pre-recorded damages. The current structure to be diagnosed is then associated with a damage based on the minimum distance to a cluster.

3.1. Data collection

The strategy uses data from an aluminum plate with four PZTs. Each PZT can operate as actuator —exciting the plate with a excitation signal— or as sensor —measuring signals. The number of PZTs defines the number of actuation phases, and each actuation phase defines a particular PZT as actuator and the rest of the PZTs as sensors:

Table 1 – Actuation phases.

Actuation phase	Actuator PZT	Sensor PZTs
1	1	$2-3-4$
2	2	$1-3-4$
3	3	$1-2-4$
4	4	$1-2-3$

Four data files are obtained from each scenario, one for each actuation phase. Each file is organized as follows: 25 experiments are performed for each structural state. Consequently, each file consists of 100 rows (25 experiments $\times$ 4 structural states). That is, the first 25 rows are captured without damage, the next 25 with Damage 1, the next 25 with Damage 2 and, finally, the last 25 with Damage 3. Regarding the columns, 60000 measurements are performed for each PZT that works as sensor. Therefore, each file contains 180000 columns (60000 measurements $\times$ 3 sensors). In matrix notation, the data are represented as follows:

$$\mathbf{Z}^{(i)} = \begin{pmatrix} z^{(i)}_{1,1} & z^{(i)}_{1,2} & \cdots & z^{(i)}_{1,180000} \\ z^{(i)}_{2,1} & z^{(i)}_{2,2} & \cdots & z^{(i)}_{2,180000} \\ \vdots & \vdots & \ddots & \vdots \\ z^{(i)}_{100,1} & z^{(i)}_{100,2} & \cdots & z^{(i)}_{100,180000} \end{pmatrix} \in \mathscr{M}_{100\times 180000}(\mathbb{R}), \tag{1}$$

where $i = 1,\ldots,4$ is the $i-$th actuation phase.
Finally, the data from all the actuation phases are stored in a matrix $\mathbf{Z}$:

$$\mathbf{Z} = \left(\mathbf{Z}^{(1)},\ldots,\mathbf{Z}^{(4)}\right) \in \mathscr{M}_{100\times(180000\cdot 4)}(\mathbb{R}) = \mathscr{M}_{100\times 720000}(\mathbb{R}), \tag{2}$$

this allows to analyze the information of all the actuation phases at one time. Figure 3 shows schematically the organization of the data captured in each scenario.

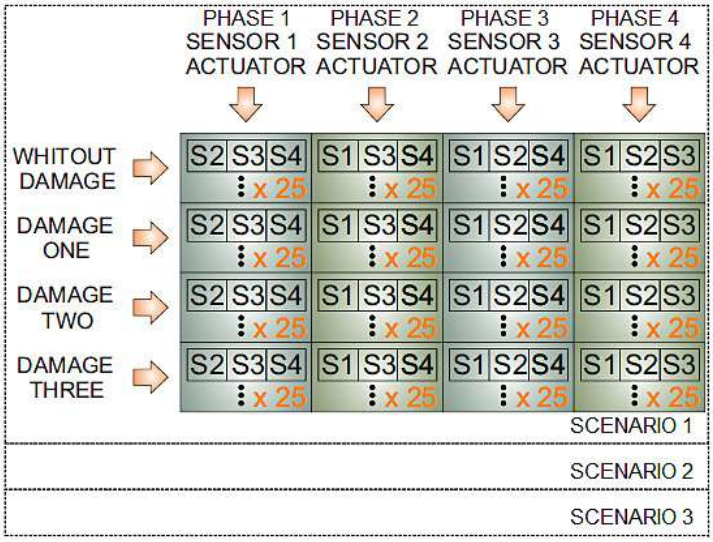

Figure 3 – Data organization per each scenario. Source: modified from Vitola et al. (2017b) [18].

3.2. Baseline data and test data

To obtain the baseline data and test data of this experimental study, a 5-fold cross validation is performed with matrix $\mathbf{Z}$, see Equation (2), to estimate the overall accuracy and avoid overfitting. In each iteration, the baseline

data, matrix **X**, are obtained with 5 consecutive rows of each structural state of **Z**, and with the rest of the rows of each state, 20, the test data, matrix **Y**, is formed. For more details see Table 2.

Table 2 – Baseline data and test data obtained with 5-fold Cross Validation.

Iteration	Rows of each structural state of **Z** that form baseline data, **X**	Rows of each structural state of **Z** that form test data, **Y**
1	1:5	6:25
2	6:10	1:5 y 11:25
3	11:15	1:10 y 16:25
4	16:20	1:15 y 21:25
5	21:25	1:20

Therefore, from the matrix **Z**, defined in Equation (2), five matrices $\mathbf{X} \in \mathscr{M}_{20\times 720000}(\mathbb{R})$ and five matrices $\mathbf{Y} \in \mathscr{M}_{80\times 720000}(\mathbb{R})$ are obtained, whose arrangement of their rows is:

Table 3 – Rows of matrices **X** and **Y**.

Rows		Structural
X	**Y**	state
1:5	1:20	$D0$
6:10	21:40	$D1$
11:15	41:60	$D2$
16:20	61:80	$D3$

In matrix notation, the baseline data are represented as follows:

$$\mathbf{X} = \left(\begin{array}{ccc|ccc|c|ccc} x_{1,1}^{1,1} & \cdots & x_{1,1}^{1,60000} & x_{1,1}^{2,1} & \cdots & x_{1,1}^{2,60000} & \cdots & x_{1,1}^{12,1} & \cdots & x_{1,1}^{12,60000} \\ \vdots & \ddots & \vdots & \vdots & \ddots & \vdots & \ddots & \vdots & \ddots & \vdots \\ x_{5,1}^{1,1} & \cdots & x_{5,1}^{1,60000} & x_{5,1}^{2,1} & \cdots & x_{5,1}^{2,60000} & \cdots & x_{5,1}^{12,1} & \cdots & x_{5,1}^{12,60000} \\ \vdots & \ddots & \vdots & \vdots & \ddots & \vdots & \ddots & \vdots & \ddots & \vdots \\ x_{1,4}^{1,1} & \cdots & x_{1,4}^{1,60000} & x_{1,4}^{2,1} & \cdots & x_{1,4}^{2,60000} & \cdots & x_{1,4}^{12,1} & \cdots & x_{1,4}^{12,60000} \\ \vdots & \ddots & \vdots & \vdots & \ddots & \vdots & \ddots & \vdots & \ddots & \vdots \\ x_{5,4}^{1,1} & \cdots & x_{5,4}^{1,60000} & x_{5,4}^{2,1} & \cdots & x_{5,4}^{2,60000} & \cdots & x_{5,4}^{12,1} & \cdots & x_{5,4}^{12,60000} \end{array}\right), \tag{3}$$

where each element of that matrix

$$x_{i,l}^{k,j}, \quad k = 1,\ldots,12, \quad j = 1,\ldots,60000, \quad i = 1,\ldots,5, \quad l = 1,\ldots,4, \tag{4}$$

comes from the $j-$th measurement of the $k-$th sensor of the $l-$th structural state in the $i-$th experiment. Summarizing, there are 12 sensors, 60000 measurements per sensor, 4 structural states and 5 rows associated with each structural state.
In matrix notation, the test data are represented as follows:

$$\mathbf{Y} = \left(\begin{array}{ccc|ccc|c|ccc} y_{1,1}^{1,1} & \cdots & y_{1,1}^{1,60000} & y_{1,1}^{2,1} & \cdots & y_{1,1}^{2,60000} & \cdots & y_{1,1}^{12,1} & \cdots & y_{1,1}^{12,60000} \\ \vdots & \ddots & \vdots & \vdots & \ddots & \vdots & \ddots & \vdots & \ddots & \vdots \\ y_{20,1}^{1,1} & \cdots & y_{20,1}^{1,60000} & y_{20,1}^{2,1} & \cdots & y_{20,1}^{2,60000} & \cdots & y_{20,1}^{12,1} & \cdots & y_{20,1}^{12,60000} \\ \vdots & \ddots & \vdots & \vdots & \ddots & \vdots & \ddots & \vdots & \ddots & \vdots \\ y_{1,4}^{1,1} & \cdots & y_{1,4}^{1,60000} & y_{1,4}^{2,1} & \cdots & y_{1,4}^{2,60000} & \cdots & y_{1,4}^{12,1} & \cdots & y_{1,4}^{12,60000} \\ \vdots & \ddots & \vdots & \vdots & \ddots & \vdots & \ddots & \vdots & \ddots & \vdots \\ y_{20,4}^{1,1} & \cdots & y_{20,4}^{1,60000} & y_{20,4}^{2,1} & \cdots & y_{20,4}^{2,60000} & \cdots & y_{20,4}^{12,1} & \cdots & y_{20,4}^{12,60000} \end{array}\right), \tag{5}$$

where each element of that matrix

$$y_{i,l}^{k,j}, \quad k=1,\ldots,12, \quad j=1,\ldots,60000, \quad i=1,\ldots,20, \quad l=1,\ldots,4, \tag{6}$$

comes from the $j-$th measurement of the $k-$th sensor of the $l-$th "unknown" structural state to be diagnosed in the $i-$th experiment.

3.3. Mean-centered group scaling (MCGS)

The data in matrix $\mathbf{X}$ are normalized by mean-centered group scaling method [19]. The main reasons to normalize the raw data are two: (i) data come from several sensors and could have different scales; and (ii) to simplify the computations in the PCA decomposition. MCGS is based on the mean of all experiments of the sensor at the same column and the standard deviation of all experiments of the sensor. More accurately, it is defined:

$$\mu^{k,j} = \frac{1}{n}\sum_{l=1}^{4}\sum_{i=1}^{5} x_{i,l}^{k,j}, \quad n=5 \text{ rows} \times 4 \text{ structural states} = 20, \quad k=1,\ldots,12, \quad j=1,\ldots,60000, \tag{7}$$

$$\sigma^{k} = \sqrt{\frac{1}{n\cdot 60000}\sum_{l=1}^{4}\sum_{i=1}^{5}\sum_{j=1}^{60000}(x_{i,l}^{k,j}-\mu^{k})^2}, \quad k=1,\ldots,12, \tag{8}$$

$$\mu^{k} = \frac{1}{n\cdot 60000}\sum_{l=1}^{4}\sum_{i=1}^{5}\sum_{j=1}^{60000} x_{i,l}^{k,j}, \quad k=1,\ldots,12, \tag{9}$$

where $\mu^{k,j}$ is the arithmetic mean of data that are at the same column, that is the arithmetic mean of the n experiments of $k-$th sensor in $j-$th measure; and σ^k and μ^k are the standard deviation and the arithmetic mean of all experiments of sensor k, respectively. Then, the elements $x_{i,l}^{k,j}$ of matrix $\mathbf{X}$ are normalized to define a new matrix $\breve{\mathbf{X}} = \mathbf{X}_{MCGS} = (\breve{x}_{i,l}^{k,j})$ as:

$$\breve{x}_{i,l}^{k,j} := \frac{x_{i,l}^{k,j}-\mu^{k,j}}{\sigma^{k}}, \;\; k=1,\ldots,12, \;\; j=1,\ldots,60000, \;\; i=1,\ldots,5, \;\; l=1,\ldots,4, \tag{10}$$

One of the properties of the normalized matrix $\breve{\mathbf{X}}$ is that each column has an arithmetic mean of zero and that all experiments of sensor k have a standard deviation of one.

Then, the test data are processed in an identical manner as the baseline data. This means that these data are normalized by MCGS, but respect to data $\mathbf{X}$:

$$\breve{y}_{i,l}^{k,j} := \frac{y_{i,l}^{k,j}-\mu^{k,j}}{\sigma^{k}}, \;\; k=1,\ldots,12, \;\; j=1,\ldots,60000, \;\; i=1,\ldots,20, \;\; l=1,\ldots,4, \tag{11}$$

obtaining the matrix $\breve{\mathbf{Y}}$, and where $\mu^{k,j}$ and σ^k are defined in Equations (7) and (8), respectively.

3.4. Principal component analysis (PCA)

In the next step, the normalized baseline data, $\breve{\mathbf{X}}$, are pre-processed using PCA [20] to reduce its dimensionality before performing t-SNE. The main objective of PCA is to reduce the calculation time in t-SNE. By using PCA with $\breve{\mathbf{X}}$, PCA model is obtained, that is, the square matrix $\mathbf{P} \in \mathscr{M}_{720000\times 720000}(\mathbb{R})$ used to project the data stored in $\breve{\mathbf{X}}$ and $\breve{\mathbf{Y}}$ with the corresponding matrix product:

$$\mathbf{T}_1 = \breve{\mathbf{X}}\cdot\mathbf{P} \in \mathscr{M}_{20\times 720000}(\mathbb{R}), \tag{12}$$

$$\mathbf{T}_2 = \breve{\mathbf{Y}}\cdot\mathbf{P} \in \mathscr{M}_{80\times 720000}(\mathbb{R}). \tag{13}$$

3.5. Projected data fusion

The projected data are assembled, that is:

$$\mathbf{T} = \begin{pmatrix} \mathbf{T}_1 \\ \mathbf{T}_2 \end{pmatrix} \in \mathscr{M}_{(20+80)\times 720000}(\mathbb{R}), \tag{14}$$

so $\mathbf{T}$ has 100 points in a space of dimension $\mathbb{R}^{720000}$. In this case, a single row of $\mathbf{T}_2$ is added each time, i.e., $\mathbf{T}$ has $20+1=21$ points. This new row introduced represents the new datum from the structure to be diagnosed, which is in an "unknown" state. This means that we try to classify the structural state of a system one at a time.

3.6. t-Distributed stochastic neighbor embedding (t-SNE)

t-SNE is an improved variation of the technique so-called stochastic neighbor embedding (SNE) [9]: t-SNE is much easier to optimize and produces better visualizations, since it reduces the tendency to crowd points in the center of the distribution (the so-called *crowding problem*[1]). These improvements are due to the fact that the cost function used by t-SNE differs from the one used by SNE in two aspects: (i) t-SNE uses a symmetrized version of the SNE cost function with simpler gradients; and (ii) t-SNE uses a t-Student distribution, instead of a Gaussian, to compute the similarity between two points in the low-dimensional space.

Following with the proposed strategy, t-SNE is executed with the matrix $\mathbf{T}$, obtaining a succession of 21 points in the plane $\mathbb{R}^2$. The result of t-SNE in the final iteration is such that:

$$\mathbf{S} = \left(\begin{array}{ccc|c|ccc|c} s^1_{1,1} & \cdots & s^1_{5,1} & \cdots & s^4_{1,1} & \cdots & s^4_{5,1} & s_{1,1} \\ s^1_{1,2} & \cdots & s^1_{5,2} & \cdots & s^4_{1,2} & \cdots & s^4_{5,2} & s_{1,2} \end{array} \right)^{\mathsf{T}}, \tag{15}$$

where the element $s^l_{i,j}$ corresponds to the $j-$th measurement of $l-$th structural state of the $i-$th experiment. The last element of each row correspond to the "unknown" structural state to be diagnosed. A brief description of key mathematical and statistical concepts of t-SNE is introduced below.

3.6.1. *t-SNE: brief description*

Given a collection of high-dimensional data points $X = \{x_1, ..., x_n\} \subset \mathbb{R}^D$, the objective is to find a collection of low-dimensional map points $Y = \{y_1, ..., y_n\} \subset \mathbb{R}^d$ (typical values for d are 2 or 3), where $d \ll D$, such that the lower dimension preserves, as much as possible, the local structure of the original data X. That is, if two data points are neighbors, it wants the two corresponding map points also to be neighbors. To this end, t-SNE first converts the high-dimensional Euclidean distances between data points x_i and x_j, $\|x_i - x_j\|$, into conditional probabilities by centering a Gaussian distribution at x_i, computing the density of x_j under this Gaussian distribution, and renormalizing:

$$p_{j|i} = \frac{\exp(-\|x_i - x_j\|^2/2\sigma_i^2)}{\sum_{k \neq i} \exp(-\|x_i - x_k\|^2/2\sigma_i^2)}, \quad \forall i \forall j : i \neq j, \tag{16}$$

where $\|x_i - x_j\|^2/2\sigma_i^2$ (scaled squared Euclidean distance or "affinity") is the dissimilarity between data points x_i and x_j. The variance of the Gaussian distribution, σ_i^2, is calculated automatically (for more details, see the original t-SNE paper [12]). Since only pairwise similarities between data points are of interest, t-SNE establishes $p_{i|i} = 0$. This conditional probability measures the similarity of x_j to x_i, i.e., the probability that x_i would pick x_j as its neighbor. If two data points are near, $p_{j|i}$ will be high. Whereas if two data points are separated, $p_{j|i}$ will be low.

Then, by symmetrizing two conditional probabilities, t-SNE defines the joint probability, that is a symmetrized version of the conditional similarity because it has the property that $p_{ij} = p_{ji}$ for $\forall i, j$:

$$p_{ij} = \frac{p_{j|i} + p_{i|j}}{2n}, \quad p_{ii} = 0. \tag{17}$$

The joint probability also measures the pairwise similarity between data points x_i and x_j. Thus it is obtained the similarity matrix $\mathbf{P}$ for high-dimensional data points. In practice, the use of conditional or joint probabilities produces similar results, but it is less computationally expensive the optimization of the joint model [12]. The objective of t-SNE is to model each data point x_i by a map point y_i such that the pairwise similarities p_{ij} are modeled as well as possible in the low-dimensional space.

Once obtained the similarity matrix for the data points X, let's also define the similarity matrix $\mathbf{Q}$ for the map points Y. It is the same idea as for the data points, but with a renormalized t-Student distribution with one degree of freedom and $\sigma_i^2 = \frac{1}{2}$ for all i, instead of a Gaussian distribution:

$$q_{ij} = \frac{(1 + \|y_i - y_j\|^2)^{-1}}{\sum_k \sum_{l \neq k} (1 + \|y_k - y_l\|^2)^{-1}}, \quad \forall i \forall j : i \neq j, \quad q_{ii} = 0, \quad q_{ij} = q_{ji} \forall i, j, \tag{18}$$

i.e., q_{ij} is the low-dimensional counterpart of p_{ij} and it represents the local structure of the data points in the low-dimensional space. The heavy tails of the t-Student distribution allow dissimilar data points x_i and x_j to be modeled by map points y_i and y_j that are separated: the probability of being neighbor falls off more slowly and therefore there is less need to move some points away and crowd remaining points in the center of the distribution (*crowding problem*). In other words, t-SNE allows data points that are only slightly similar to be visualized more

[1] SNE suffers from a *crowding problem* that is the result of the exponential volume difference between high and low-dimensional spaces [12].

separated in the low-dimensional space. But the choice of the t-Student distribution for the map points goes further since it alleviates both the crowding problem and the optimization problems of SNE [12].
Whereas the similarity matrix **P** is fixed, the similarity matrix **Q** depends on the map points, and what is wanted is that these two similarity matrices are closer as possible. This is achieved by minimizing a cost function which is the Kullback-Leibler (KL) divergence between both joint distributions [9, 10, 12]:

$$C = KL(P\|Q) = \sum_i \sum_{j\neq i} p_{ij} \log \frac{p_{ij}}{q_{ij}}. \tag{19}$$

The KL divergence between the joint probability distributions **P** and **Q** measures the distance between the two similarity matrices, and therefore minimizing the KL divergence reduces the error between these matrices. In other words, the map points of similar data points need to be close together and the map points of dissimilar data points need to be far in order to minimize the cost function C. Note that (i) KL divergence is nonnegative and 0 iff the distributions are equal —the similarity between the data points x_i and x_j is correctly modeled by the map points y_i and y_j—, and (ii) C is generally non-convex and different runs might produce different results. To minimize C, it is perform a gradient descent[2] method:

$$\frac{\partial C}{\partial y_i} = 4 \sum_{j\neq i} (p_{ij} - q_{ij})(y_i - y_j)(1 + \|y_i - y_j\|^2)^{-1}. \tag{20}$$

This gradient expresses the sum of all forces applied to map point y_i, i.e., the sum of forces pulling map point y_i toward all other map points y_j or pushing it away. And the locations of the map points Y are determined by minimizing C.
Then y_i is updated by the next equation:

$$y_i^{(t)} = y_i^{(t-1)} + \eta \frac{\partial C}{\partial y_i} + \alpha(t)(y_i^{(t-1)} - y_i^{(t-2)}), \tag{21}$$

where $y_i^{(t)}$ is the solution at iteration t, η is the learning rate, and $\alpha(t)$ is the momentum term at iteration t. The learning rate determines the jump size between each iteration during the optimization of the cost function C. In Equation (21), a relatively large momentum term is added to accelerate the optimization and to avoid poor local minimums.
t-SNE Summary:

1. Calculate the similarity matrix for the data points, p_{ij}.
2. Calculate the similarity matrix for the map points, q_{ij}.
3. Define the cost function, $C = KL(P\|Q)$.
4. Minimize C using gradient descent algorithm.
5. Update y_i using Equation (21).

3.7. Confusion matrix

The confusion matrices are calculated as of the distances of the points $(s_{1,1}, s_{1,2}) \subset \mathbb{R}^2$, to the centroids associated with each structural state. The centroid associated with the $l-$th structural state, $l = 1, \ldots, 4$, is the point of the plane such that

$$(c_x^l, c_y^l) = \left(\frac{1}{5} \sum_{i=1}^{5} s_{i,1}^l, \frac{1}{5} \sum_{i=1}^{5} s_{i,2}^l \right). \tag{22}$$

To classify this point of the plane, the smallest point-centroid distance is used: the distance of this point $(s_{1,1}, s_{1,2}) \subset \mathbb{R}^2$ is calculated up to each of the centroids defined in Equation (22) and it is classified as structural state $m \in \mathbb{N}$ if m is such that

$$\sqrt{(s_{1,1} - c_x^m)^2 + (s_{1,2} - c_y^m)^2} = \min_{l=1,\ldots,4} \sqrt{(s_{1,1} - c_x^l)^2 + (s_{1,2} - c_y^l)^2}. \tag{23}$$

4. RESULTS

Tables 4–6 present the classification results per scenario, in the time domain. Remember that of each damage or structural state there are 100 cases (20 rows of matrix $\mathbf{Y} \times 5$ iterations of 5-fold Cross Validation, see Tables 2

[2] Gradient descent: iterative process to find the minimal of a function

and 3). The results with maximum accuracy in the classification are obtained in scenarios 1 and 3: all cases have been correctly classified. In scenario 2, the percentage of correct decisions fluctuates between 86% and 91%: it can be observed that the use of a long cable (2.5 m) from the digitizer to the sensors affects in the detection and classification method. So that, the results show the high classification accuracy and the solid performance of t-SNE algorithm. It should be noted that the environmental conditions were not considered, leaving them for future researches.

Table 4 – Confusion matrix, scenario 1, time domain.

True \ Predicted	D0	D1	D2	D3
D0	100	0	0	0
D1	0	100	0	0
D2	0	0	100	0
D3	0	0	0	100

Table 5 – Confusion matrix, scenario 2, time domain.

True \ Predicted	D0	D1	D2	D3
D0	86	1	7	6
D1	8	88	4	0
D2	1	8	89	2
D3	3	4	2	91

Table 6 – Confusion matrix, scenario 3, time domain.

True \ Predicted	D0	D1	D2	D3
D0	100	0	0	0
D1	0	100	0	0
D2	0	0	100	0
D3	0	0	0	100

5. CONCLUSIONS

In this work, a methodology to detect and classify structural changes has been proposed. Results from an aluminum plate have shown that this method is very satisfactory, given its high classification accuracy, since the number of correct decisions fluctuates between 86% and 100%. In addition, it is worth remarking that the t-SNE technique has been extended and adapted for the first time to the field of structural health monitoring, in the detection and classification of structural changes, thanks to the developed methodology.

ACKNOWLEDGEMENTS

This work has been partially funded by the Spanish Agencia Estatal de Investigación (AEI) - Ministerio de Economía, Industria y Competitividad (MINECO), and the Fondo Europeo de Desarrollo Regional (FEDER) through the research project DPI2017-82930-C2-1-R; and by the Generalitat de Catalunya through the research project 2017 SGR 388. We gratefully acknowledge the support of NVIDIA Corporation with the donation of the Titan Xp GPU used for this research. We thank the Universitat Politècnica de Catalunya (UPC) for pre-doctoral fellowship (to Agis, D.).

REFERENCES

[1] Raju, K.S., Pratap, Y., Sahni, Y., Babu, M.N., "Implementation of a WSN system towards SHM of civil building structures", Proceedings of Intelligent Systems and Control (ISCO), 2015 IEEE 9th International Conference on, IEEE, 2015, pp. 1–7.

[2] Rolfes, R., Zerbst, S., Haake, G., Reetz, J., Lynch, J.P., "Integral SHM-system for offshore wind turbines using smart wireless sensors", Proceedings of Proceedings of the 6th International Workshop on Structural Health Monitoring, DEStech Publications Inc. Stanford, CA, USA, 2007, pp. 11–13.

[3] Ciang, C.C., Lee, J.R., Bang, H.J., "Structural health monitoring for a wind turbine system: a review of damage detection methods", Measurement Science and Technology, 19(12), 2008, p. 122001.

[4] Nisha, M., "Structural health monitoring of aircraft wing using wireless network", Int. J. Technol. Explor. Learn. www. ijtel. org Struct, 3(1), 2014, pp. 341–343.

[5] Ward, M.O., Grinstein, G., Keim, D., Interactive data visualization: foundations, techniques, and applications, AK Peters/CRC Press, 2015.

[6] Tenenbaum, J.B., De Silva, V., Langford, J.C., "A global geometric framework for nonlinear dimensionality reduction", Science, 290(5500), 2000, pp. 2319–2323.

[7] Kambhatla, N., Leen, T.K., "Dimension reduction by local principal component analysis", Neural Computation, 9(7), 1997, pp. 1493–1516.

[8] Cao, L., Chua, K.S., Chong, W., Lee, H., Gu, Q., "A comparison of PCA, KPCA and ICA for dimensionality reduction in support vector machine", Neurocomputing, 55(1-2), 2003, pp. 321–336.

[9] Hinton, G.E., Roweis, S.T., "Stochastic neighbor embedding", Proceedings of Advances in Neural Information Processing Systems, 2003, pp. 857–864.

[10] Min, R., A non-linear dimensionality reduction method for improving nearest neighbour classification, University of Toronto, 2005.

[11] Sharma, A., Paliwal, K.K., Onwubolu, G.C., "Class-dependent PCA, MDC and LDA: A combined classifier for pattern classification", Pattern Recognition, 39(7), 2006, pp. 1215–1229.

[12] Maaten, L.v.d., Hinton, G., "Visualizing data using t-SNE", Journal of Machine Learning Research, 9(Nov), 2008, pp. 2579–2605.

[13] Wilson, N.K., Kent, D.G., Buettner, F., Shehata, M., Macaulay, I.C., Calero-Nieto, F.J., Castillo, M.S., Oedekoven, C.A., Diamanti, E., Schulte, R., et al., "Combined single-cell functional and gene expression analysis resolves heterogeneity within stem cell populations", Cell Stem Cell, 16(6), 2015, pp. 712–724.

[14] Gouws, S., Søgaard, A., "Simple task-specific bilingual word embeddings", Proceedings of Proceedings of the 2015 Conference of the North American Chapter of the Association for Computational Linguistics: Human Language Technologies, 2015, pp. 1386–1390.

[15] Traven, G., Matijevič, G., Zwitter, T., Žerjal, M., Kos, J., Asplund, M., Bland-Hawthorn, J., Casey, A.R., De Silva, G., Freeman, K., et al., "The Galah survey: classification and diagnostics with t-SNE reduction of spectral information", The Astrophysical Journal Supplement Series, 228(2), 2017, p. 24.

[16] Li, W., Cerise, J.E., Yang, Y., Han, H., "Application of t-SNE to human genetic data", Journal of Bioinformatics and Computational Biology, 15(04), 2017, p. 1750017.

[17] Vitola, J., Pozo, F., Tibaduiza, D.A., Anaya, M., "A sensor data fusion system based on *k*-nearest neighbor pattern classification for structural health monitoring applications", Sensors, 17(2), 2017, p. 417.

[18] Vitola, J., Pozo, F., Tibaduiza, D.A., Anaya, M., "Distributed piezoelectric sensor system for damage identification in structures subjected to temperature changes", Sensors, 17(6), 2017, p. 1252.

[19] Pozo, F., Vidal, Y., Salgado, Ó., "Wind Turbine Condition Monitoring Strategy through Multiway PCA and Multivariate Inference", Energies, 11(4), 2018, p. 749.

[20] Pozo, F., Vidal, Y., "Wind turbine fault detection through principal component analysis and statistical hypothesis testing", Energies, 9(1), 2015, p. 3.

VIBRATION-BASED STRUCTURAL HEALTH MONITORING USING PIEZOELECTRIC TRANSDUCERS AND PARAMETRIC t-SNE

D. Agis[1] and F. Pozo[1]

[1]*Control, Modeling, Identification and Applications (CoDAlab), Department of Mathematics, Escola d'Enginyeria de Barcelona Est (EEBE), Universitat Politècnica de Catalunya (UPC), Campus Diagonal-Besòs (CDB), Eduard Maristany, 16, 08019 Barcelona, Spain*

e-mail: francesc.pozo@upc.edu

Abstract

In this paper, we evaluate the performance of the so-called parametric t-distributed stochastic neighbor embedding (P-t-SNE), comparing it to the performance of the t-SNE —the non-parametric version—. P-t-SNE is an unsupervised dimensionality reduction technique, that learns a parametric mapping between the high-dimensional data space and the low-dimensional latent space, preserving the local structure of the data as well as possible in the latent space. The methodology used in this study is introduced for the purposes of detection and classification of structural changes in the field of structural health monitoring (SHM). The method is based on the combination of principal component analysis (PCA) and P-t-SNE, and it is applied to an experimental case study of an aluminum plate with four piezoelectric transducers (PZTs). The results, in frequency domain, manifest the strong performance of P-t-SNE, which is comparable to the performance of t-SNE but outperforming t-SNE in terms of computational cost and runtime.

1. Introduction

In the real world, data sets usually have a high dimensionality, and to be able to work with them, their dimensionality needs to be reduced. Dimensionality reduction is the process of reducing the number of high-dimensional variables by obtaining a low-dimensional set of variables. This reduced representation must correspond to the intrinsic information of the data. Dimensionality reduction is very important, since it alleviates undesired properties of high-dimensional spaces, such as the curse of dimensionality. In the literature, various dimensionality reduction methods have been proposed: (i) linear methods, such as principal component analysis (PCA) and linear discriminant analysis (LDA); and (ii) nonlinear methods, such as isometric mapping (ISOMAP) and the non-parametric version of t-distributed stochastic neighbor embedding (t-SNE) [3].

In general, real world data is likely to be highly nonlinear and, therefore, unsupervised nonlinear dimensionality reduction techniques are widely used in many applications for pattern recognition or classification, visualization, and compression of big data sets. Among this type of techniques, t-SNE is extensively adopted, but this method is not designed to generate the incorporation of out-of-sample data, that is, the embedding of new data. To avoid this problem, the method so-called parametric t-SNE (P-t-SNE) [2] is proposed, which employs a neural network (NN) to learn an explicit parametric mapping function from a high-dimensional data space to a low-dimensional space, and in this way it can be incorporated out-of-sample data. Another advantage of P-t-SNE is that it can be applied to large-scale data sets, while t-SNE can only be applied to data sets with a size not greater to the order of thousands.

To address the above-mentioned problems about t-SNE, in this work, we propose a strategy that combines PCA and P-t-SNE. This combination is much better than the combination with t-SNE since it produces similar embedding performance but having a much lower computational cost and runtime, as experimental results on an aluminum plate instrumented with four piezoelectric transducers (PZTs) show. Therefore, the aims of this paper are (i) to compare both approaches —P-t-SNE versus t-SNE—; and (ii) to identify the advantages of the parametric version. To do this, we will use scenarios 1 of the paper [1]. In addition, we will approach the damage detection and classification problem in the frequency domain, as recommended in the same paper [1]. The final classification of the current state of the structure is based on two different *voting* systems, the so-called *majority voting* and *sum of the inverse distances* [1].

2. Experimental set-up

In this work, we consider the same structure and experiment used in the paper [1]. This structure is a square aluminum plate manufactured to demonstrate the accuracy of the vibration-based method. The dimension of the plate is $40 \times 40 \times 0.2$ cm. The plate is instrumented with four PZTs and a mass of 17.2916 grams is introduced to simulate the damage —in a non-destructive way, producing changes in the propagated wave—. Each of the PZTs can work exciting the aluminum plate —actuator mode— with a burst signal or detecting a time-varying mechanical response —sensor mode—. The location of the mass defines each damage, and as a result $J = 4$ structural states are considered —healthy state and three different types of damage—. The plate is isolated from the vibration and noise in the laboratory.

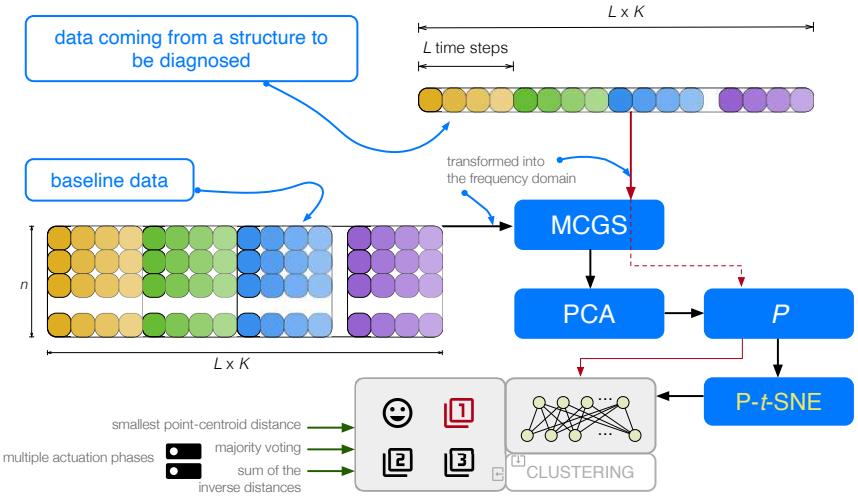

Figure 1: Flowchart of the proposed procedure. Data coming from a structure are first scaled by MCGS and then projected into the PCA model. Finally, P-t-SNE is applied to generate the clusters that will be used in the vibration-based detection and classification of structural changes.

3. Results

When the method is based on P-t-SNE and the majority voting approach is used, the overall accuracy is very good. Specifically, 398 observations out of 400 cases have been correctly classified —which corresponds to an overall accuracy of 99.5%—. When the t-SNE-based method is used, an overall accuracy of 100% is achieved. A similar performance is obtained using the sum of the inverse distances approach. As it can be seen, both parametric and non-parametric approaches obtain practically the same results. However, the P-t-SNE based damage detection and classification dramatically reduces the processing time, it goes from 40 minutes and 15 seconds —t-SNE— to 2 minutes and 34 seconds —P-t-SNE—.

Acknowledgments This research has been partially funded by the Spanish Agencia Estatal de Investigación (AEI) - Ministerio de Economía, Industria y Competitividad (MINECO), and the Fondo Europeo de Desarrollo Regional (FEDER) through the research project DPI2017-82930-C2-1-R; and by the Generalitat de Catalunya through the research project 2017 SGR 388. We thank the Universitat Politècnica de Catalunya (UPC) for pre-doctoral fellowship (to David Agis).

References

[1] David Agis and Francesc Pozo. A frequency-based approach for the detection and classification of structural changes using t-sne. *Sensors*, 19(23):5097, 2019.

[2] Laurens Van Der Maaten. Learning a parametric embedding by preserving local structure. In *Proceedings of the 12th International Conference on Artificial Intelligence and Statistics*, pages 384–391, 2009.

[3] Laurens Van Der Maaten and Geoffrey E Hinton. Visualizing data using t-SNE. *Journal of Machine Learning Research*, 9(Nov):2579–2605, 2008.

Bibliografía

Alonso, FJ y DR Salgado (2008). «Analysis of the structure of vibration signals for tool wear detection». En: *Mechanical Systems and Signal Processing* 22.3, págs. 735-748.

Balamurali, Mehala y Arman Melkumyan (2016). «*t*-SNE based visualisation and clustering of geological domain». En: *International Conference on Neural Information Processing*, págs. 565-572.

Blanco, Haydee *et al.* (2018). «An integrated structural health monitoring system for determining local/global responses of historic masonry buildings». En: *Structural Control and Health Monitoring* 25.8, e2196.

Caggiano, Alessandra (2018). «Tool wear prediction in Ti-6Al-4V machining through multiple sensor monitoring and PCA features pattern recognition». En: *Sensors* 18.3, pág. 823.

Carden, E Peter y James MW Brownjohn (2008). «ARMA modelled time-series classification for structural health monitoring of civil infrastructure». En: *Mechanical systems and signal processing* 22.2, págs. 295-314.

Cho, Hwanjeong *et al.* (2019). «Nonlinear guided wave technique for localized damage detection in plates with surface-bonded sensors to receive Lamb waves generated by shear-horizontal wave mixing». En: *NDT & E International* 102, págs. 35-46.

Ciang, Chia Chen *et al.* (2008). «Structural health monitoring for a wind turbine system: a review of damage detection methods». En: *Measurement Science and Technology* 19.12, pág. 122001.

Cremona, Christian y Joao Santos (2018). «Structural health monitoring as a big-data problem». En: *Structural Engineering International* 28.3, págs. 243-254.

De Bodt, Cyril *et al.* (2018). «Perplexity-free *t*-SNE and twice Student *tt*-SNE.» En: *ESANN*.

Elvira, María *et al.* (2019). «Pseudo-online BMI based on EEG to detect the appearance of sudden obstacles during walking». En: *Sensors* 19.24, pág. 5444.

Gierahn, Todd M *et al.* (2017). «Seq-Well: portable, low-cost RNA sequencing of single cells at high throughput». En: *Nature Methods* 14.4, pág. 395.

Gisbrecht, Andrej *et al.* (2015). «Parametric nonlinear dimensionality reduction using kernel *t*-SNE». En: *Neurocomputing* 147, págs. 71-82.

Giurgiutiu, Victor (2005). «Tuned Lamb wave excitation and detection with piezoelectric wafer active sensors for structural health monitoring». En: *Journal of intelligent material systems and structures* 16.4, págs. 291-305.

Goodfellow, Ian *et al.* (2016). *Deep learning*. MIT press.

Gryllias, Konstantinos C y Ioannis A Antoniadis (2012). «A Support Vector Machine approach based on physical model training for rolling element bearing fault detection in industrial environments». En: *Engineering Applications of Artificial Intelligence* 25.2, págs. 326-344.

Gu, Jiu *et al.* (2019). «Wind farm NWP data preprocessing method based on *t*-SNE». En: *Energies* 12.19, pág. 3622.

Gui, Guoqing *et al.* (2017). «Data-driven support vector machine with optimization techniques for structural health monitoring and damage detection». En: *KSCE Journal of Civil Engineering* 21.2, págs. 523-534.

Gulgec, Nur Sila *et al.* (2017). «Current challenges with bigdata analytics in structural health monitoring». En: *Structural Health Monitoring & Damage Detection, Volume 7*. Springer, págs. 79-84.

Hameed, Nazia *et al.* (2019). «An intelligent computer-aided scheme for classifying multiple skin lesions». En: *Computers* 8.3, pág. 62.

He, Liqun *et al.* (2018). «Single-cell RNA sequencing of mouse brain and lung vascular and vessel-associated cell types». En: *Scientific Data* 5, pág. 180160.

Hinton, Geoffrey E (2002). «Training products of experts by minimizing contrastive divergence». En: *Neural computation* 14.8, págs. 1771-1800.

– (2012). «A practical guide to training restricted Boltzmann machines». En: *Neural networks: Tricks of the trade*. Springer, págs. 599-619.

Hinton, Geoffrey E y Sam T Roweis (2003). «Stochastic neighbor embedding». En: *Advances in Neural Information Processing Systems*, págs. 857-864.

Hoshyarmanesh, Hamidreza *et al.* (2017). «Design and implementation of an accurate, portable, and time-efficient impedance-based transceiver for structural health monitoring». En: *IEEE/ASME Transactions on Mechatronics* 22.6, págs. 2809-2814.

Hossin M.; Sulaiman, M.N. (2015). «A review on evaluation metrics for data classification evaluations». En: *International Journal of Data Mining & Knowledge Management Process (IJDKP)* 5.2, págs. 1-11.

Hou, Jilin *et al.* (2015). «Frequency-domain substructure isolation for local damage identification». En: *Advances in Structural Engineering* 18.1, págs. 137-153.

Ioffe, Sergey y Christian Szegedy (2015). «Batch normalization: Accelerating deep network training by reducing internal covariate shift». En: *arXiv preprint arXiv: 1502.03167*.

Jeong, Minjoong *et al.* (2014). «Isomap-based damage classification of cantilevered beam using modal frequency changes». En: *Structural Control and Health Monitoring* 21.4, págs. 590-602.

Jiménez, Alfredo Arcos *et al.* (2019). «Dirt and mud detection and diagnosis on a wind turbine blade employing guided waves and supervised learning classifiers». En: *Reliability Engineering & System Safety* 184, págs. 2-12.

Jiménez, Luis O y David A Landgrebe (1998). «Supervised classification in high-dimensional space: geometrical, statistical, and asymptotical properties of multivariate data». En: *IEEE Transactions on Systems, Man, and Cybernetics, Part C (Applications and Reviews)* 28.1, págs. 39-54.

Kinet, Damien *et al.* (2014). «Fiber Bragg grating sensors toward structural health monitoring in composite materials: Challenges and solutions». En: *Sensors* 14.4, págs. 7394-7419.

Kirk, Brian *et al.* (2016). «Kepler eclipsing binary stars. VII. The catalog of eclipsing binaries found in the entire Kepler data set». En: *The Astronomical Journal* 151.3, pág. 68.

Krüger, Frank (2016). «Activity, context, and plan recognition with computational causal behaviour models». Tesis doct. University of Rostock, Mecklenburg, Germany.

Langone, Rocco *et al.* (2017). «Automated structural health monitoring based on adaptive kernel spectral clustering». En: *Mechanical Systems and Signal Processing* 90, págs. 64-78.

Li, Hong-Nan *et al.* (2016). «State-of-the-art in structural health monitoring of large and complex civil infrastructures». En: *Journal of Civil Structural Health Monitoring* 6.1, págs. 3-16.

Li, Jun y Hong Hao (2016). «A review of recent research advances on structural health monitoring in Western Australia». En: *Structural Monitoring and Maintenance* 3.1, pág. 33.

Liu, Yingtao *et al.* (2011). «Application of system-identification techniques to health monitoring of on-orbit satellite boom structures». En: *Journal of Spacecraft and Rockets* 48.4, págs. 589-598.

Loh, Chin-Hsiung *et al.* (2017). «Vibration-based system identification of wind turbine system». En: *Structural Control and Health Monitoring* 24.3, e1876.

López-Higuera, José Miguel *et al.* (2011). «Fiber optic sensors in structural health monitoring». En: *Journal of lightwave technology* 29.4, págs. 587-608.

Lu, Chen *et al.* (2016). «Fault diagnosis for rotating machinery: A method based on image processing». En: *PLOS ONE* 11.10, e0164111.

Macaulay, Iain C *et al.* (2016). «Single-cell RNA-sequencing reveals a continuous spectrum of differentiation in hematopoietic cells». En: *Cell Reports* 14.4, págs. 966-977.

Mehta, Sumet *et al.* (2018). «A new nearest centroid neighbor classifier based on *k* local means using harmonic mean distance». En: *Information* 9.9, pág. 234.

Mesquita, Esequiel *et al.* (2016). «Global overview on advances in structural health monitoring platforms». En: *Journal of Civil Structural Health Monitoring* 6.3, págs. 461-475.

Min, Renqiang (2005). «A non-linear dimensionality reduction method for improving nearest neighbour classification». Tesis doct. University of Toronto.

Min, Renqiang *et al.* (2018). «Parametric *t*-distributed stochastic exemplar-centered embedding». En: *Joint European Conference on Machine Learning and Knowledge Discovery in Databases*. Springer, págs. 477-493.

Mujica, LE *et al.* (2011). «Q-statistic and T2-statistic PCA-based measures for damage assessment in structures». En: *Structural Health Monitoring* 10.5, págs. 539-553.

Mujica, LE *et al.* (2013). «A structural damage detection indicator based on principal component analysis and statistical hypothesis testing». En: *Smart Materials and Structures* 23.2, pág. 025014.

Nisha, MS (2014). «Structural health monitoring of aircraft wing using wireless network». En: *International Journal of Technological Exploration and Learning* 3.1, págs. 341-343.

Ochôa, Pedro *et al.* (2019). «Systematic multiparameter design methodology for an ultrasonic health monitoring system for full-scale composite aircraft primary structures». En: *Structural Control and Health Monitoring* 26, e2340.

Orfanidis, Sophocles J (1995). *Introduction to signal processing*. Upper Saddle River, NJ, USA: Prentice-Hall, Inc.

Ou, Jinping y Hui Li (2010). «Structural health monitoring in mainland China: review and future trends». En: *Structural health monitoring* 9.3, págs. 219-231.

Pozo, Francesc y Yolanda Vidal (2015). «Wind turbine fault detection through principal component analysis and statistical hypothesis testing». En: *Energies* 9.1, pág. 3.

Pozo, Francesc *et al.* (2016). «Detection of structural changes through principal component analysis and multivariate statistical inference». En: *Structural Health Monitoring* 15.2, págs. 127-142.

Pozo, Francesc *et al.* (2018). «Wind turbine condition monitoring strategy through multiway PCA and multivariate inference». En: *Energies* 11.4, pág. 749.

Qing, Xinlin *et al.* (2019). «Piezoelectric transducer-based structural health monitoring for aircraft applications». En: *Sensors* 19.3, pág. 545.

Raju, Kota Solomon *et al.* (2015). «Implementation of a WSN system towards SHM of civil building structures». En: *2015 IEEE 9th International Conference on Intelligent Systems and Control (ISCO)*, págs. 1-7.

Rizzo, Piervincenzo *et al.* (2009). «An unsupervised learning algorithm for fatigue crack detection in waveguides». En: *Smart Materials and Structures* 18.2, pág. 025016.

Rutherford, Amanda C *et al.* (2007). «Non-linear feature identifications based on self-sensing impedance measurements for structural health assessment». En: *Mechanical Systems and Signal Processing* 21.1, págs. 322-333.

Seok, Ho-Sik (2019). «Performance comparison of dimensionality reduction methods on RNA-Seq data from the GTEx project». En: *Genes & Genomics*, págs. 1-10.

Sharma, Alok *et al.* (2006). «Class-dependent PCA, MDC and LDA: A combined classifier for pattern classification». En: *Pattern Recognition* 39.7, págs. 1215-1229.

Sikdar, Shirsendu *et al.* (2019). «Nondestructive analysis of debonds in a composite structure under variable temperature conditions». En: *Sensors* 19.16, pág. 3454.

Smolensky, Paul (1986). «Information processing in dynamical systems: foundations of harmony theory». En: *Parallel distributed processing: explorations in the microstructure of cognition, foundations* 1, págs. 194-281.

Sohn, Hoon *et al.* (2001). «Structural health monitoring using statistical pattern recognition techniques». En: *J. Dyn. Sys., Meas., Control* 123.4, págs. 706-711.

Tardy, Benjamin *et al.* (2019). «Assessment of optimal transport for operational land-cover mapping using high-resolution satellite images time series without reference data of the mapping period». En: *Remote Sensing* 11.9, pág. 1047.

Taskesen, Erdogan y Marcel JT Reinders (2016). «2D representation of transcriptomes by *t*-SNE exposes relatedness between human tissues». En: *PLOS ONE* 11.2, e0149853.

Tenenbaum, Joshua B *et al.* (2000). «A global geometric framework for nonlinear dimensionality reduction». En: *Science* 290.5500, págs. 2319-2323.

Tibaduiza, DA *et al.* (2013). «Damage classification in structural health monitoring using principal component analysis and self-organizing maps». En: *Structural Control and Health Monitoring* 20.10, págs. 1303-1316.

Tibaduiza, DA *et al.* (2016). «A sensor fault detection methodology applied to piezoelectric active systems in structural health monitoring applications». En: *IOP Conf. Ser. Mater. Sci. Eng*. Vol. 138. 1, pág. 12016.

Tibaduiza, DA *et al.* (2018). «A damage classification approach for structural health monitoring using machine learning». En: *Complexity* 2018.

Tsogka, Chrysoula *et al.* (2017). «The stretching method for vibration-based structural health monitoring of civil structures». En: *Computer-Aided Civil and Infrastructure Engineering* 32.4, págs. 288-303.

Ugarte, Maria Dolores *et al.* (2015). *Probability and Statistics with R*. Chapman y Hall / CRC.

Ullah, Saeed *et al.* (2018). «Nondestructive inspection of reinforced concrete utility poles with ISOMAP and random forest». En: *Sensors* 18.10, pág. 3463.

Van Der Maaten, Laurens (2009). «Learning a parametric embedding by preserving local structure». En: *Proceedings of the 12th International Conference on Artificial Intelligence and Statistics* (Clearwater Beach, Florida). USA, págs. 384-391.

Van Der Maaten, Laurens y Geoffrey E Hinton (2008). «Visualizing data using *t*-SNE». En: *Journal of Machine Learning Research* 9.Nov, págs. 2579-2605.

Vidal, Yolanda *et al.* (2018). «Wind turbine multi-fault detection and classification based on SCADA data». En: *Energies* 11.11, pág. 3018.

Vidal, Yolanda *et al.* (2020). «Structural Health Monitoring for Jacket-Type Offshore Wind Turbines: Experimental Proof of Concept». En: *Sensors* 20.7, pág. 1835.

Vitola, Jaime *et al.* (2017a). «A sensor data fusion system based on *k*-nearest neighbor pattern classification for structural health monitoring applications». En: *Sensors* 17.2, pág. 417.

– (2017b). «Distributed piezoelectric sensor system for damage identification in structures subjected to temperature changes». En: *Sensors* 17.6, pág. 1252.

Ward, Matthew O *et al.* (2015). *Interactive data visualization: foundations, techniques, and applications*. Boca Raton, FL, USA: CRC Press.

Westerhuis, Johan A *et al.* (1999). «Comparing alternative approaches for multivariate statistical analysis of batch process data». En: *Journal of Chemometrics: A Journal of the Chemometrics Society* 13.3-4, págs. 397-413.

Worden, K y EJ Cross (2018). «On switching response surface models, with applications to the structural health monitoring of bridges». En: *Mechanical Systems and Signal Processing* 98, págs. 139-156.

Xu, Fan *et al.* (2019). «Bearing performance degradation assessment based on ensemble empirical mode decomposition and affinity propagation clustering». En: *IEEE Access* 7, págs. 54623-54637.

Yan, Jiajia *et al.* (2019). «Active monitoring of fatigue crack in the weld zone of bogie frames using ultrasonic guided waves». En: *Sensors* 19.15, pág. 3372.